

# Anyonic, cosmic, and chaotic: three faces of Majorana fermions

Proefschrift

ter verkrijging van  
de graad van doctor aan de Universiteit Leiden,  
op gezag van rector magnificus prof. dr. ir. H. Bijl,  
volgens besluit van het college voor promoties  
te verdedigen op donderdag 17 november 2022  
klokke 13.45 uur

door

Yevheniia Ihorivna Cheipesh

geboren te Uzhgorod, Oekraïne  
in 1994

Promotores: Prof. dr. C. W. J. Beenakker  
Dr. A. R. Akhmerov (TU Delft)

Promotiecommissie: Dr. L. Fritz (Universiteit Utrecht)  
Dr. A. Kou  
(University of Illinois, Urbana, USA)  
Prof. dr. J. Aarts  
Prof. dr. K. E. Schalm  
Prof. dr. J. Zaanen

Casimir PhD Series Delft-Leiden 2022-32

ISBN 978-90-8593-542-1

An electronic version of this thesis can be found at <https://openaccess.leidenuniv.nl>

The cover shows artistic representation of the portraits of three scientists that made significant contribution to the fields studied in this thesis. Ettore Majorana (upper right) proposed a solution to the Dirac equation that corresponds to a fermion that can be its own anti-particle. Such fermion was later called Majorana. Alexei Kitaev (left) contributed a lot to the study of the SYK model. Wolfgang Pauli (lower right) invented neutrinos to explain  $\beta$ -decay spectrum of radioactive atoms. The green stripe symbolizes unification of the corresponding topics in this thesis. The plant on the back is Marjoram which in Ukrainian is spelled in the same way as Majorana. The cover is a digital painting made by the author of the thesis.

*To my first scientific mentor, V. Yu Reshetnyak*  
*Моему першому науковому наставнику, В. Ю. Решетняку*



# Contents

<b>1</b>	<b>Introduction</b>	<b>1</b>
1.1	Preface	1
1.2	Majorana fermions as fundamental particles	3
1.2.1	Dirac equation	4
1.2.2	Majorana solution	6
1.3	Majorana fermions in condensed matter physics	6
1.3.1	The need in superconductivity	7
1.3.2	Topologically protected zero modes	8
1.3.3	Andreev levels	10
1.4	Anyonic Majorana fermions	12
1.5	Chaotic Majorana fermions	18
1.5.1	Mean field solution for cSYK	20
1.5.2	SYK in the lab	24
1.6	Cosmic Majorana fermions	26
1.6.1	$\beta$ decay on the surface	29
1.7	This thesis	34
1.7.1	Chapter 2	35
1.7.2	Chapter 3	35
1.7.3	Chapter 4	35
1.7.4	Chapter 5	35
1.7.5	Chapter 6	36
1.7.6	Chapter 7	36
1.7.7	Chapter 8	36
<b>2</b>	<b>Pfaffian formula for fermion parity fluctuations in a superconductor and application to Majorana fusion detection</b>	<b>39</b>
2.1	Introduction	39
2.2	Pfaffian fermion-parity formula	41

2.2.1	Kitaev's formula for an isolated system . . . . .	41
2.2.2	Pfaffian formula for a subsystem . . . . .	42
2.3	Connection with the Majorana fusion rule . . . . .	43
2.4	Random-matrix theory . . . . .	45
2.4.1	Skew Circular Real Ensemble . . . . .	45
2.4.2	Distribution of the local fermion parity in the skew-CRE . . . . .	47
2.4.3	RMT model of weakly coupled quantum dots . . . . .	49
2.5	Effect of an isolated Majorana zero-mode . . . . .	52
2.6	Conclusion . . . . .	52
2.7	Appendix: Derivation of the Pfaffian formula from Klich's counting statistics theory . . . . .	53
2.8	Appendix: Moments of determinants of antisymmetric random matrices . . . . .	56
2.8.1	Principal minor of antisymmetric orthogonal matrix . . . . .	56
2.8.2	Antisymmetric Hermitian matrix . . . . .	57
<b>3</b>	<b>Dynamical signatures of ground-state degeneracy to discriminate against Andreev Levels in a Majorana fusion experiment</b>	<b>59</b>
3.1	Introduction . . . . .	59
3.2	Adiabatic evolution to test for ground-state degeneracy . . . . .	60
3.3	Topologically degenerate ground state . . . . .	62
3.4	Accidentally degenerate Andreev levels . . . . .	63
3.5	Conclusion . . . . .	67
<b>4</b>	<b>Reentrant superconductivity in a quantum dot coupled to a Sachdev-Ye-Kitaev metal</b>	<b>69</b>
4.1	Introduction . . . . .	69
4.2	Main part . . . . .	70
4.3	Conclusion . . . . .	77
4.4	Appendix: Derivation of the gap equation . . . . .	78
4.5	Appendix: Saddle-point numerical analysis . . . . .	80
4.5.1	The algorithm . . . . .	80
4.5.2	Precision and grid . . . . .	82
<b>5</b>	<b>Quantum tunneling dynamics in a complex-valued Sachdev-Ye-Kitaev model quench-coupled to a cool bath</b>	<b>85</b>
5.1	Introduction . . . . .	85
5.2	The model . . . . .	86
5.3	Relaxation after the quench . . . . .	88

5.4	Tunneling current . . . . .	93
5.5	Conclusion . . . . .	97
5.6	Appendix: Derivation of the Kadanoff-Baym equations from the SYK saddle-point . . . . .	98
5.6.1	Saddle-point equations . . . . .	98
5.6.2	Reservoir as an external potential . . . . .	100
5.6.3	Dynamics of the SYK subsystem . . . . .	101
<b>6</b>	<b>Navigating the pitfalls of relic neutrino detection</b>	<b>103</b>
6.1	Introduction . . . . .	103
6.2	Defining the problem . . . . .	105
6.3	Estimate . . . . .	108
6.4	Discussion . . . . .	110
6.5	Appendix: Quantum derivation of the energy uncertainty . . . . .	112
<b>7</b>	<b>Can we use heavy nuclei to detect relic neutrinos?</b>	<b>117</b>
7.1	Introduction . . . . .	117
7.2	Quantum mechanics of $\beta$ -interaction and crude estimate of neutrino capture . . . . .	119
7.2.1	Crude estimate of neutrino capture . . . . .	121
7.3	Experimental determination of the neutrino capture rate from the end of the $\beta$ decay spectrum . . . . .	123
7.4	Conclusion and discussion . . . . .	125
<b>8</b>	<b>Screening effects in the graphene-based relic neutrino detection experiment</b>	<b>129</b>
8.1	Introduction. . . . .	129
8.2	Defining the problem . . . . .	130
8.3	Charge screening effects . . . . .	132
8.4	Electron-hole pair creation . . . . .	135
8.5	Conclusions . . . . .	136
8.6	Appendix: Average work performed by the electrons in graphene on the emitted $\beta$ -electron . . . . .	137
8.7	Appendix: Cross section of the process of the electron-hole creation in graphene . . . . .	139
	<b>Bibliography</b>	<b>143</b>
	<b>Summary</b>	<b>163</b>

<b>Samenvatting</b>	<b>165</b>
<b>Curriculum Vitæ</b>	<b>167</b>
<b>List of Publications</b>	<b>169</b>

# Chapter 1

## Introduction

### 1.1 Preface

This thesis is devoted to the study of a model that finds useful and important applications in a wide range of physical systems, from cosmology and particle physics to condensed matter physics and quantum computers. It tries to support the idea that working on the intersection of different fields of physics is extremely fruitful and that studying low energy effective field theories can give us a lot of insight about high energy fundamental theories.

The state of the art of modern physics describes matter as consisting of fermionic particles that interact through bosonic mediators (with the Higgs boson playing yet another special role). Attempts to build a closed, complete and self-consistent quantum mechanical description of atomic and sub-atomic physics started at the beginning of 20th century and culminated in the so-called Standard Model [1]. At the moment, it describes a zoo of all particles that have been detected so far. These particles have many interesting and peculiar properties such as chiral interactions, non-abelian symmetries, etc. To study them, particle physicists build larger and larger facilities such as accelerators, colliders, gigantic detectors.

A complementary avenue to study the properties of the particles on low energy scales is provided by condensed matter physics. Both at the high-(particle physics) and low-energy end (condensed matter physics), physics is of irreducible emergent many-particle nature and it is only in the middle (atomic and nuclear physics) that few-particle systems come into play. Collective degrees of freedom of a many-body system can be described by so-called “quasi particles” [2]. Such many-body systems are governed by qual-

itatively new principles (also called “laws of emergent behaviours”), compared to few-particle systems [3].

The properties of these quasi-particles such as statistic, charge, effective mass, etc. are typically defined not by the microscopic details, but by the universal properties of the system, *e.g.* its symmetries. Modern technologies allow to fabricate complex many-body systems that can host quasi particles with predefined properties, which can be probed experimentally. On the other hand, the principle of adiabatic continuity allows us to study such systems theoretically. One can forget about microscopic details and consider simpler “toy” effective models with specified symmetries [3].

One interesting and yet not fully studied example are the so-called Majorana fermions – neutral particles with fermionic (or, in general, anyonic) statistics that have a peculiar property: they can be considered as their own anti-particles [4]. Although no elementary particles has so far been confirmed to be a Majorana fermion, they play a very important role both in fundamental and applied physics. From the point of the former, there are several reasons to consider Majorana fermions:

1. ordinary Standard Model neutrinos may appear to be Majorana fermions. This possibility is being tested in, *e.g.*, experiments of the so-called neutrino-less double  $\beta$  decay [5–7].
2. despite the great experimental success of the Standard Model, which has been verified to a high precision in thousands of different channels, we know for sure that it is incomplete. This means that there should exist some new particles. Majorana fermions could be a very good candidate for several reasons:
  - (a) Majorana fermions have been proposed as a dark matter particle (*e.g.* WIMPs, sterile neutrinos) [8–10].
  - (b) a Majorana lepton breaks lepton number conservation. This is the key element of the so-called thermal leptogenesis – one of the most popular mechanisms for the explanation of the matter-antimatter asymmetry [11, 12].
  - (c) the Majorana mass of right-handed neutrinos provides a very natural explanation of the minuteness of normal neutrino masses (seesaw mechanism) [13].

We do not know what is the correct extension of the Standard Model. Even if Majoranas are not the right candidates and do not exist in nature as

a fundamental particle, we are still left with a lot of motivation to study them from the perspective of mesoscopic physics, where they can be constructed out of electron and hole excitations [14–16].

Recently, there has been a lot of attention to so-called *Majorana zero modes* (MZMs) – subgap states in superconductors [16–19]. There they arise as a quasiparticle excitation localized at the boundaries. Such MZMs are spatially separated, pinned to have exactly zero energy and free of decoherence thanks to the particle-hole symmetry of the superconducting state. Moreover, unlike ordinary fermions and bosons, they have a non-abelian anyonic statistics under the exchange. Thanks to these properties one can use them as building blocks for a protected quantum memory [17, 20, 21] for a fault-tolerant quantum computer.

The effective low energy field theory of the MZMs in superconductors is a non-interacting theory. A very interesting physics emerges also if one looks at a different end - strongly interacting Majorana modes in the many-body systems. If one couples  $N \gg 1$  such modes in a way that the coupling is all-to-all and random [22, 23], the resulting system would have a non-Fermi liquid phase, where there is no clear Fermi surface even at zero temperature and the description of the system in terms of quasiparticles is not possible [24]. The theoretical toy model for such system is called Sachdev-Ye-Kitaev (SYK) model [25, 26] and it appears to be theoretically solvable under the mean-field approximation. It can be fruitful to study this toy model since there is still a need in the development of a general theory of the non-Fermi liquid ground state(s) of an interacting many-body fermionic system [24] and there are hints that SYK is capable of describing them to some extent. For example, the SYK model can reproduce some aspects of certain strongly correlated materials called strange metals [27]. Moreover, such a toy model has an emergent conformal symmetry in the infrared and saturates the upper bound on quantum chaos [28]. These aspects led to considering the SYK model to be a holographic dual of black hole horizons [29–31].

The points mentioned above are only a small part of the extensive list of arguments that make Majorana fermions an extremely interesting and rich subject of study.

## 1.2 Majorana fermions as fundamental particles

We start our investigation by looking at how the Majorana fermions emerge as elementary particles - real solutions of the fundamental Dirac equation [4].

### 1.2.1 Dirac equation

The first attempt to write a relativistic version of the Schrödinger equation  $i\hbar\partial_t|\psi\rangle = \frac{\hat{p}^2}{2m}|\psi\rangle$  was made by Oskar Klein and Walter Gordon in 1926 by following the same logic of exploiting the dispersion relation, but in the relativistic form  $E = \sqrt{p^2c^2 + m^2c^4}$  [32, 33]. However, such operator would be non-local, which is incompatible with the finite speed of light propagation. To get the local equation one needs to take the square of the dispersion relation, arriving to the famous Klein-Gordon equation  $(\square + (\frac{mc}{\hbar})^2)\psi = 0$ , where  $\square = g^{\mu\nu}\partial_\mu\partial_\nu = \frac{1}{c^2}\partial_t^2 - \nabla^2$  is a Lorentz-invariant combination.

However, the total probability  $P = \int d\vec{r}|\psi(\vec{r}, t)|^2$ , that used to be positive definite and conserved in time for the states obeying Schrödinger equation, loses its probabilistic interpretation in the Klein-Gordon equation, since we have also included the negative energy states when we took the square of  $E(p)$ . Indeed, the zeroth component of the conserved current  $J_\mu \sim \psi^*\partial_\mu\psi - \psi\partial_\mu\psi^*$  can not be treated as the probability density since  $J_0 = -\frac{\hbar|\psi|^2}{mc^2}\frac{\partial\arg(\psi)}{\partial t}$  can change sign.<sup>1</sup>

An alternative equation, proposed by Dirac in 1928, had the form of  $i\hbar\partial_t|\psi\rangle = \hat{H}|\psi\rangle$  with  $\hat{H} = \boldsymbol{\alpha} \cdot \hat{\mathbf{p}} + \beta m$  [32, 34]. In this case the probabilistic interpretation occurs automatically as the probability density is conserved for such equation with any Hermitian  $\hat{H}$ . Let us first consider the case of zero mass  $m = 0$ . Then, it can be shown that  $\alpha_i$  do not commute, but rather satisfy  $\{\alpha_i, \alpha_j\} = 2\delta_j^i$  which means that they are not numbers but matrices. One can also show that these matrices should be Hermitian, even-dimensional, traceless and that their eigenvalues are  $\pm 1$ . The minimal set that satisfies these conditions are Pauli matrices  $\sigma_{x,y,z}$  and the corresponding form of the Dirac equation is called *Weyl equation*  $i\sigma^\mu\partial_\mu|\psi\rangle = 0$ <sup>2</sup>. Let us call *right spinor*  $\psi_R$  the 2-component wave function  $\psi = (\psi_1, \psi_2)$  that is the solution of the corresponding Weyl equation. However, one can see that there is also another choice of  $\alpha^i = -\sigma^i$  compatible with all the constraints that leads to the Weyl equation on left spinor  $i\bar{\sigma}^\mu\partial_\mu\psi_L = 0$ , where  $\bar{\sigma}^\mu = (1, -\sigma^i)$ . The names left and right come from the fact that one spinor relates to another through a parity transformation  $P : \mathbf{r} \rightarrow -\mathbf{r}$  such that  $\psi_L = \hat{P}\psi_R$ .

Now let us try to introduce the mass into this equation. An important ob-

---

The contents of this chapter is mostly based on textbook material, for example one can follow the references [32]

<sup>1</sup>Klein-Gordon equation is, in essence, classical equation.

<sup>2</sup>Where we introduced the 4-vector  $\sigma^\mu = (1, \sigma^i)$ .

servation in this regard is that in order for the theory to be Lorentz-covariant, namely  $i\sigma^\mu \partial'_\mu \psi'_R = i\sigma^\mu \Lambda_\nu^\mu \partial^\nu S_R \psi_R = S (i\sigma^\mu \partial_\mu \psi_R) = 0$ <sup>3</sup> (and the same holds for  $\psi_L$  but with some other matrices  $S_L, \tilde{S}$ ), one has to require  $S = S_L$  and  $\tilde{S} = S_R$ . In other words, the equation for the right spinor transforms as the left spinor and vice versa. This leads to the fact that the mass would mix right and left spinors since it is the only Lorentz-covariant way to introduce it

$$\begin{cases} i\sigma_\mu \partial^\mu \psi_R = m\psi_L \\ i\bar{\sigma}_\mu \partial^\mu \psi_L = m\psi_R \end{cases} . \quad (1.1)$$

Introducing the *Dirac spinor*  $\Psi^T = (\psi_L, \psi_R)$  and the matrices  $\gamma^\mu = \begin{pmatrix} 0 & \sigma^\mu \\ \bar{\sigma}^\mu & 0 \end{pmatrix}$ , equations 1.1 become

$$(i\gamma_\mu \partial^\mu - m) \Psi = 0. \quad (1.2)$$

This representation of  $\gamma$ -matrices is not unique and is called *Weyl representation*.

Since the Hamiltonian of the Dirac equation commutes with  $p^\mu$  the solutions are of a plane wave form with some spinor structure  $\Psi(x) = u(p)e^{-ip^\mu x_\mu}$ . By plugging it in the equation 1.2 and requiring to have a non-trivial solution for  $u(p)$  we arrive at the constraint on the two solutions:  $E = \pm\sqrt{\mathbf{p}^2 + m^2}$ . Therefore, the general solution to the Dirac equation takes form  $\Psi(x) = u(p)e^{-ip^\mu x_\mu} + v(p)e^{+ip^\mu x_\mu}$ , where the spinors  $u(p), v(p)$  have the interpretation of the particle and anti-particle.

The particle/antiparticle nature of the two solutions to the Dirac equation can be seen if one tries to build the positive energy counter-part  $\psi_c$  to the negative energy solution  $\psi = v(p)e^{ip^\mu x_\mu}$ . One can convince themselves that simple complex conjugation will not work and one should instead take  $\psi_c = \hat{C}\psi^*$ , where  $\hat{C} = i\gamma^2$ . Only in this case the opposite energy states  $\psi$  and  $\psi_c$  simultaneously solve Dirac equation. Physically,  $\hat{C}$  is the operator of the charge conjugation, since in the presence of the electromagnetic field  $\psi_c$  satisfies the equation  $(i\gamma^\mu(\partial_\mu + eA_\mu) - m)\psi_c = 0$ , while for  $\psi$  the charge is opposite. This interpretation of the negative energy states comes very handy as it saves us from the catastrophe of the infinite negative energy sea of states (so-called Dirac sea).

---

<sup>3</sup>Where  $\Lambda_\nu^\mu$  is a boost matrix.

### 1.2.2 Majorana solution

In 1937, before disappearing, Majorana posed the question of whether we could look for a real solution to the Dirac equation [4]. This would be possible if one imposed the following constraint on the  $\gamma$  matrices present in the Dirac equation:  $(i\hat{\gamma}^\mu)^* = i\hat{\gamma}^\mu$  (Majorana representation)<sup>4</sup>. Since the charge conjugation operator is generally chosen such that  $-\hat{\gamma}^\mu\hat{C} = \hat{C}(\hat{\gamma}^\mu)^*$ , for Majorana representation it commutes with  $\gamma$ -matrices and therefore the Majorana solutions are also eigenstates of the charge conjugation operator. In other words, the Majorana particle is electrically neutral and hence its own antiparticle  $\Psi_c \equiv \hat{C}\Psi = \Psi$ . The latter relation is what defines a Majorana particle in any representation and is called *Majorana condition*.

The Majorana solution can be written both in terms of a real four-component spinor, and as a complex two-component spinor. The equation on this two-component spinor can be understood from the following consideration. The charge conjugation operator in the Majorana representation is just a complex conjugation. This means that it changes the momentum of the state, but not the spin. For the massless case it would mean that the charge conjugation operator transforms the left spinor into the right<sup>5</sup>, namely  $\chi_{L/R}^c = \chi_{R/L}$ . The Majorana spinor  $\chi$  satisfies the equation

$$i\sigma^\mu\partial_\mu\chi - m\chi^c = 0. \quad (1.3)$$

## 1.3 Majorana fermions in condensed matter physics

Now when we are familiar with the Majorana fermions on the fundamental level, let us see how these (quasi)particles emerge in many-body condensed matter systems as effective low-energy degrees of freedom. The connection of the effective description of the low energy modes in many-body systems with the fundamental equations is very frequent with the most obvious example being graphene [35], followed by Weyl semimetals [36], etc. This should not be surprising, as the theory on low energies does not “see” the microscopic structure of the material, only its global symmetries.

---

<sup>4</sup>We note that the solutions *can* be real, but they do not need to, same as for the case of Klein-Gordon or Maxwell equations

<sup>5</sup>Dirac Hamiltonian commutes with the so-called helicity operator  $\hat{h} = \hat{p} \cdot \hat{\Sigma}/|p|$ . When  $m = 0$ ,  $\gamma_5$  also commutes with  $H$  and therefore the eigenstates have both fixed helicity and parity.

### 1.3.1 The need in superconductivity

Majorana fermions may or may not exist in Nature as elementary building blocks, but in condensed matter they can be constructed out of electron and hole excitations. In order to get the excitation that is charge neutral one needs superconductivity where the quasiparticles are coherent superpositions of electrons and holes – so-called *Bogoliubov quasiparticles*.

The mean-field Bardeen–Cooper–Schrieffer (BCS) Hamiltonian [37, 38] describing the conventional s-wave (the meaning of it will be elaborated further) superconductor is quadratic but includes so-called anomalous terms

$$H_{\text{BCS}} = \sum_{\mathbf{k}} \left[ (\varepsilon_{\mathbf{k}} - \mu) (c_{\mathbf{k},\uparrow}^\dagger c_{\mathbf{k},\uparrow} + c_{-\mathbf{k},\downarrow}^\dagger c_{-\mathbf{k},\downarrow}) + \Delta^* c_{-\mathbf{k},\downarrow} c_{\mathbf{k},\uparrow} + \Delta c_{\mathbf{k},\uparrow}^\dagger c_{-\mathbf{k},\downarrow}^\dagger \right], \quad (1.4)$$

where  $\Delta = \frac{g_0}{V} \sum_{\mathbf{k}} \langle c_{-\mathbf{k},\downarrow} c_{\mathbf{k},\uparrow} \rangle$ ,  $V$  is a system volume and  $g_0$  is some positive interaction constant.

Such kind of Hamiltonians are known to be diagonalized by the so-called Bogoliubov transformation which is in essence a rotation in the particle-hole space

$$\begin{aligned} \gamma_{\mathbf{k},1}^\dagger &= u_{\mathbf{k}} c_{\mathbf{k},\uparrow}^\dagger + v_{\mathbf{k}} c_{-\mathbf{k},\downarrow} \\ \gamma_{-\mathbf{k},2} &= v_{\mathbf{k}}^* c_{\mathbf{k},\uparrow}^\dagger - u_{\mathbf{k}}^* c_{-\mathbf{k},\downarrow} \end{aligned} \quad (1.5)$$

with the condition that  $u_{\mathbf{k}}^2 + v_{\mathbf{k}}^2 = 1$  and canonical commutation relations on quasiparticles  $\{\gamma_{\mathbf{k},\alpha}, \gamma_{\mathbf{k}',\beta}^\dagger\} = \delta_{\mathbf{k},\mathbf{k}'} \delta_{\alpha,\beta}$ . The Hamiltonian becomes diagonal  $H_{\text{BCS}} = \sum_{\mathbf{k}} E_{\mathbf{k}} (\gamma_{\mathbf{k},1}^\dagger \gamma_{\mathbf{k},1} + \gamma_{\mathbf{k},2}^\dagger \gamma_{\mathbf{k},2}) + E_0$  with the eigenvalues

$$E_{\mathbf{k}} = \sqrt{(\varepsilon_{\mathbf{k}} - \mu)^2 + |\Delta|^2} \quad (1.6)$$

We can view  $\gamma_{-\mathbf{k},2}$  as a creation operator of the particle with the negative energy and then the spectrum would look symmetric around  $E = 0$ . This means that the system has particle-hole symmetry – each eigenfunction  $\Psi$  at energy  $E > 0$  has a copy  $\Psi' = \hat{C}\Psi$  at energy  $-E$ , where  $\hat{C}$  is a charge conjugation operator. Only at zero energy the particle and antiparticle can coincide which means that despite the fact that the quasiparticle excitations are coherent superposition of the particle and hole, we can not have Majorana quasiparticles in such a system because it would mean that we need to close the energy gap. Naively, if we allow for the superconducting gap  $\Delta$  to become

$k$ -dependent this obstacle can be bypassed and we can close the gap<sup>6</sup>.

Let us consider a more general case where the Cooper pairing correlation (gap parameter) is a  $k$ -dependent tensor  $\Delta_{\alpha\beta}(\mathbf{k}) \propto \langle c_{\alpha}(\mathbf{k})c_{\beta}(-\mathbf{k}) \rangle$  with  $\alpha, \beta$  being the spin indices. When there is no spin-orbit coupling, both the spin and the momentum are good quantum numbers, and one can separate  $\Delta_{\alpha\beta}(\mathbf{k}) = \chi_{\alpha\beta}\Delta(\mathbf{k})$  with  $\chi_{\alpha\beta}$  a spinor matrix and  $\Delta(\mathbf{k})$  a function. Then, there are two possibilities:

1.  $\chi_{\alpha\beta} = -\chi_{\beta\alpha}, \Delta(\mathbf{k}) = \Delta(-\mathbf{k})$  – the spin-singlet pairing.
2.  $\chi_{\alpha\beta} = \chi_{\beta\alpha}, \Delta(\mathbf{k}) = -\Delta(-\mathbf{k})$  – the spin-triplet pairing.

One can write a general form of the order parameter as

$$\Delta_{\alpha\beta}(\mathbf{k}) = (\Delta_0(\mathbf{k}) + \mathbf{d}(\mathbf{k}) \cdot \boldsymbol{\sigma}) (i\sigma_2)_{\alpha\beta}, \quad (1.7)$$

where  $\Delta_0(\mathbf{k})$  encodes the singlet component and  $\mathbf{d}(\mathbf{k})$  is a vector encoding the triplet state. Their functional dependence is generally unknown and depends on the particular lattice under consideration.

### 1.3.2 Topologically protected zero modes

If we do not have translational invariance in the system namely we have a system with an edge or a defect and if on top of that we also break the spin conservation, we can build Bogoliubov quasiparticle out of the creation and annihilation operator of the same mode [17, 39]

$$\begin{aligned} \gamma_{n1} &= c_n + c_n^\dagger \\ \gamma_{n2} &= i(c_n - c_n^\dagger). \end{aligned} \quad (1.8)$$

One can also think about it as simply a change of the basis where we double the degrees of freedom going to real modes – *Majorana representation*. For the systems with particle-hole symmetry we have a requirement that such states come in pairs at  $\pm E$  with the possibility of an unpaired state at  $E = 0$ . The simplest example of the appearance of such a Majorana zero modes (MZM) is in the toy model called Kitaev chain [17]. There, the two MZMs are localized at the ends of the fermion chain.

Thanks to the particle-hole symmetry, the state at  $E = 0$  is protected against any local perturbation that does not break particle-hole symmetry –

---

<sup>6</sup>Due to the symmetry of the spectrum with respect to  $\vec{k} \rightarrow -\vec{k}$  this would be at the  $k = 0$  or  $k = \pm\pi$  points.

it simply is not able to shift from zero since the spectrum should be symmetric [15]. Such state is called *topologically protected*. One can also think about it as following - the Hamiltonian that has particle-hole symmetry commutes with the parity operator which means that different parity sectors are decoupled. The presence or absence of the zero energy state correspond to parity odd sectors. The only way for such state to disappear would be to bring the two Majorana modes that encode it close to each other such that their wave functions overlap. In this case the ground state will split and no longer be degenerate. For the example of the Kitaev chain it means that if the chain has finite length  $L$  then the state with MZMs at the end of the wire will have the energy of order  $\varepsilon \sim e^{-L}$  instead of zero.

The presence or absence of the unpaired zero energy level is therefore in one-to-one mapping with the parity of the ground state that is a topological invariant protected by the particle-hole symmetry. Kitaev identified this invariant to be defined by the Pfaffian of the Hamiltonian in the basis of Majorana fermions  $H = \frac{1}{2}\gamma \cdot \mathcal{A} \cdot \gamma$ ,  $\mathcal{P}_0 = \text{signPf}(-i\mathcal{A})$ <sup>7</sup> [17]. The transition involving the change of the sign of the Pfaffian should necessarily involve closing of the gap.

It appears, that such topologically protected MZMs can appear not only in the toy models, but rather in real materials. We can depart from the superconductor with the presence of a defect or a boundary and see which additional constraints we have to impose. The first important ingredient to this story is that the zero energy level should be non-degenerate otherwise the two states at  $E = 0$  can merge as  $|11\rangle \rightarrow |00\rangle$ <sup>8</sup>. This process is not forbidden in the superconductor since the latter only preserves the parity, not the particle number. It is known that the half-integer states in the system that has time reversal symmetry are doubly degenerate – so-called Kramers degeneracy [40]. The time-reversal operator changes both the direction of the spin and momentum. The two possible ways to break it are:

1. Take a  $p$ -wave superconductor with  $\Delta_{\alpha\beta}(\mathbf{k}) \propto \begin{pmatrix} 1 & 0 \\ 0 & 0 \end{pmatrix} (k_x + ik_y)$  [15, 18, 41]. Such superconductors are called unconventional which reflects the fact that they are extremely rare in nature. Moreover,  $p$ -wave pairing is fragile, easily destroyed by disorder.

---

<sup>7</sup>The fact that the Hamiltonian can be represented as  $H = i\mathcal{A}$ , where  $\mathcal{A}$  is a real antisymmetric matrix follows from the particle-hole symmetry which is just  $H^* = -H$  in Majorana basis.

<sup>8</sup>Here we denote by  $|1\rangle$  the presence of the state at zero energy.

2. A much simpler solution is to introduce the magnetic field that would break the time-reversal symmetry. Since the magnetic field is repelled from the superconductor (Meissner effect) and can only penetrate it in the form of vortices, we introduce superconductivity by proximitizing the semi-conductor with the superconductor. We take the *s*-wave superconductor since most superconductors in nature are of this kind. A singlet superconductor, however, has an important property: the total spin of every excitation is conserved. Zeeman field conserves the spin in *z*-direction, so together every single state of our system has to have a definite spin, including the Majoranas. Majoranas are their own particle-hole partners, and that means that they cannot have any spin (energy, charge, or any other observable property at all). This would mean that in such a system they can not appear. Therefore, the spin conservation needs to be broken and the simplest plausible way to do so is via the spin-orbit coupling (also referred to as Rashba coupling).

To conclude this analysis, in the system that consists of the semi-conductor, proximitized by the *s*-wave superconductor, with magnetic field and spin-orbit coupling one can have Majorana zero modes bound to a defect or a boundary that are spatially separated and protected from the local perturbations. Indeed, it happens so that by varying the strength of the magnetic field, chemical potential and superconducting gap one can close the gap in the energy spectrum and reopen it entering the so-called topological phase with the protected zero energy level.

There exist many proposals for the experimental realization of the topologically protected Majorana zero modes including chiral *p*-wave superconductors [42, 43], topological insulators in the proximity to the *s*-wave superconductor [16], semiconductors with Rashba spin-orbit coupling [19, 44, 45] (see Fig. 1.1).

### 1.3.3 Andreev levels

As was discussed above, the spectrum of the ideal topological superconductor under the mean field approximation is gapped (the gap being the mean field order parameter), so the zero energy level (if present) is well separated from the continuum. But is it still same for the “dirty” system with some disorder? The tool that can describe universal properties of disordered metals and superconductors [46, 47] depending on the symmetry class that it belongs to [48] is called Random matrix theory (RMT). The main idea is that instead

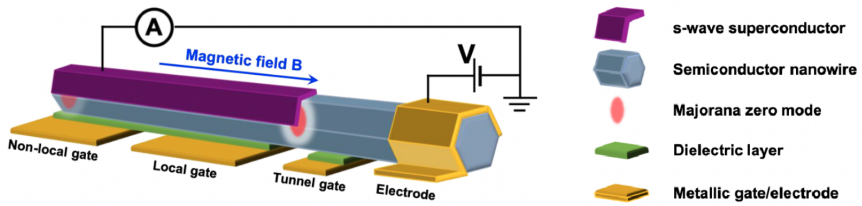


**Figure 1.1.** Schematic experimental setup of Majorana nanowire device. *The figure is reprinted with permission from Zhang, Hao, Dong E. Liu, Michael Wimmer, and Leo P. Kouwenhoven, Nature communications 10, no. 1, (2019)*

of considering one “ideal” Hamiltonian we take an ensemble of the Hamiltonians with some probability distribution  $P(H) \sim \exp(-\frac{c}{N} \text{Tr}H^2)$  where  $c$  is a parameter that is the same for the classes of Hamiltonians that share same universal symmetries [46].

When classifying the Hamiltonian classes we look only on anti-unitary symmetries that come in two types: the Hamiltonian can either commute (time-reversal symmetry) or anti-commute (particle-hole symmetry) with the anti-unitary operator. All the unitary symmetries can be disregarded by restricting ourselves to one symmetry sector (block in the Hamiltonian matrix) and the unitary symmetry that anti-commutes with the Hamiltonian (called chiral symmetry) can be obtained as a product of particle-hole and time-reversal operators [49]. According to this, different combinations of these “non-reducible” symmetries give us 10 different classes of Hamiltonians [48] (corresponding to all the possible combinations of the symmetries).

In case of the systems that can host topologically protected Majorana zero modes, the spin-rotation symmetry is broken by spin-orbit coupling, while the particle-hole symmetry is present. The corresponding systems are in symmetry class D.

If one looks at the ensemble-averaged density of states for the class D system (Fig. 1.2), one would see that in the topologically non-trivial phase (green color and red delta-function contribution) there is a clear zero energy mode (corresponding to MZMs) that is well separated from the continuum – there is a dip in the density of states around zero. However, despite the fact that there is no sharp line at  $E = 0$  for the topologically trivial case, the density of states is still peaked around zero [48, 50, 51].

This poses a fundamental obstacle on the route to measuring topologically protected zero modes since the accidentally low lying states (also called Andreev levels) in the trivial phase can mimic the true MZMs in the observables.

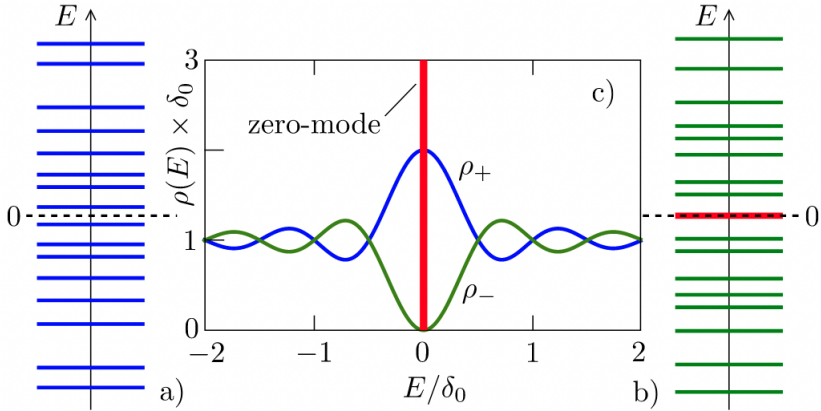


**Figure 1.2.** Panels a) and b) show the spectrum of a class-D superconductor. The unpaired MZMs are present on panel b). In the middle: the ensemble-averaged density of states. The green line and the delta-function contribution from the zero-mode correspond to the topological phase, while the blue line - to the trivial phase. *The figure is reprinted with permission from Beenakker, C. W. J, Reviews of Modern Physics, 2015*

The particular case when the observable is the parity of the sub-system of the system with  $2N$  MaZMs is considered in Chapter 1.7.1 and Chapter 1.7.2.

## 1.4 Anyonic Majorana fermions

By definition, Majorana zero modes (MZMs) are real ( $\gamma_i^\dagger = \gamma_i$ ) so we need two of them to encode a single complex fermion (each Majorana is an equal-weight superposition of the electron and hole excitation, Eq. 1.8). Moreover, in case of the topologically protected MZMs bound to defects or at the boundaries, such a fermion is de-localized.

For  $N$  zero energy levels we have  $2N$  Majoranas and the degeneracy of the ground state is  $2^N$ . The degeneracy of the ground state is a key element to the most valuable property of the topological superconductors - the non-Abelian statistic of the MZMs under the adiabatic exchange between one another

$$|\Psi\rangle \rightarrow \hat{U} |\Psi\rangle, \quad \text{where } U_{nm} = \exp\left(\pm \frac{\pi}{4} \gamma_n \gamma_m\right) = \frac{1}{\sqrt{2}} (1 \pm \gamma_n \gamma_m). \quad (1.9)$$

Such exchange of two MZMs out of the group is called *braiding* and is a key element in building the quantum computer – with its help we can construct

gates and operate the state. In case when the MZMs are bound to vortex cores, it can be realized when a vortex from one pair is adiabatically<sup>9</sup> moved around a vortex from the other pair at a large distance without ever approaching it. Each of the two selected MZMs can be seen as one fermionic mode with fixed parity  $P_n = 1 - 2c_n^\dagger c_n \equiv i\gamma_{2n-1}\gamma_{2n}$ . Despite the fact that the total parity  $P_{\text{tot}} = \prod_n P_n$  is conserved, the parity of each pair can be changed during braiding, the procedure called *quantum state transfer*.

In order to have a fully functional quantum computer, we need to be able to generate arbitrary  $n$ -qubit unitary gate. However, not all the unitary operations can be performed using braiding [52, 53]. For the single-qubit operation we need the minimal set of 4 MZMs such that the qubit for the case of the odd total parity can be encoded depending on where does the fermion “sit”:  $|0\rangle \equiv |+\rangle|-\rangle, |0\rangle \equiv |-\rangle|+\rangle$ <sup>10</sup> (see Fig. 1.3, panel a) for an example of implementation of the qubit on 4 MZMs bound to vortices). Exchange of two MZMs (also called “half-braid”) corresponds to the square root of the Pauli matrices  $\sqrt{\sigma_i}$  depending on which Majoranas are getting exchanged [14]<sup>11</sup> (example of the implementation of  $\sqrt{\sigma_x}$  can be seen on Fig. 1.3, panel c)). The latter correspond to the rotation of the qubit by  $\pi/2$  with respect to the orthogonal axes on the Bloch sphere. It can be shown, that if we add a  $\pi/4$  rotation around z-axis to our set of operations, a rotation by an arbitrary angle around any axis can be approximated with arbitrary accuracy [54]. However, that  $\pi/4$  rotation which is also called T-gate can not be realized with braiding [14].

In order to construct any multi-qubit unitary operation, one needs a combination of a two-qubit gate (e.g CNOT that flips or not the state of the target qubit depending on the state of the control qubit) with single-qubit rotations [55]. The latter can be realized if we add the parity measurement that define the last step of the operation and the ancilla qubit [14] (see Fig. 1.4, left panel).

Braiding operation is very non-trivial and yet no one has succeeded in performing it. The MZMs bound to a defect or the end-point of a nanowire (as compared to the quantum Hall edge states) are immobile and therefore most proposals to demonstrate non-Abelian statistics generate the unitary braiding operation without physically moving the zero-modes in real space [20, 56–59]. Instead, the braiding is done in the parametric space. In the tri-junction

<sup>9</sup>The adiabaticity of the process is important to avoid Landau-Zener transitions.

<sup>10</sup>Equivalently, we could encode the qubit in the states  $|-\rangle|-\rangle, |+\rangle|+\rangle$  if the total parity is even.

<sup>11</sup>For  $\sqrt{\sigma_x}$  corresponds to the exchange of Majorana 2 and 3,  $\sqrt{\sigma_y}$  - to the exchange of Majorana 1 and 3 and  $\sqrt{\sigma_z}$  - to the exchange of Majorana 1 and 2.

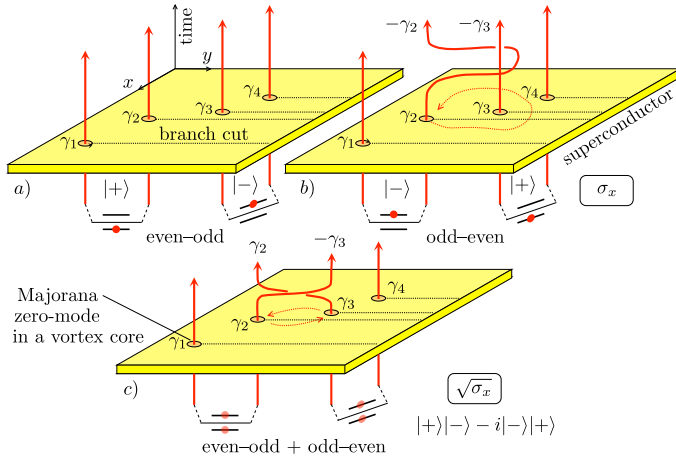


**Figure 1.3.** Panel a): a qubit  $|0\rangle \equiv |+\rangle |-\rangle$ ,  $|1\rangle \equiv |-\rangle |+\rangle$  built out of the four Majorana zero modes bound to vortices. Panel b) and c): operations  $\sigma_x$ ,  $\sqrt{\sigma_x}$  respectively performed by exchanging the vortices. *The figure is reprinted with permission from Beenakker, C. W. J, SciPost Phys. Lect. Notes, 2020*

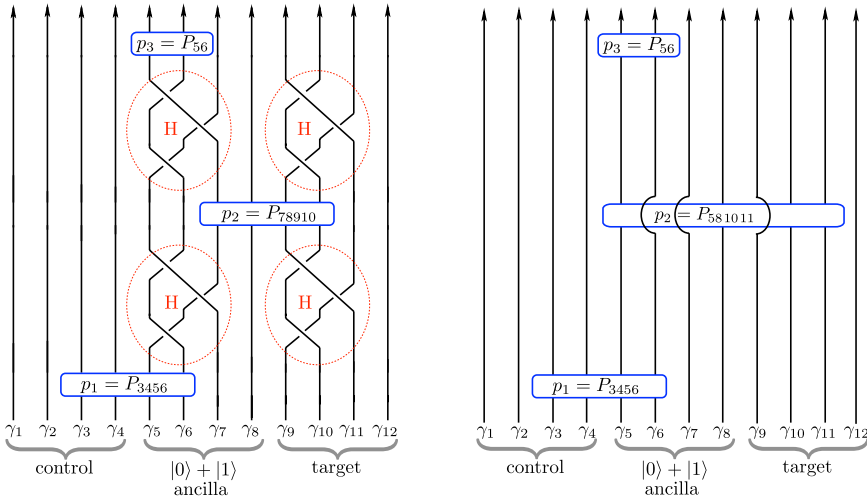


**Figure 1.4.** Two-qubit CNOT gate realized through braiding (left) and solely realized by projective parity measurements. *The figure is reprinted with permission from Beenakker, C. W. J, SciPost Phys. Lect. Notes, 2020*

introduced by Alicea et al. [20] by varying the couplings between Majoranas  $H(t) = \sum_{i=1}^3 \Delta_i(t) i\gamma_0 \gamma_i$  and can transfer a Majorana zero-mode is transferred

from one end point to another (see Fig. 1.5). On practice, this can be either done by the electrostatic control using gate voltage [60] or by magnetic control tuning the magnetic flux through the Josephson junctions (see Fig 1.6) [57]. The advantage of the latter over the former is in the fact that the charge-sensitivity can be switched on and off with exponential accuracy by varying the magnetic flux through a split Josephson junction [61]. This gives us a macroscopic handle on the interaction of pairs of Majorana fermions.

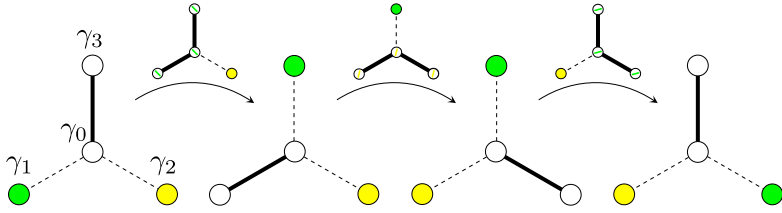


**Figure 1.5.** Braiding of Majorana zero modes ( $\gamma_1$  and  $\gamma_2$  in tri-junction.)  $\gamma_0$  is an effective zero mode created when three MZMs got coupled in the middle of the tri-junction. To perform the braiding operation, one varies the couplings between the MZMs, thick lines denoting coupled Majoranas while dashed lines - decoupled. *The figure is reprinted with permission from Beenakker, C. W. J, SciPost Phys. Lect. Notes, 2020*

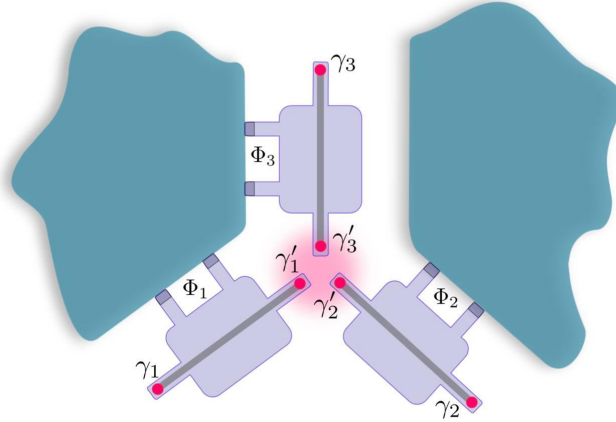


**Figure 1.6.** Three Cooper pair boxes with two Majorana zero-modes in each (pink dots). The three overlapping Majorana zero-modes that meet at the center of the tri-junction split to produce two no-zero levels and a single zero-mode. The coupling between the Majoranas in each Cooper pair box  $\gamma_i, \gamma'_i$  is varied by varying the flux  $\Phi_i$  through the corresponding Josephson junction.

An arguably easier operation as compared to braiding appears to be able to completely substitute it [56]. This operation is a projective measurement called *fusion*. Physically, it is realized by bringing the vortices together so that the wave-functions of the zero-modes overlap. As a result, they split energetically, allowing to measure the fermion parity. The outcome of such a measurement is specified by the fusion rules. If we prepare the qubit in the state where  $\gamma_1, \gamma_2$  and  $\gamma_3, \gamma_4$  form states with definite fermion parity, the ground state degeneracy of the whole system will manifest itself in the non-deterministic outcome for the parity of the state formed from  $\gamma_2, \gamma_3$ . It follows from the anti-commutation relation for MZM which leads to  $\langle P_{23} \rangle = \langle P_{12} P_{23} P_{12} \rangle = -\langle P_{12} P_{12} P_{23} \rangle = -\langle P_{23} \rangle$ . In a formal notation the fusion rule is expressed by

$$\gamma_2 \times \gamma_3 = 1 + \psi, \quad (1.10)$$

where  $\psi$  indicates the presence of an unpaired fermion and  $1$  – no unpaired fermions [14]. Since the fusion rule 1.10 is a manifestation of the degenerate ground state and we know that the latter implies non-Abelian exchange statistic, one can conclude that the observation of the corresponding fusion rule is sufficient to announce the indirect demonstration of non-Abelian statistics.

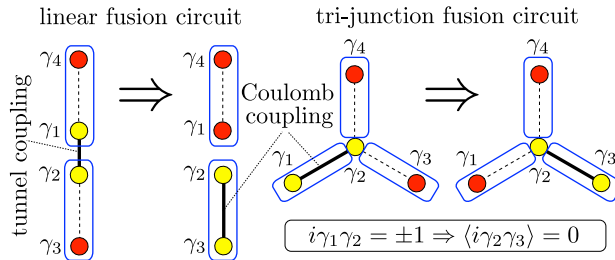


**Figure 1.7.** Two geometries to detect the fusion rule. *The figure is reprinted with permission from Beenakker, C. W. J, SciPost Phys. Lect. Notes, 2020*

Two easiest geometries to detect the fusion rule are presented on Fig. 1.7. In both geometries we perform a sequence of coupling and decoupling of the MZMs between each other. The difference between the linear and tri-junction is only in the mechanism of tuning the coupling (flux-controlled in the latter while in the former we have flux-controlled coupling inside the island and gate-controlled coupling between the islands). the sequence of steps is following [60]:

1. Start by coupling  $\gamma_1$  and  $\gamma_2$  performing the projective parity measurement  $P_{12}$  such that we effectively have one superconducting nanowire. The ground state is fixed by the total parity.

2. Decouple  $\gamma_1$  and  $\gamma_2$  and couple  $\gamma_2$  and  $\gamma_3$ . The parity  $P_{23}$  is expected to have equal probability to be  $\pm 1$ .

To experimentally perform a projective measurement on practice, one needs an observable that couples to it. The possible measurement schemes are:

- Majorana interferometry [58]. One brings the superconducting nanowire with MZMs into a weak contact with the normal metal and measures the current passing through it. The switches in parity result in parity-dependent Aharonov-Bohm oscillations in the magnetoconductance.
- Inductive coupling to a flux qubit [62]. The topological one-dimensional wire gets closed into circle by broken superconducting ring [63]. The section of the wire bridging the break of the superconducting ring remains nontopological and acts as a weak link (Josephson junction) between the two topological regions. Measuring the Josephson supercurrent can probe the  $4\pi$  Josephson effect [17].
- Microwave coupling to a transmon qubit<sup>12</sup>. The nanowire with MZMs is incorporated into the Cooper pair box, the effective low energy Hamiltonian of which gets the term that depends on the parity of the nanowire [57]. The Cooper pair box is then placed in a microwave transmission line resonator changing its resonance frequency depending on the parity of the MZMs in the Cooper pair box [64].
- Capacitive coupling to a quantum dot. The superconducting nanowire is coupled to semiconductor quantum dots modulating the charge on them depending on the fermion parity of the zero-modes. The charge of the semiconductor quantum dots is then read-out capacitively [59, 65].
- If one wants to make a scalable read-out circuit performing a joint parity measurement on arbitrary pairs of Majorana zero-modes, one has to use Random Access Majorana Memory (RAMM) [66].

Bonderson, Freedman, and Nayak [56] showed how braiding of two MZMs (e.g.  $\gamma_1$  and  $\gamma_2$  as on Fig. 1.5) can be performed through the sequence of projective measurements  $\Pi_{kl} = \frac{1}{2}(1 + P_{kl})$  (Fig. 1.8). The idea is to project the state onto the state with definite parity (e.g.  $+1$ ). This can be done by measuring the parity and disregarding all the instances when it was equal

---

<sup>12</sup>The transmon is a type of superconducting charge qubit

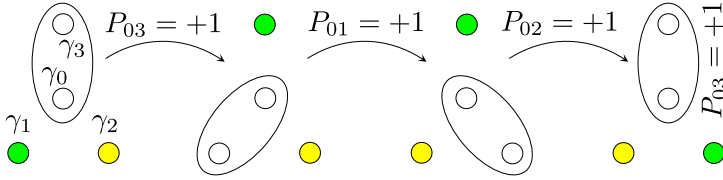


**Figure 1.8.** Braiding of Majorana zero modes ( $\gamma_1$  and  $\gamma_2$  in tri-junction.)  $\gamma_0$  is an effective zero mode created when three MZMs got coupled in the middle of the tri-junction. To perform the braiding operation, one performs a sequence of projective measurements  $P_{kl} = i\gamma_k\gamma_l$ . The operations proceed only in case  $P_{kl} = +1$ , otherwise we need to start over. *The figure is reprinted with permission from Beenakker, C. W. J, SciPost Phys. Lect. Notes, 2020*

to  $-1$ . In this case, if we initialize the system in the state of even fermion parity and then we subsequently make sure that the parities  $P_{03}$  and then  $P_{01}, \dots, P_{03}$  is equal to  $+1$  then due to the total parity conservation Majorana 1 must have been transferred to Majorana 3. The two-qubit operation CNOT can be also fully realized using projective measurements of parity.

It looks convincing that projective parity measurement is an important ingredient both in showing the non-Abelian statistic of the MZMs and for actually building a fault-tolerant quantum computer. As we have discussed in section 1.3.3, however, for the generic system that can host topologically protected MZMs, namely for a topological superconductors there exist parasitic low lying states (Andreev levels) that can contribute to the observables. The density of states of a “dirty” topological superconductor has a peak near zero energies, in Chapters 2 and 3 we have studied what influence these states can have on the measurement of the fusion rule.

## 1.5 Chaotic Majorana fermions

The Majorana zero modes that appear in the topological superconductors are non-interacting. The different point of view that considers the extreme case of strongly-correlated Majorana zero-modes can be studied and it appears to have many interesting and peculiar properties.

The SYK model was introduced by Kitaev [25] as a follow-up on the original disordered quantum Heisenberg model by Sachdev and Ye [26]. It contains  $N \gg 1$  Majorana fermions in  $0+1$  dimensions, with the Hamiltonian consisting

of a sum of all possible 4-fermion terms with random matrix elements

$$H = \frac{1}{4!} \sum_{i,j,k,l=1}^N J_{ijkl} \gamma_i \gamma_j \gamma_k \gamma_l, \quad (1.11)$$

where  $\gamma_i$  are Majorana zero modes, the couplings  $J_{ijkl}$  are drawn independently from Gaussian distribution with zero mean  $\overline{J_{ijkl}} = 0$  and finite variance  $\overline{J_{ijkl}^2} = 3!J^2/N^3$ . The parameter  $J$  regulates the degree of entanglement in the system and by varying it we can enter phases with different qualitative behaviour of the system (we will elaborate on it later).

One can make two generalizations of this model:

1. Consider  $q$ -fermion interactions instead of 4-fermion as in 1.11 [31]. However, it appears that the non-trivial behaviour of the system shows up already for  $q = 4$  therefore we will proceed with this “minimal” case further on in this thesis.
2. One can write the same model for complex fermions instead of real Majorana fermions (so-called cSYK) described by the Hamiltonian<sup>13</sup>.

$$H_{\text{SYK}} = \frac{1}{(2N)^{3/2}} \sum_{i,j,k,l=1}^N J_{ij;kl} c_i^\dagger c_j^\dagger c_k c_l, \quad (1.12)$$

where again  $J_{ij;kl} = J_{kl;ij}^*$  is a standard complex normal random variable with zero mean and variance  $J^2$ .

The SYK model drew the attention to itself due to a list of peculiar properties such as saturating the upper bound on quantum chaos [28] which is also the case for holographic duals of black hole horizons [29] and the absence of the well defined quasi-particles in strong coupling limit ( $J/T \gg 1$ ). Let us elaborate on it a bit.

The degree to which the system is chaotic of the system is usually formulated in terms of the so-called Out-Of-Time-Order-Correlation function (OTOC) introduced by Larkin and Ovchinnikov [67].

$$C(t) \equiv -\langle [W(t), V(0)]^2 \rangle \quad (1.13)$$

where  $\langle \dots \rangle$  represents the thermal average. A naive understanding of the connection between the OTOC and chaos can be seen from the following

---

<sup>13</sup>The features of the SYK model mentioned in this section are valid for both models with real (Majorana) and complex fermions

consideration. Take  $W(t) = x(t)$  be the position operator and  $V(t) = p(t)$  the momentum operator in a quantum system. Then, in the semiclassical limit we replace the commutator  $[x(t), p(0)]$  in the OTOC by the Poisson bracket  $\{x(t), p(0)\} = \delta x(t)/\delta x(0)$ . For a classically chaotic system, the latter would grow exponentially in time with the so-called Lyapunov exponent  $\lambda$ :  $\delta x(t)/\delta x(0) \sim e^{\lambda t}$ .

It was recently shown by Maldacena, Shenker, and Stanford [28] that in the many-body quantum system OTOC can not grow faster than exponentially with a characteristic time-scale  $t_L \leq \hbar/(2\pi k_B T)$  which is correspondingly called Lyapunov time. It was also shown that in SYK OTOC behaves exactly in this way: it has the exponential growth with the precisely saturates the upper bound on the Lyapunov time [28].<sup>14</sup>

Another peculiar property of the SYK model is the power-law behaviour of the spectral function in the low energy region  $\omega \ll J$ . Meanwhile, the absence of long-living quasiparticles in high-temperature superconducting materials above the critical temperature is an immutable characteristic of the so-called strange metal state. Strange metals also exhibit a power-law behavior in the spectral function similarly to SYK. A lack of quasiparticles manifests itself in fast equilibration at low temperature on a timescale set by the Planckian relaxation time  $t_P = \hbar/(2\pi k_B T)$  that is the same timescale that appears as an upper bound on quantum chaos. The extensions of this model to the cSYK coupled clusters predict thermal diffusivity [68]  $\propto t_P$  and reproduce the linear in temperature resistivity, [69] observed in strange metals. [70, 71] Recently, a proposed theory of a Planckian metal, [27] based on the destruction of a Fermi surface by the cSYK-like interactions, shows that the universal scattering time equals the Planckian time  $t_P$ . The latter one characterizes the linear in temperature resistivity property [72] and was detected in cuprates, [73] pnictides, [74] and twisted bilayer graphene, [75] regardless of their different microscopic nature.

### 1.5.1 Mean field solution for cSYK

The SYK model appears to be tractable in the limit when we have many flavours of the fermions  $N \gg 1$  (so-called large  $N$  limit). Let us try to derive the solution in this limit and study it closer. To do so, let us calculate the

---

<sup>14</sup>For the quantum mechanical system, however, the OTOC does not grow eternally but saturates at the Ehrenfest time  $t_E$  (by which the wave function have spread over the whole system).

partition function of the cSYK model and look for the saddle-point solution (mean field approach).

We start with the Gaussian probability distribution for the complex variable  $J_{ij;kl}$  with mean zero and variance  $J^2/2$ ,

$$\mathcal{P}(J_{ij;kl}, J_{ij;kl}^*) = \frac{1}{\sqrt{2\pi J^2}} \exp\left(-\sum_{ij;kl} \frac{J_{ij;kl} J_{ij;kl}^*}{2J^2}\right) \quad (1.14)$$

In the limit  $N \rightarrow \infty$  we can calculate the averaged<sup>15</sup> partition function accounting for the constraints  $J_{ij;kl}^* = J_{kl;ij}$  and the symmetry under  $i \leftrightarrow j$  and  $k \leftrightarrow l$

$$Z = \int \mathcal{D}[c, c^\dagger] \int dJ_{ij;kl} dJ_{ij;kl}^* \delta(J_{ij;kl}^* - J_{kl;ij}) \delta(J_{ij;kl} + J_{ji;kl}) \delta(J_{ij;kl} + J_{ij;lk}) \times \\ \times \mathcal{P}(J_{ij;kl}, J_{ij;kl}^*) \exp(iS[c, c^\dagger]) \quad (1.15)$$

where later on we will denote  $\delta(J_{ij;kl}^* - J_{kl;ij}) \delta(J_{ij;kl} + J_{ji;kl}) \delta(J_{ij;kl} + J_{ij;lk}) = \delta(J)$ .

### Kadanoff-Baym equations

When we are in the non-equilibrium case we have to employ the Schwinger-Keldysh formalism. The action is

$$S[c, c^\dagger] = \sum_{s=\pm} \int dt \left( is \sum_i c_{is}^\dagger \partial_t c_{is} - \frac{s}{(2N)^{3/2}} \sum_{ij;kl=1}^N J_{ij;kl} c_{is}^\dagger c_{js}^\dagger c_{ks} c_{ls} \right), \quad (1.16)$$

where  $s = \pm$  denotes forward and backward branches of the Keldysh time contour [76].

Disorder average will boil down to calculation of the following integral where we re-scaled  $J_{ij;kl} \rightarrow J_{ij;kl}/\sqrt{2}J$

$$I = \int dJ_{ij;kl} dJ_{ij;kl}^* \frac{\delta(J)}{\sqrt{\pi}} e^{-\sum_{ij;kl} \left( J_{ij;kl} J_{kl;ij} + i \sum_{s=\pm} \frac{s\sqrt{2}J}{(2N)^{3/2}} \int dt J_{ij;kl} c_{is}^\dagger c_{js}^\dagger c_{ks} c_{ls} \right)} \quad (1.17)$$

---

<sup>15</sup>For many quantities, the model is self-averaging, and computing with some randomly chosen, but fixed, couplings should give the same result as averaging over the couplings. We also assume that there is no replica symmetry breaking.

We decompose the SYK part into two

$$\sum_{ij;kl} J_{ij;kl} c_{is}^\dagger c_{js}^\dagger c_{ks} c_{ls} = \frac{1}{2} \sum_{ij;kl} \left( J_{ij;kl} c_{is}^\dagger c_{js}^\dagger c_{ks} c_{ls} + J_{ij;kl}^* c_{ls}^\dagger c_{ks}^\dagger c_{js} c_{is} \right) \quad (1.18)$$

Then one can see that

$$\begin{aligned} & \sum_{ij;kl} \left( J_{ij;kl} + \frac{iJ}{\sqrt{2}(2N)^{3/2}} \int dt \sum_{s=\pm} s c_{ls}^\dagger c_{ks}^\dagger c_{js} c_{is} \right) \times \\ & \times \left( J_{ij;kl}^* + \frac{iJ}{\sqrt{2}(2N)^{3/2}} \int dt \sum_{s=\pm} s c_{is}^\dagger c_{js}^\dagger c_{ks} c_{ls} \right) = \\ & = \sum_{ij;kl} \left( J_{ij;kl} J_{ij;kl}^* + i \sum_{s=\pm} \frac{s\sqrt{2}J}{(2N)^{3/2}} \int dt J_{ij;kl} c_{is}^\dagger c_{js}^\dagger c_{ks} c_{ls} - \right. \\ & \quad \left. - \frac{J^2}{2(2N)^3} \sum_{s,s'=\pm} ss' \int dt \int dt' c_{ls}^\dagger c_{ks}^\dagger c_{js} c_{is} c_{is'}^\dagger c_{js'}^\dagger c_{ks'} c_{ls'} \right) \end{aligned} \quad (1.19)$$

One can integrate over the  $J_{ij;kl}^*$  using the delta-function and shift the constant

$$J_{ij;kl} \rightarrow J_{ij;kl} + \frac{iJ}{\sqrt{2}(2N)^{3/2}} \int dt \sum_{s=\pm} s c_{ls}^\dagger c_{ks}^\dagger c_{js} c_{is}$$

and obtain

$$\begin{aligned} I &= \int dJ_{ij;kl} \delta(J_{ij;kl} + J_{ji;kl}) \delta(J_{ij;kl} + J_{ij;lk}) \frac{1}{\sqrt{\pi}} \exp \left( - \sum_{ij;kl} J_{ij;kl} J_{kl;ij} \right) \times \\ & \times \exp \left( - \sum_{ij;kl} \frac{J^2}{2(2N)^3} \sum_{s,s'=\pm} ss' \int dt \int dt' c_{ls}^\dagger c_{ks}^\dagger c_{js} c_{is} c_{is'}^\dagger c_{js'}^\dagger c_{ks'} c_{ls'} \right) \end{aligned} \quad (1.20)$$

Note that now we do not have the condition  $J_{ij;kl}^* = J_{kl;ij}$ . Therefore

$$I = K(J) e^{-\sum_{ij;kl} \frac{J^2}{2(2N)^3} \sum_{s,s'=\pm} ss' \int dt \int dt' c_{ls}^\dagger c_{ks}^\dagger c_{js} c_{is} c_{is'}^\dagger c_{js'}^\dagger c_{ks'} c_{ls'}} \quad (1.21)$$

which gives the following partition function

$$\begin{aligned} Z &= K(J) \int \mathcal{D}[c, c^\dagger] \exp \left( - \sum_{s=\pm} s \int dt \sum_i c_{is}^\dagger \partial_t c_{is} - \right. \\ & \quad \left. - \sum_{ij;kl} \frac{J^2}{2(2N)^3} \sum_{s,s'=\pm} ss' \int dt dt' c_{ls}^\dagger c_{ks}^\dagger c_{js} c_{is} c_{is'}^\dagger c_{js'}^\dagger c_{ks'} c_{ls'} \right) \end{aligned} \quad (1.22)$$

Introducing bilocals  $G_{s,s'}(t,t') = iN^{-1} \sum_i c_{is'}^\dagger(t') c_{is}(t)$  we arrive at effective action written with  $\Sigma_{ss'}(t,t')$ ,  $\Pi_{ss'}(t,t')$  as the corresponding Lagrange multipliers

$$S = -iN \text{trln} \left[ \sigma_{ss'}^z \delta(t-t') (i\partial_t + \mu) - \Sigma_{ss'}(t,t') \right] - iN \sum_{ss'} \int dt dt' \left( \Sigma_{ss'}(t,t') G_{s's'}(t',t) - \frac{ss'J^2}{4} G_{ss'}(t,t')^2 G_{s's'}(t',t)^2 \right)$$

In the large  $N$  limit, the saddle-point equations are

$$\begin{aligned} \Sigma_{ss'}(t,t') &= J^2 G_{ss'}(t,t')^2 G_{s's'}(t',t) \quad (1.23) \\ \sum_r \int_{-\infty}^{+\infty} du \left( \sigma_{sr}^z \delta(t-u) (i\partial_t + \mu) - sr \Sigma_{sr}(t,u) \right) G_{rs'}(u,t') &= \delta_{ss'} \delta(t-t'). \end{aligned}$$

### Schwinger-Dyson equations

The same kind of analysis with disorder averaging can be applied for the equilibrium case at some temperature  $T$  using Matsubara formalism. The imaginary time action averaged over disorder is

$$S = \int_0^\beta d\tau \left[ \sum_{i=1}^N \bar{c}_i \partial_\tau c_i + \int_0^\beta d\tau' \frac{J^2}{4N^3} \sum_{i,j,k,l=1}^N \bar{c}_i \bar{c}_j c_k c_l(\tau) \bar{c}_l \bar{c}_k c_j c_i(\tau') \right], \quad (1.24)$$

where  $\beta$  is the inverse temperature. Same as for non-equilibrium, we make Hubbard-Stratonovich transformation introducing bilocals  $G(\tau, \tau') = -N^{-1} \sum_{i=1}^N c_i(\tau) \bar{c}_i(\tau')$  together with  $\Sigma(\tau, \tau')$  as the corresponding Lagrange multipliers we get:

$$\begin{aligned} S &= -N \sum_{n=-\infty}^{+\infty} \log \left[ i\omega_n - \Sigma_c(i\omega_n) \right] - \\ &\quad - \int_0^\beta d\tau \int_0^\beta d\tau' \left[ N \left( \Sigma_c(\tau, \tau') G_c(\tau', \tau) + \frac{J^2}{4} G_c(\tau, \tau')^4 \right) \right], \quad (1.25) \end{aligned}$$

where  $\omega_n = \pi(2n+1)/\beta$  are Matsubara frequencies. In the limit of  $N \gg 1$ , the saddle-point equations are:

$$\begin{aligned} \Sigma(\tau) &= J^2 G(\tau)^3 \\ G(i\omega_n)^{-1} &= i\omega_n - \Sigma(i\omega_n), \quad (1.26) \end{aligned}$$

where  $\omega_n = \pi T(2n+1)$  are Matsubara frequencies.

### Emergent conformal symmetry

In the long time limit  $1 \ll J\tau \ll N$ , we can neglect the term with the derivative  $\partial_t$  and the theory becomes invariant under the re-scaling of the time  $\tau \rightarrow f(\tau)$ . The Kadanoff-Baym equations reduce to

$$-J^2 \sum_r sr \int_{-\infty}^{\infty} du G_{sr}(t, u)^2 G_{rs}(u, t) G_{rs'}(u, t') = \delta_{ss'} \delta(t - t') \quad (1.27)$$

with the solutions

$$\begin{aligned} G_{ss}(t) &= -i \operatorname{sign}(t) \cdot s \cdot \frac{e^{-is\pi/4}}{\sqrt{\sinh(\pi|t|/\beta)}}, \\ G_{ss'}(t) &= -is' \cdot \frac{e^{-i \operatorname{sign}(t)s'\pi/4}}{\sqrt{\sinh(\pi|t|/\beta)}} \end{aligned} \quad (1.28)$$

with  $b = \pi^{1/4}/\sqrt{2\beta J}$ .

For Matsubara formalism we get

$$G(\tau) = \frac{b}{\sqrt{\tau}} \operatorname{sign}(\tau). \quad (1.29)$$

### 1.5.2 SYK in the lab

We see that seemingly simple and somewhat solvable SYK model shares many phenomena intrinsic to the mysterious strongly correlated systems that do not yet have a clear theoretical description. It inspired several proposals to realize the SYK model in a condensed matter platform in the lab [22, 23, 77–79]. For the corresponding realistic systems, SYK is expected to arise as a low-energy effective description.

Let us take a closer look into one of the mentioned proposals. Chen et al. [77] propose a to take a graphene flake with irregular boundary in the external magnetic field (see Fig. 1.9). The spectrum of graphene in a perpendicular magnetic field  $B$  consists of quantized Landau levels  $E_n \simeq \hbar v \sqrt{2n(eB/\hbar c)}$ . The chiral symmetry of graphene protects the 0<sup>th</sup> Landau level from the presence of disorder. Therefore, if we project on the low energy sector, we get a highly degenerate subspace<sup>16</sup> with the wave functions  $\Phi_i(\mathbf{r})$  being random in space thanks to the disordered boundary. The SYK model arises as the

<sup>16</sup>The degeneracy of the 0<sup>th</sup> Landau level is proportional to the flux of the magnetic field through the flake

effective model for the low energy sector when Coulomb repulsion  $V(\mathbf{r} - \mathbf{r}')$ <sup>17</sup> is added into the consideration. The the corresponding interaction matrix elements between the zero modes are given by

$$J_{ij;kl} = \int d\mathbf{r} \int d\mathbf{r}' \Phi_i^*(\mathbf{r}) \Phi_j^*(\mathbf{r}') V(\mathbf{r} - \mathbf{r}') \Phi_k(\mathbf{r}) \Phi_l(\mathbf{r}'). \quad (1.30)$$

Thanks to the randomness in the spatial distribution of  $\Phi(\mathbf{r})$  the distribution of the coupling constants  $J_{ij;kl}$  can be approximated by the Gaussian to an arguably good extend (see Fig. 1.9, right panel). The effective Hamiltonian is therefore of the form of the complex SYK model (cSYK) 1.12.

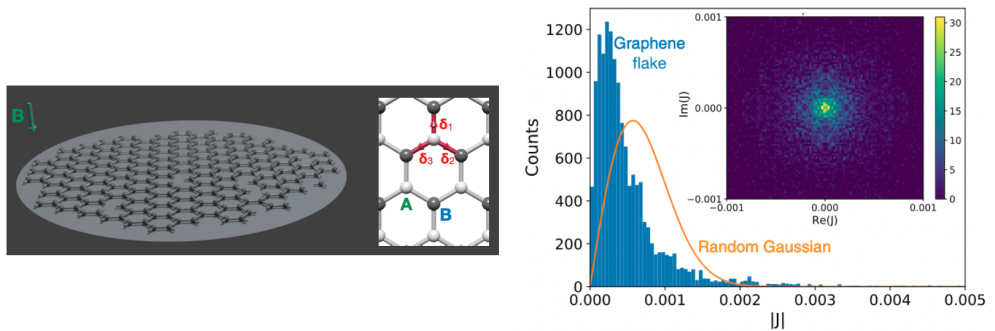


**Figure 1.9.** Left panel: Schematic depiction of the proposed design of the experimental simulation of the cSYK model. Graphene flake with the irregular boundary in the external perpendicular magnetic field. Inset: lattice structure of graphene. Right panel: Histogram of the coupling constants  $|J_{ij;kl}|$  from Eq. 1.30 for  $N = 16$  compared to the Gaussian distribution (orange line) with the same variance. *The figure is reprinted with permission from Anffany Chen, R. Ilan, F. de Juan, D. I. Pikulin, and M. Franz, Phys. Rev. Lett. 121, 036403, (2018)*

However, after building the setup it is good to check whether the system that we prepared in the lab is actually close enough to the SYK and if it possesses the same fundamental properties e.g. whether it is in the non-Fermi liquid phase. There are many reasons why it may not be so, for example: the wave-function of the ground state is not random enough such that the effective coupling strength  $J_{ij;kl}$  do not follow the Gaussian distribution or the microscopic parameters are not tuned such that we are not in the strong coupling regime  $J/T \gg 1$ . Also, it is known, that adding even an infinitesimal quadratic term (simple hopping) to the SYK model can destroy its non-trivial

<sup>17</sup>The screened Coulomb potential is  $V(\mathbf{r}) = (e^2/\epsilon r)e^{-r/\lambda}$  with  $\epsilon$  being the dielectric constant and  $\lambda$  - Thomas-Fermi length.

transform it to free random fermions (Fermi liquid phase) [80]. And probing the experimental setup that is allegedly described by the SYK model would mean coupling it by tunneling to a fermion bath in one way or another. In Chapters 4 and 5 we study several possible observable signatures of the non-Fermi liquid phase in the SYK as well as the robustness of this phase when we couple the SYK to a fermion bath.

## 1.6 Cosmic Majorana fermions

One more place where we can meet Majorana fermions (in form of fundamental particles) is neutrino physics. When Ettore Majorana was writing his famous equation, he was surely inspired by the particles that were introduced seven years prior by Pauli. Despite the fact that these particles are not yet fully understood theoretically (for example, the value of the masses and its mechanism), they are not in any sense rare, quite the opposite – we are being surrounded by them. In fact, there are approximately as many neutrinos flying around us as there are photons, order of hundred in every  $\text{cm}^3$ !

In fact, the analogy with the photons goes further – there is a radiation background similar to the Cosmic Microwave Background (CMB) that is correspondingly called Cosmic Neutrino Background or  $C\nu\text{B}$ . The mechanism of both is the same: the very early universe was filled with the relativistic particles that scatter between one another. As the universe was expanding approximately at the moment when the rate of the scattering processes became equal to the Hubbard parameter the corresponding particles decoupled – the Universe became transparent for them. Starting from that moment they were penetrating the universe moving (almost) freely. Such particles are called relic and by detecting them we are able to look into the early universe. CMB is a “photograph” of relic photons that were decoupled when the Universe was hundred thousands years old. The same cold,  $T = 1.95 \text{ K}$ , radiation for neutrinos that decoupled much earlier than photons (when the Universe was only living for seconds) is called Cosmic Neutrino Background ( $C\nu\text{B}$ ) [81].

Despite many similarities,  $C\nu\text{B}$  and CMB have a drastic difference – neutrinos are much harder to detect. Indirect evidence for the existence of the relic neutrinos was found in the observed CMB [82], however, due to the extreme weakness of the interactions between neutrinos and other forms of matter, direct detection of the  $C\nu\text{B}$  remains a major experimental challenge.

Today it is widely accepted that the most practicable route to the direct detection of the  $C\nu\text{B}$  lies through the measurement of the fine structure of the

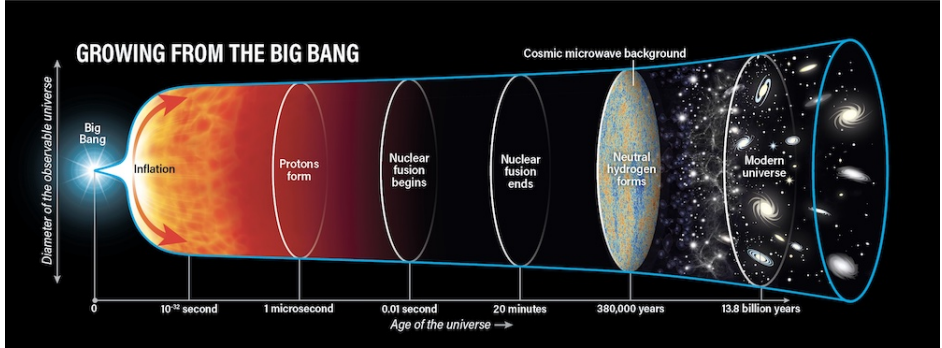
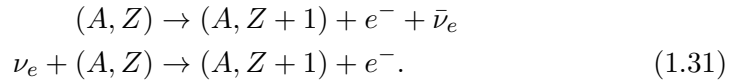


**Figure 1.10.** Schematic depiction of the expanding Universe after the Big Bang. *The picture taken from Astronomy: Roen Kelly, after BICEP2 Collaboration*

$\beta$ -spectrum of a radioactive element [83–87]. Let us consider a general case of nuclear  $\beta$ -decay and neutrino capture



The processes of capture of cosmic neutrino having mass  $m_\nu$  by a sample of radioactive atoms characterized by the beta-decay energy  $Q$  are predicted to leave a potentially discernible signature in the form of an extremely faint peak at the energy  $Q + m_\nu^0 c^2$  in the beta spectrum of the sample [83–87] (see Fig. 1.11)<sup>18</sup>. On the other hand, the major part of the spectrum of the radioactive element consists of the events of the spontaneous  $\beta$  decay and forms a continuum with the upper cut-off energy  $Q - m_\nu^0 c^2$ . Therefore, one expects the neutrino capture peak to be separated from the end of the spontaneous  $\beta$ -spectrum by an energy gap of at least one neutrino mass and for that reason to be discernible at least in principle.

From the first glance, it is obvious why such an experiment can be very challenging: we are trying to measure a meV<sup>19</sup> feature on the background of keV. This requires extreme energy resolution (order of 10 meV). However, another major challenge lies in the weakness of the signal. A naive estimate for the neutrino capture cross section is  $\sigma_\nu \simeq (\tau Q)^{-1}$  [86], where  $Q \sim 10$  keV is the energy released in the  $\beta$ -decay and  $\tau$  is the lifetime of the  $\beta$  emitter.

<sup>18</sup>There are, generally, three mass generations of neutrino. This fact does not influence our considerations so we will omit it further. Here  $m_\nu^0$  is a mass of the lightest neutrino.

<sup>19</sup>The best up to date bound on the effective neutrino mass is  $m_\nu < 0.8$  eV as obtained by the KATRIN experiment using gaseous molecular tritium [89].

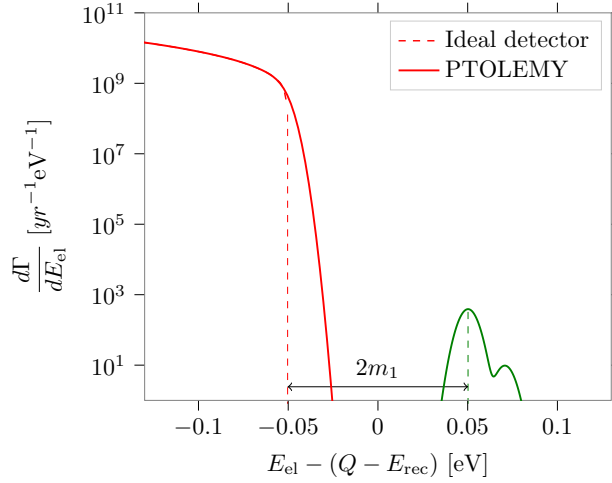


**Figure 1.11.**  $^3\text{He}$   $\beta$ -spectrum of free monoatomic Tritium centered around  $Q - E_{\text{rec}}$ , where  $Q$  is the decay energy and  $E_{\text{rec}}$  - recoil of the nucleus in the vacuum. The normal neutrino mass hierarchy [88] is assumed with the mass of the lightest neutrino  $m_1 = 50$  meV. The spontaneous  $\beta$ -decay spectrum is shown in red while the  $\text{C}\nu\text{B}$  feature is shown in green. The solid lines are drawn assuming a 10 meV resolution of the detector.

We have a lower bound on the lifetime (otherwise we would not be able to assemble the experimental setup)  $\tau \gtrsim 1$  yr and also all the viable emitters have  $Q \sim 10$  keV. Therefore, we arrive at the conclusion that in order to have at least one neutrino capture event per year we need large amounts of the radioactive atoms (at least 100 g in order to achieve one event per year in the case of atomic Tritium).

The lower bound on the size of the experimental setup comes from a very simple consideration – it should be bigger than the mean free path of the emitted electron with respect to the hard core collisions with the other emitters. Otherwise, the scattering processes will corrupt the energy resolution. The mean free path is given by the cross section  $\sigma = R_{\text{atom}}^2$  and the concentration of the emitters  $n = N/L^3$ . The number of the emitters is fixed  $N \sim 10^{23}$  from the requirements of sufficient activity, the radius of the atom is also known. If we calculate the numbers, we would see that the very rough estimate of the lower bound on the linear size of the experimental setup is of the order of 1 km. The biggest relic neutrino detector nowadays is KATRIN that has the cross-section area of the container about  $50 \text{ cm}^2$ , so the effective mass of

tritium molecules is only about  $50 \mu\text{g}$  [90].

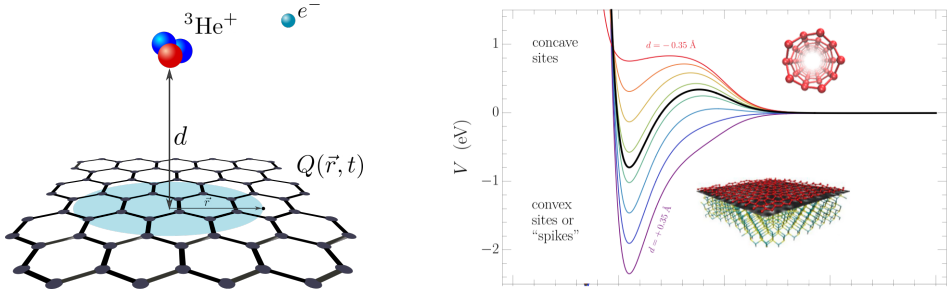


**Figure 1.12.** Left panel: Schematic depiction of the decaying Tritium atom attached to the graphene sheet. Right panel: Graphene–hydrogen binding potential as a function of the distance from the binding site. Different colors correspond to different local curvatures (puckering) of the binding site. Flat graphene corresponds to  $d = 0$  (thick black line), while  $d > 0$  corresponds to convex sites and  $d < 0$  to concave ones.

The only viable solution to the problem of the controllable handling of such a large amount of radioactive material nowadays is proposed by the PTOLEMY collaboration [85]. It is based on the idea to use a solid state-based experimental architecture. In this proposal, the tritium atoms are deposited on the graphene substrate which can efficiently store atomic tritium by locally binding it to carbon atoms (either by chemisorption, physisorption). Along with the high tritium storage, PTOLEMY also offers a very precise control over the emitted electrons with the help of the elaborate configuration of the electric and magnetic fields that “guide” the electrons to the detector. An overall energy resolution of  $10 \text{ meV}$  is achieved.

### 1.6.1 $\beta$ decay on the surface

As was first pointed out [91], the coupling of the  $\beta$ -emitter to the many-body solid state system comes at the price of introducing additional intrinsic energy uncertainty to the  $\beta$  spectrum. Indeed, when we are interested in the processes on as low energy scales as  $\text{meV}$ , the solid state substrate becomes a jungle filled with many-body phenomena.

In order to understand how the spectrum will look for the  $\beta$ -decaying atom bounded to the substrate, let us apply the Fermi Golden Rule to the whole system containing  $\beta$ -decaying constituents and the substrate. Let us denote the total state of such a system (atom + environment) as  $|\alpha, z\rangle$ . Since the whole system is closed, the Fermi Golden Rule holds where the total energy

is conserved.

$$\Gamma = \frac{2\pi}{\hbar} \sum_{\text{final states}} |\langle \text{final} | \hat{H}^\beta | \text{initial} \rangle|^2 \delta(E_{\text{in}} - E_{\text{fin}}), \quad (1.32)$$

where we know that the initial and final states have different number of protons and neutrons that is why only the Hamiltonian of the weak interaction  $H^\beta$  survives. Let us specify how initial and final states look like and what are their quantum numbers

$$\begin{aligned} |\text{initial}\rangle &= |\alpha_0, z\rangle \\ |\text{final}\rangle &= |\alpha, z + 1\rangle |k\rangle |p\rangle, \end{aligned} \quad (1.33)$$

where there are 3 quantum numbers: an abstract label for the atom together with the environment state  $\alpha$ , electron momentum  $k$  and neutrino momentum  $p$ <sup>20</sup>.

The Hamiltonian density of the  $\beta$ -interaction in the full generality is

$$H^\beta = \frac{G}{\sqrt{2}} \bar{e}(x) \gamma^\mu (1 - \gamma_5) \nu_e(x) \hat{J}_\mu^{\text{nucl}}(x) + \text{h.c.}, \quad (1.34)$$

where  $e(x), \nu_e(x)$  are electron and neutrino fields and  $\hat{J}_\mu^{\text{nucl}}(x)$  is a nuclear part which depends on the atom itself and we do not specify it. We get

$$\Gamma = \frac{V^2}{\hbar} \int \frac{d^3k d^3p}{(2\pi)^6} \sum_{\alpha} |\langle k | \langle p | \langle \alpha, z + 1 | H^\beta | \alpha_0, z \rangle|^2 \int d\tau e^{i\tau(E_e + E_\nu - E_{\alpha_0} + E_\alpha)}, \quad (1.35)$$

where we used that  $\delta(E_{\text{in}} - E_{\text{fin}}) = \int \frac{d\tau}{2\pi} e^{i\tau(E_e + E_\nu - E_{\alpha_0} + E_\alpha)}$ . Expanding  $|\cdot|^2$  we get

$$\begin{aligned} \Gamma &= \frac{1}{\hbar} \int \frac{d^3k d^3p}{(2\pi)^6} \int dx dx' j_{\text{lept}}^\mu(x, \vec{p}, \vec{k}) j_{\text{lept}}^{*\nu}(x', \vec{p}, \vec{k}) \times \\ &\quad \times \sum_{\alpha} \langle \alpha_0, z | \hat{J}_\mu^{\text{nucl}}(x) | \alpha, z + 1 \rangle \langle \alpha, z + 1 | \hat{J}_\nu^{\dagger, \text{nucl}}(x') | \alpha_0, z \rangle \times \\ &\quad \times \int d\tau e^{i\tau(E_e + E_\nu + E_\alpha - E_{\alpha_0})}, \end{aligned} \quad (1.36)$$

---

<sup>20</sup>We note that in this we neglect the Coulomb interaction of the emitted electron with the nucleus and with the surroundings. Therefore, the emitted electron is a plane wave that is characterized by the momentum  $k$ . Neutrino does not interact with anything so it is generally a plane wave (specified by the momentum  $p$ ).

where  $j_{\text{lept}}^\mu(x, \vec{p}, \vec{k}) = \bar{\psi}_e(x, \vec{k})\gamma^\mu(1 - \gamma_5)\psi_\nu^c(x, \vec{p})$  and  $\psi$  has both functional dependence (plane wave  $e^{ipx}$  without normalization factor as we already took it into account) and spinor structure. Accounting for

$$\sum_{\alpha} e^{i\tau E_{\alpha}} |\alpha, z+1\rangle \langle \alpha, z+1| = e^{i\tau \hat{H}_{z+1}^{\alpha}}, \quad (1.37)$$

where  $\hat{H}^{\alpha, z+1}$  is the Hamiltonian that describes the system that consists of the isotope of the initial atom with the charge  $z+1$  and environment, we get<sup>21</sup>

$$\begin{aligned} \Gamma = \frac{1}{\hbar} \int \frac{d^3k d^3p}{(2\pi)^6} & \left| \int dx j_{\text{lept}}^\mu(x, \vec{p}, \vec{k}) J_{\mu}^{\text{nucl}}(x) \right|^2 \times \\ & \times \int d\tau \langle \alpha_0, z | \hat{\chi}^\dagger e^{i\tau \hat{H}_{z+1}^{\alpha}} \hat{\chi} | \alpha_0, z \rangle e^{i\tau(E_e + E_\nu - E_{\alpha_0})}, \end{aligned} \quad (1.38)$$

where  $\hat{\chi}$  changes the charge of the nucleus by one and  $|\alpha, z\rangle$  only has the information about the surroundings and the electron orbitals of the atom, not the nucleus itself, the latter is in  $J^{\text{nucl}}(x)$ . Denoting

$$\frac{1}{2\pi} \int d\tau \langle \alpha_0, z | \hat{\chi} e^{i\tau \hat{H}_{z+1}^{\alpha}} \hat{\chi}^\dagger | \alpha_0, z \rangle e^{i\tau\omega} = \mathcal{F}(\omega), \quad (1.39)$$

we get the generalized Fermi Golden rule that accounts for the interactions of the nucleus with the surroundings

$$\Gamma = \frac{1}{\hbar} \int \frac{d^3k d^3p}{(2\pi)^6} \left| \int dx j_{\text{lept}}^\mu(x, \vec{p}, \vec{k}) J_{\mu}^{\text{nucl}}(x) \right|^2 \mathcal{F}(E_e + E_\nu - E_{\alpha_0}). \quad (1.40)$$

Or

$$\begin{aligned} \frac{d\Gamma}{dE_e} &= \frac{4E_e p(E_e)}{(2\pi)^4 \hbar} \int E_\nu k(E_\nu) dE_\nu \times \\ & \times \left| \int dx j_{\text{lept}}^\mu(x, E_e, E_\nu) J_{\mu}^{\text{nucl}}(x) \right|^2 \mathcal{F}(E_e + E_\nu - E_{\alpha_0}). \end{aligned} \quad (1.41)$$

If we compare it with the Fermi Golden Rule for the  $\beta$ -decay in the vacuum

---

<sup>21</sup>With the assumption that the wave function of the atom is a product of the wave function of the nucleus and the wave function of the electron shells that only depends on the charge of the nucleus.

$$\begin{aligned} \frac{d\Gamma^{(0)}}{dE_e} &= \frac{4E_e p(E_e)}{(2\pi)^4 \hbar} \int E_\nu k(E_\nu) dE_\nu \times \\ &\times \left| \int dx j_{\text{lept}}^\mu(x, E_e, E_\nu) J_\mu^{\text{nucl}}(x) \right|^2 \delta(E_e + E_\nu - E_{\alpha_0}). \end{aligned} \quad (1.42)$$

We see that the presence of the substrate leads to the finite lifetime of the daughter atom (that is encoded in the function  $\mathcal{F}(\omega)$ ). This leads to the broadening of the  $\beta$ -spectrum. It includes all the types of the interactions of the emitter with the substrate. Among them (the list is not by any means exhaustive):

1. Zero-point motion of the emitter [91].
2. Finite lifetime of the daughter ion due to redistribution of the charges on its shells and tunneling to graphene.
3. Breakdown of the angular momentum conservation due to the presence of the substrate.
4. Sudden emission of an electron from a beta-decayer leaves behind a positively charged centre which attracts the electric current carriers in of the substrate. This effect results in what is known as the X-ray edge anomaly - a gamma-shaped broadening of the emission peak [92].
5. Creation of vibrational excitations of the lattice.
6. Emission of plasmons and surface polaritons.
7. Inhomogeneous broadening due to any kind of inhomogeneities in the emitter arrangement.

However, the spectrum described by Eq. 1.40 does not include the interaction of the emitted electron with the substrate that can also manifest itself through many different mechanisms such as

1. Screening of the daughter atom by the charges in graphene.
2. Creation of shock wave emission due to the motion of the emitted electron at grazing angles at speeds exceeding the Fermi velocity.
3. Etc.

The investigation of one of the points in this list, namely the zero-point motion of the emitter (Chapter 6) rules out the Tritium-on graphene design and calls for substantially heavier beta-decayers. As is described in Chapter 7, it was found [93] that the best candidates in terms of the suppression of zero-point motion (also accounting for other criteria such as long enough lifetimes, stable daughter nucleus, single  $\beta$  decay branch, etc.) are  $^{171}\text{Tm}$  and  $^{151}\text{Sm}$ . These isotopes have lower neutrino capture cross sections as compared to Tritium:  $\approx 50$  times smaller for  $^{171}\text{Tm}$  and 3 orders of magnitude lower for  $^{151}\text{Sm}$ [93].

Some aspects of the electric effects of the interaction of the emitted electron with the substrate are considered in Chapter 8 and it seems that they are much less dangerous as compared to the effects due to interaction of the  $\beta$ -emitter with the substrate. Naively, this can be motivated by the fact that the emitted electron near the edge of the spectrum has quite high velocity  $v \approx 0.3c$ . Therefore it leaves the system pretty fast and does not “notice” many effects that take place on longer timescales.

To conclude, the research in the condensed matter side of this experimental setup is only starting, many effects have not yet been investigated. Before building a full scale experiment, both theoretical and, especially, experimental programs in condensed matter physics and surface science are required to study quantum devices with a mono-layer of rare earth elements (such as Thulium) attached to graphene substrate.

## 1.7 This thesis

This thesis aims to touch several questions about Majoranas of various origin:

1. For Majorana modes in superconductor. In the systems of the symmetry class D (to which topological superconductors belong) Majorana zero modes at zero energy can be mimicked by Andreev levels.

Can the vanishing fermion parity in the superconductor fusion experiment be taken as a distinctive signature of the isolated Majorana modes? If not, what would be the alternative scenario that would allow to discriminate true degenerate ground state against the accidental degeneracies of Andreev levels?

2. What signatures of the non-Fermi liquid phase can we see by probing the SYK model by the means of transport and beyond?
3. It is known, that adding even an infinitesimal quadratic term (simple hopping) to the SYK model can destroy its non-trivial transform it to free random fermions (Fermi liquid phase) [80]. So, if we want to probe the SYK experimentally by the means of transport, it would inevitable mean coupling it to the some kind of lead. We want to know whether there is some domain of stability of the non-Fermi liquid phase of SYK under such a perturbation.
4. The last question that is considered in this thesis is very practical. We want to know what limitation do the many-body effects in the experimental device impose on the energy resolution of the whole set-up. In particular, it concerns the experiment of the relic neutrino detection. It is still unclear whether the neutrino is a Majorana particle or not and what is the absolute scale of its masses [94]. Along with answering on this question, relic neutrino detection will allow us to look in the very early universe (much earlier then the Cosmic Microwave Background allows us to see). Such an experiment is therefore of fundamental importance. The state of the art proposal for it requires big amount of the source material (order of  $10^{23}$  of heavy radioactive elements) and an extreme energy resolutions (order of 10 meV) [85]. It is widely accepted that the only way to have a chance to full fill such requirements is to used a solid state based experimental device which again brings us to the interplay of high energy physics and low energy phenomena.

Below, I briefly highlight the main results presented in the thesis.

### 1.7.1 Chapter 2

Kitaev's Pfaffian formula equates the ground-state fermion parity of a closed system to the sign of the Pfaffian of the Hamiltonian in the Majorana basis. Using Klich's theory of counting statistics for paired fermions we generalize the Pfaffian formula to account for quantum fluctuations in the fermion parity of an open subsystem. A statistical description in the framework of random-matrix theory is used to answer the question when a vanishing fermion parity in a superconductor fusion experiment becomes a distinctive signature of an isolated Majorana zero-mode.

### 1.7.2 Chapter 3

Detection of the fusion rule of Majorana zero-modes is a near-term milestone on the road to topological quantum computation. An obstacle is that the non-deterministic fusion outcome of topological zero-modes can be mimicked by the merging of non-topological Andreev levels. To distinguish these two scenarios, we search for dynamical signatures of the ground-state degeneracy that is the defining property of non-Abelian anyons. By adiabatically traversing parameter space along two different pathways one can identify ground-state degeneracies from the breakdown of adiabaticity. We show that the approach can discriminate against accidental degeneracies of Andreev levels.

### 1.7.3 Chapter 4

The Planckian relaxation rate  $\hbar/t_P = 2\pi k_B T$  sets a characteristic timescale for both the equilibration of quantum critical systems and maximal quantum chaos. In this note, we show that at the critical coupling between a superconducting dot and the complex Sachdev-Ye-Kitaev model, known to be maximally chaotic, the pairing gap  $\Delta$  behaves as  $\eta \hbar/t_P$  at low temperatures, where  $\eta$  is an order one constant. The lower critical temperature emerges with a further increase of the coupling strength so that the finite  $\Delta$  domain is settled between the two critical temperatures.

### 1.7.4 Chapter 5

The Sachdev-Ye-Kitaev (SYK) model describes interacting fermionic zero modes in zero spatial dimensions, *e.g.* quantum dot, with interactions strong enough to completely washout quasiparticle excitations in the infrared. In this paper, we consider the complex-valued SYK model at initial temperature  $T$  and

chemical potential  $\mu$  coupled to a large reservoir by a quench at time  $t = 0$ . The reservoir is kept at zero temperature and charge neutrality. We find that the dynamics of the discharging process of the SYK quantum dot reveals a distinctive characteristic of the SYK non-Fermi liquid (nFl) state. In particular, we focus on the tunneling current induced by the quench. We show that the temperature dependent contribution to the current's half-life scales linearly in  $T$  at low temperatures for the SYK nFl state, while for the Fermi liquid it scales as  $T^2$ .

### 1.7.5 Chapter 6

Beta-spectrum of radioactive atoms was long ago predicted to bear an imprint of the Cosmic Neutrino Background (C $\nu$ B) [95]. Over the years, it has been recognised that the best chance of achieving the signal-to-noise ratio required for the observation of this effect lies with solid-state designs [96]. Here we bring to the fore a fundamental quantum limitation on the type of beta-decayer that can be used in a such a design. We derive a simple usability criterion and show that  $^3\text{H}$ , which is the most popular choice, fails to meet it. We provide a list of potentially suitable isotopes and discuss why their use in C $\nu$ B detection requires further research.

### 1.7.6 Chapter 7

Recent analysis of the viability of solid state-based relic neutrino detectors has revealed the fundamental necessity for the use of heavy,  $A > 100$ ,  $\beta$ -decayers as neutrino targets. Of all heavy isotopes,  $^{171}\text{Tm}$  and  $^{151}\text{Sm}$  stand out for their sufficiently low decay energies, reasonable half-life times and stable daughter nuclei. However, the crucial bit of information, that is the soft neutrino capture cross-section is missing for both isotopes. The main reason for that is a particular type of  $\beta$ -decay, which precludes a simple link between the isotope's half-life time and the neutrino capture rate. Here we propose an experimental method to bypass this difficulty and obtain the capture cross-section of a soft neutrino by a given isotope from the isotope's  $\beta$ -spectrum.

### 1.7.7 Chapter 8

The only promising experimental architecture for the Cosmic Neutrino Background (C $\nu$ B) detection nowadays exploits  $\beta$ -decay of the emitters bounded to a solid state substrate. The artifact of such a design is the appearance

---

of the additional intrinsic bounds on the energy resolution coming from the various types of interactions of the  $\beta$ -decaying atom with the collective modes in the substrate. In this work, we only focus on the electromagnetic effects, namely: 1) charge relaxation of the electrons in the substrate as a response to the ionization of the  $\beta$  emitter, 2) electron-hole pairs creation by the emitted  $\beta$  electron.



## Chapter 2

# Pfaffian formula for fermion parity fluctuations in a superconductor and application to Majorana fusion detection

### 2.1 Introduction

The pairing interaction in a superconductor favors a ground state with an *even* number of electrons, but when both time-reversal and spin-rotation symmetry are broken the ground state may have *odd* parity — for example when a magnetic impurity binds an unpaired electron [97]. While the connection between fermion-parity switches and level crossings was noticed already in 1970 by Sakurai [98], these only became a topic of intense research activity after Kitaev [17] made the connection with topological phase transitions and Majorana fermions: The absence of level repulsion at a fermion-parity switch indicates a change in a topological quantum number, which Kitaev identified as the sign of the Pfaffian of the Hamiltonian in the basis of Majorana fermions.

An open subsystem need not be in a state of definite fermion parity  $\mathcal{P} = \pm 1$ , the fermion parity expectation value  $\langle \mathcal{P} \rangle$  may take on any value in the interval  $[-1, 1]$ . Here we generalize Kitaev's Pfaffian formula so that it can describe both closed and open systems. This generalization has a computational

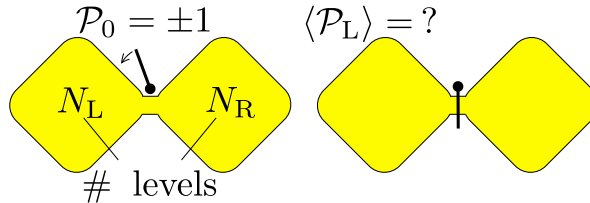


**Figure 2.1.** The left panel shows two superconducting regions (quantum dots) connected (fused) by a point contact. The entire system is in a state of definite fermion parity  $\mathcal{P}_0$ , even (+1) or odd (-1). The parity  $\mathcal{P}_L$  of the occupation number of the  $N_L$  electronic levels in one single quantum dot has quantum fluctuations. The expectation value  $\langle \mathcal{P}_L \rangle \in [-1, 1]$  may be obtained by rapidly closing the point contact and decoupling the quantum dots (right panel), followed by a measurement of the fermion parity of a single dot. The effective number of levels  $N_{\text{dot}} \simeq \hbar/\delta_0\tau_c$  in each quantum dot that contributes to the fermion parity fluctuations is determined by the single-particle level spacing  $\delta_0$  and the time scale  $\tau_c$  on which the interdot coupling is broken [99]. We address the question when a vanishing fermion parity  $\langle \mathcal{P}_L \rangle \approx 0$  in such a fusion experiment is a signature of isolated Majorana zero-modes.

as well as a conceptual merit. Computationally, it reduces the complexity of a calculation of  $\langle \mathcal{P} \rangle$  for  $N$  levels from order  $2^N$ , when all possible occupation numbers are enumerated, down to order  $N^3$ . Conceptually, it allows us to make contact with the random-matrix theory of topological superconductivity [48, 49], and identify the origin of a statistical peak at  $\langle \mathcal{P} \rangle = 0$  discovered recently in computer simulations [99]. These findings have implications for proposed experiments [60] to search for signatures of isolated Majorana zero-modes in the fermion parity of two superconductors that have first been fused and then decoupled (see Fig. 2.1).

The outline of the paper is as follows. In the next section we derive the Pfaffian formula for the average subsystem fermion parity. This generalization of Kitaev’s formula [17] can be seen either as an application of the Wick theorem for Majorana operators [100–102] (cf. a similar application in Ref. [103]), or as an application of Klich’s theory of counting statistics for paired fermions [104]. In Sec. 2.3 we use the fermion parity formula to establish the connection between vanishing average fermion parity and the presence of isolated Majorana zero-modes in the decoupled quantum dot. We continue in Sec. 2.4 with a statistical description of the double quantum dot geometry of Fig. 2.1, by identifying the random-matrix ensemble in symmetry class DIII that describes the fermion parity fluctuations. We contrast the case of strongly coupled quantum dots in Sec. 2.4.2 with the case of weak coupling in Sec. 2.4.3.

In Sec. 2.5 we show how weak coupling by a single-mode quantum point contact can distinguish quantum dots with or without isolated Majorana zero-modes. In the concluding Sec. 2.6 we discuss the implications of our analysis for the detection of Majorana zero-modes by means of a fusion experiment.

## 2.2 Pfaffian fermion-parity formula

### 2.2.1 Kitaev's formula for an isolated system

To set the stage we recall some basic facts [105] needed to present Kitaev's formula [17] for the ground-state fermion parity of an isolated superconductor.

At the mean-field level the Hamiltonian of a superconductor is a Hermitian quadratic form in the fermion creation and annihilation operators  $a^\dagger$ ,  $a$ ,

$$H = \sum_{n,m=1}^N V_{nm} \left( a_n^\dagger a_m - \frac{1}{2} \delta_{nm} \right) + \frac{1}{2} \sum_{n,m=1}^N \left( \Delta_{nm} a_n a_m + \Delta_{nm}^* a_m^\dagger a_n^\dagger \right). \quad (2.1)$$

The indices  $n, m$  label spin and orbital degrees of freedom of  $N$  fermionic modes. The  $N \times N$  Hermitian matrix  $V$  represents the kinetic and potential energy and the antisymmetric matrix  $\Delta$  is the pair potential.

More compactly, Eq. (2.1) can be written in the matrix form

$$H = \frac{1}{2} \sum_{n,m=1}^N \Psi_n^\dagger \cdot \mathcal{B}_{nm} \cdot \Psi_m, \quad (2.2a)$$

$$\Psi_n = \begin{pmatrix} a_n \\ a_n^\dagger \end{pmatrix}, \quad \mathcal{B}_{nm} = \begin{pmatrix} V_{nm} & -\Delta_{nm}^* \\ \Delta_{nm} & -V_{nm}^* \end{pmatrix}. \quad (2.2b)$$

The  $2N \times 2N$  Hermitian matrix  $\mathcal{B}$  is called the Bogoliubov-De Gennes (BdG) Hamiltonian [106]. Its eigenvalues come in pairs  $\pm E_1, \pm E_2, \dots, \pm E_N$  of opposite sign, with the positive entries equal to the single-particle excitation energies of the many-particle Hamiltonian  $H$ .

The unitary transformation

$$\mathcal{B}_{nm} \mapsto U \mathcal{B}_{nm} U^\dagger \equiv \mathcal{A}_{nm}, \quad \text{with } U = \frac{1}{\sqrt{2}} \begin{pmatrix} 1 & 1 \\ -i & i \end{pmatrix}, \quad (2.3)$$

maps  $\mathcal{B}$  onto the  $2N \times 2N$  imaginary antisymmetric matrix  $\mathcal{A}$  with elements

$$\mathcal{A}_{nm} = \begin{pmatrix} i \operatorname{Im}(V_{nm} + \Delta_{nm}) & i \operatorname{Re}(\Delta_{nm} + V_{nm}) \\ i \operatorname{Re}(\Delta_{nm} - V_{nm}) & i \operatorname{Im}(V_{nm} - \Delta_{nm}) \end{pmatrix} = -\mathcal{A}_{mn}^\top. \quad (2.4)$$

The superscript T denotes the transpose. An antisymmetric matrix is also referred to as “skew-symmetric”.

The transformed state

$$\gamma = (\gamma_1, \gamma_2, \dots, \gamma_{2N}), \quad \text{with} \quad \begin{pmatrix} \gamma_{2n-1} \\ \gamma_{2n} \end{pmatrix} = U \begin{pmatrix} a_n \\ a_n^\dagger \end{pmatrix}, \quad (2.5)$$

contains  $2N$  Hermitian operators  $\gamma_n = \gamma_n^\dagger$ , with anticommutator

$$\gamma_n \gamma_m + \gamma_m \gamma_n = \delta_{nm}, \quad \gamma_n^2 = 1/2. \quad (2.6)$$

This is the Clifford algebra of Majorana operators.

The global fermion parity operator

$$\mathcal{P} = (-1)^{\sum_{n=1}^N a_n^\dagger a_n} = (-2i)^N \gamma_1 \gamma_2 \cdots \gamma_{2N} \quad (2.7)$$

commutes with  $H$ , so energy eigenstates have a definite fermion parity  $\pm 1$ . Kitaev’s formula [17] equates the fermion parity  $\mathcal{P}_0$  of the ground state to the Pfaffian<sup>1</sup> (Pf) of the Hamiltonian in the Majorana basis,

$$\mathcal{P}_0 = \text{sign Pf}(-i\mathcal{A}), \quad \text{for} \quad H = \frac{1}{2} \gamma \cdot \mathcal{A} \cdot \gamma. \quad (2.8)$$

## 2.2.2 Pfaffian formula for a subsystem

Our objective is to calculate the ground-state expectation value of the fermion parity  $\mathcal{P}_L$  of an open subsystem, say the left quantum dot with  $N_L$  fermionic modes in Fig. 2.1 .

A direct way to proceed, used for example in Ref. [99], is to calculate the many-particle ground state  $|\Psi_0\rangle$  in the basis of occupation numbers and evaluate

$$\langle \mathcal{P}_L \rangle = \langle \Psi_0 | (-1)^{\sum_{n=1}^{N_L} a_n^\dagger a_n} | \Psi_0 \rangle. \quad (2.9)$$

Since the Fock space of occupation numbers has dimension  $2^N$ , this direct approach scales exponentially with system size and is therefore prohibitively expensive for large systems.

Klich [104] has developed an efficient method, with a polynomial scaling in  $N$ , to calculate squares of expectation values of operators  $\exp(i\chi \sum_n a_n^\dagger a_n)$ . This gives  $\langle \mathcal{P}_L \rangle^2$  if one sets  $\chi = \pi$  and restricts the sum to indices  $n$  in L. In App. 2.7 we show how the Klich method can be adapted to give also the sign

<sup>1</sup>Wikipedia has a helpful collection of Pfaffian formulas.

of  $\langle \mathcal{P} \rangle_L$ . That calculation is technically rather involved, but the final result can be easily understood as follows.

We make the flat-band transformation  $\mathcal{A} \mapsto \bar{\mathcal{A}}$ , which consists in replacing each of the  $2N$  eigenvalues  $\pm E_n$  of  $\mathcal{A}$  by their sign. (We assume that no eigenvalue is identically zero, meaning that we are not precisely at a fermion-parity switch.) Since no eigenvalue crosses zero when it is replaced by its sign, the flat-band transformation leaves the sign of the Pfaffian (2.8) invariant. And because the Pfaffian of  $-i\bar{\mathcal{A}}$  can only equal  $\pm 1$  we no longer need to take the sign in Eq. (2.8), hence the global fermion parity is

$$\mathcal{P}_0 = \text{Pf}(-i\bar{\mathcal{A}}). \quad (2.10)$$

At this point one may surmise that the desired subsystem generalization of Eq. (2.8) simply amounts to taking the Pfaffian of the  $2N_L \times 2N_L$  submatrix  $[\bar{\mathcal{A}}]_{LL}$  restricted to the subspace of modes in the left quantum dot,

$$\langle \mathcal{P}_L \rangle = \text{Pf}[-i\bar{\mathcal{A}}]_{LL}. \quad (2.11)$$

This is indeed the correct expression, as one can see by application of the Wick theorem for Majorana operators [100–102],

$$\langle \gamma_1 \gamma_2 \cdots \gamma_{2s} \rangle = \text{Pf}_{1 \leq k < l \leq 2s} \langle \gamma_k \gamma_l \rangle. \quad (2.12)$$

Substitution of  $\mathcal{P}_L = (-2i)^{N_L} \gamma_1 \gamma_2 \cdots \gamma_{2N_L}$  on the left-hand-side and  $-2i \langle \gamma_k \gamma_l \rangle = -i\bar{\mathcal{A}}_{kl}$  on the right-hand-side results in Eq. (2.11). This is how an equivalent formula was derived recently for a different problem [103].

Eq. (2.11) is computationally efficient because the Pfaffian of an  $N \times N$  matrix can be calculated in a time that scales polynomially with  $N$  [107, 108]: It has the same  $\mathcal{O}(N^3)$  complexity as the eigenvalue decomposition one needs for the flat-band transformation  $\mathcal{A} \mapsto \bar{\mathcal{A}}$ . Note that the flat-band transformation needs to be performed *before* the subblock restriction  $\bar{\mathcal{A}} \mapsto [\bar{\mathcal{A}}]_{LL}$  — the two operations do not commute.

## 2.3 Connection with the Majorana fusion rule

As a fundamental application of Eq. (2.11), consider the case that each quantum dot in Fig. 2.1 has a single electronic mode ( $N_L = N_R = 1$ ), each consisting of two Majorana modes with inter-dot coupling matrix  $\Gamma$  but vanishing intra-dot coupling — so these become fully isolated zero-modes when the

quantum dots are decoupled. The Hamiltonian in the Majorana basis is

$$\mathcal{A} = \begin{pmatrix} 0 & i\Gamma \\ -i\Gamma^T & 0 \end{pmatrix}. \quad (2.13)$$

The global fermion parity is

$$\mathcal{P}_0 = \text{sign Pf}(-i\mathcal{A}) = -\text{sign Det } \Gamma. \quad (2.14)$$

To obtain the average local fermion parity we use that the real  $2 \times 2$  coupling matrix  $\Gamma$  has the singular value decomposition  $\Gamma = O_1 \text{diag}(\kappa_1, \kappa_2) O_2$ , with  $O_1, O_2$  real orthogonal matrices and  $\kappa_1, \kappa_2 > 0$ . The eigenvalues of  $\mathcal{A}$  are  $\pm\kappa_1, \pm\kappa_2$ . In the flat-band transformation  $\{\kappa_1, \kappa_2\} \mapsto \{1, 1\}$ , which gives

$$\bar{\mathcal{A}} = \begin{pmatrix} 0 & iO_1O_2 \\ -iO_2^T O_1^T & 0 \end{pmatrix} \Rightarrow [\bar{\mathcal{A}}]_{\text{LL}} = 0 \Rightarrow \langle \mathcal{P}_L \rangle = 0, \quad (2.15)$$

so the average fermion parity in a single quantum dot vanishes. This is a manifestation of the Majorana fusion rule [53]: The fusion of the two Majorana zero-modes  $\gamma_1$  and  $\gamma_2$  produces an *equal-weight* superposition of a state of even and odd fermion parity.<sup>2</sup>

Several recent experimental proposals [60, 99, 109] are based on the connection between the Majorana fusion rule and vanishing average fermion parity. The implication “isolated Majorana zero-modes  $\Rightarrow \langle \mathcal{P}_L \rangle = 0$ ” holds if there are only two pairs of Majorana zero-modes. For  $N_L$  or  $N_R$  greater than 1 the implication breaks down, as is demonstrated by the following counterexample for  $N_L = N_R = 2$ :

$$\mathcal{A} = \begin{pmatrix} i\Omega & i\Gamma \\ -i\Gamma^T & i\Omega \end{pmatrix}, \quad \Omega = \begin{pmatrix} 0 & 0 & 0 & 0 \\ 0 & 0 & 0 & 0 \\ 0 & 0 & 0 & 1 \\ 0 & 0 & -1 & 0 \end{pmatrix}, \quad \Gamma = \begin{pmatrix} 0 & 0 & 1 & 0 \\ 0 & 0 & 0 & 1 \\ 1 & 0 & 0 & 0 \\ 0 & 1 & 0 & 0 \end{pmatrix}, \quad (2.16a)$$

$$\Rightarrow \bar{\mathcal{A}} = \frac{1}{\sqrt{5}} \begin{pmatrix} i\Omega' & i\Gamma' \\ -i\Gamma'^T & i\Omega' \end{pmatrix}, \quad \Gamma' = 2\Gamma, \quad \Omega' = \begin{pmatrix} 0 & -1 & 0 & 0 \\ 1 & 0 & 0 & 0 \\ 0 & 0 & 0 & 1 \\ 0 & 0 & -1 & 0 \end{pmatrix}, \quad (2.16b)$$

$$\Rightarrow [\bar{\mathcal{A}}]_{\text{LL}} = \frac{i}{\sqrt{5}} \Omega' \Rightarrow \text{Pf}[-i\bar{\mathcal{A}}]_{\text{LL}} = -\frac{1}{5}, \quad (2.16c)$$

<sup>2</sup>The converse is not excluded:  $\langle \mathcal{P}_L \rangle = 0$  without an isolated Majorana zero-mode is possible, for example for

$$\mathcal{A} = i \begin{pmatrix} 0 & \lambda_1 & 0 & \lambda_2 \\ -\lambda_1 & 0 & -\lambda_2 & 0 \\ 0 & \lambda_2 & 0 & \lambda_1 \\ -\lambda_2 & 0 & -\lambda_1 & 0 \end{pmatrix} \text{ with } \lambda_1 < \lambda_2.$$

and hence  $\langle \mathcal{P}_L \rangle = -1/5$  does not vanish even though each quantum dot has a pair of Majorana zero-modes without intra-dot coupling ( $\gamma_1$  and  $\gamma_2$  in the left dot,  $\gamma_5$  and  $\gamma_6$  in the right dot).

Since  $\text{Pf}(-i\mathcal{A}) = +1$  the global fermion parity is even, hence the negative sign for  $\langle \mathcal{P}_L \rangle$  means that the states with odd-odd occupation numbers in the left and right quantum dot have a greater weight in the ground state than the states with even-even occupation numbers — even though the fusion of the Majorana modes  $\gamma_1$  and  $\gamma_2$  would favor equal weight of even and odd fermion parity.

As a check on the formalism, we have also calculated the average fermion parity directly from the many-particle ground state wave function  $|\Psi_0\rangle$  of the Hamiltonian  $H = \frac{1}{2}\gamma \cdot \mathcal{A} \cdot \gamma$ . We find

$$|\Psi_0\rangle = \frac{\sqrt{5}}{10} [2i(a_1^\dagger a_2^\dagger + a_3^\dagger a_4^\dagger) - (1 + \sqrt{5})a_1^\dagger a_3^\dagger - (1 - \sqrt{5})a_2^\dagger a_4^\dagger] |0\rangle, \quad (2.17)$$

which indeed gives  $\langle \mathcal{P}_L \rangle = -1/5$  upon calculation of the expectation value (2.9).

In this case with  $N = N_L + N_R = 4$  electronic levels the size  $2^{N-1} = 8$  of the basis of many-particle states in the even-parity sector is the same as the size  $2N = 8$  of the basis of single-particle states, so the two calculations based on Eq. (2.9) or on Eq. (2.11) are equally efficient. For larger  $N$  the single-particle approach based on the Pfaffian formula has the more favorable scaling (polynomial instead of exponential).

## 2.4 Random-matrix theory

For a statistical description of the fermion parity fluctuations we apply the methods of random-matrix theory (RMT). In Sec. 2.4.2 we assume a strong mixing of the states in the two quantum dots of Fig. 2.1, and then in Sec. 2.4.3 we consider the opposite regime of weakly coupled quantum dots. We will need results [110] from the RMT in symmetry class DIII, which we summarize in Sec. 2.4.1.

### 2.4.1 Skew Circular Real Ensemble

The matrix  $[-i\bar{\mathcal{A}}]_{LL}$  which in view of Eq. (2.11) determines the local fermion parity is a  $2N_L \times 2N_L$  submatrix of a matrix  $\mathcal{S} = -i\bar{\mathcal{A}}$  that is an antisymmetric (skew-symmetric) element of the real orthogonal group  $O(2N)$ , with

$N = N_L + N_R$ . The corresponding ensemble from RMT is the class-DIII circular ensemble, which differs from the class-D circular ensemble by the antisymmetry restriction [49]. The latter is called the *Circular Real Ensemble* (CRE) and we will refer to the former as the *skew-Circular Real Ensemble* (skew-CRE).<sup>3</sup> The switch from symmetry class D to DIII is remarkable, because class DIII was originally introduced [48] in superconductors with preserved time-reversal symmetry — which is broken in our physical system.

Two equivalent methods to randomly choose a matrix from the skew-CRE are:

1. Generate a real antisymmetric matrix  $-i\mathcal{A}$  with independent Gaussian elements on the upper diagonal (zero mean and unit variance), and perform the flat-band transformation to obtain  $\mathcal{S} = -i\bar{\mathcal{A}}$ .
2. Draw a random element  $O$  from  $O(2N)$ , uniformly with the invariant Haar measure, and construct

$$\mathcal{S} = O \begin{pmatrix} 0_{N \times N} & 1_{N \times N} \\ -1_{N \times N} & 0_{N \times N} \end{pmatrix} O^T. \quad (2.18)$$

The two methods are equivalent because the distribution  $P(\mathcal{A}) \propto \exp(\frac{1}{4}\text{Tr } \mathcal{A}^2)$  as well as the flat-band transformation  $\mathcal{A} \mapsto \bar{\mathcal{A}}$  are invariant under orthogonal transformations  $\mathcal{A} \mapsto O\mathcal{A}O^T$ , so the matrix  $O$  in the decomposition (2.18) is distributed according to the invariant Haar measure.

The matrix  $\mathcal{S}$  has the block decomposition

$$\mathcal{S} = \begin{pmatrix} \mathcal{S}_{LL} & \mathcal{S}_{LR} \\ \mathcal{S}_{RL} & \mathcal{S}_{RR} \end{pmatrix}, \quad \mathcal{S}_{LL} = [-i\bar{\mathcal{A}}]_{LL}, \quad (2.19)$$

with  $\mathcal{S}_{XY}$  a matrix of dimension  $N_X \times N_Y$ . In the context of scattering problems, where the skew-CRE ensemble was studied previously [49], this is analogous to a decomposition of the scattering matrix into reflection and transmission matrices. In that context the eigenvalues  $\pm i\lambda_n$  of the upper-left submatrix  $\mathcal{S}_{LL}$  correspond to reflection amplitudes.<sup>4</sup> Their joint probability

<sup>3</sup>The qualifier “real” for the  $O(N)$  ensemble is used instead of “orthogonal” because the name *Circular Orthogonal Ensemble* (COE) was already used by Dyson [111] for the coset  $U(N)/O(N)$ .

<sup>4</sup>Eq. (2.20) follows from equation 5 of Ref. [110] upon change of variables from transmission probabilities  $T_n$  to reflection amplitudes  $\lambda_n = \sqrt{1 - T_n}$ .

distribution in the skew-CRE is known [110],

$$P(\lambda_1, \lambda_2, \dots, \lambda_{N_{\min}}) \propto \prod_n (1 - \lambda_n^2)^{|N_L - N_R|} \prod_{j < k} (\lambda_k^2 - \lambda_j^2)^2, \\ N_{\min} = \min(N_L, N_R), \quad 0 \leq \lambda_n \leq 1. \quad (2.20)$$

If  $N_L > N_R$  there are additionally  $2(N_L - N_R)$  trivial eigenvalues pinned at  $\pm 1$ , not included in the distribution (2.20).

Symmetry class DIII has the  $\mathbb{Z}_2$  invariant  $\text{Pf } \mathcal{S} = \pm 1$ , which in view of Kitaev's formula (2.10) is the global fermion parity  $\mathcal{P}_0$ . This does not enter in Eq. (2.20) because in the skew-CRE the distribution of the  $\lambda_n$ 's is independent of the  $\mathbb{Z}_2$  invariant [110].

The density  $\rho(\lambda)$  of the nontrivial eigenvalues has  $\pm\lambda$  symmetry with a three-peak structure: There are two peaks at the band edges  $\pm\lambda_c$ , with [110]

$$\lambda_c = (2/N)(N_L N_R)^{1/2}, \quad (2.21)$$

and a peak at the band center<sup>5</sup> described by [48, 51, 112]

$$\rho(\lambda) = \frac{1}{\delta_{\text{eff}}} + \frac{\sin(2\pi\lambda/\delta_{\text{eff}})}{2\pi\lambda}, \quad \lambda \lesssim 1/\delta_{\text{eff}}. \quad (2.22)$$

The parameter  $\delta_{\text{eff}} = \pi/2N_{\min}$  is the mean eigenvalue spacing in the center of the band. The peak at  $\lambda = 0$  is a weak antilocalization effect in the scattering context [113].

Fig. 2.2 shows the eigenvalue density for  $N_L = N_R = N_{\text{dot}}$  ranging from 1 to 6. The three-peaked structure is evident except for  $N_{\text{dot}} = 1$ , when the density profile is flat.

### 2.4.2 Distribution of the local fermion parity in the skew-CRE

The peak at  $\lambda = 0$  in the eigenvalue density  $\rho(\lambda)$  increases the probability for vanishing local fermion parity, since

$$|\langle \mathcal{P}_L \rangle| = \prod_{n=1}^{N_{\min}} \lambda_n = \sqrt{\text{Det } \mathcal{S}_{LL}}. \quad (2.23)$$

---

<sup>5</sup>For the density profile near  $\lambda = 0$  we can approximate the distribution (2.20) by  $P(\{\lambda\}) \propto \prod_{j < k} (\lambda_k^2 - \lambda_j^2)^2$  and ignore the restriction  $|\lambda_n| \leq 1$ . The distribution of the  $\lambda_n$ 's is then identical to the distribution of the energy levels of a Hermitian matrix in symmetry class D, which has the spectral peak (2.22). A Hermitian matrix in class DIII, rather than class D, has a vanishing density of states at zero energy, but this is not relevant for  $\rho(\lambda)$ .

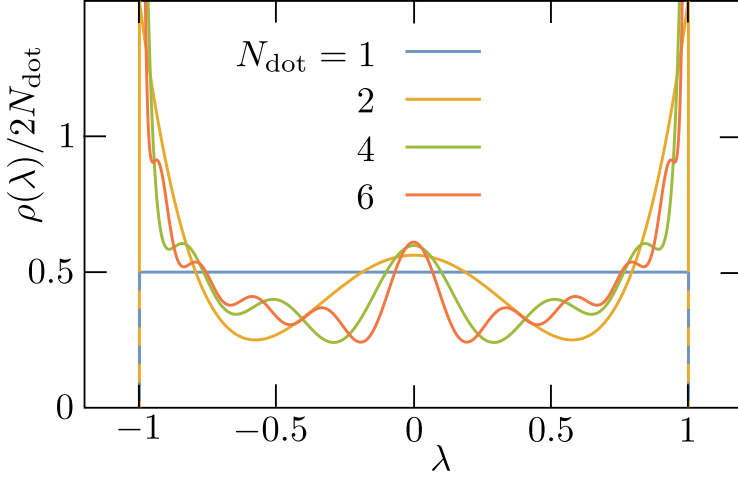


**Figure 2.2.** Density  $\rho(\lambda)$  of the eigenvalues of the  $2N_L \times 2N_L$  matrix  $[-i\bar{\mathcal{A}}]_{LL}$  in the skew-CRE, calculated by integration of the distribution (2.20) for  $N_L = N_R = N_{\text{dot}} \in \{1, 2, 4, 6\}$ . The density has a peak at the band edges and at the band center.

Indeed, as shown in Fig. 2.3, while the distribution of  $\langle \mathcal{P}_L \rangle$  in the skew-CRE is broad for a single electronic level  $N_{\text{dot}} = 1$  in each quantum dot, it quickly narrows to a sharp peak at  $\langle \mathcal{P}_L \rangle = 0$  with just a few levels — in accord with numerical calculations reported by Clarke, Sau, and Das Sarma [99].

The peak at zero  $\langle \mathcal{P}_L \rangle \equiv p$  appears as a sharp cusp in Fig. 2.3, it has a logarithmic singularity  $\propto (p^2 \ln |p|)^{N_{\text{dot}}-1}$ , for example

$$P(\langle \mathcal{P}_L \rangle = p) = \frac{45}{32} \left(1 - p^4 + 4p^2 \ln |p|\right), \quad N_{\text{dot}} = 2, \quad |p| \leq 1. \quad (2.24)$$

For large- $N_{\text{dot}}$  the width of the distribution becomes exponentially small, as follows from the variance

$$\text{Var} \langle \mathcal{P}_L \rangle = \frac{(2N_{\text{dot}})!^3}{(N_{\text{dot}})!^2 (4N_{\text{dot}})!} = \frac{\sqrt{2}}{4^{N_{\text{dot}}}} [1 + \mathcal{O}(1/N_{\text{dot}})], \quad (2.25)$$

see App. 2.8.

We may quantify the effect of the spectral peak in  $\rho(\lambda)$  on the distribution of the local fermion parity by comparing with a set of independent  $\lambda_n$ 's with uniform density. In that uniform case one would have the fermion parity distribution

$$P_{\text{uniform}}(\langle \mathcal{P}_L \rangle = p) = \frac{(-\ln |p|)^{N_{\text{dot}}-1}}{2(N_{\text{dot}}-1)!}, \quad |p| \leq 1, \quad (2.26)$$

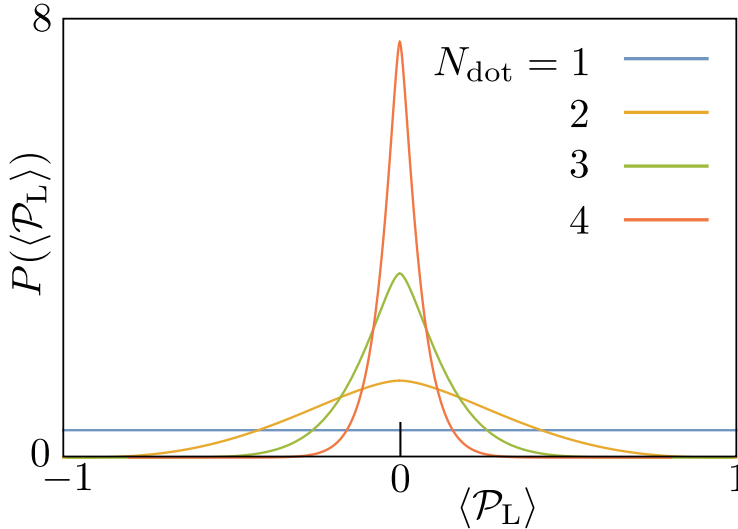


**Figure 2.3.** Probability distribution of the local fermion parity in the ensemble of antisymmetric orthogonal matrices (skew-CRE), representative of strongly coupled quantum dots. The curves are calculated from Eq. (2.20) for  $N_L = N_R = N_{\text{dot}} \in \{1, 2, 3, 4\}$ . It takes just a few levels in the quantum dot to have  $\langle \mathcal{P}_L \rangle \approx 0$  with high probability, so equal weight of even and odd fermion parity.

with a variance  $3^{-N_{\text{dot}}}$  that decays less rapidly than Eq. (2.25).

### 2.4.3 RMT model of weakly coupled quantum dots

The RMT description in terms of the skew-CRE from the previous subsection assumes a strong (chaotic) mixing in the entire phase space, appropriate for strongly coupled quantum dots. To describe also the weakly coupled regime, we consider an alternative approach where the RMT ensemble is applied to the two quantum dots individually, rather than to the system as a whole.

In the Majorana representation, the Hamiltonian  $H = \frac{1}{2}\gamma \cdot \mathcal{A} \cdot \gamma$  of the two coupled quantum dots of Fig. 2.1 has the block structure

$$\mathcal{A} = \begin{pmatrix} i\Omega_L & i\Gamma \\ -i\Gamma^T & i\Omega_R \end{pmatrix}. \quad (2.27)$$

The real antisymmetric matrices  $\Omega_X$  of size  $2N_X \times 2N_X$ , with  $X \in \{R, L\}$ , describe the left and right quantum dot in isolation, while the  $2N_L \times 2N_R$  real matrix  $\Gamma$  describes the coupling via a quantum point contact (QPC) with  $N_{\text{QPC}}$  propagating fermionic modes. In what follows we take  $N_L = N_R = N_{\text{dot}}$ .

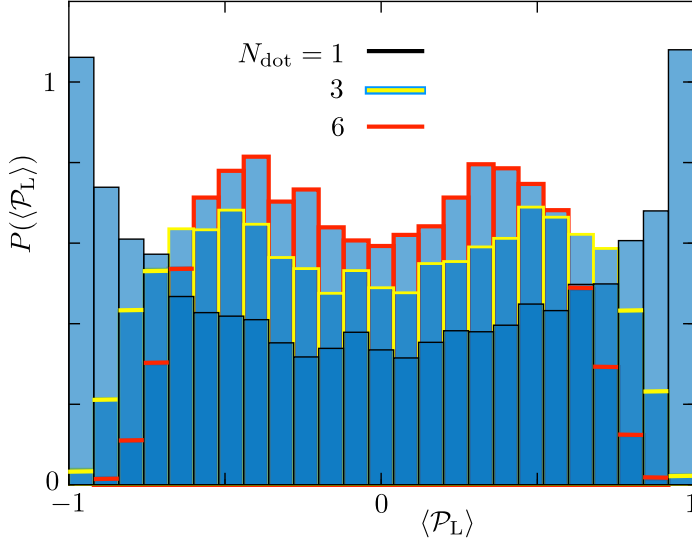


**Figure 2.4.** Probability distribution of the local fermion parity for the RMT model (2.27) of two weakly coupled quantum dots, calculated numerically by sampling the Gaussian matrix elements in  $\Omega_L, \Omega_R, \Gamma$  for  $N_{\text{QPC}} = 1$ ,  $N_L = N_R = N_{\text{dot}} \in \{1, 3, 6\}$ . In contrast to the strongly coupled skew-CRE ensemble of Fig. 2.3, the distribution narrows only slowly with increasing  $N_{\text{dot}}$ .

The number  $N_{\text{dot}}$  counts the number of electronic modes in each quantum dot. One electronic mode  $a_n$  corresponds to two Majorana modes  $\gamma_{2n-1}$  and  $\gamma_{2n}$ , according to

$$a_n = (\gamma_{2n-1} + i\gamma_{2n})/\sqrt{2}, \quad (2.28)$$

cf. Eq. (3.4). Because of this double-counting, the mean level spacing  $\delta_0$  of eigenstates of  $\Omega_X$  is one half the electronic mean level spacing of a quantum dot (taken the same in each dot, for simplicity).

For a statistical description we take independent Gaussian distributions for the two matrices  $\Omega_X$ . Each upper-diagonal matrix element has zero mean and variance  $2N_{\text{dot}}\delta_0^2/\pi^2$ , corresponding to superconductors in symmetry class D (broken time-reversal and broken spin-rotation symmetry) [48, 49].

Following Refs. [114, 115], the quantum dots are coupled by a Gaussian

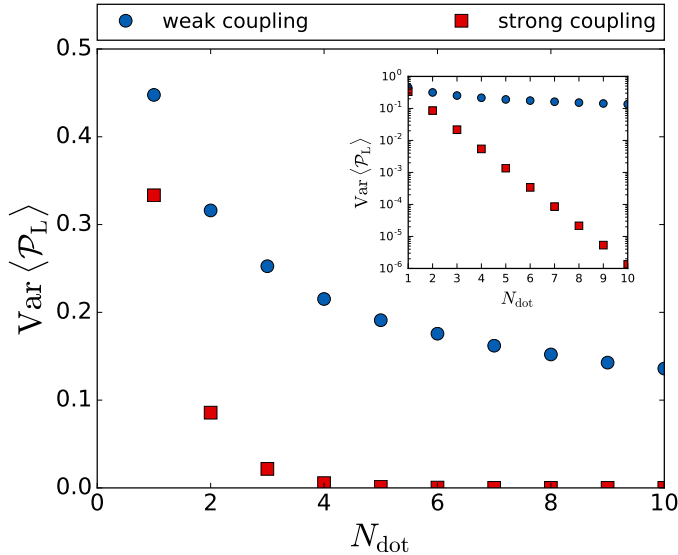


**Figure 2.5.** Comparison of the variance of  $P(\langle \mathcal{P} \rangle)$  in the skew-CRE of strongly coupled quantum dots [red data points, calculated from Eq. (2.25)] and in the weakly coupled ensemble (blue data points, numerical results for  $N_{\text{QPC}} = 1$ ). The inset shows that the decay is exponential in both cases, but with widely different decay rates.

random matrix  $\Gamma$  of rank  $N_{\text{QPC}}$ , with elements<sup>6</sup>

$$\Gamma_{kl} = \frac{2N_{\text{dot}}\delta}{\pi} \sum_{n=1}^{2N_{\text{QPC}}} v_k^{(n)} w_l^{(n)}, \quad (2.29)$$

in terms of  $2N_{\text{QPC}}$  real Gaussian vectors  $v^{(n)}$  and  $w^{(n)}$  of unit average length (each element independently distributed with zero mean and variance  $1/2N_{\text{dot}}$ ).

For the weak coupling regime we focus on the case of a single propagating electronic mode in the point contact,  $N_{\text{QPC}} = 1$ , corresponding to two propagating Majorana modes. We do not have an analytical solution, so we show numerical results in Fig. 2.4 for the probability distribution of  $\langle \mathcal{P}_L \rangle = \text{Pf}(-i\bar{A})$  in the ensemble of random matrices  $\Omega_L$ ,  $\Omega_R$ , and  $\Gamma$ . The variance of the distribution is compared with that in the skew-CRE in Fig. 2.5. The two figures show that the distribution of the local fermion parity is much broader when the coupling is via a single-mode point contact.

<sup>6</sup>The coupling matrix (2.29) describes a ballistic point contact. For tunnel coupling, rather than ballistic coupling, the coupling strength  $\delta_0/\pi$  is to be multiplied by  $T_n^{-1}(2 - T_n - 2\sqrt{1 - T_n})$ , with  $T_n$  the tunnel probability of the  $n$ -th mode in the QPC, see Ref. [49].

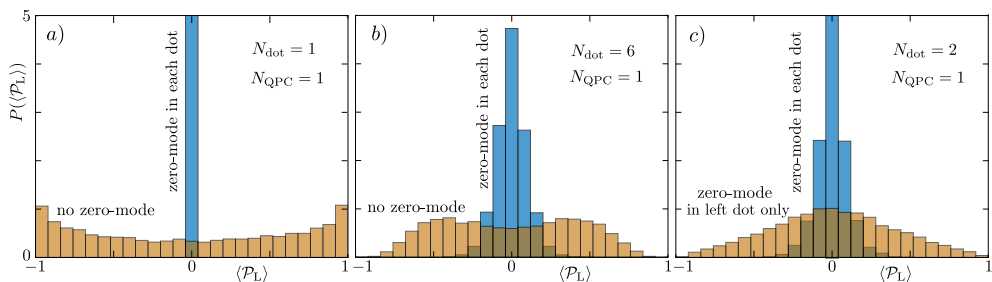


**Figure 2.6.** Same as Fig. 2.4, but now comparing the situation with or without isolated Majorana zero-modes in a quantum dot. The quantum dots are weakly coupled ( $N_{\text{QPC}} = 1$ ) and they have the same number of electronic levels  $N_L = N_R = N_{\text{dot}}$ . For the blue histograms each quantum dot has a pair of isolated Majorana zero-modes (no intradot coupling, only interdot coupling). For the brown histograms there are either no isolated zero-modes at all (panels a and b), or they are only in one of the two quantum dots (panel c). Weak coupling ensures that the peak at vanishing local fermion parity becomes a distinctive feature of isolated Majorana zero-modes in each quantum dot.

## 2.5 Effect of an isolated Majorana zero-mode

The random Hamiltonians of the previous section do not contain isolated Majorana zero-modes: the  $2N_{\text{dot}}$  Majorana modes in each quantum dot have intradot coupling as well as interdot coupling. We may introduce a pair of isolated Majorana zero-modes in a quantum dot by setting to zero one row and one column of the submatrix  $\Omega_L$  or  $\Omega_R$  in the Hamiltonian (2.27). (The row and column number should be the same to preserve the antisymmetry of  $\Omega_X$ .) The effect on the distribution of the local fermion parity is shown in Fig. 2.6. The distribution of the local fermion parity is strongly peaked at zero if and only if there is a pair of isolated Majorana zero-modes in each of the two quantum dots.

## 2.6 Conclusion

In summary, we have studied the fusion of Majorana zero-modes using a generalization of Kitaev's Pfaffian formula [17] for the global fermion parity of the superconducting ground state, to include local fermion parity fluctuations in an open subsystem. The Pfaffian formula in Eq. (2.11), and an equivalent formulation from Ref. [103], is computationally efficient since it works with the single-particle (Bogoliubov-De Gennes) Hamiltonian rather than with the

many-particle Hamiltonian. One limitation of the single-particle formulation is that it is limited to a mean-field description of the superconductor — in particular we are assuming that the quantum dots in the geometry of Fig. 2.1 have a sufficiently large capacitance that Coulomb charging energies can be neglected.

The Pfaffian fermion parity formula is particularly suited to an analysis in terms of random-matrix theory, in an ensemble of antisymmetric matrices [49]. For strongly coupled quantum dots the circular ensemble in symmetry class DIII is the appropriate ensemble, which allows for analytical results for the statistical distribution of the local fermion parity. There is no eigenvalue repulsion at the particle-hole symmetry point in such an ensemble [48], and the resulting accumulation of near-zero eigenvalues enforces a nearly equal-weight superposition of even and odd fermion parity in a quantum dot.

This is a nontopological mechanism for vanishing expectation value  $\langle \mathcal{P}_L \rangle \approx 0$  of the local fermion parity. The Majorana fusion rule provides a fundamentally different, topological mechanism [53]: The merging or “fusion” of two isolated Majorana zero-modes (“isolated” in the sense of zero intradot coupling, while allowing for interdot coupling) also favors a vanishing  $\langle \mathcal{P}_L \rangle$  because the two fusion channels, with or without an unpaired quasiparticle, have equal weight.

To carry out such a fusion experiment it is proposed [60] that one would rapidly decouple the subsystems, on a time scale  $\tau_c$  sufficiently short that quasiparticles from the environment cannot leak in. The complication [99] is that even if there are isolated Majorana zero-modes, the presence of even a small number  $N_{\text{dot}}$  of higher levels at energies below  $\hbar/\tau_c$  may hide the presence of the zero-modes by favoring  $\langle \mathcal{P}_L \rangle \approx 0$  (see Fig. 2.3).

Fig. 2.6 illustrates our proposal to distinguish the two mechanisms for vanishing local fermion parity: A low-rank coupling between the quantum dots, via a single-mode quantum point contact, suppresses the nontopological effect from levels at nonzero energy, without affecting the topological effect from the fusion of isolated Majorana zero-modes.

## 2.7 Appendix: Derivation of the Pfaffian formula from Klich's counting statistics theory

We follow the steps of Klich's theory of counting statistics of paired fermions [104], to reproduce his result for  $\langle \mathcal{P}_L \rangle^2$ . Then we will resolve the sign ambiguity to arrive at Eq. (2.11) for  $\langle \mathcal{P}_L \rangle$ . An equivalent formula is obtained by a different

method in Ref. [103], Appendix B.

The superconductor in Fig. 2.1 is assumed to be an isolated system, so that the global fermion parity does not fluctuate. For the derivation of the subsystem fermion parity formula (2.11) it is convenient to start from the more general case that the superconductor is in contact with a reservoir in thermal equilibrium at temperature  $T$ . We will then take the  $T \rightarrow 0$  limit at the end of the calculation in order to describe an isolated system.

At inverse temperature  $\beta = 1/k_B T$  the average fermion parity  $\langle \mathcal{P}_L \rangle$  of subsystem L (the left quantum dot in Fig. 2.1) is given by the trace of the equilibrium density matrix

$$\rho_{\text{eq}} = \frac{1}{Z} e^{-\beta H}, \quad Z = \text{Tr} \rho_{\text{eq}}, \quad (2.30)$$

acting on the fermion parity operator

$$\mathcal{P}_L = \exp \left( i\pi \sum_{n \in L} a_n^\dagger a_n \right). \quad (2.31)$$

Because  $H = \frac{1}{2} \sum_{n,m} \mathcal{A}_{nm} \gamma_n \gamma_m$  in the basis of Majorana operators  $\gamma_n$ , and  $a_n^\dagger a_n = i\gamma_{2n-1} \gamma_{2n} + \frac{1}{2}$ , this can be written as

$$\begin{aligned} \langle \mathcal{P}_L \rangle &= \frac{e^{i\pi N_L/2}}{Z} \text{Tr} \left[ \exp \left( -\frac{1}{2} \beta \sum_{n,m} \mathcal{A}_{nm} \gamma_n \gamma_m \right) \right. \\ &\quad \left. \times \exp \left( -\frac{1}{2} i\pi \sum_{n,m} (\sigma_y \otimes P_L)_{nm} \gamma_n \gamma_m \right) \right]. \end{aligned} \quad (2.32)$$

The matrix  $\sigma_y$  is a Pauli matrix and the operator  $P_L$  projects onto  $N_L$  fermionic modes in subsystem L.

Application of the identity [104]

$$\left[ \text{Tr} \prod_k e^{\gamma \cdot O_k \cdot \gamma} \right]^2 = e^{\sum_k \text{Tr} O_k} \text{Det} \left( 1 + \prod_k e^{O_k - O_k^T} \right), \quad (2.33)$$

results in

$$\begin{aligned} \langle \mathcal{P}_L \rangle^2 &= e^{i\pi N_L} \frac{\text{Det} [1 + \exp(-\beta \mathcal{A}) \exp(-i\pi \sigma_y \otimes P_L)]}{\text{Det} [1 + \exp(-\beta \mathcal{A})]} \\ &= (-1)^{N_L} \text{Det} \left[ 1 - \frac{2}{1 + \exp(\beta \mathcal{A})} (\sigma_0 \otimes P_L) \right]. \end{aligned} \quad (2.34)$$

In the second equality we made use of the identity

$$e^{i\chi\sigma_y\otimes P_L} = 1 + \sigma_0 \otimes P_L(\cos\chi - 1) + i\sigma_y \otimes P_L \sin\chi, \quad (2.35)$$

with  $\chi = \pi$ . (The matrix  $\sigma_0 = \sigma_y^2$  is the  $2 \times 2$  unit matrix.) Note that, in a basis of energy eigenstates of the BdG Hamiltonian, the operator  $(1 + e^{\beta\mathcal{A}})^{-1}$  is the Fermi function  $f(E) = (1 + e^{\beta E})^{-1}$ .

Eq. (2.34) is Klich's result for the square of the average fermion parity (equation 84 in Ref. [104]). Klich shows how the sign of  $\langle \mathcal{P}_L \rangle$  can be recovered if the determinant is known analytically as a function of the matrix elements. Here we take a different route, more suitable for numerical calculations, which gives the sign directly upon evaluation of a Pfaffian instead of a determinant.

Any  $2N \times 2N$  imaginary anti-symmetric matrix  $\mathcal{A}$  can be decomposed as

$$\mathcal{A} = iO(J \otimes \mathcal{E})O^T, \quad J = \begin{pmatrix} 0 & 1 \\ -1 & 0 \end{pmatrix}, \quad (2.36)$$

where  $O$  is a  $2N \times 2N$  real orthogonal matrix and  $\mathcal{E} = \text{diag}(E_1, E_2, \dots, E_N)$  is an  $N \times N$  real diagonal matrix. Substitution into Eq. (2.34) gives

$$\begin{aligned} \langle \mathcal{P}_L \rangle^2 &= (-1)^{N_L} \text{Det} \left[ 1 - O \frac{2}{1 + \exp(i\beta J \otimes \mathcal{E})} O^T (\sigma_0 \otimes P_L) \right] \\ &= (-1)^{N_L} \text{Det} \left[ 1 - O [1 - iJ \otimes \tanh(\tfrac{1}{2}\beta\mathcal{E})] O^T (\sigma_0 \otimes P_L) \right]. \end{aligned} \quad (2.37)$$

This may be written in a more compact form by defining the restriction  $[M]_{LL}$  of a  $2N \times 2N$  matrix  $M$  to the  $2N_L \times 2N_L$  submatrix of modes in region L,

$$\begin{aligned} \langle \mathcal{P}_L \rangle^2 &= (-1)^{N_L} \text{Det} [O[iJ \otimes \tanh(\tfrac{1}{2}\beta\mathcal{E})]O^T]_{LL} \\ &= \text{Det} [O[J \otimes \tanh(\tfrac{1}{2}\beta\mathcal{E})]O^T]_{LL}. \end{aligned} \quad (2.38)$$

Note that, because of the submatrix restriction, the product rule  $\text{Det}(AB) = (\text{Det} A)(\text{Det} B)$  cannot be applied to  $\text{Det}[AB]_{LL}$ , so the orthogonal matrix  $O$  cannot be cancelled with the inverse  $O^T$ .

We have now arrived at the determinant of a real antisymmetric matrix, hence we can take the square root without introducing branch cuts,

$$\langle \mathcal{P}_L \rangle = \text{Pf} [O[J \otimes \tanh(\tfrac{1}{2}\beta\mathcal{E})]O^T]_{LL}. \quad (2.39)$$

In the zero-temperature,  $\beta \rightarrow \infty$  limit this reduces to

$$\langle \mathcal{P}_L \rangle = \text{Pf} [O[J \otimes (\text{sign } \mathcal{E})]O^T]_{\text{LL}}, \quad (2.40)$$

which is Eq. (2.11) with  $-i\bar{\mathcal{A}} = O[J \otimes (\text{sign } \mathcal{E})]O^T$ . Kitaev's formula (2.8) for the global ground-state fermion parity is recovered when L is the entire isolated system. This correspondence also identifies  $\sqrt{\text{Det}}$  with  $+\text{Pf}$  rather than with  $-\text{Pf}$ .

## 2.8 Appendix: Moments of determinants of anti-symmetric random matrices

In Sec. 2.4.2 we used a formula for the average determinant of a submatrix (a principal minor) of an antisymmetric real orthogonal matrix. This would seem like a classic result in RMT, but we have not found it in the literature on such matrices [116–118]. We therefore give the derivation in this appendix, and for completeness and reference also derive the corresponding result for antisymmetric Hermitian matrices.

### 2.8.1 Principal minor of antisymmetric orthogonal matrix

Consider a  $2N \times 2N$  antisymmetric real orthogonal matrix  $\mathcal{S}$ , with a uniform distribution in  $O(2N)$  subject to the antisymmetry constraint. This is the class-DIII circular ensemble of RMT [48, 49], referred to as the skew-Circular Real Ensemble (skew-CRE) in the main text.<sup>7</sup>

The  $2N_L \times 2N_L$  upper-left submatrix  $\mathcal{S}_{\text{LL}}$  has eigenvalues  $\pm i\lambda_n$ ,  $0 \leq \lambda_n \leq 1$ . Denoting  $N_R = N - N_L$  and  $N_{\text{min}} = \min(N_L, N_R)$ , we have that  $N - N_{\text{min}}$  of the  $\lambda_n$ 's are pinned to +1. The set  $\{\lambda_n\} = \{\lambda_1, \lambda_2, \dots, \lambda_{N_{\text{min}}}\}$  can vary freely in the interval  $[0, 1]$ , with joint probability distribution [110]

$$P(\{\lambda_n\}) \propto \prod_n (1 - \lambda_n^2)^{|N_L - N_R|} \prod_{i < j} (\lambda_i^2 - \lambda_j^2)^2. \quad (2.41)$$

The determinant of  $\mathcal{S}_{\text{LL}}$  is a principal minor given by

$$\text{Det } \mathcal{S}_{\text{LL}} = \prod_{n=1}^{N_L} (i\lambda_n)(-i\lambda_n) = \prod_{n=1}^{N_{\text{min}}} \lambda_n^2. \quad (2.42)$$

<sup>7</sup>The antisymmetric orthogonal matrices form a disconnected set in  $O(2N)$ , distinguished by the sign of the Pfaffian. For the probability distribution (2.41) it does not matter whether or not we restrict the ensemble to  $\text{Pf } \mathcal{S} = \pm 1$ .

We seek the moments  $\mu_q = \mathbb{E}[(\text{Det } \mathcal{S}_{\text{LL}})^q]$  of this determinant in the skew-CRE.

For that purpose we make a change of variables from  $\lambda_n$  to  $R_n = \lambda_n^2 \in [0, 1]$ , with distribution

$$P(\{R_n\}) \propto \prod_n R_n^{-1/2} (1 - R_n)^{|N_{\text{L}} - N_{\text{R}}|} \prod_{i < j} (R_i - R_j)^2. \quad (2.43)$$

We can then compute the moments of the determinant from

$$\mu_q = \frac{\int_0^1 d\{R_n\} \prod_{i < j} (R_i - R_j)^2 \prod_n (1 - R_n)^{|N_{\text{L}} - N_{\text{R}}|} R_n^{q-1/2}}{\int_0^1 d\{R_n\} \prod_{i < j} (R_i - R_j)^2 \prod_n (1 - R_n)^{|N_{\text{L}} - N_{\text{R}}|} R_n^{-1/2}}, \quad (2.44)$$

where we abbreviated  $\int_0^1 d\{R_n\} = \int_0^1 dR_1 \cdots \int_0^1 dR_{N_{\text{min}}}$ .

These so-called Selberg integrals have a closed-form expression [119],

$$\mu_q = \prod_{j=0}^{N_{\text{min}}-1} \frac{\Gamma(\max(N_{\text{L}}, N_{\text{R}}) + j + \frac{1}{2}) \Gamma(q + j + \frac{1}{2})}{\Gamma(\max(N_{\text{L}}, N_{\text{R}}) + q + j + \frac{1}{2}) \Gamma(j + \frac{1}{2})}. \quad (2.45)$$

For the first few moments, Eq. (2.45) reduces to

$$\mu_1 = \frac{(2N_{\text{L}})!(2N_{\text{R}})!N!}{N_{\text{L}}!N_{\text{R}}!(2N)!}, \quad (2.46)$$

$$\mu_2 = \frac{(2N_{\text{L}} + 1)(2N_{\text{R}} + 1)}{2N + 1} \mu_1^2. \quad (2.47)$$

Eq. (2.25) in the main text is Eq. (2.46) for  $N_{\text{L}} = N_{\text{R}} = N_{\text{dot}} = N/2$ .

## 2.8.2 Antisymmetric Hermitian matrix

A similar calculation can be carried out for moments of the determinant of a  $2N \times 2N$  antisymmetric Hermitian matrix  $\mathcal{A}$ , in the Gaussian ensemble of independent upper-diagonal elements with a normal distribution (zero mean and unit variance).

The  $2N$  eigenvalues come in pairs  $\pm\lambda_n$ . The  $N$  eigenvalues  $\lambda_n \geq 0$  have the joint distribution [51]

$$P(\{\lambda_n\}) \propto \prod_n e^{-\lambda_n^2/2} \prod_{i < j} (\lambda_i^2 - \lambda_j^2)^2. \quad (2.48)$$

The determinant is

$$\text{Det } \mathcal{A} = (-1)^N \prod_{n=1}^N \lambda_n^2. \quad (2.49)$$

Let us introduce the variables  $x_n = \lambda_n^2/2 \geq 0$ , with distribution

$$P(\{x_n\}) \propto \prod_n x_n^{-1/2} e^{-x_n} \prod_{i<j} (x_i - x_j)^2. \quad (2.50)$$

The  $q$ -th moment  $\mu_q$  of the determinant of  $\mathcal{A}$  is given by

$$\mu_q = (-2)^{Nq} \frac{\int_0^\infty d\{x_n\} \prod_{i<j} (x_i - x_j)^2 \prod_n x_n^{q-1/2} e^{-x_n}}{\int_0^\infty d\{x_n\} \prod_{i<j} (x_i - x_j)^2 \prod_n x_n^{-1/2} e^{-x_n}}, \quad (2.51)$$

with  $\int_0^\infty d\{x_n\} = \int_0^\infty dx_1 \cdots \int_0^\infty dx_N$ . This is the ratio of normalisation constants of Laguerre distributions, which is known [119]. We thus obtain

$$\mu_q = (-2)^{Nq} \prod_{j=0}^{N-1} \frac{\Gamma\left(q + N - j - \frac{1}{2}\right)}{\Gamma\left(N - j - \frac{1}{2}\right)}. \quad (2.52)$$

For  $q = 1, 2$  this reduces to

$$\begin{aligned} \mu_1 &= (-1)^N \frac{(2N)!}{2^N N!}, \quad \mu_2 = \frac{(2N+1)!(2N)!}{2^{2N} (N!)^2}, \\ \Rightarrow \text{Var}(\text{Det } \mathcal{A}) &= 2N [\mathbb{E}(\text{Det } \mathcal{A})]^2. \end{aligned} \quad (2.53)$$

The average determinant of antisymmetric Hermitian matrices increases exponentially with  $N$ ,

$$\mu_1 = \sqrt{2}(-2/e)^N N^N [1 + \mathcal{O}(1/N)], \quad (2.54)$$

in contrast to the exponential decay for antisymmetric orthogonal matrices, cf. Eq. (2.25).

## Chapter 3

# Dynamical signatures of ground-state degeneracy to discriminate against Andreev Levels in a Majorana fusion experiment

### 3.1 Introduction

Non-Abelian anyons hold much potential for a quantum information processing that is robust to decoherence [52, 53]. The qubit degree of freedom is protected from local sources of decoherence since it is encoded nonlocally in a ground-state manifold of exponentially large degeneracy (of order  $d^M$  for  $M$  anyons with quantum dimension  $d > 1$ ). The degeneracy is called topological to distinguish it from accidental degeneracies that require fine tuning of parameters. The non-Abelian statistics follows from the ground-state degeneracy because exchange operations (braiding) correspond to non-commuting unitary operations in the ground-state manifold [120].

Majorana zero-modes, midgap states in a superconductor, are non-Abelian anyons with quantum dimension  $d = \sqrt{2}$  [21, 121]: Two zero-modes may or may not share an unpaired fermion, so that the ground state of  $M$  zero-modes has degeneracy  $2^{M/2}$ . To demonstrate the topological degeneracy of Majorana zero-modes is a near-term milestone on the road towards a quantum computer

based on Majorana qubits [60].

The general strategy for such a demonstration has been put forward by Aasen *et al.* [60]. A set of four Majorana zero-modes  $\gamma_1, \gamma_2, \gamma_3, \gamma_4$  is pairwise coupled (fused) in two different ways: Either  $\gamma_2$  with  $\gamma_3$  or  $\gamma_1$  with  $\gamma_2$ . The zero-modes are then decoupled and the fermion parity  $P_{12}$  of  $\gamma_1$  and  $\gamma_2$  is measured ( $P_{12} = +1$  for even fermion number and  $P_{12} = -1$  for odd fermion number). The  $E = 0$  ground-state degeneracy manifests itself in a nondeterministic outcome in the first case, with expectation value  $\bar{P}_{12} = 0$ . The second case serves as a control experiment with a deterministic outcome of  $+1$  or  $-1$  depending on the sign of the coupling.

A challenge for the approach is formed by the tendency for non-topological Andreev levels to accumulate at  $E = 0$ , resulting in a mid-gap peak in the density of states and a proliferation of accidental ground-state degeneracies [49]. The ground-state wave function of a few Andreev levels has local fermion-parity fluctuations that may mimic the non-deterministic fusion of Majorana zero-modes [99, 122].

Here we present a dynamical description of the fusion strategy of Aasen *et al.*, to search for signatures that make it possible to exclude spurious effects from Andreev levels. We traverse the parameter space of coupling constants along two pathways A and B such that the fermion parity measurement is non-deterministic along both pathways, but with identical expectation value  $\bar{P}_{12}(A) = \bar{P}_{12}(B)$  when the evolution is adiabatic. Ground-state degeneracies are identified from the breakdown of adiabaticity, which causes  $\bar{P}_{12}(A) \neq \bar{P}_{12}(B)$  in a way that is statistically distinct for Andreev levels and Majorana zero-modes.

## 3.2 Adiabatic evolution to test for ground-state degeneracy

We consider a Majorana qubit consisting of 4 Majorana zero-modes with 3 adjustable couplings, in either a linear geometry or a tri-junction geometry, see Fig. 3.1. The linear circuit contains two superconducting islands with adjustable Coulomb couplings in each island and a tunnel coupling between the islands. In the tri-junction there are three strongly coupled islands and only the Coulomb coupling within each island is adjustable.

The state  $|\pm\rangle$  of the Majorana qubit is encoded in the fermion parity of one of the islands, say the island containing Majorana zero-modes 1 and 2. The fermion parity operator  $P_{12} = -2i\gamma_1\gamma_2$  is the product of the two Majorana

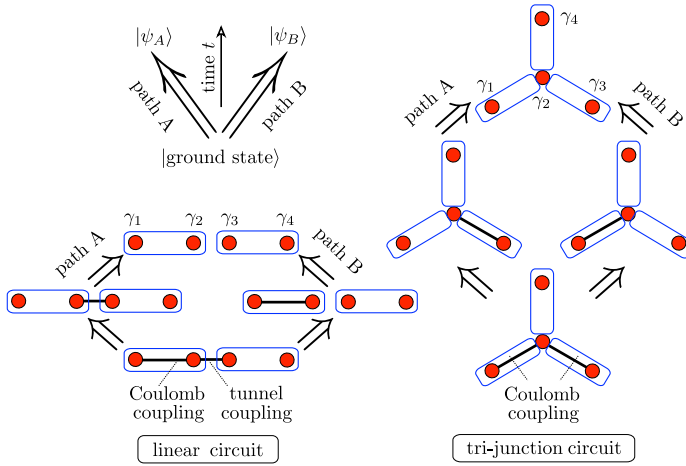


**Figure 3.1.** Two pathways A and B for the evolution of a Majorana qubit, encoded in four Majorana zero-modes (red dots) in a linear or tri-junction geometry. The blue contours represent superconducting islands and the black solid lines indicate which zero-modes are coupled. At the end of the evolution the Hamiltonian is the same for both pathways, but the final states  $|\psi_A\rangle$  or  $|\psi_B\rangle$  may depend on the pathway if adiabaticity breaks down because of a degenerate ground state.

operators. Its eigenvalues are  $+1$  or  $-1$  depending on whether the fermion parity in that island is even or odd. For definiteness we will assume that the fermion parity of the entire system is even, and then  $P_{34} = P_{12}$ .

As illustrated in Fig. 3.1, in each geometry the system is initialized in the ground state with two of the three couplings on and the third coupling off. The final state with all couplings off is reached via one of two pathways, A or B, depending on which coupling is turned off first.

Notice that at each instant in time the system contains at least two uncoupled zero-modes:  $\gamma_4$  and an  $E = 0$  superposition  $\gamma_0$  of  $\gamma_1, \gamma_2, \gamma_3$  (which must exist because of the  $\pm E$  symmetry of the spectrum [20]). Pathway A is the fusion process discussed by Aasen *et al.* [60], while pathway B is an element in the braiding process of Ref.[57].

If the ground state remains nondegenerate during this dynamical process, separated from excited states by a gap  $E_{\text{gap}}$  larger than the decoupling rate, then the adiabatic theorem ensures that the final state  $|\psi\rangle_A = |\psi\rangle_B$  does not depend on the pathway. By measuring the expectation values

$$\bar{P}_A = \langle \psi_A | P_{12} | \psi_A \rangle, \quad \bar{P}_B = \langle \psi_B | P_{12} | \psi_B \rangle, \quad (3.1)$$

one can detect a breakdown from adiabaticity. This might be due to an accidental gap closing during the evolution, or due to the topological ground-state degeneracy of Majorana zero-modes.

We will consider the effect of an accidental degeneracy in Sec. 3.4, in the next section we first address the topological degeneracy.

### 3.3 Topologically degenerate ground state

We summarize some basic facts about Majorana zero-modes (see reviews [14, 53] for more extensive discussions).

An even number  $M = 2N$  of uncoupled Majorana zero-modes has a  $2^{N-1}$ -fold degenerate ground-state manifold for a given global fermion parity. The degeneracy is removed by coupling, as described by the Hamiltonian

$$H = \frac{1}{2} \sum_{n,m=1}^{2N} A_{nm} i \gamma_n \gamma_m. \quad (3.2)$$

The  $2N \times 2N$  matrix  $A$  is real antisymmetric,  $A_{nm} = -A_{mn} = A_{nm}^*$  and the Majorana operators  $\gamma_n = \gamma_n^\dagger$  are Hermitian operators with anticommutator

$$\gamma_n \gamma_m + \gamma_m \gamma_n = \delta_{nm}, \quad \gamma_n^2 = 1/2. \quad (3.3)$$

The fermion creation and annihilation operators  $a^\dagger$ ,  $a$  are related to the  $\gamma$ 's by

$$\begin{pmatrix} \gamma_{2n-1} \\ \gamma_{2n} \end{pmatrix} = U \begin{pmatrix} a_n \\ a_n^\dagger \end{pmatrix}, \quad U = \frac{1}{\sqrt{2}} \begin{pmatrix} 1 & 1 \\ -i & i \end{pmatrix}. \quad (3.4)$$

The fermion operators define a basis of occupation numbers,  $|s_1, s_2, \dots, s_N\rangle$ , such that  $a_n^\dagger a_n |s_1, s_2, \dots, s_N\rangle = s_n |s_1, s_2, \dots, s_N\rangle$ ,  $s_n \in \{0, 1\}$ .

For  $N = 2$  and assuming even global fermion parity the Hamiltonian (3.2) in the basis of occupation numbers  $|00\rangle \equiv |+\rangle$  and  $|11\rangle \equiv |-\rangle$  reads

$$H = \frac{1}{2} \begin{pmatrix} -\Gamma & \Gamma'^* \\ \Gamma' & \Gamma \end{pmatrix}, \quad \Gamma = A_{12} + A_{34}, \quad (3.5)$$

$$\Gamma' = -A_{14} - A_{23} - iA_{24} + iA_{13}.$$

The fermion parity operator  $P_{12} = \sigma_z$  in this basis. Its expectation value in the ground state  $|\text{GS}\rangle$  follows from

$$|\text{GS}\rangle \propto (\Gamma + \sqrt{\Gamma^2 + |\Gamma'|^2})|+\rangle + \Gamma'|-\rangle$$

$$\Rightarrow \langle \text{GS} | P_{12} | \text{GS} \rangle = \frac{\Gamma}{\sqrt{\Gamma^2 + |\Gamma'|^2}}. \quad (3.6)$$

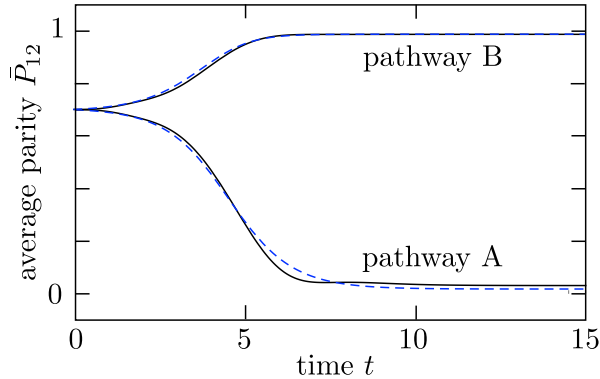


**Figure 3.2.** Solid curves: Expectation value  $\bar{P}_{12}(t) = \langle \psi(t) | P_{12} | \psi(t) \rangle$  calculated numerically from the solution of the differential equation (3.7), for the Hamiltonian (3.5) with time dependent coupling constants  $\Gamma(t) = 1 - \tanh[(t - t_0)/\delta t]$  and  $\Gamma'(t) = 1 - \tanh[(t - t'_0)/\delta t]$  for  $\delta t = 2$ . The decoupling times are chosen at  $t_0 = 4, t'_0 = 8$  for pathway A and  $t_0 = 8, t'_0 = 4$  for pathway B. The dashed curves show the corresponding evolution of the expectation value in the ground state of  $H(t)$ , calculated from Eq. (3.6). The close agreement of solid and dashed curves indicates that the dynamics is nearly adiabatic.

Eq. (3.6) is a known result [99], which shows that for  $|\Gamma| \ll |\Gamma'|$  the ground state of the Majorana qubit is in an even-odd superposition of nearly equal weight. Applied to Fig. 3.1 the same Eq. (3.6) shows that the two pathways A and B correspond to an exchange of limits:  $\Gamma \rightarrow 0$  before  $\Gamma' \rightarrow 0$  for pathway A, resulting in  $\bar{P}_{12} \rightarrow 0$ , or the other way around for pathway B with  $|\bar{P}_{12}| \rightarrow 1$ .

In Fig. 3.2 we show how this works out dynamically, by integrating the evolution equation

$$i\hbar \frac{\partial}{\partial t} |\psi(t)\rangle = H(\Gamma(t), \Gamma'(t)) |\psi(t)\rangle, \quad (3.7)$$

with initial condition that  $|\psi(0)\rangle$  is the ground state of  $H$  at  $t = 0$ .

### 3.4 Accidentally degenerate Andreev levels

To assess the breakdown of the adiabatic evolution as a result of (nearly) degenerate Andreev levels we consider the double quantum dot geometry of Fig. 3.3. There are  $N_L$  Andreev levels in the left dot and  $N_R$  Andreev levels in the right dot. The quantum dots are coupled to each other by an adjustable

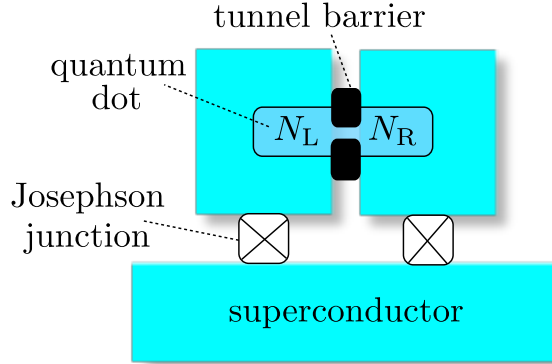


**Figure 3.3.** Two quantum dots on a superconducting substrate (blue), containing  $N_L$  and  $N_R$  Andreev levels coupled via a tunnel barrier. The coupling strength is adjustable via a pair of gate electrodes (black). The fermion parity  $P_L$ ,  $P_R$  in each quantum dot is regulated by the ratio  $E_J/E_C$  of Josephson and charging energies, which is adjustable via the magnetic flux through a Josephson junction. In this way we can drive the system away from the ground state via the two pathways of Fig. 3.1, either by switching off first the fermion-parity coupling and then the tunnel coupling (pathway A) or the other way around (pathway B). At the end of each process the fermion parity  $P_L$  is measured.

tunnel barrier and each has an adjustable coupling to a bulk superconductor by a Josephson junction.

For strong Josephson coupling the Coulomb charging energy may be neglected and the Hamiltonian of the double-quantum dot is bilinear in the creation and annihilation operators,

$$\mathcal{H}_0 = \frac{1}{2} \sum_{n,m=1}^N \Psi_n^\dagger \cdot \mathcal{B}_{nm} \cdot \Psi_m, \quad (3.8a)$$

$$\Psi_n = \begin{pmatrix} a_n \\ a_n^\dagger \end{pmatrix}, \quad \mathcal{B}_{nm} = \begin{pmatrix} V_{nm} & -\Delta_{nm}^* \\ \Delta_{nm} & -V_{nm}^* \end{pmatrix}. \quad (3.8b)$$

The indices  $n, m$  label spin and orbital degrees of freedom of the  $N = N_L + N_R$  Andreev levels. The  $N \times N$  Hermitian matrix  $V$  represents the kinetic and potential energy. The  $N \times N$  antisymmetric matrix  $\Delta$  is the pair potential.

As the ratio  $E_J/E_C$  of Josephson and charging energy is reduced, the Coulomb interaction in a quantum dot becomes effective. In the regime

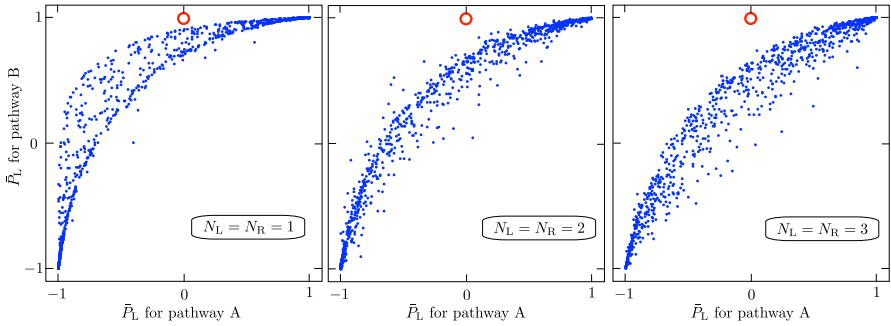


**Figure 3.4.** Scatter plot that illustrates how the expectation value  $\bar{P}_L$  of the fermion parity in the left quantum dot depends on the pathway A or B that is followed in parameter space. Each blue dot results from one realization of the class-D ensemble of random Hamiltonians  $\mathcal{H}_0$ . In units such that the mean Andreev level spacing  $\delta_0 \equiv 1$ , the parameters in Eqs. (3.10) and (3.12) are  $\delta t = \delta t' = 2$ ,  $\kappa_0 = 1/4$  for both pathways, and  $t_0 = 4, t'_0 = 8$  for pathway A,  $t_0 = 8, t'_0 = 4$  for pathway B. The fermion parity is evaluated at time  $t = 15$ . The red circle indicates the expected outcome for a Majorana qubit, which is well separated from the scatter plot of Andreev levels.

$E_J/E_C \gtrsim 1$  the interaction term only depends on the fermion parity [57],

$$\begin{aligned} \mathcal{H}_C &= -\kappa_L P_L - \kappa_R P_R, \\ P_L &= (-1)^{\sum_{n \in L} a_n^\dagger a_n}, \quad P_R = (-1)^{\sum_{n \in R} a_n^\dagger a_n}. \end{aligned} \quad (3.9)$$

The two coupling constants  $\kappa_L$  and  $\kappa_R$  depend exponentially  $\propto e^{-\sqrt{8E_J/E_C}}$  on the Josephson energy [123], which can be varied by adjusting the magnetic flux through the Josephson junction connected to the left or right quantum dot. We set  $\kappa_R \equiv 0$  for all times while  $\kappa_L(t)$  drops from  $\kappa_0$  to 0 in an interval  $\delta t$  around  $t = t_0$ . We choose a tanh profile,

$$\kappa_L(t) = \frac{1}{2}\kappa_0 - \frac{1}{2}\kappa_0 \tanh[(t - t_0)/\delta t]. \quad (3.10)$$

For each of the two dynamical pathways A and B we start at  $t = 0$  with a strong tunnel coupling between the quantum dots. We model this statistically by means of the Gaussian ensemble of random-matrix theory in symmetry class D (broken time-reversal and broken spin-rotation symmetry) [48, 49].

The ensemble is constructed as follows. A unitary transformation to the Majorana basis,

$$UB_{nm}U^\dagger = i\mathcal{A}_{nm}, \quad U = \frac{1}{\sqrt{2}} \begin{pmatrix} 1 & 1 \\ -i & i \end{pmatrix}, \quad (3.11)$$

see Eq. (3.4), expresses the Hamiltonian (3.8) in terms of a real antisymmetric  $2N \times 2N$  matrix  $\mathcal{A}$ . We take independent Gaussian distributions for each upper-diagonal matrix element of  $\mathcal{A}$ , with zero mean and variance  $2N\delta_0^2/\pi^2$ , where  $\delta_0$  is the mean spacing of the Andreev levels.

For strongly coupled quantum dots we do not distinguish statistically between matrix elements  $\mathcal{A}_{nm}$  that refer to levels  $n$  and  $m$  in the same dot or in different dots. To decouple the quantum dots by the tunnel barrier we suppress the inter-dot matrix elements,

$$\mathcal{A}_{nm}(t) = \mathcal{A}_{nm}(0) \times \begin{cases} 1 & \text{if } n, m \text{ in the same dot,} \\ \kappa_{\text{LR}}(t) & \text{if } n, m \text{ in different dots,} \end{cases} \quad (3.12a)$$

$$\kappa_{\text{LR}}(t) = \frac{1}{2} - \frac{1}{2} \tanh[(t - t'_0)/\delta t']. \quad (3.12b)$$

We solve the Schrödinger equation

$$i\hbar \frac{\partial}{\partial t} |\psi\rangle = (\mathcal{H}_0 + \mathcal{H}_C) |\psi\rangle, \quad (3.13)$$

by first calculating the Hamiltonian in the  $2^{N_L+N_R-1}$  dimensional basis of occupation numbers in the left and right dot, for even global fermion parity  $P_L P_R = +1$ . (We used the ZITKO2011SNEG package to take over this tedious calculation [124].) Starting from the ground state at  $t = 0$  we switch off  $\kappa_L$  and  $\kappa_{\text{LR}}$  along pathways A or B (first switching off  $\kappa_L$  or first switching off  $\kappa_{\text{LR}}$ , respectively). At the end of the process we calculate the expectation value of the fermion parity  $\bar{P}_L$  in the left dot.

The calculation is repeated for a large number of realizations of the Hamiltonian  $\mathcal{H}_0$  in the class-D ensemble. A scatter plot of  $\bar{P}_L(\text{A})$  versus  $\bar{P}_L(\text{B})$  is shown in Fig. 3.4 for a few values of  $N_L, N_R$ . Significant deviations are observed from the line  $\bar{P}_L(\text{A}) = \bar{P}_L(\text{B})$  of adiabatic evolution, but the scatter plot stays clear of the point  $\bar{P}_L(\text{A}) = 0, \bar{P}_L(\text{B}) = 1$  that characterizes a Majorana qubit.

Two ingredients in the fusion protocol are essential for this to work: Firstly, the fermion-parity coupling should be smaller than or comparable to the tunnel coupling, in order for pathway B to have a nondeterministic fusion outcome. Secondly, the tunnel coupling should be cut slowly on the scale of the inverse mean level spacing, to promote adiabatic evolution in pathway A. In Fig. 3.5 we show the scatter plot when both these conditions are violated: There is now no clear separation from the Majorana qubit.

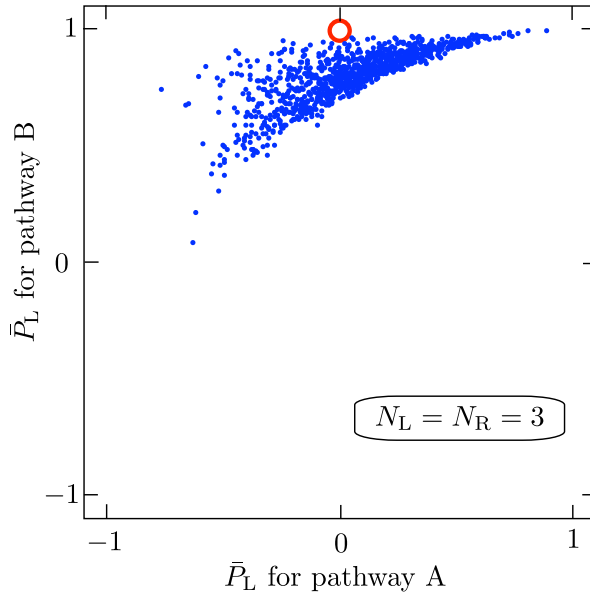


**Figure 3.5.** Same as Fig. 3.4, but now for a stronger fermion-parity coupling ( $\kappa_0 = 2$ ) and abrupt removal of the tunnel coupling ( $\delta t' = 1/4$ , all other parameters unchanged). The outcome for a Majorana qubit is now no longer well separated from the scatter plot of the outcome from Andreev levels.

### 3.5 Conclusion

A successful demonstration of the non-deterministic fusion of two Majorana zero-modes would be a milestone in the development of a topological quantum computer [60]. Its significance would be both conceptual (because it implies non-Abelian braiding statistics [120]) and practical (because fusion can substitute for braiding in a quantum computation [14, 125]).

In this work we have investigated the dynamics of the fusion process, to see how spurious effects from the merging of Andreev levels can be eliminated. We compare the time-dependent evolution in the parameter space of coupling constants (tunnel coupling and Coulomb coupling) via two alternative pathways. The topological ground-state degeneracy of Majorana zero-modes causes a breakdown of adiabaticity that can be measured as a pathway-dependent fermion parity. Andreev levels can produce accidental degeneracies, and a non-deterministic fermion parity outcome, but the correlation between the two pathways is distinct from what would follow from the Majorana fusion rule (see Fig. 3.4).

Initial experimental steps towards the detection of the Majorana fusion rule have been reported [126]. Typical spacings  $\delta_0$  of sub-gap Andreev levels in these nanowire geometries are  $10 \mu\text{eV}$ , so the adiabatic decoupling time scale  $\delta t = 2\hbar/\delta_0$  in Fig. 3.4 would be on the order of 0.1 ns, well below expected quasiparticle poisoning times of  $1 \mu\text{s}$  [127].

## Chapter 4

# Reentrant superconductivity in a quantum dot coupled to a Sachdev-Ye-Kitaev metal

### 4.1 Introduction

The Bardeen-Cooper-Schrieffer mechanism of conventional superconductivity [38] requires two species of fermions coupled by an attractive two-body interaction. [128] The mean-field analysis of such a model results in the gapped quasiparticle excitation spectrum below the critical temperature. Meanwhile, the absence of long-living quasiparticles in high-temperature superconducting materials *above* the critical temperature is an immutable characteristic of the so-called strange metal state. [129, 130] In contrast to the quasiparticle nature of superconductors, strange metals exhibit a power-law behavior in the spectral function, [131] similarly to quantum critical systems. [132] A lack of quasiparticles manifests itself in fast equilibration at low temperature on a timescale set by the Planckian relaxation time  $t_P = \hbar / (2\pi k_B T)$ . [132, 133] The same timescale appears as an upper bound on quantum chaos setting the maximal rate of information scrambling. [31] It is usually formulated [31, 134, 135] in terms of the out-of-time ordered correlator [67] (OTOC): In quantum many-body systems the OTOC grows no faster than exponentially  $e^{t/t_L}$  with the Lyapunov time  $t_L$  bounded from below as  $t_L \geq t_P$ . [31]

The widely known Sachdev-Ye-Kitaev (SYK) model, [136] describing strongly interacting Majorana zero modes in  $0 + 1$  dimensions, saturates the chaos bound  $t_L = t_P$ . [28, 136] It does not possess an underlying quasiparticle de-

scription while being solvable in the infrared, with a spectral function that scales as a power law of frequency. These properties do not change upon replacing Majoranas with conventional fermions (complex SYK model). [137, 138] The extensions of this model to the cSYK coupled clusters predict thermal diffusivity [68]  $\propto t_P$  and reproduce the linear in temperature resistivity, [69] observed in strange metals. [70, 71] Recently, a proposed theory of a Planckian metal, [27] based on the destruction of a Fermi surface by the cSYK-like interactions, shows that the universal scattering time equals the Planckian time  $t_P$ . The latter one characterizes the linear in temperature resistivity property [72] and was detected in cuprates, [73] pnictides, [74] and twisted bilayer graphene, [75] regardless of their different microscopic nature.

The success in applying the SYK model to qualitative studies of strange metals and the minimalistic structure of the model itself fostered the effort to find a mechanism by which the superconducting state is formed out of an incoherent SYK metal. [139–142] Driven by the same curiosity, we consider a (0+1)-dimensional toy model which consists of a superconducting quantum dot [143] coupled to the complex-valued SYK model. [137] At the critical coupling the pairing gap turns out to be proportional to the Planckian relaxation rate at low temperatures,

$$\Delta \approx \eta \frac{\hbar}{t_P}, \quad (4.1)$$

where  $\eta$  is a number close to one. This theoretical finding that we refer to as a Planckian superconductor draws parallels to the phenomenon of reentrant superconductivity [144, 145] in Kondo superconductors [146–148] and the physics of Andreev billiards. [149–153]

## 4.2 Main part

We start with a superconducting Hamiltonian  $H_{SC}$  that contains  $2M$  modes described by the Richardson Hamiltonian [154–156] without single-particle energies coupled to the SYK model  $H_{SYK}$  with  $N$  fermions through a random

tunneling term  $H_{\text{tun}}$ ,

$$H = H_{\text{SC}} + H_{\text{SYK}} + H_{\text{tun}}, \quad (4.2)$$

$$H_{\text{SC}} = -\frac{U}{M} \sum_{i,j=1}^M \psi_{\uparrow i}^\dagger \psi_{\downarrow i}^\dagger \psi_{\downarrow j} \psi_{\uparrow j} - \mu \sum_{i=1}^M \sum_{\sigma=\uparrow,\downarrow} \psi_{\sigma i}^\dagger \psi_{\sigma i}, \quad (4.3)$$

$$H_{\text{SYK}} = \frac{1}{(2N)^{3/2}} \sum_{i,j,k,l=1}^N J_{ij;kl} c_i^\dagger c_j^\dagger c_k c_l, \quad (4.4)$$

$$H_{\text{tun}} = \frac{1}{(MN)^{1/4}} \sum_{i=1}^N \sum_{j=1}^M \sum_{\sigma=\uparrow,\downarrow} \left( t_{ij}^\sigma c_i^\dagger \psi_{\sigma j} + \text{h.c.} \right). \quad (4.5)$$

The couplings  $t_{ij}^\sigma$  and  $J_{ij;kl}$  are assumed to be independent Gaussian random variables with finite variances  $\overline{t_{ij}^{\sigma*} t_{ij}^{\sigma'}} = t^2 \delta_{\sigma\sigma'}$ ,  $\overline{|J_{ij;kl}|^2} = J^2$  ( $J_{ij;kl} = -J_{ji;kl} = -J_{ij;lk} = J_{kl;ij}^*$ ), and zero means.

The interaction terms in the Hamiltonian (4.2) are decoupled within the Hubbard-Stratonovich transformations, [128, 137] so that in the large  $M, N$  limit the self-consistent saddle-point equations are (see Appendix 4.4)

$$\Sigma_c(\tau) = J^2 G_c(\tau)^3 + 2\sqrt{p} t^2 G_+(\tau), \quad (4.6)$$

$$G_c(i\omega_n)^{-1} = i\omega_n - \Sigma_c(i\omega_n), \quad (4.7)$$

$$G_+(i\omega_n) = \frac{i\omega_n - \frac{t^2}{\sqrt{p}} G_c(i\omega_n)}{\left( i\omega_n - \frac{t^2}{\sqrt{p}} G_c(i\omega_n) \right)^2 - |\Delta|^2}, \quad (4.8)$$

$$\frac{1}{U} = T \sum_{n=-\infty}^{+\infty} \frac{1}{\left( \omega_n + \frac{it^2}{\sqrt{p}} G_c(i\omega_n) \right)^2 + |\Delta|^2}, \quad (4.9)$$

where  $\omega_n = \pi T(2n+1)$  are Matsubara frequencies and  $p = M/N$  controls the ratio between the “sites” [157–159] in the superconductor/SYK sector. The self-energy of the SYK fermions appears in the equations 4.6, 4.7 as  $\Sigma_c(\tau)$ , while  $G_c(\tau)$  denotes the corresponding Green’s function  $-N^{-1} \sum_{i=1}^N \langle T_\tau c_i(\tau) \bar{c}_i(0) \rangle$ . The Green’s functions of the  $\uparrow, \downarrow$  fermions in the superconductor  $G_\sigma(\tau) = -M^{-1} \sum_{i=1}^M \langle T_\tau \psi_{i\sigma}(\tau) \bar{\psi}_{i\sigma}(0) \rangle$  enter the equation 4.8 as a half trace of the Gor’kov’s function [160]  $G_+(\tau) = \frac{1}{2}(G_\uparrow + G_\downarrow)(\tau)$ . Finally, relation 4.9 is a modified gap equation, [128] which accounts for the amount of the SYK impurity in the superconductor through  $G_c(\tau)$  under the assumption of frequency independent pairing  $\Delta$ . The chemical potential  $\mu$  can be accounted in the

equations 4.6-4.9 by the shift  $|\Delta|^2 \rightarrow |\Delta|^2 + \mu^2$ . Below, we set  $\mu = 0$ . In the normal phase ( $\Delta = 0$ ) the equations 4.6-4.8 can be written as

$$\Sigma(\tau) = J^2 G_c(\tau)^3, \quad (4.10)$$

$$(i\omega_n - \Sigma(i\omega_n)) G_c(i\omega_n) = \frac{i\omega_n - \frac{t^2(1-2p)}{\sqrt{p}} G_c(i\omega_n)}{i\omega_n - \frac{t^2}{\sqrt{p}} G_c(i\omega_n)}, \quad (4.11)$$

ensuring a convenient self-energy translation  $\Sigma \equiv \Sigma_c - 2\sqrt{p}t^2G_+$ . If  $p \ll 1/2$  ( $2M \ll N$ ), the bare SYK Green's function  $G_{\text{SYK}}(i\omega_n) = -i\pi^{1/4}\text{sgn}(\omega_n)/\sqrt{|J\omega_n|}$  solves the equations 4.10,4.11 in the infrared  $\omega_n \ll J$ . In this regime, the Green's function of the  $\psi$  fermions  $G_+(i\omega_n)$  scales as  $\sqrt{\omega_n}$  for  $\omega_n/J \ll p^{-1/3}(t/J)^{4/3}$ . In the equal sites case  $2M = N$ , which corresponds to  $p = 1/2$ , the bare SYK Green's function survives for  $(t/J)^{4/3} \ll \omega_n/J \ll 1$ . Another solution appears at  $p = 1/2$  if one supposes  $\omega_n \ll \{t^2|G_c|, |\Sigma|\}$ . Then the equation 4.11 shortens to

$$\Sigma(i\omega_n) = \frac{i\omega_n}{\sqrt{2}t^2} G_c(i\omega_n)^{-2}. \quad (4.12)$$

The Green's function that satisfies the equations 4.10,4.12 is  $G_c(i\omega) \propto -i\text{sgn}(\omega)/(J^2t^2|\omega_n|)^{-1/5}$  for the frequencies  $(t/J)^3 \ll \omega_n/J \ll (t/J)^{4/3}$ , that are achievable in the weak tunneling limit  $t \ll J$ . Note that the frequency window strictly depends on the coupling  $t$ . For  $p \gg 1/2$ , the Green's function of the  $c$  fermions in the low-frequency limit is  $G_c(i\omega_n) \propto -i\omega_n$ , [159] which leads to the density of states  $-\pi^{-1}\text{Im}G_c(i\omega_n \rightarrow \omega + i0^+) \simeq 0$  vanishing in the SYK sector. Therefore, at large  $p$ , the normal phase is given by the free fermions in the  $\psi$ -dot, whose Green's function is  $G_+(i\omega_n) = -i/\omega_n$ . To follow the frequency scaling of the Green's function  $G_c(i\omega_n)$  while changing  $p$ , we introduce the logarithmic derivative  $\nu = \partial \ln G_c / \partial \ln \omega_n$  plotted in Figure ?? at low temperatures. Summarizing, the normal phase in the infrared limit is described by the inverse Green's function of the SYK model at small  $p$ , whereas it crosses over to free fermions for large  $p$  values.

The gap equation 4.9 at  $\Delta = 0$  makes a boundary in between the normal phase and the superconducting one by setting the critical temperature  $T_c$  as a function of the coupling rate  $t$ . Let us notice that the SYK model 4.4 does not have a spin degree of freedom after disorder averaging (see Appendix 4.4). Thus, it may be thought of as spin polarized. It suppresses superconductivity similar to magnetic impurities: Increase of the coupling to the SYK subsystem

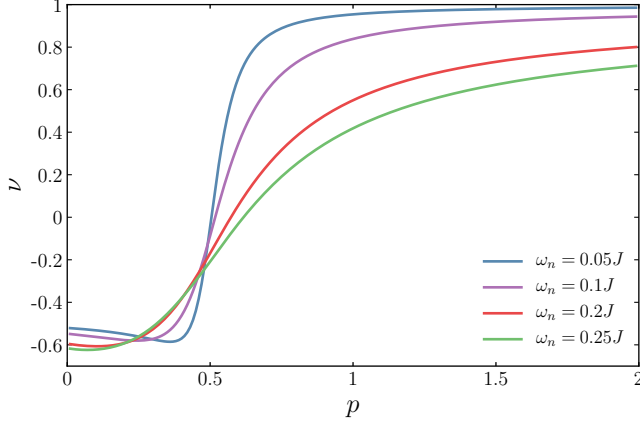


**Figure 4.1.** Scaling of the Green's function  $G_c$  in the normal phase. We plot  $\nu = \partial \ln G_c / \partial \ln \omega_n$  as a function of  $p$  at given frequencies and finite coupling  $t = 0.475J$ . At low frequencies,  $\nu$  close to  $-1/2$  is robust against  $p$  increase for  $p < 1/2$ . The frequency rise moves  $\nu$  towards  $-1$  (free fermion limit), while  $\nu$  crosses over to 1 for large  $p$ . The temperature is  $T = 10^{-4}J$ .

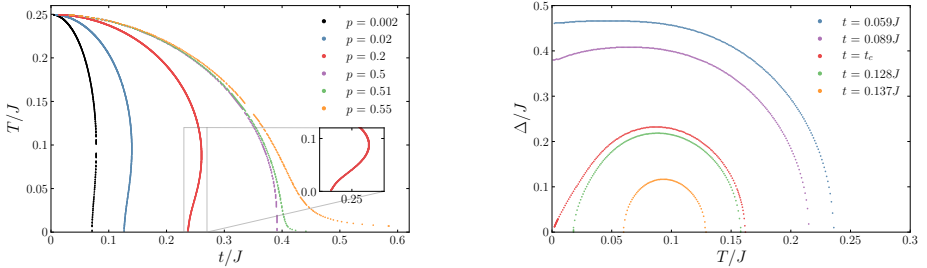


**Figure 4.2.** Left panel: **Critical temperature** as a function of the coupling strength to the SYK dot. The curves for  $p < 0.5$  are bent at low temperatures. This illustrates the presence of **two critical temperatures**. At  $p = 0.5$  the bend disappears, whereas for the values of  $p > 0.5$  a single critical temperature decays to zero asymptotically. Right panel: **The pairing gap** as a function of temperature at  $p = 0.02$ . The critical coupling value is  $t_c \approx 0.127J$ .  $U$  is set equal to  $J$  in both panels.

decreases the critical temperature. [106] There exists a critical coupling  $t_c$ ,

$$\frac{1}{U} = \int_{-\infty}^{+\infty} \frac{d\omega}{2\pi} \left( \omega + \frac{it_c^2}{\sqrt{p}} G_c(\omega) \right)^{-2}, \quad (4.13)$$

such as to abolish superconductivity at zero temperature. The constraint 4.13 follows from the gap equation 4.9 when  $\Delta, T = 0$ .

There are three competing phases contributing to the denominator of the self-consistency relation 4.9: SYK non-Fermi liquid, free fermions, and superconducting condensate  $\Delta$ . If there are enough of the SYK fermions ( $N > 2M$ ),  $\Delta$  interplays with the non-Fermi liquid at zero temperature. The latter one falls off with an increase in temperature, making room for the superconducting phase beyond the critical coupling, which results in the growth of the critical temperature. Indeed, Figure 4.2 (left) shows the bend of the critical temperature in the vicinity of the critical coupling <sup>1</sup>. This phenomenon resembles the reentrant superconductivity [144, 145] in superconductors with Kondo impurities. [146–148] The pairing gap goes down at low temperatures with an increase in coupling as in Figure 4.2 (right). Achieving the critical coupling when  $\Delta$  vanishes at zero temperature leads to the appearance of the lower critical temperature. In contrast, the reentrant superconducting regime is absent for  $N < 2M$ , since the normal phase behaves as the conventional Fermi liquid at low temperatures and large  $p$ , as was noticed earlier. In Figure 4.2 (left), we show <sup>1</sup> that  $p = 1/2$  ( $N = 2M$ ) separates the regions with one or two critical temperatures. Similarly, consideration of the random free fermion model  $\sum_{ij} J_{ij} c_i^\dagger c_j$  instead of the SYK model does not give the reentrance effect. In this case, the self-energy equation 4.6 changes to  $\Sigma_c(i\omega_n) = J^2 G_c(i\omega_n) + 2\sqrt{p} t^2 G_+(i\omega_n)$ . The results for the critical temperature are presented in Figure 4.3. It is still possible to suppress the superconductivity at zero temperature providing sufficient impurities, but there is only a single critical temperature as the normal phase is always set by the free fermions <sup>2</sup>.

From Figure 4.2 (right), one notices the pairing gap at the critical coupling is  $\propto T$  at low temperatures. We numerically examine <sup>1</sup>  $\Delta$  in the reentrant phase  $p < 1/2$  for several values of  $p$  and  $U$  (see Figure 4.4). The gap saturates  $2\pi T$  almost irrespective of parameters of the problem. Unit recovery brings us to the above-mentioned relation 4.1 so that the gap is set by the inverse Planckian time  $1/t_P$  multiplied by  $\hbar$ .

This observation seems to be reminiscent of quite a peculiar feature of an Andreev billiard: [163] In a clean chaotic cavity proximate to a super-

<sup>1</sup>The full self-consistent scheme 4.6–4.9 is solved numerically with the adaptive golden ratio algorithm [161] (see Appendix 4.5)

<sup>2</sup>Earlier it was shown that the superconducting instability in the unparticle system leads to the reentrance effect as well [162], whereas restoration of the quasiparticles makes the critical temperature a single-valued function of the pairing strength.

conductor, the induced gap equals  $\hbar/t_E = \hbar/(t_L \ln \frac{p_F l}{\hbar})$ , [151–153] where  $t_E$  is the Ehrenfest time (the typical timescale of quantum dynamics),  $t_L$  is the Lyapunov time,  $p_F$  is the Fermi momentum, and  $l$  is the characteristic cavity length. The effect is predicted in the regime of the Ehrenfest time far exceeds  $\tau$  the typical lifetime of an electron/hole excitation in the cavity. Oppositely, if  $t_E \ll \tau$ , the gap behaves as  $\hbar/\tau$ , where  $\tau$  does not depend on the Planck constant. [149, 150] In the SYK model the Lyapunov time coincides with the Planckian relaxation time  $t_L = \hbar/(2\pi k_B T) = t_P$ , [28, 136] although those are different physical quantities<sup>3</sup>. However, the Ehrenfest time is  $t_L \ln N \gg \hbar/(2\pi k_B T)$ , which differs from  $t_P$  predicted in the pairing gap 4.1 by  $\ln N$ .

To estimate the gap behavior at the critical coupling we consider the equa-

<sup>3</sup>The equilibration time and the Lyapunov time are a priori different physical quantities. Nevertheless, the fact that both quantities are subjected to the same bound raises the question of whether those two seemingly independent quantities might be related. This hypothesis has been intensively investigated in the context of the AdS/CFT correspondence, in large- $N$  vector models and spin systems (see [164] and the references therein). In systems with a small parameter (large- $N$  quantum field theories or weakly coupled field theories) where a regime of exponential growth is present in the OTOC, however, they are set by the same physics even though they are quantitatively different [165, 166].

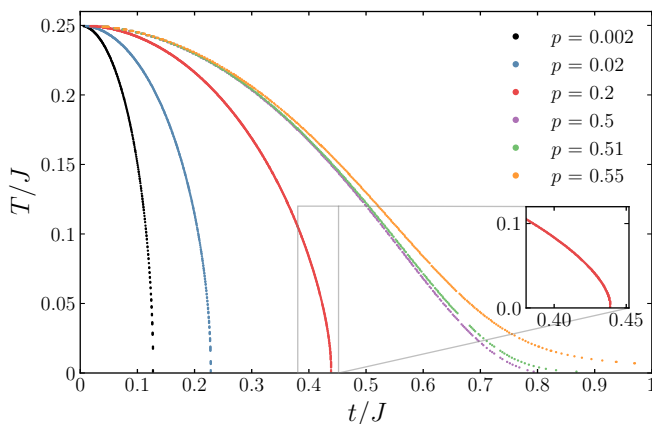


**Figure 4.3.** Critical temperature as a function of the coupling strength to the random free fermions model.

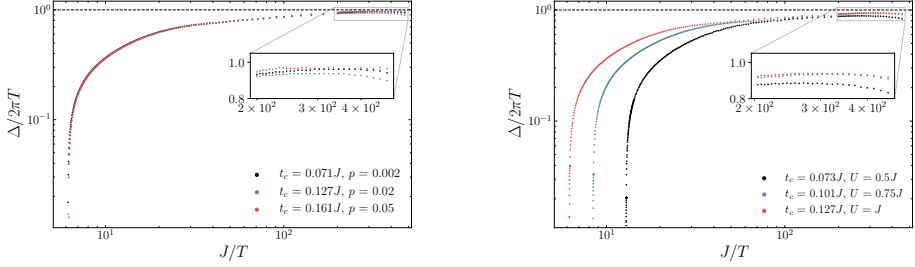


**Figure 4.4.** The gap to temperature ratio as a function of inverse temperature at the critical coupling depends on neither the mode ratio  $p$  (fixed  $U = J$ , **left panel**) nor the Richardson interaction strength  $U$  (fixed  $p = 0.02$ , **right panel**). In both cases,  $\Delta$  saturates  $2\pi T$  at low temperatures. In the right panel, we notice that a decrease of the interaction in the superconducting dot reduces the critical temperature as in the bare Richardson model 4.3.

tions 4.6-4.8 at finite  $\Delta$ ,

$$\left(i\omega_n - \Sigma(i\omega_n)\right)G_c(i\omega_n) = \frac{\left(i\omega_n - \frac{t^2}{\sqrt{p}}G_c(i\omega_n)\right)\left(i\omega_n - \frac{t^2(1-2p)}{\sqrt{p}}G_c(i\omega_n)\right) - |\Delta|^2}{\left(i\omega_n - \frac{t^2}{\sqrt{p}}G_c(i\omega_n)\right)^2 - |\Delta|^2}, \quad (4.14)$$

whereas the self-energy equation 4.10 stays unchanged. The right-hand side of the equation 4.14 tends to unity for  $p \ll 1/2$ . Thus it is sufficient to substitute the SYK Green's function in the gap equation 4.9 in this regime.

As we look for a low-temperature correction to zero  $\Delta$  at the critical coupling, we expand the gap equation 4.9 in powers of  $\Delta$  up to the second order,

$$\frac{1}{U} \simeq 2T \sum_{n=0}^{+\infty} \frac{1}{\left(\omega_n + \frac{it_c^2}{\sqrt{p}}G_c(\omega_n)\right)^2} \left(1 - \frac{|\Delta|^2}{\left(\omega_n + \frac{it_c^2}{\sqrt{p}}G_c(\omega_n)\right)^2}\right). \quad (4.15)$$

The SYK Green's function diverges at low frequencies as  $1/\sqrt{\omega_n}$  and decays as  $1/\omega_n$  in the ultraviolet. Hence the principal contribution to the sum 4.15 from the high frequencies is given by the bare  $\omega_n$  in the denominator. On the other hand, a divergent Green's function is crucial at low frequencies. Assuming  $G_c$  decays fast enough in comparison to  $\omega_n$ , we replace  $G_c$  with the infrared SYK Green's function  $G_{\text{SYK}}(i\omega_n) = -i\pi^{1/4}\text{sgn}(\omega_n)/\sqrt{|J\omega_n|}$  in expression 4.15.

The low-temperature version of relation 4.15 can be written by means of the Euler-Maclaurin formula, [167]

$$\frac{1}{U} \simeq \int_0^{+\infty} d\omega \frac{1}{\pi \left( \omega + \frac{it_c^2}{\sqrt{p}} G_{SYK}(\omega) \right)^2} \left( 1 - \frac{|\Delta|^2}{\left( \omega + \frac{it_c^2}{\sqrt{p}} G_{SYK}(\omega) \right)^2} \right) - \frac{pT}{t_c^4 G_{SYK}(\pi T)^2} \left( 1 + \frac{2\pi T}{3} \frac{\partial G_{SYK}(\pi T)/\partial \omega}{G_{SYK}(\pi T)} \right), \quad (4.16)$$

where we expand up to  $T^2$  keeping in mind that  $\Delta \propto T$  at the critical coupling<sup>4</sup>. Finally, one notices two terms in the top row of the equation 4.16 that match the critical coupling condition 4.13. Therefore, we obtain<sup>5</sup>.

$$\Delta(T) \simeq \sqrt{6}\pi T. \quad (4.17)$$

Although this estimate gives  $\eta \approx 1.22$  that exceeds the found numerical value  $\eta \approx 0.96$  for the pairing gap  $\Delta \approx \eta \hbar/t_P$ , the derived low-temperature gap behavior 4.17 is independent of the problem parameters as in Figure 4.4<sup>6</sup>.

### 4.3 Conclusion

In this manuscript, we considered the superconducting proximity effect for the Sachdev-Ye-Kitaev model. We have shown, that the superconducting dot coupled to the complex SYK model possesses reentrant superconductivity. At the critical coupling, which gives rise to the occurrence of a lower critical temperature, the pairing gap disappears at  $T = 0$  and grows linearly with an increase in temperature. The linear- $T$  growth of the gap is given by  $\hbar/t_P$ , where  $t_P = \hbar/(2\pi k_B T)$  is the Planckian relaxation time. The same timescale serves as an ultimate bound on many-body quantum chaos, [31] saturated in strongly coupled systems without quasiparticle excitations. Thereby a natural question arises whether the pairing gap is an appropriate physical observable for the Lyapunov spectrum [169] of the SYK model. Accurate studies of the

<sup>4</sup>Similarly, in large- $N$  models, the primary contribution of low Matsubara frequencies  $\omega_n = \pm\pi T$  to the gap equation leads to  $\Delta \propto T$  [168].

<sup>5</sup>We use  $\int_0^\infty \frac{d\omega}{\pi} \left( \omega + \frac{it_c^2}{\sqrt{p}} G_{SYK}(\omega) \right)^{-4} = \frac{\pi J}{9\pi^{3/2} t_c^4}$

<sup>6</sup>The gap decrease in Figure 4.4 at very low temperatures (see the enlarged segments) has a numerical origin. As Matsubara frequencies are  $\propto T$ , achieving temperatures close to zero requires a sufficient increase of the numerical grid. This leads to the accuracy reduce due to the computer memory overflow (see Appendix 4.5).

OTOC in the proposed system 4.2 might shed light on that. On its own,  $\Delta \approx \eta \hbar/t_P$  may be used to characterize the cSYK quantum dots. [77, 78] However, this requires consideration of a more realistic setup such as a superconducting lead attached to the particular realization of the complex SYK model.

## 4.4 Appendix: Derivation of the gap equation

The imaginary time action averaged over disorder is

$$\begin{aligned}
S = \int_0^\beta d\tau & \left[ \sum_{i=1}^N \bar{c}_i \partial_\tau c_i + \sum_{i=1}^M \sum_{\sigma=\uparrow,\downarrow} \bar{\psi}_{\sigma i} (\partial_\tau - \mu) \psi_{\sigma i} - \frac{U}{M} \sum_{i,j=1}^M \bar{\psi}_{\uparrow i} \bar{\psi}_{\downarrow i} \psi_{\downarrow j} \psi_{\uparrow j} \right] \\
& - \int_0^\beta d\tau \int_0^\beta d\tau' \left[ \frac{t^2}{\sqrt{NM}} \sum_{i=1}^N \sum_{j=1}^M \sum_{\sigma=\uparrow,\downarrow} \bar{c}_i \psi_{\sigma j}(\tau) \bar{\psi}_{\sigma j} c_i(\tau') - \right. \\
& \quad \left. - \frac{J^2}{4N^3} \sum_{i,j,k,l=1}^N \bar{c}_i \bar{c}_j c_k c_l(\tau) \bar{c}_l \bar{c}_k c_j c_i(\tau') \right], \quad (4.18)
\end{aligned}$$

where  $\beta$  is the inverse temperature. Following Refs. [128, 137], we decouple the interaction term on the top line of the action 4.18 with the Hubbard–Stratonovich transformation and introduce three non-local fields

$$G_\sigma(\tau, \tau') = -M^{-1} \sum_{i=1}^M \psi_{i\sigma}(\tau) \bar{\psi}_{i\sigma}(\tau') \quad (4.19)$$

$$G_c(\tau, \tau') = -N^{-1} \sum_{i=1}^N c_i(\tau) \bar{c}_i(\tau') \quad (4.20)$$

together with  $\Sigma_\sigma(\tau, \tau')$ ,  $\Sigma_c(\tau, \tau')$  as the corresponding Lagrange multipli-

ers:

$$\begin{aligned}
S = & \int_0^\beta d\tau \int_0^\beta d\tau' \left[ \frac{M}{U} \delta(\tau - \tau') |\Delta|^2 - \right. \\
& - \sum_{i=1}^M \bar{\Psi}_i(\tau) \begin{pmatrix} -\delta(\tau - \tau') (\partial_\tau - \mu) - \Sigma_\uparrow(\tau, \tau') & \delta(\tau - \tau') \Delta \\ \delta(\tau - \tau') \bar{\Delta} & -\delta(\tau - \tau') (\partial_\tau + \mu) - \Sigma_\downarrow(\tau, \tau') \end{pmatrix} \Psi_i(\tau') \\
& - \sum_{i=1}^N \bar{c}_i(\tau) (-\delta(\tau - \tau') \partial_\tau - \Sigma_c(\tau, \tau')) c_i(\tau') - \\
& - M \sum_{\sigma=\uparrow, \downarrow} \left( \Sigma_\sigma(\tau, \tau') - \sqrt{\frac{N}{M}} t^2 G_c(\tau, \tau') \right) G_\sigma(\tau', \tau) \\
& \left. - N \left( \Sigma_c(\tau, \tau') G_c(\tau', \tau) + \frac{J^2}{4} G_c(\tau, \tau')^4 \right) \right], \tag{4.21}
\end{aligned}$$

where  $\bar{\Psi}_i = (\bar{\psi}_{\uparrow i} \quad \bar{\psi}_{\downarrow i})$  and  $\Psi_i = (\psi_{\uparrow i} \quad \psi_{\downarrow i})^T$  are Nambu spinors. Integrating out fermions and assuming constant  $\Delta$ , we get:

$$\begin{aligned}
S = & \frac{\beta M}{U} |\Delta|^2 - M \sum_{n=-\infty}^{+\infty} \log \left[ (i\omega_n - \Sigma_\uparrow(i\omega_n) + \mu) (i\omega_n - \Sigma_\downarrow(i\omega_n) - \mu) - |\Delta|^2 \right] - \\
& - N \sum_{n=-\infty}^{+\infty} \log \left[ i\omega_n - \Sigma_c(i\omega_n) \right] - \\
& - \int_0^\beta d\tau \int_0^\beta d\tau' \left[ M \sum_{\sigma=\uparrow, \downarrow} \left( \Sigma_\sigma(\tau, \tau') - \sqrt{\frac{N}{M}} t^2 G_c(\tau, \tau') \right) G_\sigma(\tau', \tau) + \right. \\
& \left. + N \left( \Sigma_c(\tau, \tau') G_c(\tau', \tau) + \frac{J^2}{4} G_c(\tau, \tau')^4 \right) \right], \tag{4.22}
\end{aligned}$$

where  $\omega_n = \pi(2n+1)/\beta$  are Matsubara frequencies. In the limit of  $M, N \gg 1$ ,

the saddle-point equations are:

$$\Sigma_{\uparrow}(\tau) = \frac{t^2}{\sqrt{p}}G_c(\tau), \quad \Sigma_{\downarrow}(\tau) = \frac{t^2}{\sqrt{p}}G_c(\tau), \quad (4.23)$$

$$\Sigma_c(\tau) = J^2G_c(\tau)^3 + \sqrt{p}t^2 \sum_{\sigma=\uparrow,\downarrow} G_{\sigma}(\tau), \quad (4.24)$$

$$G_{\uparrow}(i\omega_n) = \frac{i\omega_n - \mu - \Sigma_{\downarrow}(i\omega_n)}{(i\omega_n - \Sigma_{\uparrow}(i\omega_n) + \mu)(i\omega_n - \Sigma_{\downarrow}(i\omega_n) - \mu) - |\Delta|^2}, \quad (4.25)$$

$$G_{\downarrow}(i\omega_n) = \frac{i\omega_n + \mu - \Sigma_{\uparrow}(i\omega_n)}{(i\omega_n - \Sigma_{\uparrow}(i\omega_n) + \mu)(i\omega_n - \Sigma_{\downarrow}(i\omega_n) - \mu) - |\Delta|^2}, \quad (4.26)$$

$$G_c(i\omega_n)^{-1} = i\omega_n - \Sigma_c(i\omega_n), \quad (4.27)$$

$$\frac{1}{U} = \frac{1}{\beta} \sum_{n=-\infty}^{+\infty} \frac{1}{(\omega_n + i\Sigma_{\uparrow}(i\omega_n) - i\mu)(\omega_n + i\Sigma_{\downarrow}(i\omega_n) + i\mu) + |\Delta|^2}, \quad (4.28)$$

where we introduced the parameter  $p = M/N$  representing the amount of the SYK ‘‘impurities’’ in the superconductor sector.

We exclude the self-energies  $\Sigma_{\sigma}$  4.23, so that one obtains four Schwinger-Dyson equations:

$$\Sigma_c(\tau) = J^2G_c(\tau)^3 + 2\sqrt{p}t^2G_+(\tau), \quad (4.29)$$

$$G_+(i\omega_n) = \frac{i\omega_n - \frac{t^2}{\sqrt{p}}G_c(i\omega_n)}{\left(i\omega_n - \frac{t^2}{\sqrt{p}}G_c(i\omega_n)\right)^2 - \mu^2 - |\Delta|^2}, \quad (4.30)$$

$$G_c(i\omega_n)^{-1} = i\omega_n - \Sigma_c(i\omega_n), \quad (4.31)$$

$$\frac{1}{U} = \frac{1}{\beta} \sum_{n=-\infty}^{+\infty} \frac{1}{\left(\omega_n + \frac{it^2}{\sqrt{p}}G_c(i\omega_n)\right)^2 + \mu^2 + |\Delta|^2}, \quad (4.32)$$

where the latter one 4.32 is a modified BCS gap equation [128] and  $G_+ = \frac{1}{2}(G_{\uparrow} + G_{\downarrow})$ .

## 4.5 Appendix: Saddle-point numerical analysis

### 4.5.1 The algorithm

To solve the equations 4.29-4.32, we use an iterative approach that is equivalent to finding the fixed point (the point to which the iterative procedure converges)

of the operator  $\hat{T}$  representing the Schwinger-Dyson equations 4.29-4.31 set on a fixed grid of Matsubara frequencies <sup>7</sup>. One starts with an empty seed  $G^0$  and applies iterations

$$G^{k+1} = \hat{T}G^k \quad (4.33)$$

until

$$\|G^{k+1} - G^k\| \leq \varepsilon, \quad (4.34)$$

where we set the precision to  $\varepsilon = 10^{-4}$  and  $\|\cdot\|$  denotes the euclidean norm of the vector.

The straightforward approach 4.33 converges rarely. One improves convergence modifying 4.33 as

$$G^{k+1} = \lambda G^k + (1 - \lambda)\hat{T}G^k, \quad (4.35)$$

where  $0 < \lambda < 1$  is a tunable parameter. This particular approach 4.35 has been used to compute the Green's function of the SYK model. [28] However, the convergence of the algorithm 4.35 may sufficiently slow down when one considering extra Schwinger-Dyson equations coupled to those of the bare SYK model or expands the parameter space. In our case, that happens due to coupling of the SYK model to a superconductor. To cope with this problem, we suggest using the adaptive golden ratio algorithm, [161] where the weight  $\lambda$  is not fixed but automatically adjusted to the local properties of the operator  $\hat{T}$ :

$$\lambda_k = \min \left\{ \frac{10}{9}\lambda_{k-1}, \frac{9}{16\lambda_{k-2}} \frac{\|G^k - G^{k-1}\|^2}{\|G^k - \hat{T}G^k - G^{k-1} + \hat{T}G^{k-1}\|^2} \right\}, \quad (4.36)$$

$$\bar{G}^k = \frac{G^k + 2\bar{G}^{k-1}}{3}, \quad (4.37)$$

$$G^{k+1} = \bar{G}^k - \lambda_k G^k + \lambda_k \hat{T}G^k. \quad (4.38)$$

Above we introduce  $\bar{G}$  as an auxiliary function that requires  $\bar{G}^0 = G^1$  and  $\lambda_0 = \lambda_{-1} > 0$ . Computationally, the algorithm 4.36-4.38 is of the same complexity as 4.33 and 4.35, while the adaptive step allows for a significant speedup.

We treat the pairing gap  $\Delta$ , the temperature  $T$ , and the coupling strength  $t$  that enter the equations 4.29-4.31 as an external set of parameters. Once

---

<sup>7</sup>We compute the corresponding Green's functions in time representation with the adapted Fast Fourier Transform each iteration.

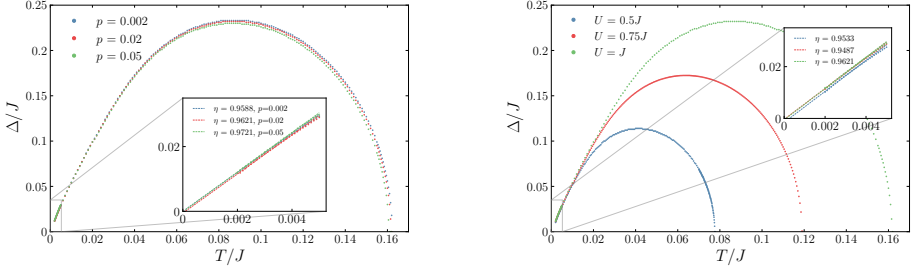


**Figure 4.5.** The pairing gap as a function of temperature at the critical coupling. **Left panel:** fixed  $U = J$ . **Right panel:** fixed  $p = 0.02$ .

$p$	0.002	0.02	0.02	0.02	0.05
$U$	1.0	1.0	0.75	0.5	1.0
$t_c$	$0.0710112J$	$0.126827J$	$0.10057J$	$0.07294J$	$0.1607J$
$\eta$	0.9588	0.9621	0.9487	0.9533	0.9721
$\delta$	$-2.96 \times 10^{-5}$	$-5.47 \times 10^{-4}$	$-3.73 \times 10^{-4}$	$-1.54 \times 10^{-3}$	$-9.86 \times 10^{-5}$

**Table 4.1.** The values of the **critical coupling** and the interpolation parameters for given  $p$  and  $U$ .

the Green's functions are found within the procedure 4.36-4.38, we choose the data that satisfies the self-consistency relation 4.32 to produce the finite-temperature phase diagrams.

#### 4.5.2 Precision and grid

Matsubara frequencies  $\omega_n = \pi T(2n + 1)$  define a natural discrete grid. We set the ultraviolet cut-off  $N$  such that  $n \in [-N, -N + 1, \dots, N - 1, N]$ , where the reliable  $N$  is of the order  $10^4$ - $10^5$  with the accuracy criteria 4.34  $\varepsilon = 10^{-4}$ . The numerical analysis becomes more demanding as one enters the low-temperature regime in the vicinity of the critical coupling. We reach the lowest temperature of  $T \sim 10^{-3}$  using  $N = 1.5 \times 10^6$ , with a main computational bottleneck coming from the computer memory. Also, the computation of the lowest critical temperatures requires an increase of the accuracy for the self-consistency condition 4.32 and  $\varepsilon$  4.34 to  $10^{-5}$ - $10^{-6}$ .

One of the objectives of this manuscript is to study the pairing gap at the critical coupling and low temperatures. In this regime, the gap grows linearly in temperature as shown in Figure 4.5. The critical coupling  $t_c$  is found as a condition when the off-set  $\delta$  of the interpolating function  $\Delta = 2\pi\eta T + \delta$

---

vanishes (see numerical values in Table 4.1). The system is sensitive to the coupling changes for small values of  $p$ , therefore, the precision of  $t_c$  reaches  $10^{-7}$  for  $p = 0.002$ .



## Chapter 5

# Quantum tunneling dynamics in a complex-valued Sachdev-Ye-Kitaev model quench-coupled to a cool bath

### 5.1 Introduction

Non-equilibrium dynamics of the celebrated Sachdev-Ye-Kitaev (SYK) model [25, 26] – dual to a black hole in a two-dimensional anti-de Sitter space – instantaneously coupled to a larger cold media has been recently scrutinized [170, 171] intending to mimic black hole evaporation [172–176] in a compact quantum mechanical setup. Alongside, several platforms have been proposed for experimental realization of the SYK model: as a low-energy effective description of a topological insulator/superconductor interface with an irregular opening [23], Majorana wires coupled through a disordered quantum dot [22], ultracold atoms trapped in optical lattices [177, 178], graphene flake with a random boundary [77], and digital quantum simulation [179–181]. In this context, opening up the system to an outer environment arises naturally as the “black-hole chip” [23] is necessarily in contact with a substrate and probes.

Once the system is opened due to quench-coupling, it starts to equilibrate with the external reservoir. Of particular interest is how the initial shock and the subsequent equilibration affects the initial SYK state and transport observables. The SYK model describes strongly interacting fermions in  $(0+1)$ -dimensions. As such, it can be considered as a quantum dot that is usually

characterized via tunneling current. In this manuscript, we consider the complex SYK model [137, 182] abruptly coupled to a zero temperature bath. We input the initial electrochemical potential in the SYK subsystem to enable quantum charge tunneling apart from the temperature drop between the SYK dot and the reservoir [170, 171]. Unlike equilibrium transport in the SYK quantum dot coupled to metallic leads [183–187], we are focused on the time evolution of both spectral properties and the tunneling current.

It was indicated earlier that right after the quench the SYK subsystem surprisingly heats up despite coupling to the colder bath [170, 171] and cools down later equilibrating with the reservoir’s temperature. In the holographic picture this initial heating is aligned with the increase of the subsystem energy that accompanies the information carried by the quench-induced shock-wave falling into the black hole [175]. We recover this result in the absence of a potential difference and confirm that the applied quench protocol cools down the SYK dot preserving an exotic SYK non-Fermi liquid phase after the relaxation. Proceeding to transport, we analyze the tunneling current evolution at low temperatures. We observe numerically that the current half-life – the time required for current to relax back to half its maximum value – grows linearly with the initial temperature of the SYK quantum dot. In contrast, replacing the SYK subsystem with a disordered Fermi liquid leads to a quadratic temperature increment of the current’s half-life. This enables one to distinguish the SYK non-Fermi liquid from a more common disordered phase by means of the quench-tunneling protocol.

## 5.2 The model

We begin our analysis with the SYK model in thermal equilibrium (chemical potential  $\mu$ , temperature  $T$ ) coupled to a reservoir at zero chemical potential and zero temperature via tunneling term at time  $t = 0$ . The Hamiltonian reads

$$H = H_{SYK} + H_{res} + \theta(t)H_{tun}, \quad (5.1)$$

$$H_{SYK} = \frac{1}{(2N)^{3/2}} \sum_{i,j,k,l=1}^N J_{ij;kl} c_i^\dagger c_j^\dagger c_k c_l - \mu \sum_{i=1}^N c_i^\dagger c_i, \quad (5.2)$$

$$H_{res} = \frac{1}{\sqrt{M}} \sum_{\alpha,\beta=1}^M \xi_{\alpha\beta} \psi_\alpha^\dagger \psi_\beta + h.c., \quad (5.3)$$

$$H_{tun} = \frac{1}{(NM)^{1/4}} \sum_{i=1}^N \sum_{\alpha=1}^M \lambda_{i\alpha} c_i^\dagger \psi_\alpha + h.c., \quad (5.4)$$

where  $J_{ij;kl} = J_{kl;ij}^* = -J_{ji;kl} = -J_{ij;lk}$ ,  $\xi_{\alpha\beta}$ , and  $\lambda_{i\alpha}$  are Gaussian random variables with finite variances  $\overline{|J_{ij;kl}|^2} = J^2$ ,  $\overline{|\xi_{\alpha\beta}|^2} = \xi^2$ ,  $\overline{|\lambda_{i\alpha}|^2} = \lambda^2$  and zero means. Below we assume the reservoir much larger than the SYK subsystem, which imposes  $M \gg N$  for the modes numbers. The charging energy [185, 187–189] is supposed to be negligible comparing to the SYK band-width  $J$ .

The conventional way to address non-equilibrium dynamics of a quantum many-body system is solving Kadanoff-Baym (KB) equations for the two-point functions  $G^{\gtrless}(t, t') = -iN^{-1} \sum_{i=1}^N \langle c_i(t_{\mp}) \bar{c}_i(t'_{\pm}) \rangle$ , where  $\pm$  denotes the top/bottom branches of the Keldysh time contour [76]. Inasmuch as Schwinger-Keldysh formalism has been widely applied to the SYK model in both thermalization [170, 171, 190–193] and transport [183, 184, 194] context, we leave the detailed derivation for Appendix 5.6 and proceed straight to the Kadanoff-Baym equations that hold in the large  $N, M$  limit:

$$(i\partial_t + \mu) G^{\gtrless}(t, t') = \int_{-\infty}^{+\infty} du \left( \Sigma_R(t, u) G^{\gtrless}(u, t') + \Sigma^{\gtrless}(t, u) G_A(u, t') \right), \quad (5.5)$$

$$(-i\partial_{t'} + \mu) G^{\gtrless}(t, t') = \int_{-\infty}^{+\infty} du \left( G_R(t, u) \Sigma^{\gtrless}(u, t') + G^{\gtrless}(t, u) \Sigma_A(u, t') \right), \quad (5.6)$$

The self-energy

$$\Sigma^{\gtrless}(t, t') = J^2 G^{\gtrless}(t, t')^2 G^{\lesseqgtr}(t', t) + \sqrt{p} \lambda^2 \theta(t) \theta(t') Q^{\gtrless}(t, t') \quad (5.7)$$

includes the contribution of the cool-bath as a time dependent background

$$Q^{\gtrless}(t, t') = - \frac{\mathbf{H}_1(2\xi(t-t')) \pm iJ_1(2\xi(t-t'))}{2\xi(t-t')} \quad (5.8)$$

expressed through Struve  $\mathbf{H}_1$  and Bessel  $J_1$  functions [167]; see Appendix 5.6. Here we introduce the ratio  $p = M/N$  and limit ourselves to the large reservoir case  $p \gg 1$ . Below we assume  $\xi = J$  for brevity.

The initial state of the system is settled by the thermal state of the bare SYK model (5.2) in absence of coupling to the reservoir. At the moment of quench the SYK subsystem (5.2) begins to deviate from the initial thermal state until it finally thermalizes at late times. Characterizing thermalization dynamics requires notion of the retarded, advanced, and Keldysh Green's functions

$$G_R(t, t') = \theta(t - t') \left( G^>(t, t') - G^<(t, t') \right), \quad (5.9)$$

$$G_A(t, t') = -\theta(t' - t) \left( G^>(t, t') - G^<(t, t') \right), \quad (5.10)$$

$$G_K(t, t') = G^>(t, t') + G^<(t, t') \quad (5.11)$$

expressed above in terms of the “greater” and “lesser” components. The same rules (5.9–5.11) apply to the self-energy (5.7).

The Green's functions are found numerically from the KB equations (5.5, 5.6) with the self-energies (5.7, 5.8). At first, we calculate the equilibrium Green's functions of the bare SYK model using an iterative approach [195, 196]. We apply an extra constraint manifesting the fluctuation-dissipation relation at initial temperature and chemical potential <sup>1</sup>. The equilibrium Green's functions set the initial condition for the Kadanoff-Baym equations and evolve as follows: the integrals in the KB equations are computed with the trapezoidal rule and the remaining differential equations are solved by the predictor-corrector scheme. The corrector adjusts self-consistently at every iteration [190, 191]. For the spectral properties we use the two-dimensional time grid with a step  $\delta t = 0.02$  and  $n \sim 10^4$  points in each direction, while for the transport calculations the numerical grid is more refined  $\delta t = 0.005$  but has a smaller size  $n \sim 10^3$ .

### 5.3 Relaxation after the quench

In a while after the quench the system relaxes and approaches a thermal state. To demonstrate that, we rotate the time frame  $t, t'$  in the numerically computed Green's functions towards  $\tau = t - t'$ ,  $\mathcal{T} = (t + t')/2$  and make a Fourier transform along  $\tau$ . Indeed, the system returns to a nearly-thermal

---

<sup>1</sup>In thermal equilibrium the fluctuation dissipation relation states [76]:  $G_K(\omega) = 2i \text{Im} G_R(\omega) \tanh \frac{\omega - \mu}{2T}$

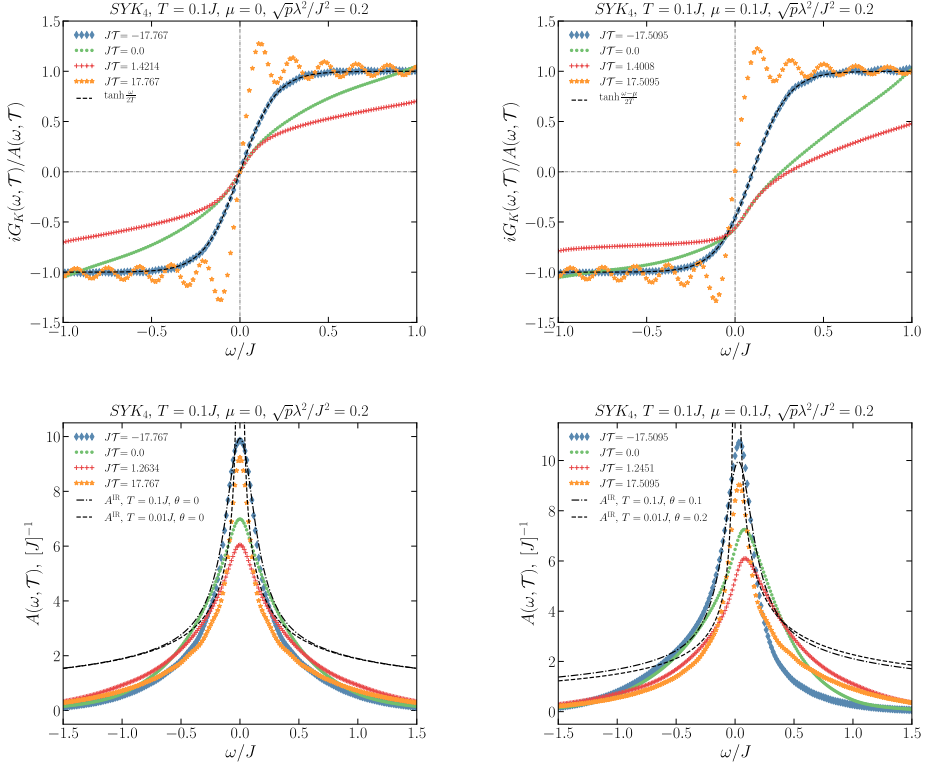


**Figure 5.1.** [Top] Deviation of the SYK subsystem from the initial thermal state: ratio between the Keldysh Green’s function and the spectral function of the SYK model at charge neutrality (*Left panel*) and at finite chemical potential (*Right panel*). The equilibrium distribution functions at the initial temperature are profiled with the dashed lines. The oscillations noticeable in the orange curves have a numerical origin, viz. the quality of the computation depends on the size and refinement of the time grid. The time grid is designated in the  $t, t'$  space, while Fourier transform is done along diagonal  $\tau = t - t'$ . Ergo, the  $\tau$ -lattices differ by length for separate slices of  $\mathcal{T}$ . Extension and refinement of the time grid suppress the oscillations. [Bottom] Spectral function of the SYK model as a function of frequency at charge neutrality (*Left panel*) and at finite chemical potential (*Right panel*). The dashed/dash-dot lines show the equilibrium SYK spectral function in the infrared regime for different parameters.

state if the extended fluctuation dissipation relation

$$\frac{iG_K(\omega, \mathcal{T})}{A(\omega, \mathcal{T})} = \tanh \frac{\omega - \tilde{\mu}(\mathcal{T})}{2\tilde{T}(\mathcal{T})} \quad (5.12)$$

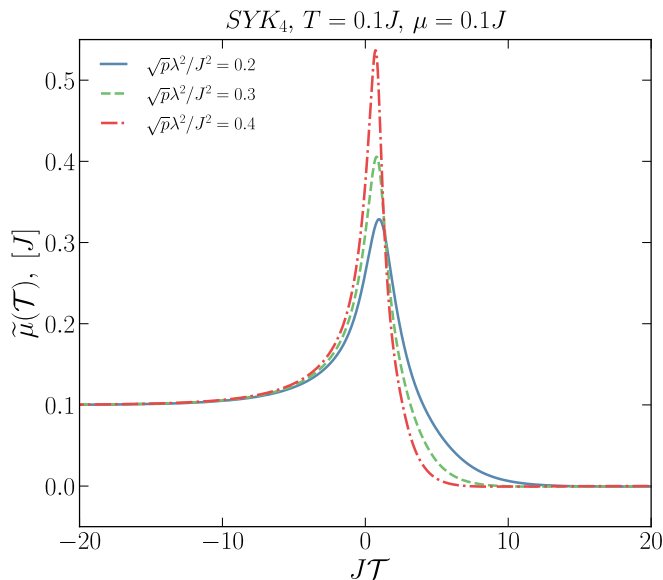


**Figure 5.2.** Effective chemical potential in the SYK quantum dot coupled to a large reservoir with  $T_{res} = 0$  and  $\mu_{res} = 0$ .

is fulfilled at frequencies in the vicinity of  $\tilde{\mu}$ , where  $A(\omega, \mathcal{T}) = -2\text{Im}G_R(\omega, \mathcal{T})$  is the SYK spectral function. In contrast to the equilibrium case, the extended fluctuation dissipation relation (5.12) is manifestly time dependent via the “centre of mass” coordinate  $\mathcal{T}$  which enters the effective temperature  $\tilde{T}$  and chemical potential  $\tilde{\mu}$ . Overall, the ratio (5.12) determines the effective distribution function of the SYK fermions in a quasi-equilibrium state, since  $\tanh \frac{\omega - \tilde{\mu}}{2\tilde{T}} = 1 - 2n_F(\omega - \tilde{\mu}, T)$ , where  $n_F$  is the Fermi distribution function.

The effective temperature can be extracted from the fluctuation dissipation relation (5.12) by an inverse slope of the Green’s functions ratio

$$\tilde{T}(\mathcal{T}) = \left( \frac{\partial}{\partial \omega} \frac{2iG_K(\omega, \mathcal{T})}{A(\omega, \mathcal{T})} \Big|_{\omega=\tilde{\mu}} \right)^{-1} \quad (5.13)$$

at  $\omega = \tilde{\mu}$ . Following the top panel of Fig. 5.1, that shows the ratio (5.12), one notices the temperature increase around  $\mathcal{T} = 0$ , in spite of coupling to a colder reservoir. The initial temperature increment is followed by the subsequent temperature decay to the reservoir’s temperature  $T = 0$ . This behavior was

revealed earlier for the SYK model with Majorana zero-modes [170, 171]. At late times  $J\mathcal{T} \simeq 17.8$ , the system clearly relaxes after the quench since the ratio (5.12) corresponds to the Fermi distribution at low temperature.

In comparison to the previous studies [170, 171], the new ingredient here is a charge imbalance between the SYK quantum dot and the cool-bath. Thereby, we track the electrochemical potential in the SYK subsystem which changes substantially once the quench is on. The effective chemical potential  $\tilde{\mu}(\mathcal{T})$  is set by the frequency where the ratio (5.12) turns to zero, as shown in Fig. 5.1 (*top right*). We plot the SYK chemical potential in Fig. 5.2, where  $\tilde{\mu}$  originates from the initial value  $\mu = 0.1J$  in the SYK quantum dot for  $\mathcal{T} \rightarrow -\infty$  and adjusts to the reservoir's  $\mu_{res} = 0$  at late times  $\mathcal{T} \rightarrow +\infty$ . As noted in Fig. 5.2, the chemical potential responds to the quench with a non-monotonic behavior as a function of time  $\mathcal{T}$ , akin to the temperature. Note that the ‘‘centre of mass’’ time coordinate  $\mathcal{T}$  and the actual time are not equivalent unless in a long-time limit. This explains why the chemical potential can already rise at small negative  $\mathcal{T}$ .

Since the tunneling between the SYK quantum dot and the reservoir turns on not adiabatically, of importance is whether the SYK non-Fermi liquid phase survives the quench. We compare the SYK spectral function  $A(\omega, \mathcal{T})$  a while after the quench to the equilibrium spectral function of the bare SYK model  $A^{\text{IR}}(\omega) = -2\text{Im}G_R^{\text{IR}}(\omega)$  in the infrared regime  $J/N \ll \omega, T \ll J$ , where

$$G_R^{\text{IR}}(\omega) = -i \frac{C(\theta)e^{-i\theta} \Gamma\left(\frac{1}{4} - i\frac{\omega}{2\pi T} + i\mathcal{E}\right)}{\sqrt{2\pi J\mathcal{T}} \Gamma\left(\frac{3}{4} - i\frac{\omega}{2\pi T} + i\mathcal{E}\right)}, \quad (5.14)$$

$$e^{2\pi\mathcal{E}} = \frac{\sin\left(\frac{\pi}{4} + \theta\right)}{\sin\left(\frac{\pi}{4} - \theta\right)}, \quad C(\theta) = \left(\frac{\pi}{\cos 2\theta}\right)^{1/4}. \quad (5.15)$$

The low-frequency asymptotic (5.14), known as the conformal Green’s function of the SYK model, does not explicitly depend on chemical potential. Instead, it depends on the independent parameter – the spectral asymmetry angle [137, 182]. The asymmetry angle  $\theta$  [197] is nonzero away from charge neutrality ( $\mu \neq 0$ ) and related to the charge per site on the SYK quantum dot

$$\langle \mathcal{Q} \rangle = \frac{1}{N} \sum_{i=1}^N \langle c_i^\dagger c_i \rangle - \frac{1}{2} = -\frac{\theta}{\pi} - \frac{\sin 2\theta}{4}, \quad (5.16)$$

where  $\langle \mathcal{Q} \rangle \in (-1/2, 1/2)$  and  $\theta \in (-\pi/4, \pi/4)$  [137, 182].

As mentioned earlier, the system relaxes to the low-temperature Fermi distribution at  $J\mathcal{T} \simeq 17.8$  (see Fig. 5.1 (*top left*)). In Fig. 5.3 we plot

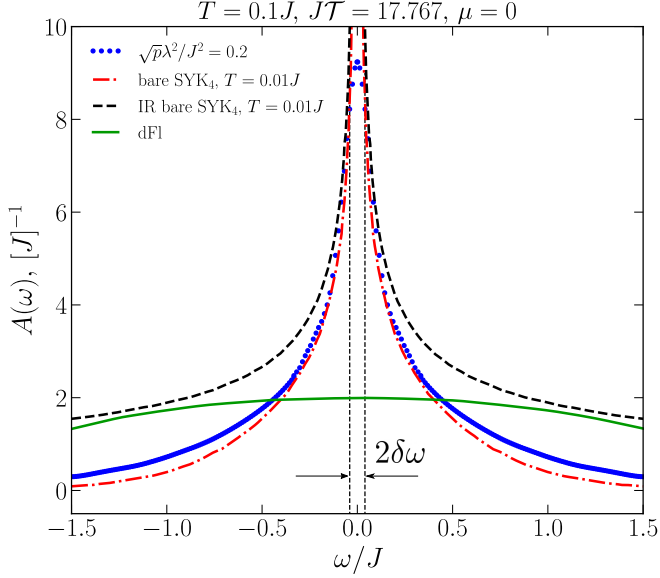


**Figure 5.3. Spectral of the SYK quantum dot after the quench as a function of frequency.** The blue dots show the result of the saddle-point numerics done for the evolution of the SYK subsystem with the initial temperature  $T = 0.1J$  connected to a zero temperature reservoir with a coupling strength  $\sqrt{p}\lambda^2/J^2 = 0.2$ . The red dash-dot curve is the equilibrium saddle-point numerics for the bare SYK model at low temperature, the black dashed line is the infrared (IR) solution of the bare SYK model (5.14), and the green line is the spectral function of the disordered Fermi liquid (dFl). The energy scale  $\delta\omega = p\lambda^4/J^3$  indicates the region where the SYK nFl crosses over to a Fermi liquid.

the spectral function of the SYK quantum dot in this regime. The spectral function after the quench is well aligned with the bare SYK spectral function at low temperature. The SYK nFl state is known to break down in presence of a Fermi liquid [80, 198]. Here we can estimate the timescale of the crossover to a Fermi liquid from the self-energy (5.7) comparing the SYK nFl and the reservoir's contributions. Indeed, substitution of the Green's functions  $G(t) \propto 1/\sqrt{Jt}$  and  $Q(t) \propto 1/(Jt)$  to the self-energy (5.7) shows that the crossover to a Fermi liquid happens for  $t_{FL} \gtrsim 1/\delta\omega$ , where  $\delta\omega = p\lambda^4/J^3$ . This implies that after relaxation from the quench the SYK nFl behavior can be read out from

the spectral function for

$$\delta\omega \lesssim \omega \ll J. \quad (5.17)$$

The lower bound in inequality (5.17) can be suppressed as  $\sqrt{p}\lambda^2/J \ll J$  in the weak tunneling limit. This observation agrees with the long timescale of the SYK nFI/Fermi liquid crossover found earlier in equilibrium studies [80, 185, 194, 199].

In Figs. 5.1 (*top right*), 5.2 we demonstrate that the system at finite initial  $\mu$  tends to zero chemical potential in the long time limit. This is aligned with the discharging of the SYK quantum dot coupled to the large reservoir, which is kept at charge neutrality. At the level of the the equilibrium SYK Green's function (5.14), this naively implies  $\theta \approx 0$ . However, the spectral function in Fig. 5.1 (*bottom right*) at long times is close enough to the conformal one with non-zero asymmetry angle  $\theta$ . We plot the conformal spectral function with  $\theta = 0.2$  as a reference. The origin of this mismatch may be that the asymmetry parameter  $\theta$  is usually related to  $\partial\mu/\partial T$  but not to the equilibrium value of the chemical potential [137]. In its turn, the temperature-independent part of the chemical potential in the SYK model is not a monotonic function of the asymmetry parameter [200]. Additionally, the SYK subsystem after the quench suffers the particle leak, that may require to account not only for a self-energy shift by the real-valued  $\mu$  [137], but also an extra imaginary contribution to the self-energy. This issue could lead to the renormalization of  $\theta$  in the final state, which is beyond the scope of this paper.

## 5.4 Tunneling current

Having discussed the SYK subsystem inner properties we proceed to transport. Specifically, we focus on the tunneling current:

$$\dot{Q} = i[H, \mathcal{Q}] = -\frac{i}{N} \frac{\theta(t)}{(NM)^{1/4}} \sum_{i=1}^N \sum_{\alpha=1}^M \lambda_{i\alpha} c_i^\dagger \psi_\alpha + h.c. \quad (5.18)$$

The current's expectation value in the SYK quantum dot/cool-bath system is found from the generating functional  $\ln Z[\chi]$  [183]

$$\mathcal{I} = \frac{1}{t_m} \int_0^{t_m} dt \langle \dot{Q}(t) \rangle = \frac{1}{t_m} \frac{\partial}{\partial(i\chi)} \ln Z[\chi] \Big|_{\chi=0}, \quad (5.19)$$

$$Z[\chi] = \left\langle \text{Tr} C e^{-i \int_C dt H(x)} \right\rangle = \int \mathcal{D}[\bar{c}, c] \mathcal{D}[\bar{\psi}, \psi] e^{iS[\chi]}, \quad (5.20)$$

where  $T_C$  is the time ordering along the Keldysh contour,  $t_m$  is the measurement time, and  $S[\chi]$  is the effective action of the model with a counting field  $\chi$  [201, 202]. The counting field  $\chi$  transforms the tunneling Hamiltonian

$$H(\chi) = H_{\text{SYK}} + H_{\text{res}} + \theta(t)H_{\text{tun}}(\chi), \quad (5.21)$$

$$H_{\text{tun}}(\chi) = \frac{1}{(NM)^{1/4}} \sum_{i=1}^N \sum_{\alpha=1}^M \lambda_{i\alpha} e^{\frac{i\chi(t)}{2N}} c_i^\dagger \psi_\alpha + h.c., \quad (5.22)$$

so that

$$\chi(t) = \begin{cases} \chi & \text{for } 0 < t < t_m \\ 0 & \text{otherwise} \end{cases}, \quad (5.23)$$

The factor of two in the coupling phase in the tunneling term (5.22) accounts for the doubling due to the forward and backward branches of the Keldysh time contour.

One notices that the Hamiltonian transformation (5.22) is equivalent to a simple rotation of the coupling constants  $\lambda_{i\alpha} \rightarrow \lambda_{i\alpha} e^{\frac{i\chi(t)}{2N}}$  in the original theory (5.1). Thus, the Kadanoff-Baym equations (5.5,5.6) describe the valid saddle-point for the partition function (5.20) up to the redefinition of the coupling constants  $\lambda_i$ . Indeed, the current can be deduced from the tunneling part of the effective action

$$S_{\text{tun}}(\chi) = i\sqrt{NM}\lambda^2 \sum_{ss'=\pm} \int_0^{+\infty} dt dt' ss' e^{\frac{i(s\chi(t)-s'\chi(t'))}{2N}} \times G_{ss'}(t, t') Q_{s's}(t', t). \quad (5.24)$$

Here the Green's functions  $G_{ss'}$  and  $Q_{s's}$  describe the saddle-point of the SYK-bath system and are found from the equations (5.5-5.8), where  $s = \pm$  denotes the forward and backward branch of the Keldysh contour. Accordingly, the counting field  $\chi$  is defined on the Keldysh contour as  $\chi_s(t) = s\chi(t)$ . Leaving the detailed derivation of the full effective action of the SYK-bath coupled system for the Appendix 5.6, we proceed to the tunneling current

Applying the prescription (5.19), we derive the expectation value of current

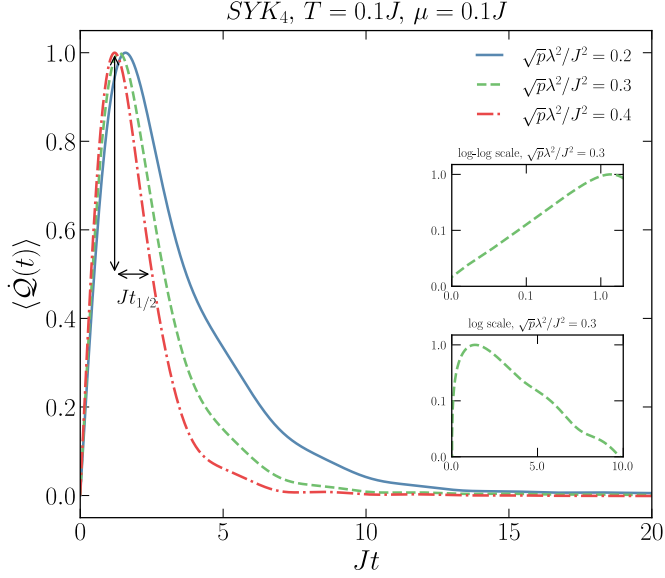


**Figure 5.4.** Tunneling current as a function of time normalized on its maximum value. The insets show time dependence of the current in log-log and log scales for  $\sqrt{p}\lambda^2/J^2 = 0.3$ . The log-log plot reveals the initial power law increase of the tunneling current, while the log plot is consistent with the exponential decay. We illustrate the current's half-life  $t_{1/2}$  for  $\sqrt{p}\lambda^2/J^2 = 0.4$ .

as a function of the measurement time  $t_m$ :

$$\begin{aligned}
 \mathcal{I} &= -\frac{\sqrt{p}\lambda^2}{2t_m} \sum_{ss'} \int_0^{t_m} dt \int_0^{+\infty} dt' \left( G_{ss'}(t, t') s' Q_{s's}(t', t) \right. \\
 &\quad \left. - Q_{s't}(t, t') s G_{ss'}(t', t) \right) \\
 &= -\frac{\sqrt{p}\lambda^2}{2t_m} \int_0^{t_m} dt \int_0^{+\infty} dt' \text{tr} \left( \sigma^x \hat{G}(t, t') \hat{Q}(t', t) \right. \\
 &\quad \left. - \sigma^x \hat{Q}(t, t') \hat{G}(t', t) \right), \tag{5.25}
 \end{aligned}$$

where

$$\hat{G} = \begin{pmatrix} G_R & G_K \\ 0 & G_A \end{pmatrix}, \quad \hat{Q} = \begin{pmatrix} Q_R & Q_K \\ 0 & Q_A \end{pmatrix} \tag{5.26}$$

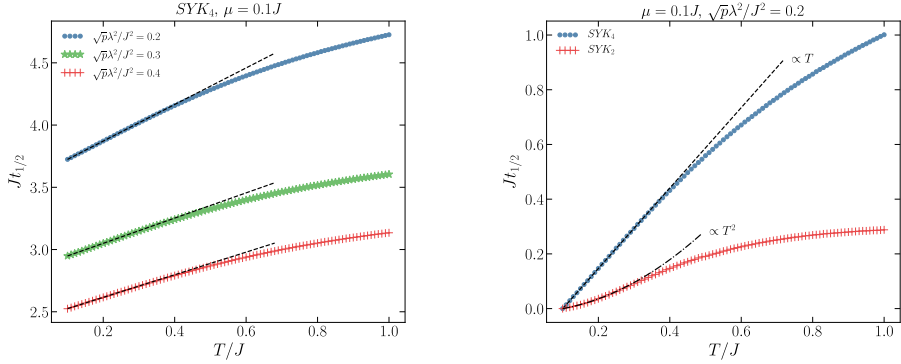


**Figure 5.5. Half-life of the tunneling current** as a function of the initial temperature. In the *left panel*, we compare the half-lives for the SYK model connected to a cool-bath for different coupling strengths. Meanwhile in the *right panel*, we show the difference between  $\text{SYK}_4$  (SYK non-Fermi liquid initial state) and  $\text{SYK}_2$  (disordered Fermi liquid initial state) behavior as a tested subsystem; the curves are shifted to the same origin for better visual comparison. The initial temperature changes from  $T = 0.1J$  to  $T = J$  with a step  $\delta T = 0.01J$ . The dashed/dashdot lines stand for the linear/quadratic fits made for the temperature interval  $T \in [0.1J, 0.2J]$ .

are the Green's functions of the SYK quantum dot and the cool-bath set by the equations (5.5-5.8) and transformed to the  $R, A, K$  basis according to the rules (5.9-5.11)<sup>2</sup>. From here, the dynamics of the tunneling current is given by

$$\langle \dot{Q}(t) \rangle = -\frac{\sqrt{p}\lambda^2}{2}\theta(t) \int_0^t dt' \mathcal{J}(t, t'), \quad (5.27)$$

$$\begin{aligned} \mathcal{J}(t, t') &= G_R(t, t')Q_K(t', t) - Q_K(t, t')G_A(t', t) \\ &\quad - Q_R(t, t')G_K(t', t) + G_K(t, t')Q_A(t', t). \end{aligned} \quad (5.28)$$

Time dependence of the tunneling current is shown in Fig. 5.4. The current grows initially as a power law, reaches the maximum value, and decays exponentially to zero consistently with the discharging process of the SYK

<sup>2</sup>In equilibrium the fluctuation dissipation relation holds  $G_K(\omega) = -2\pi i(1 - 2n_{\text{SYK}}(\omega))\nu_{\text{SYK}}(\omega)$ ,  $Q_K(\omega) = -2\pi i(1 - 2n_{\text{res}}(\omega))\nu_{\text{res}}(\omega)$ , where  $n_{\text{SYK}}$  and  $n_{\text{res}}$  are the Fermi distribution functions and  $\nu_{\text{SYK}} = -\frac{1}{\pi}\text{Im}G_R$  and  $\nu_{\text{res}} = -\frac{1}{\pi}\text{Im}Q_R$  are the densities of states. Substituting those to Eq. (5.25), one gets a familiar Fermi golden rule formula for the tunneling current [76]:

$$\mathcal{I} = 2\pi\sqrt{p}\lambda^2 \int d\omega \nu_{\text{SYK}}(\omega)\nu_{\text{res}}(\omega)(n_{\text{SYK}}(\omega) - n_{\text{res}}(\omega)).$$

quantum dot. With intention to mark the lifetime of the effect we extract the half-life – the time in which the current is decreased in half of its maximum value. Varying the initial temperature  $T$  of the SYK quantum dot, we show the current’s half-life for several coupling strengths in Fig. 5.5 (*left*). The stronger the coupling, the shorter the half-life of the tunneling current. Oppositely, the half-life increases with the initial temperature rise. For the temperatures  $T \lesssim 0.4J$  the tunneling current half-life grows linearly in  $T$ .

To check if the  $T$ -linear current’s half-life is specific for the SYK state, we substitute the SYK model with the one-body random Hamiltonian (5.3), often referred to as the SYK<sub>2</sub> model, the same that describes the reservoir. This model has a typical Fermi liquid Green’s function  $G_R(t) \propto 1/t$  in the long time limit  $Jt \gg 1$ , which makes it legitimate to build the SYK nFl/Fermi liquid comparison. Matching the tunneling current half-life for the SYK vs SYK<sub>2</sub> model in Fig. 5.5 (*right*), we ascertain that their temperature dependencies are drastically different. The current’s half-life in the system of the SYK<sub>2</sub> quantum dot coupled to the cold bath increases as  $T^2$  at low temperatures, which discerns it from the SYK model cooling protocol displaying the linear in temperature increase.

Duration of the tunneling event in our system is defined by the tunneling contact resistance, similarly to an exponentially relaxing capacitor discharge. As such, our results resemble the prominent resistivity predictions for strange metals  $\rho_{SM} \sim T$  [194, 199, 203] and Fermi liquid  $\rho_{FL} \sim T^2$ .

## 5.5 Conclusion

The Sachdev-Ye-Kitaev model quench-coupled with a cold bath has been a subject of close attention aiming to simulate evaporation of a black hole [170, 171]. At the same time, both connecting the system to the environment and its further characterization are inherent for realization proposals of the SYK model in condensed matter systems [22, 23, 77, 177, 178]. In this manuscript, we consider a quantum dot described by the complex SYK model at finite temperature instantaneously coupled to a zero temperature reservoir. Analyzing the dynamical spectral function of the SYK quantum dot at charge neutrality, we show that the considered quench protocol preserves the SYK non-Fermi liquid state for the energies  $\delta\omega \ll \omega \ll J$ . Here the lower bound  $\delta\omega$  is suppressed in the weak tunneling limit. Further, we put an initial electrochemical potential in the quantum dot and compute the tunneling current dynamics due to discharging of the dot. The tunneling current half-life shows

distinct temperature dependencies for different systems that are being cooled down. In case of the SYK quantum dot, the half-life increases linearly in the initial temperature  $T$ , while for the Fermi liquid the increase is  $\propto T^2$ . Therefore, this temperature dependence of the tunneling current half-life provides a distinguishing feature for the disordered quantum dot exhibiting the SYK nFl phase against more common Fermi liquid behavior.

## 5.6 Appendix: Derivation of the Kadanoff-Baym equations from the SYK saddle-point

Here we derive the Kadanoff-Baym equations for the SYK quantum dot coupled to a cool-bath by a quench.

### 5.6.1 Saddle-point equations

We perform the disorder average of with the Hamiltonian (5.1), pursuing [184, 194]. The effective action can be written in terms of bilocal fields  $G_{s's}(t', t) = iN^{-1} \sum_i \bar{c}_{is}(t) c_{is}(t')$ ,  $Q_{s's}(t', t) = iM^{-1} \sum_\alpha \bar{\psi}_{\alpha s}(t) \psi_{\alpha s}(t')$  and  $\Sigma_{ss'}(t, t')$ ,  $\Pi_{ss'}(t, t')$  as the corresponding Lagrange multipliers

$$\begin{aligned}
S = & -iN \text{tr} \ln \left[ \sigma_{ss'}^z \delta(t-t') (i\partial_t + \mu) - \Sigma_{ss'}(t, t') \right] - \\
& -iN \sum_{ss'} \int dt dt' \left( \Sigma_{ss'}(t, t') G_{s's}(t', t) - \frac{ss' J^2}{4} G_{ss'}(t, t')^2 G_{s's}(t', t)^2 \right) - \\
& -iM \text{tr} \ln \left[ \sigma_{ss'}^z \delta(t-t') i\partial_t - \Pi_{ss'}(t, t') \right] - \\
& -iM \sum_{ss'} \int dt dt' \left( \Pi_{ss'}(t, t') Q_{s's}(t', t) - \frac{ss' \xi^2}{2} Q_{ss'}(t, t') Q_{s's}(t', t) \right) \\
& + i\sqrt{NM} \sum_{ss'} \int dt dt' ss' \lambda^2 \theta(t) \theta(t') G_{ss'}(t, t') Q_{s's}(t', t). \tag{5.29}
\end{aligned}$$

where  $s = \pm$  denotes forward and backward branches of the Keldysh time contour [76]. In the large  $N, M$  limit, the saddle-point equations are

$$\Sigma_{ss'}(t, t') = J^2 G_{ss'}(t, t')^2 G_{s's}(t', t) + \sqrt{p} \lambda^2 \theta(t) \theta(t') Q_{ss'}(t, t'), \quad (5.30)$$

$$\Pi_{ss'}(t, t') = \xi^2 Q_{ss'}(t, t') + \frac{\lambda^2}{\sqrt{p}} \theta(t) \theta(t') G_{ss'}(t, t'), \quad (5.31)$$

$$\sum_r \int_{-\infty}^{+\infty} du \left( \sigma_{sr}^z \delta(t-u) (i\partial_t + \mu) - sr \Sigma_{sr}(t, u) \right) G_{rs'}(u, t') = \delta_{ss'} \delta(t-t'), \quad (5.32)$$

$$\sum_r \int_{-\infty}^{+\infty} du \left( \sigma_{sr}^z \delta(t-u) i\partial_t - sr \Pi_{sr}(t, u) \right) Q_{rs'}(u, t') = \delta_{ss'} \delta(t-t'), \quad (5.33)$$

where  $p = M/N$  is the mode ratio.

Following Ref. [190], we derive the self-consistent Kadanoff-Baym equations considering  $s, s' = \pm, \mp$  components of Eqs. (5.32, 5.33):

$$(i\partial_t + \mu) G^{\cong}(t, t') = \int_{-\infty}^{+\infty} du \left( \Sigma_R(t, u) G^{\cong}(u, t') + \Sigma^{\cong}(t, u) G_A(u, t') \right), \quad (5.34)$$

$$(-i\partial_{t'} + \mu) G^{\cong}(t, t') = \int_{-\infty}^{+\infty} du \left( G_R(t, u) \Sigma^{\cong}(u, t') + G^{\cong}(t, u) \Sigma_A(u, t') \right), \quad (5.35)$$

$$i\partial_t Q^{\cong}(t, t') = \int_{-\infty}^{+\infty} du \left( \Pi_R(t, u) Q^{\cong}(u, t') + \Pi^{\cong}(t, u) Q_A(u, t') \right), \quad (5.36)$$

$$-i\partial_{t'} Q^{\cong}(t, t') = \int_{-\infty}^{+\infty} du \left( Q_R(t, u) \Pi^{\cong}(u, t') + Q^{\cong}(t, u) \Pi_A(u, t') \right), \quad (5.37)$$

where the self-energies are

$$\Sigma^{\cong}(t, t') = J^2 G^{\cong}(t, t')^2 G^{\leq}(t', t) + \sqrt{p} \lambda^2 \theta(t) \theta(t') Q^{\cong}(t, t'), \quad (5.38)$$

$$\Pi^{\cong}(t, t') = \xi^2 Q^{\cong}(t, t') + \frac{\lambda^2}{\sqrt{p}} \theta(t) \theta(t') G^{\cong}(t, t'). \quad (5.39)$$

### 5.6.2 Reservoir as an external potential

Since we assume the reservoir to be large enough  $p \gg 1$ , it can be considered as a closed dynamic background to the SYK subsystem

$$\int_{-\infty}^{+\infty} du \left( \delta(t-u) i \partial_t - \xi^2 \hat{Q}(t, u) \right) \hat{Q}(u, t') = \delta(t-t') \quad (5.40)$$

describing a decoupled random free fermion in equilibrium. Here we perform a rotation towards retarded, advanced, and Keldysh basis

$$\hat{Q} = \begin{pmatrix} Q_R & Q_K \\ 0 & Q_A \end{pmatrix} = L \sigma^z \begin{pmatrix} Q_{++} & Q_{+-} \\ Q_{-+} & Q_{--} \end{pmatrix} L^\dagger, \quad L = \frac{1}{\sqrt{2}} \begin{pmatrix} 1 & -1 \\ 1 & 1 \end{pmatrix}.$$

The retarded Green's function is found from

$$(\omega - \xi^2 Q_R(\omega)) Q_R(\omega) = 1 \quad (5.41)$$

$$Q_R(\omega) = \frac{\omega}{2\xi^2} - \frac{i}{\xi} \sqrt{1 - \frac{\omega^2}{4\xi^2}} = \frac{2}{\omega + 2i\xi \sqrt{1 - (\omega/2\xi)^2}} \quad (5.42)$$

where the spectral function obeys the semicircle law  $\rho(\omega) = -2 \text{Im} Q_R(\omega) = \frac{2}{\xi} \text{Re} \sqrt{1 - \frac{\omega^2}{4\xi^2}}$ . Let's derive the time representation of  $Q_R$ :

$$\begin{aligned} Q_R(t, t') &= Q_A(t', t)^* = \int_{-\infty}^{+\infty} \frac{d\omega}{2\pi} e^{-i\omega(t-t')} Q_R(\omega) = \\ &= - \lim_{\delta \rightarrow 0^+} \int_{-\infty}^{+\infty} \frac{d\omega}{2\pi} e^{-i\omega(t-t')} e^{\delta(t-t')} \frac{1}{2\xi^2} \sqrt{(\omega + i\delta)^2 - 4\xi^2}. \end{aligned} \quad (5.43)$$

Here the branch cut is in the lower half plane, so we close the contour correspondingly for  $t - t' > 0$ . Since there are no poles in the lower half plane, we shrink the contour to the anticlockwise traverse around the branch cut. Note that an additional phase is acquired when crossing the branch cut  $\sqrt{\omega^2 - 4\xi^2} \rightarrow e^{\frac{1}{2} \ln(\omega^2 + 4\xi^2) + i\pi} = e^{i\pi} \sqrt{\omega^2 - 4\xi^2}$ . Therefore, we get

$$\begin{aligned} Q_R(t, t') &= -\theta(t-t') \frac{1 - e^{i\pi}}{4\pi\xi^2} \int_{-2\xi}^{2\xi} d\omega e^{-i\omega(t-t')} \sqrt{\omega^2 - 4\xi^2} = \\ &= -i\theta(t-t') \frac{J_1(2\xi(t-t'))}{\xi(t-t')}, \end{aligned} \quad (5.44)$$

where  $J_1$  is the first Bessel function of the first kind. The Keldysh component at zero temperature is

$$\begin{aligned} Q_K(t, t') &= \int_{-\infty}^{+\infty} \frac{d\omega}{2\pi} e^{-i\omega(t-t')} Q_K(\omega) = \int_{-\infty}^{+\infty} \frac{d\omega}{2\pi} e^{-i\omega(t-t')} 2i \operatorname{sgn}(\omega) \operatorname{Im} Q_R(\omega) \\ &= -\frac{i}{2\pi\xi^2} \int_{-2\xi}^{2\xi} d\omega e^{-i\omega(t-t')} \operatorname{sgn}(\omega) \sqrt{4\xi^2 - \omega^2} = -\frac{\mathbf{H}_1(2\xi(t-t'))}{\xi(t-t')}, \end{aligned} \quad (5.45)$$

where  $\mathbf{H}_1$  is the first Struve function.

### 5.6.3 Dynamics of the SYK subsystem

In the large  $p$  limit, the dynamics of the SYK subsystem is described by Eqs. (5.34, 5.35, 5.38), where the reservoir Green's function  $Q(t-t')$  enters the SYK self-energy (5.38) as the external potential derived in Section ???. Thereby, the Kadanoff-Baym equations simplify to

$$(i\partial_t + \mu) G^{\geq}(t, t') = \int_{-\infty}^{+\infty} du \left( \Sigma_R(t, u) G^{\geq}(u, t') + \Sigma^{\geq}(t, u) G_A(u, t') \right), \quad (5.46)$$

$$(-i\partial_{t'} + \mu) G^{\geq}(t, t') = \int_{-\infty}^{+\infty} du \left( G_R(t, u) \Sigma^{\geq}(u, t') + G^{\geq}(t, u) \Sigma_A(u, t') \right), \quad (5.47)$$

with the self-energy (5.30)

$$\Sigma^{\geq}(t, t') = J^2 G^{\geq}(t, t')^2 G^{\leq}(t', t) + \sqrt{p} \lambda^2 \theta(t) \theta(t') Q^{\geq}(t, t'), \quad (5.48)$$

$$Q^{\geq}(t, t') = -\frac{1}{2\xi(t-t')} \left( \mathbf{H}_1(2\xi(t-t')) \pm iJ_1(2\xi(t-t')) \right). \quad (5.49)$$

Here we introduced [76]  $G^>(t, t') \equiv G_{-+}(t, t')$ ,  $G^<(t, t') \equiv G_{+-}(t, t')$ ,  $\Sigma^>(t, t') \equiv \Sigma_{-+}(t, t')$ ,  $\Sigma^<(t, t') \equiv \Sigma_{+-}(t, t')$  and account for

$$G_{++}(t, t') = \theta(t-t') G^>(t, t') + \theta(t'-t) G^<(t, t'), \quad (5.50)$$

$$G_{--}(t, t') = \theta(t'-t) G^>(t, t') + \theta(t-t') G^<(t, t'), \quad (5.51)$$

$$\Sigma_{++}(t, t') = \theta(t-t') \Sigma^>(t, t') + \theta(t'-t) \Sigma^<(t, t'), \quad (5.52)$$

$$\Sigma_{--}(t, t') = \theta(t'-t) \Sigma^>(t, t') + \theta(t-t') \Sigma^<(t, t'). \quad (5.53)$$

The retarded, advanced, and Keldysh components are expressed in terms of  $>$  and  $<$  as

$$G_R(t, t') = \theta(t - t') \left( G^>(t, t') - G^<(t, t') \right), \quad (5.54)$$

$$G_A(t, t') = -\theta(t' - t) \left( G^>(t, t') - G^<(t, t') \right), \quad (5.55)$$

$$G_K(t, t') = G^>(t, t') + G^<(t, t'), \quad (5.56)$$

$$\Sigma_R(t, t') = \theta(t - t') \left( \Sigma^>(t, t') - \Sigma^<(t, t') \right), \quad (5.57)$$

$$\Sigma_A(t, t') = -\theta(t' - t) \left( \Sigma^>(t, t') - \Sigma^<(t, t') \right), \quad (5.58)$$

$$\Sigma_K(t, t') = \Sigma^>(t, t') + \Sigma^<(t, t'). \quad (5.59)$$

## Chapter 6

# Navigating the pitfalls of relic neutrino detection

### 6.1 Introduction

The Cosmic Neutrino Background ( $C\nu B$ ) is an unexplored source of precious cosmological data [95]. Like the CMB, it carries a photographic image of the early Universe, albeit from a much older epoch of neutrino decoupling. Although indirect evidence for the  $C\nu B$  was recently found in the Planck data [204], direct detection of the relic neutrinos remains a major experimental challenge and a problem of great significance for the understanding of the pre-recombination age. The importance and basic principles of a  $C\nu B$  detection experiment were discussed as early as 1962 in a paper by S. Weinberg [95] who put forward the idea of a kinematical signature of the cosmic neutrino capture processes in beta-spectra of radioactive atoms. This idea was further elaborated in Ref. [86].

The main roadblock in the way of the realisation of Weingerg's original proposal is the weakness of the neutrino-matter interaction, which makes it difficult to achieve a sufficient number of the relic neutrino capture events in a given radioactive sample. The problem is further compounded by the presence of a massive neutrino-emission background which imposes extremely stringent requirements on the energy resolution of the experiment [205, 206]. The magnitude of the challenge is illustrated in FIG. 6.1 showing the  $\beta$ -emission spectrum of monoatomic  ${}^3\text{H}$  in vacuum. One can see that the spectrum is dominated by the spontaneous  $\beta$ -decay background, shown in red, while the predicted signal [85] due to the relic neutrino capture process consists of a tiny feature

shown in green <sup>1</sup>. Not only is the predicted  $C\nu B$  feature quite weak, consisting of only a few events per year per 100 g of  $^3\text{H}$ , but it is also positioned within a few tens of meV from the massive spontaneous decay background, which implies that the energy resolution of the experiment needs to be as good as 20 meV. While the energy resolution specifications push the experimental apparatus towards a smaller scale, the extreme scarceness of useful events calls for a bigger working volume. The tension between these opposite requirements makes working with gaseous samples difficult, possibly impracticable. The best to date experiment, KATRIN [207], which uses gaseous molecular Tritium as the working isotope falls short of the required sample activity by six orders of magnitude. It is worth noting that the sensitivity of experiments working with gaseous Tritium is further reduced due to excitation of internal motions of the Tritium molecule and is further limited by the non-tritium background [205, 208].

Currently, the only viable alternative to the gas phase experiment is a solid state architecture where the  $\beta$ -emitters are adsorbed on a substrate [96]. Such a design can increase the event count by orders of magnitude while preserving the necessary degree of control over the emitted electrons. However, these advantages come at a price. In this paper we demonstrate that any solid state based  $\beta$ -decay experiment has fundamental limitations on its energy resolution, which are not related to the construction of the measuring apparatus. Such limitations arise from the quantum effect of the zero-point motion of the adsorbed  $\beta$ -emitter. We show that due to the extremely weak sensitivity of the zero-point motion to the details of the chemistry of adsorption, the effect mainly imposes *intrinsic* requirements on the physical properties of the emitter <sup>2</sup>. In particular, we find that Tritium used in many existing and proposed experiments is not suitable for detecting  $C\nu B$  in a solid state setup. At the end, we list candidates for a suitable  $\beta$ -emitter and comment on what future theoretical and experimental research is needed to both confirm the choice of the atom and improve the resolution of the experiment.

---

<sup>1</sup>The capture spectrum comprises of three peaks corresponding to the three neutrino mass eigenstates. The first two peaks overlap and are barely distinguishable.

<sup>2</sup>In general, the interaction of an adsorbed radioactive atom with the substrate is complicated and it gives rise to several effects each contributing to the broadening of the measured  $\beta$ -emission spectrum. In this paper, we only focus on one which is arguably the simplest and the strongest of all: the zero-point motion of an atom arising from the atom's adsorption.

## 6.2 Defining the problem

Although our analysis is not limited to a particular solid state design, we use for reference the setup of PTOLEMY [96], a state of the art experimental proposal for the  $C\nu B$  detection that aims to achieve a sufficient number of events together with the required energy resolution of the apparatus [209–213]. In PTOLEMY, mono atomic Tritium is deposited on graphene sheets arranged into a parallel stack and a clever magneto-electric design is used to extract and measure the energy of the electrons created in the two  $\beta$ -decay channels

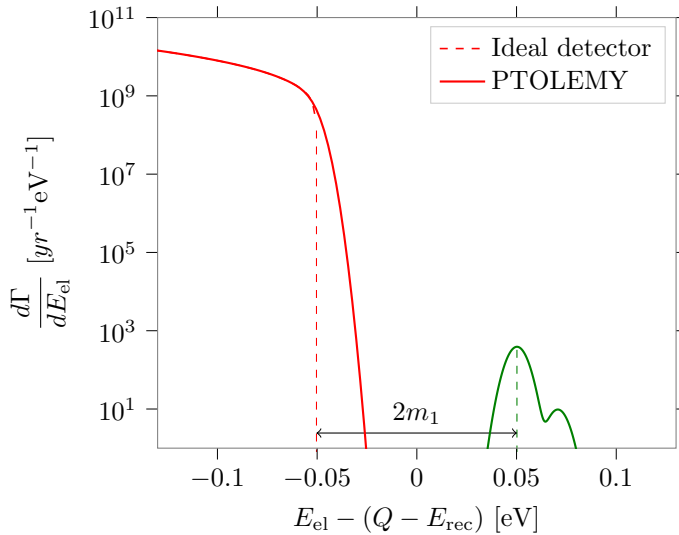


**Figure 6.1.** The  $\beta$ -spectrum of free monoatomic Tritium centered around  $Q - E_{\text{rec}}$ , where  $Q$  is the decay energy and  $E_{\text{rec}}$  - recoil of the nucleus in the vacuum. The normal neutrino mass hierarchy [88] is assumed with the mass of the lightest neutrino  $m_1 = 50$  meV. The spontaneous  $\beta$ -decay spectrum is shown in red while the  $C\nu B$  feature is shown in green. The solid lines are drawn assuming a 10 meV resolution of the detector.

The main goal of the  $C\nu B$  detection experiments is to detect the electrons produced in the neutrino capture channel (see FIG. 6.1) that depends on the

mass of the lightest neutrino and the hierarchy [85, 96, 214, 215]. Since the captured relic neutrinos are soft, it has a shape of 3 narrow peaks<sup>3</sup> separated from the end of the main part of the spectrum by double the mass of the lightest neutrino. The spectrum depicted on FIG. 6.1 is calculated for an isolated Tritium atom in the rest frame, where the recoil energy is defined by the conservation laws. However, if Tritium is absorbed on a substrate, it can not be considered at rest and the recoil energy of the nucleus acquires some amount of uncertainty and so does the measured spectrum of the emitted electron (see FIG. 6.3).

Two complementary views on such an uncertainty are possible, both leading to the same conclusion in the present context. In the “semiclassical” view the source of the uncertainty is the zero-point motion of the Tritium atom, which results in a fluctuating centre of mass frame at the moment of  $\beta$ -decay. In the fully quantum view the uncertainty results from quantum transitions of an atom into the highly excited vibrational states in the potential which confines it to the graphene sheet. We shall begin our discussion with the semi-classical picture.

It follows from Heisenberg uncertainty principle that an atom restricted to some finite region in space by the bonding potential cannot be exactly at rest. Even in the zero temperature limit it performs a zero-point motion so that its velocity fluctuates randomly obeying some probability distribution  $\mathcal{F}(\mathbf{u})$ . For localized states,  $\mathcal{F}(\mathbf{u})$  has a vanishing mean and dispersion defined by the Heisenberg uncertainty principle  $\Delta u \sim \hbar/m_{\text{nuc}}\lambda_{\text{nuc}}$ . Due to these random fluctuations in the velocity of the nucleus, the observed velocity distribution of the emitted electron in the laboratory frame is given by the convolution

$$\tilde{\mathcal{G}}(\mathbf{v}) = \int du \mathcal{F}(\mathbf{u}) \mathcal{G}(\mathbf{v} + \mathbf{u}). \quad (6.2)$$

where  $\mathcal{G}(\mathbf{v})$  is the velocity distribution of an electron emitted by a free Tritium atom at rest corresponding to the energy distribution given by a Fermi Golden Rule (see FIG. 6.1). The formal applicability condition of Eq. (8.2) is that the spacing between the energy levels of the  ${}^3\text{He}^+$  ion emerging from  $\beta$ -decay be much less than the typical recoil energy  $\Delta\varepsilon \ll E_{\text{rec}}$ . This condition is readily satisfied for the recoil energy in vacuum  $E_{\text{rec}} = 3.38$  eV. We shall revisit this argument when we turn to the fully quantum picture.

In the following analysis we will restrict ourselves to the particular case of the Tritium atoms adsorbed on the graphene following the PTOLEMY

---

<sup>3</sup>Each of the peak corresponds to a separate mass eigenstate.

proposal. However the obtained results are also valid for more general bonding potentials (see the discussion at the end).

In the zero temperature limit, the function  $\mathcal{F}(\mathbf{u})$  appearing in Eq. (8.2) is encoded in the wave function of the stationary state of a Tritium atom in the potential of the interaction of the atom with graphene. Although such a potential has a rather complicated shape, as can be seen from multiple *ab initio* studies [216–219], the large mass of the nucleus justifies the use of the harmonic approximation near a local potential minimum

$$U = \frac{1}{2}\kappa_{i,j}r_i r_j + U_0$$

where  $r_i$  are the components of the atom's displacement vector and  $\kappa$  is the Hessian tensor. Then, it follows that  $\mathcal{F}(\mathbf{u})$  is a multivariate normal distribution

$$\mathcal{F}(\mathbf{u}) = \frac{1}{(2\pi)^{3/2}} \frac{1}{\sqrt{\det \Sigma}} \exp\left(-\frac{1}{2} \sum_{i,j=1}^3 u_i \Sigma_{i,j}^{-1} u_j\right). \quad (6.3)$$

with zero mean and a covariance matrix  $\Sigma = \hbar m^{3/2} \sqrt{\kappa}$ . To find the latter, we proceed to the analysis of the bonding potential near its minima.

An adsorbed Tritium atom is predicted to occupy a symmetric position with respect to the graphene lattice, characterised by a  $C_3$  point symmetry group. For this reason, the Hessian will generally have two distinct principal values, one corresponding to the axis orthogonal to graphene and one to the motion in the graphene plane yielding two different potential profiles.

According to the *ab initio* studies [216–219], the potential that bonds the Tritium atom in the perpendicular direction has two minima, a deep chemisorption minimum (in the range of 0.7 – 3 eV for different studies) about 1.5 Å away from the graphene plane, and a shallow (about 0.2 eV) physisorption minimum 3 Å away from graphene<sup>4</sup> (see FIG. 6.2).

The lateral motion of an atom is governed by the so-called migration potential [220]. The lateral stiffness in the case of chemisorption smaller than the vertical stiffness, however is substantial, as can be seen from Table 6.1. The case of a substrate producing a negligible migration potential will be discussed below.

Introducing the normal displacement  $z$  of an atom relative to the potential minimum, we can approximate the potential in the direction perpendicular to

---

<sup>4</sup>We note, that we use the results of *ab initio* calculations for hydrogenated graphene. This is appropriate because Hydrogen is chemically equivalent to Tritium

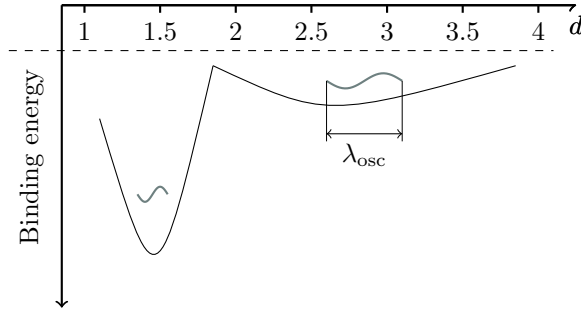


**Figure 6.2.** Schematic profile of the potential that bonds the Tritium atom in the direction perpendicular to the graphene.

the graphene as  $U(z) = \kappa z^2/2 + U_0$ . The uncertainty in the position of the nucleus is then characterised by the oscillator length  $\lambda^2 = \hbar/\sqrt{m_{\text{nucl}}\kappa}$ . The values of the constants  $\kappa$  and  $\lambda$  for different potential minima obtained from the fitting of the theoretical bonding profiles [216–219] are given in Table 6.1. The pronounced variability in the predicted values of the spring constant  $\kappa$  is explained by the diversity of approximations used in different *ab initio* schemes. Note, however that the variability in the predicted values of the oscillator length is much less significant as  $\lambda \sim \kappa^{-1/4}$ . For this reason one can crudely neglect the difference between the strength of the lateral and normal confinement and consider the function  $\mathcal{F}(\mathbf{u})$  as approximately isotropic

$$\mathcal{F}(\mathbf{u}) \approx \frac{1}{\sqrt{2\pi}\Delta u} \exp\left(-\frac{1}{2} \frac{u^2}{\Delta u^2}\right). \quad (6.4)$$

We also note that, according to the Table 6.1, the typical predicted oscillator length is about an order of magnitude less than the typical length of the bond, which provides a posterior justification for the harmonic approximation.

### 6.3 Estimate

We are now in a position to obtain an estimate for the uncertainty in the energy of an emitted electron. By virtue of Heisenberg uncertainty principle, the variance of the velocity of the nucleus near a local potential minimum is  $\Delta u \approx \hbar/m_{\text{nucl}}\lambda$ . For an electron emitted at speed  $v_{\text{el}}$  in the centre of mass frame the uncertainty of the energy measured in the laboratory frame is  $\Delta E \approx$

Potential	Source	$\kappa$ , [eV/Å <sup>2</sup> ]	$\lambda$ , [Å]	$\Delta E$ , [eV]
Chemisorption	[218]	2.15	0.16	0.60
	[216], GGA	4.62	0.13	0.73
	[216], vdW-DF	4.9	0.13	0.75
Physisorption	[219]	0.08	0.37	0.26
	[218]	0.09	0.34	0.28
	[216], GGA	0.18	0.29	0.33
	[216], vdW-DF	0.13	0.32	0.3
	[217], GGA	0.04	0.43	0.22
	[217], LDA	0.01	0.55	0.17
Migration	[220]	0.283	0.264	0.37

**Table 6.1. Harmonic fit** with the stiffness  $\kappa$  of the chemisorption, physisorption potentials and the migration potential of the chemisorbed atom profiles near the minimum.  $\lambda^2 = \hbar/\sqrt{m_{\text{nucl}}\kappa}$  and  $\Delta E$  is the energy broadening of the emitted electron estimated from Eq. (6.5).

$m_{\text{el}}v_{\text{el}}\Delta u$ , which near the edge of the electron emission spectrum can be written as

$$\Delta E \approx \frac{\hbar c}{\lambda_{\text{el}}}\gamma \quad (6.5)$$

where  $\lambda_{\text{el}}^2 \equiv \hbar/\sqrt{m_{\text{el}}\kappa}$  and we have introduced the dimensionless parameter

$$\gamma = \left[ \frac{Q^2 m_{\text{el}}}{m_{\text{nucl}}^3 c^4} \right]^{1/4}, \quad (6.6)$$

where  $Q$  is the amount of energy released during the  $\beta$  decay. Eqns. (6.5), (6.6) are the main result of this paper. This result, obtained so far using semi-classical considerations, can be cross-checked with a more precise quantum mechanical calculation. For the latter, one applies the Fermi Golden Rule to the  $\beta$ -decay process where the initial state is the ground state of the atom in the harmonic potential and the final state is a product of neutrino, electron and atomic wave-functions that are highly excited WKB states (see Appendix A for the detailed calculation). The result of such a calculation fully agrees with Eqns. (6.5), (6.6). It is worth noting that in the fully quantum picture the final  $\beta$ -spectrum in the  $C\nu B$  channel may be continuous, discrete or mixed, depending on the depth of the bonding potential, but the overall envelope

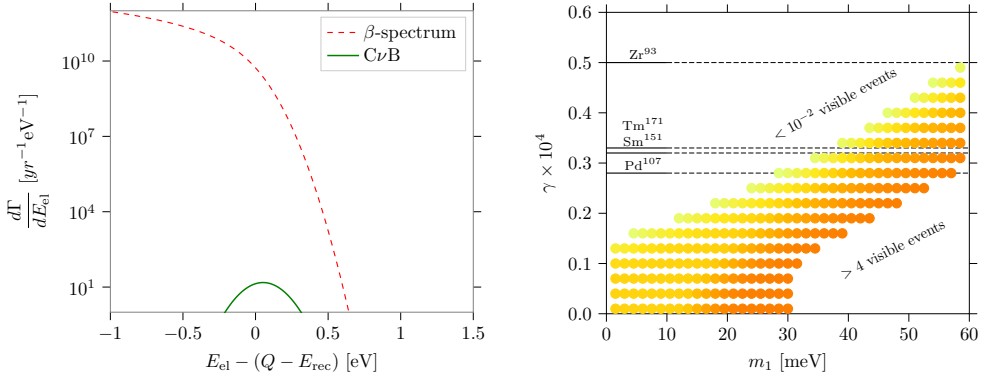


**Figure 6.3.** The estimate of the smearing of the electron emission spectrum due to the bonding of emitter to graphene. *Left panel:* The electron emission spectrum for the physisorbed atomic Tritium ( $\lambda_{\text{osc}} = 0.6 \text{ \AA}$ ) taking the hierarchy,  $m_1$  and energy resolution of the apparatus same as for the FIG. 6.1. *Right panel:* Visibility (defined by the number of  $C\nu B$  event that do not overlap with the continuous spectrum at all) of the  $C\nu B$  peak depending on the mass of the lightest neutrino  $m_1$  and a dimensionless parameter  $\gamma$  defined in Eq. (6.6) that characterizes the emitter (for the physisorbed Tritium  $\gamma \approx 3 \times 10^{-4}$ ). The white areas on the bottom right and top left are correspondingly the areas of full and zero visibility and the coloured region in between corresponds to the partial visibility.

will be Gaussian with the width  $\Delta E$ . This is in agreement with the previous results for the molecular Tritium [208]<sup>5</sup>.

## 6.4 Discussion

In this paper, we have investigated the feasibility of the solid state based approach to the long-standing problem of detection of relic neutrino background. We conclude that, due to the remarkable progress in the technology used for the measurement of electron emission spectrum (see e.g. [96]), the actual energy resolution of the experiment is now controlled by a different bottleneck - the uncertainties resulting from the interaction of the beta-emitter with the substrate. This paper addresses one type of such uncertainty considered – the zero-point motion of the  $\beta$ -emitter. For any given emitter it is practically ir-

<sup>5</sup>As an example, the value of the stiffness  $\kappa$  for the molecular tritium according to [208] is  $\kappa \approx 75 \text{ eV/\AA}^2$ . This is roughly 20 times as large as the corresponding value for the chemisorption (see Table 6.1). This means that the energy uncertainties  $\Delta E$  in these two cases are of the same order which is in agreement with [208].

reducible, which excludes certain emitters from the list of suitable candidates for solid state setups. In particular, for Tritium the uncertainty in the energy of the electrons is around  $0.3 - 0.7$  eV (see Table 6.1 for the different bonding potentials according to different *ab initio* calculations), *i.e.* several times greater than the required energy resolution.

We see from Eqns. (6.5), (6.6) that the defining factor for the energy uncertainty is the parameter  $\gamma$  (see Eq. 6.6), which only depends on the internal properties of a  $\beta$ -emitter such as the mass of the nucleus and the energy released in the decay process. Therefore, a promising route to achieve a better performance of the detector would be to substitute a widely used Tritium [85, 96, 207, 209, 211, 221] with a heavier emitter (while simultaneously satisfying other experimental constraints, e.g. sufficiently long half-life time). The effect of the parameter  $\gamma$  on the visibility of the  $C\nu B$  peak is shown on the right panel of FIG. 6.3. One can see that, e.g., Tritium which has  $\gamma \approx 3 \times 10^4$ , lies deep inside the region where the observation of the  $C\nu B$  peak is impossible. On the same figure we also indicate more suitable  $\beta$ -emitters whose energy uncertainties are not prohibitive for the detection of the relic neutrinos with the masses  $> 20$  meV.

Another important conclusion of our work is that although the energy uncertainty also depends on the bonding potential, this dependence only enters through the stiffness parameters and it is extremely weak  $\Delta E \propto \kappa^{1/4}$ . This implies that experimentation with different types of substrate is unlikely to make a substantial difference. Indeed, an order of magnitude improvement in  $\Delta E$ , (which is needed for the state of the art experimental proposal [96]) would require a four orders of magnitude reduction in the value of  $\kappa$ . Such a substantial deformation of the bonding potential presents a significant experimental challenge.

A certain improvement in terms of the bonding potential could still be achieved with adsorption that has a very weak lateral potential. One such example is physisorption of Tritium on graphene. In the limiting case of a constant lateral potential, electrons emitted at grazing angles will not have any additional uncertainty to their energy. Correspondingly, for the out-of-plane angles  $\theta < \theta_{\max} = \arcsin(\Delta E_{\max}/\Delta E)$  the energy uncertainty will be bounded by  $\Delta E_{\max}$ . Here  $\Delta E$  denotes the energy uncertainty for the isotropic case with finite mobility. Restricting the detection collection to  $\theta < \theta_{\max}$  reduces the number of events by a factor  $\eta^{-1} \approx \pi\theta_{\max}/90^\circ$ . As an example, for  $\Delta E_{\max} = 10$  meV one obtains  $\theta_{\max} \approx 3^\circ, \eta \approx 10$  which would entail the challenge of producing and handling 10 times as much radioactive material. This direction

requires a full in-depth analysis which we leave for future studies.

We conclude, that a careful selection of the  $\beta$ -emitter (Fig. 6.3) together with the use of an optimized substrate place  $C\nu B$  detection potentially within the reach of the detection technologies developed by the PTOLEMY collaboration.

One should, however, note that the zero-point motion of the emitter does not exhaust the list of mechanisms that introduce uncertainty and errors into the beta-decay spectrum. Other potentially harmful mechanisms include the electrostatic interaction of the ionized atom with the substrate, charge relaxation in graphene,  $X$ -ray edge singularity, and phonon emission. We therefore strongly believe that further progress towards  $C\nu B$  detection requires a serious concerted effort both theoretical and experimental in the characterization of the physics and chemistry of the interaction of the  $\beta$ -emitter with its solid state environment.

We are grateful to Chris Tully, A.P. Colijn and the whole PTOLEMY collaboration for fruitful discussions and feedback on the manuscript that allowed for its significant improvement. We also thank Kyrylo Bondarenko and Anastasiia Sokolenko for the useful discussion. YC is supported by the funding from the Netherlands Organization for Scientific Research (NWO/OCW) and from the European Research Council (ERC) under the European Union’s Horizon 2020 research and innovation programme. AB is supported by the European Research Council (ERC) Advanced Grant “NuBSM” (694896). VC is grateful to the Dutch Research Council (NWO) for partial support, grant No 680-91-130.

## 6.5 Appendix: Quantum derivation of the energy uncertainty

The aim of the fully quantum derivation is to underpin the semiclassical heuristic that was obtained in the main text as well as demonstrating its limitations. We note that we will not keep track of the pre-factors  $\hbar, c$  and will restore them in the end. The rate of  $\beta$ -emission of an electron is given by the Fermi Golden Rule rule

$$\frac{d\Gamma}{dE} = \sum_f 2\pi |\langle f | \hat{V} | i \rangle|^2 \delta(E_i - E_f) \delta(E - E_{f,\text{el}}). \quad (6.7)$$

Here the vector  $|i\rangle$  represents the initial state of the system having the energy  $E_i$ , the vector  $|f\rangle$ , represents a final eigenstate of the Hamiltonian having the

energy  $E_f = E_{f,\text{el}} + E_{f,\text{He}}$  where  $E_{f,\text{el}}$ , is the kinetic energy of the outgoing electron and  $E_{f,\text{He}}$ , is the energy of the  ${}^3\text{He}^+$  ion. The sum is performed over all such final states. The interaction potential  $\hat{V}$  is responsible for  $\beta$ -decay vertex and is for our purposes an ultralocal product of the creation and annihilation operators of the fields involved in the process.

We make an assumption that the neutrino has zero kinetic energy. It is equivalent to restricting ourselves to region near the edge of the spectrum, which is exactly the region of interest to us. The energy conservation implies

$$\frac{\vec{k}^2}{2m_{\text{el}}} + \frac{\vec{p}^2}{2m_{\text{nucl}}} = \tilde{Q}, \quad (6.8)$$

where  $\vec{k}$ ,  $\vec{p}$  - are two-dimensional final momenta of the electron and nucleus respectively.  $\tilde{Q}$  is the total energy of the nucleus before  $\beta$ -decay.

The initial state of the system is a product of a plane wave state of an incoming relic neutrino, which it is safe to describe as a plane wave with nearly zero momentum, and the lowest energy eigenstate of a Tritium atom in the local minimum of the bonding potential. As was discussed in the main text, such a state can be safely approximated as a ground state of a harmonic oscillator with two distinct principal stiffness eigenvalues (see table 6.1). The wave function of such a state has the form

$$\psi_i(\mathbf{r}) \propto \exp\left(-\frac{z^2}{2\lambda_{\perp}^2} - \frac{\varrho^2}{2\lambda_{\parallel}^2}\right), \quad (6.9)$$

where  $z$  stands for the orthogonal displacement and  $\varrho$  for the magnitude of the lateral displacement relative to the local potential minimum. Due to the in-plane symmetry of the graphene with respect to rotation, we can effectively restrict ourselves to a two-dimensional space  $z, \varrho$ .

The space of all possible final states  $|f\rangle$  is quite large, and their wave functions may be quite complicated due to the intricate interaction of the  ${}^3\text{He}^+$  ion with the graphene sheet. However, as we shall see momentarily the dominant contribution to the sum in (6.7) comes from the states which are amenable to the WKB approximation and are therefore analytically tractable. Introducing the notation  $\psi_f(\mathbf{r})$  for the final state of the  ${}^3\text{He}^+$  ion, we write the matrix element in (6.7) as

$$\langle f | \hat{V} | i \rangle \sim \int d\mathbf{r} \psi_f^*(\mathbf{r}) \psi_i(\mathbf{r}) e^{-i\mathbf{k}\mathbf{r}} \quad (6.10)$$

where  $\mathbf{k}$  is the wave vector of the emitted electron at kinetic energy close to  $Q$ . Since the electron's wave vector is quite large  $k \sim 10^2 \text{ \AA}^{-1}$  the rapid oscillations

suppress the integral in Eq. (6.10) unless the state  $\psi_f(\mathbf{r})$  also contains an oscillatory factor, which has a roughly opposite De Broglie wave vector near  $\mathbf{r} = 0$ , where the support of  $\psi_i(\mathbf{r})$  is concentrated. This implies that the kinetic energy of the ion needs to be on the order of 3eV, which exceeds the predicted chemisorption binding energy [216–219] and is orders of magnitude greater than the vibrational quantum near the potential minimum ( $\hbar\omega \sim 0.01$  eV). Such highly excited states are generally characterised by a level spacing which is much narrower than the vibrational quantum near the minimum. They are also well described by semiclassical WKB wave functions, which on the scale of the oscillator length are indistinguishable from a plane wave.

With these considerations in mind, the application of the Fermi Golden Rule to such states gives

$$\frac{d\Gamma}{dE} \propto \left| \int_{-\infty}^{\infty} dx \int_{-\infty}^{\infty} dy \int_{-\infty}^{\infty} dz e^{-i(k_x+p_x)x - i(k_y+p_y)y - i(k_z+p_z)z - \frac{x^2}{2\lambda_{\parallel}^2} - \frac{y^2}{2\lambda_{\parallel}^2} - \frac{z^2}{2\lambda_{\perp}^2}} \right|^2, \quad (6.11)$$

where we have extended the integration over  $z$  to  $-\infty$ . One can do it since the integrand is localized.  $k/p_{x,y,z}$ , are respectively the components of the electron and nucleus momenta that satisfy the energy conservation law

$$\begin{aligned} |p| &= \sqrt{2m_{\text{nucl}}(\tilde{Q} - E_{\text{el}})} \\ |k| &= \sqrt{2m_{\text{el}}E_{\text{el}}} \end{aligned} \quad (6.12)$$

We re-scale coordinates  $\tilde{r}_i = \frac{r_i}{\sqrt{2}\lambda_i}$  and obtain

$$\frac{d\Gamma}{dE} \propto \left| \int_{-\infty}^{\infty} d\tilde{x} \int_{-\infty}^{\infty} d\tilde{y} \int_{-\infty}^{\infty} d\tilde{z} e^{-i\sqrt{2}\lambda_{\parallel}(k_x+p_x)\tilde{x} - i\sqrt{2}\lambda_{\parallel}(k_y+p_y)\tilde{y} - i\sqrt{2}\lambda_{\perp}(k_z+p_z)\tilde{z} - \tilde{x}^2 - \tilde{y}^2 - \tilde{z}^2} \right|^2, \quad (6.13)$$

that can be brought to a Gauss integral

$$\begin{aligned} \frac{d\Gamma}{dE} &\propto e^{-\lambda_{\perp}^2(k_{\perp}+p_{\perp})^2 - \lambda_{\parallel}^2(k_{\parallel}+p_{\parallel})^2} \left| \int_{-\infty}^{\infty} d\tilde{x} \int_{-\infty}^{\infty} d\tilde{y} \int_{-\infty}^{\infty} d\tilde{z} \right. \\ &\quad \left. \exp\left(-\left(\tilde{x} + \frac{i\lambda_{\parallel}(k_x+p_x)}{\sqrt{2}}\right)^2 - \left(\tilde{y} + \frac{i\lambda_{\parallel}(k_y+p_y)}{\sqrt{2}}\right)^2 - \left(\tilde{z} + \frac{i\lambda_{\perp}(k_z+p_z)}{\sqrt{2}}\right)^2\right) \right|^2, \end{aligned} \quad (6.14)$$

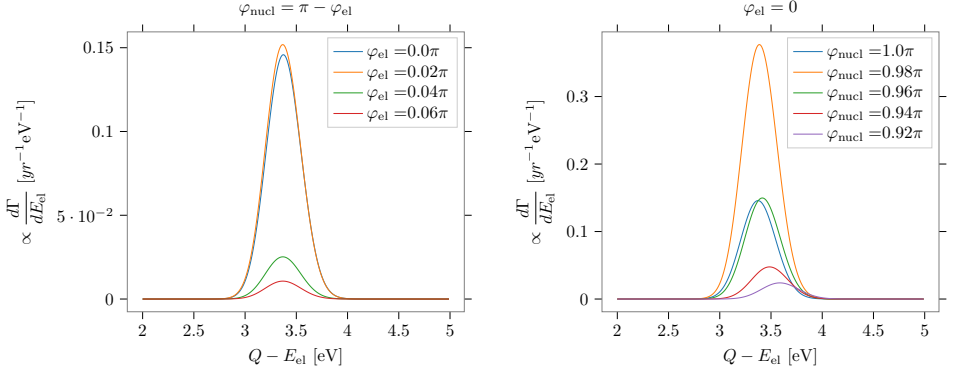


**Figure 6.4.** Distribution function (not normalized) of the energy of the electron near the edge of the spectrum. Electron and nucleus are emitted with the corresponding angles  $\varphi_{e/\text{nucl}}$  (relative to the axes perpendicular to the graphene substrate).

where  $k_{\parallel}/p_{\parallel}^2 = k_x/p_x^2 + k_y/p_y^2$ ,  $p_{\perp}/p_{\perp} = k_z/p_z$ . Integrating Eq. 6.14 gives the Gaussian distribution

$$\frac{d\Gamma}{dE} \propto e^{-\lambda_{\perp}^2(k_{\perp}+p_{\perp})^2 - \lambda_{\parallel}^2(k_{\parallel}+p_{\parallel})^2}. \quad (6.15)$$

The distribution Eq. (6.15) depends on the angles of the emitted nucleus and electron  $\varphi_{1,2}$ . These angles are taken relative to the axes perpendicular to the graphene substrate.

$$\frac{d\Gamma}{dE} \propto e^{-\lambda_{\perp}^2(|k| \cos \varphi_2 + |p| \cos \varphi_1)^2 - \lambda_{\parallel}^2(|k| \sin \varphi_2 + |p| \sin \varphi_1)^2}, \quad (6.16)$$

Let us estimate the variance of this distribution for the normal emission of the electron

$$\frac{d\Gamma}{dE} \propto e^{-\lambda^2(k-p)^2}, \quad (6.17)$$

where  $k = \sqrt{2m_{\text{el}}E_{\text{el}}}$ ,  $p = \sqrt{2m_{\text{nucl}}(\tilde{Q} - E_{\text{el}})}$ .

In order to obtain the variance, we need to expand near the maximum of the distribution that corresponds to its mean. If we write everything in terms of the deviation from the mean energy of the electron  $\delta E_{\text{el}} = \tilde{Q} - E_{\text{rec}} - E_{\text{el}}$

$$\begin{aligned} k &= \sqrt{2m_{\text{el}}(\tilde{Q} - E_{\text{rec}} - \delta E_{\text{el}})} \approx \sqrt{2m_{\text{el}}(\tilde{Q} - E_{\text{rec}})} \left(1 - \frac{\delta E_{\text{el}}}{2(\tilde{Q} - E_{\text{rec}})}\right) \\ p &= \sqrt{2m_{\text{nucl}}(E_{\text{rec}} + \delta E_{\text{el}})} \approx \sqrt{2m_{\text{nucl}}E_{\text{rec}}} \left(1 + \frac{\delta E_{\text{el}}}{2E_{\text{rec}}}\right). \end{aligned} \quad (6.18)$$

Accounting to the fact that  $E_{\text{rec}} \approx \frac{m_{\text{el}}}{m_{\text{nucl}}} \tilde{Q}$ ,

$$\begin{aligned} k &\approx \sqrt{2m_{\text{el}}\tilde{Q}} \left(1 - \frac{\delta E_{\text{el}}}{2\tilde{Q}}\right) \\ p &\approx \sqrt{2m_{\text{el}}\tilde{Q}} \left(1 + \frac{m_{\text{nucl}}}{m_{\text{el}}} \frac{\delta E_{\text{el}}}{2\tilde{Q}}\right). \end{aligned} \quad (6.19)$$

With this we obtain Gaussian distribution

$$\frac{d\Gamma}{dE} \propto \exp\left(-\frac{\lambda^2 m_{\text{nucl}}^2}{2m_{\text{el}}\tilde{Q}} \delta E_{\text{el}}^2\right),$$

with the variance with the restored units is

$$\sigma = \frac{\hbar}{\lambda} \frac{\sqrt{\tilde{Q}m_{\text{el}}}}{m_{\text{nucl}}}. \quad (6.20)$$

# Chapter 7

## Can we use heavy nuclei to detect relic neutrinos?

### 7.1 Introduction

The ambitious goal of detection [83] and the measurement of the mass [222] of the relic neutrino relies on the precise experimental knowledge of the  $\beta$ -spectrum of radioactive elements [84, 85]. Relic neutrinos, which fill the totality of space in the form of an almost ideal gas of temperature  $T_\nu \approx 1.95$  K, are expected to manifest themselves in rare neutrino capture events. Such events involving cosmic neutrinos of mass  $m_\nu$  and a sample of radioactive atoms characterized by the  $\beta$ -decay energy  $Q$  would produce an extremely faint peak at the energy  $Q + m_\nu c^2$  in the  $\beta$ -spectrum of the sample. We recall that for all radioactive elements the overwhelming bulk of the  $\beta$ -spectrum arises from spontaneous  $\beta$ -decay and forms a continuum with the upper cutoff energy  $Q - m_\nu^0 c^2$  where  $m_\nu^0$  is the mass of the lightest neutrino. For this reason one expects the neutrino capture peak to be separated from the end of the spontaneous  $\beta$ -spectrum by an energy gap of at least one neutrino mass and for that reason to be discernible at least in principle.

Despite the simplicity of its theoretical premise, a neutrino capture experiment establishing the existence of relic neutrinos has not yet materialized. The reason for this is the weakness of the neutrino-matter interaction, which makes it difficult to achieve the sufficient number of capture events in a reasonably sized radioactive sample. The requirement of a large neutrino capture cross-section combined with other important considerations such as the manageable half-life time and the stability of the daughter isotope turn out to be so

restrictive that only a handful of atoms can be viewed as viable candidates for the  $C\nu B$  detection experiment. From this perspective, Tritium has long been regarded as the best candidate  $\beta$ -emitter [85–87, 223–227], even though it was found that the workable sample of gaseous molecular Tritium falls short of the required activity levels by six orders of magnitude. Currently, the only viable alternative to the gas phase experiment is a solid state based architecture where the atomic tritium is adsorbed on a substrate [85].

The low event rate is not the only hindrance in the way of relic neutrino detection. The upper bounds on the neutrino mass [228] show that the energy gap between the signal from neutrino capture and the background is extremely small  $m_\nu/Q \ll 1$  therefore the detection of the  $C\nu B$  requires extraordinary energy resolution. It has been demonstrated that the electromagnetic guidance system and the calorimetry module of the detection apparatus can be built to such stringent specifications [85], however, as it was found recently [91], deposition of  $\beta$ -emitters on a solid-state substrate produces a new fundamental limitation on the experimental resolution originating in the zero-point motion of the emitter's centre of mass. For Tritium on solid surfaces, the best theoretical resolution is  $\Delta E \sim 0.5$  eV which is an order of magnitude worse than what is required in order to see the relic neutrino peak. Furthermore, it was shown [91] that the main factor that determines it is the ratio of the  $\beta$ -decay energy  $Q$  to the mass of the emitter nucleus  $m_{\text{nucl}}$ , namely  $\gamma = \sqrt{Q^2 m_e / m_{\text{nucl}}^3}$ . This finding opens a new avenue to search for a possible alternative for Tritium that would have both a sufficient event rate and low enough energy uncertainty. In the same work [91], it was found that the two promising candidates that have low enough  $\gamma$ -values are Thulium ( $^{171}\text{Tm}$ ) and Samarium ( $^{151}\text{Sm}$ ) with  $\gamma_{3\text{H}}/\gamma_{171\text{Tm}} = 0.11$  and  $\gamma_{3\text{H}}/\gamma_{151\text{Sm}} = 0.1$  respectively. This means that the intrinsic energy uncertainty for these isotopes is an order of magnitude smaller than that of Tritium. This value approaches the upper bound for the neutrino mass and therefore could, in principle, provide sufficient energy resolution for its detection.

The  $\gamma$ -value introduced in the previous paragraph is defined in terms of the simple intrinsic characteristics of a nucleus such as its mass and  $Q$ -value and therefore is straightforward to calculate. In contrast, the neutrino capture cross-section has not been calculated for every isotope, in particular it is not known for either of the isotopes of interest,  $^{171}\text{Tm}$  and  $^{151}\text{Sm}$ . The reason for this is twofold. Firstly, the theory of  $\beta$ -decay of certain nuclei (the ones that undergo the so-called *non-unique forbidden transitions*) is complicated [229–231] and does not provide a direct link between the observed half-life time and

the predicted neutrino capture rate. Secondly, experimental  $\beta$ -spectra are not normally known with the energy resolution sufficient for a direct inference of the capture cross section. The goal of the present paper is to show how the neutrino capture cross section of a given radioactive isotope decaying through non-unique forbidden transitions can be estimated from the experimentally accessible  $\beta$ -spectrum of that isotope.

## 7.2 Quantum mechanics of $\beta$ -interaction and crude estimate of neutrino capture

Neutrino capture and  $\beta$  decay are the same process driven by the weak interaction; they differ only in whether the (anti)neutrino is in the initial or final state. To establish the exact connection between their respective rates, we start from briefly reminding the main concepts of  $\beta$  decay theory. We consider the sibling processes of  $\beta$ -decay and neutrino capture by a generic nucleus

$$\begin{aligned} (A, Z) &\rightarrow (A, Z + 1) + e^- + \bar{\nu}_e \\ \nu_e + (A, Z) &\rightarrow (A, Z + 1) + e^-. \end{aligned} \quad (7.1)$$

which are driven by the same weak  $\beta$ -decay Hamiltonian

$$\mathcal{H}^\beta = \frac{G_\beta}{\sqrt{2}} \bar{\psi}_e \gamma^\mu (1 - \gamma_5) \psi_\nu \bar{p} \gamma_\mu (g_V + g_A \gamma_5) n + \text{h.c.}, \quad (7.2)$$

where  $G_\beta = G_F \cos \theta_C$  and  $\theta_C$  is Cabbibo angle,  $\psi_e$ ,  $\psi_\nu$  are electron and neutrino fields and  $p$ ,  $n$  being the proton and neutron fields respectively. The vector  $g_V$  and axial  $g_A$  coupling constants are renormalized by strong interactions with  $|g_A/g_V| \approx 1.27$  [232, 233].

The differential  $\beta$ -decay rate  $d\Gamma_\beta$  and the capture cross-section for spin-averaged neutrino are given by the Fermi Golden Rule and can be written as<sup>1</sup>:

$$\begin{aligned} d\Gamma_\beta &= \frac{1}{2\pi^3} \times p_\nu E_\nu p_e E_e dE_e \times W_\beta(p_e, p_\nu) \\ (\sigma v)_\nu &= \lim_{p_\nu \rightarrow 0} \frac{1}{\pi} \times p_e E_e \times W_\nu(p_e, p_\nu), \end{aligned} \quad (7.3)$$

---

<sup>1</sup>Here we use the fact that absorption of antineutrino with momentum  $p_\nu$  is equivalent to emission of neutrino with momentum  $-p_\nu$

where  $p_{e(\nu)}$  and  $E_{e(\nu)}$  are the momenta and energies of the leptons,  $W_\beta(p_e, p_\nu)$  is the average transition rate for the decay of an atom into two lepton plane waves with momenta  $p_e, p_\nu$ , and  $W_\nu(p_e, p_\nu)$  is the average transition rate for the capture of a neutrino having the momentum  $p_\nu$  and the emission of an electron with momentum  $p_e$ .

The average transition rates are expressed in terms of transition amplitudes by

$$W_{\beta,\nu}(p_e, p_\nu) = \int \frac{d\Omega_e}{4\pi} \int \frac{d\Omega_\nu}{4\pi} \sum |\mathcal{M}_{\text{if}}^{\beta,\nu}(\mathbf{p}_e, \mathbf{p}_\nu)|^2. \quad (7.4)$$

Here  $\mathcal{M}_{\text{if}}$  is the quantum transition amplitude between the initial and the final state induced by the reduced weak interaction Hamiltonian [230, 231, 234]

$$\mathcal{M}_{\text{if}} = \frac{G_\beta}{\sqrt{2}} \int \bar{\psi}_e(\mathbf{r}) \gamma^\mu (1 - \gamma_5) \psi_\nu(\mathbf{r}) \times J_{\text{nuclear}}^\mu(\mathbf{r}) d\mathbf{r}, \quad (7.5)$$

which encapsulates all information about the changes in the internal nuclear structure in a function  $J_{\text{nuclear}}^\mu(\mathbf{r})$ . This function cannot be calculated from first principles, however its transformation properties under the symmetry group of space are known for each transition. The summation symbol in Eq. (7.4) is a shorthand for the sum over the spin quantum numbers of the out-states as well as averaging over the spins of the in-states. The averaging over the directions of  $\mathbf{p}_e$  and  $\mathbf{p}_\nu$  is shown explicitly. Two important remarks are in order

- 1 For an overwhelming part of the  $\beta$ -spectrum one can consider the neutrino as a massless (Weyl) particle in both the energy conservation law and the wave functions entering the transition amplitudes. There exists a tiny energy window on the order of  $m_\nu$  near the high-energy end of the  $\beta$ -spectrum where the neutrino mass plays a role, however the resolution required for the observation of the  $\beta$ -spectrum inside that window is by far beyond the reach of the existing experimental technique. Since the existing  $\beta$ -decay experiment cannot distinguish between the massive and massless cases, *we shall throughout this note discuss the function  $W_\beta(p_e, p_\nu)$  assuming the  $m_\nu \rightarrow 0$  limit.*
- 2 Our main focus is on neutrino capture processes involving the cosmic neutrino background. For such neutrinos  $p_\nu \ll m_\nu$ , which is the opposite of the ultra-relativistic limit discussed in item 1. It is straightforward to see that for a left-handed particle with a Majorana mass term,

$$W_\nu(p_e, 0) = \frac{1}{2} \lim_{p_\nu \rightarrow 0} W_\beta(p_e, p_\nu) \quad (7.6)$$

Indeed, in the  $p_\nu \rightarrow 0$  limit the incoming massive neutrino is a superposition of a left-handed Weyl particle and a right-handed Weyl anti-particle  $|\text{Majorana}\rangle = (|\nu\rangle + |\bar{\nu}\rangle)/\sqrt{2}$ . In a process where an electron is created, the operator (7.5) only picks one term of the two, hence the corresponding transition rate is one half of the transition rate  $W_\beta$  of a Weyl neutrino.

### 7.2.1 Crude estimate of neutrino capture

In this subsection, we want to provide a simple order-of-magnitude estimate for neutrino capture cross-section. To this end, we assume that the matrix element has no dependence on the lepton energy and reduces to a constant encoding the information about the initial and final nuclear states

$$\sum |\mathcal{M}_{\text{if}}^\beta(p_e, p_\nu)|^2 = \text{const.} \quad (7.7)$$

Such an approximation neglects the Coulomb interaction between the emitted electron and the nucleus. It also assumes that the selection rules admit for the existence of the emission channel with the total angular momentum of leptons  $J = 0$ .

Assuming Eq. (7.7) to be true, all the structural information about the nuclei gets absorbed into a constant numerical factor, therefore the ratio of the  $\beta$  decay and the neutrino capture rates, Eqns. (7.3), is completely determined by the phase volume factors  $p_\nu^2 p_e E_e$  and  $p_e E_e$  accordingly. Using Eq. (7.6), this gives rise to the following relationship between the capture cross-section  $(\sigma v)_\nu$ , the total lifetime  $\tau = (\int d\Gamma_\beta)^{-1}$  of a  $\beta$ -decaying isotope, and the total kinetic energy  $Q$  released in the reaction:

$$(\sigma v)_\nu = \tau^{-1} \frac{(2\pi)^{-1} p_e E_e}{(2\pi^3)^{-1} \int_{m_e}^{m_e+Q} E'_e p'_e (Q - T'_e)^2 dE'_e}, \quad (7.8)$$

with  $T_e = E_e - m_e$  being the kinetic energy of the electron, and neutrino momentum in  $\beta$  decay is  $p_\nu = Q - T_e$ . In the particular case of nonrelativistic electron  $Q \ll m_e$ , this relation gives the following simple scaling:

$$(\sigma v)_{\text{est.}} = 5.3 \cdot 10^{-46} \text{ cm}^2 \times \frac{1 \text{ year}}{\tau} \times \left( \frac{100 \text{ keV}}{Q} \right)^3. \quad (7.9)$$

In order to quantify the error introduced by the simplifying assumptions leading up to Eq. (7.7), we introduce a correction factor  $\delta$  such that the actual cross-section is given by

$$(\sigma v)_\nu = \delta \times (\sigma v)_{\text{est.}} \quad (7.10)$$

The values of  $\delta$  for a number of elements where the exact results for the neutrino capture cross-section are known [86] are given in Fig. 7.1. One can see that in all those cases  $\delta$  is reasonably close to unity.

Isotope	$Q$ , keV	$\tau$ , year	$(\sigma v)_\nu$ , $10^{-46}$ cm <sup>2</sup>	$\delta$
<sup>3</sup> H	18.591	17.8	39.2	0.86
<sup>63</sup> Ni	66.945	145	$6.9 \cdot 10^{-2}$	0.57
<sup>93</sup> Zr	60.63	$2.27 \cdot 10^6$	$1.20 \cdot 10^{-5}$	1.15
<sup>106</sup> Ru	39.4	1.48	29.4	0.51
<sup>107</sup> Pd	33	$9.38 \cdot 10^6$	$1.29 \cdot 10^{-5}$	0.83
<sup>187</sup> Re	2.646	$6.28 \cdot 10^{10}$	$2.16 \cdot 10^{-6}$	0.48

**Table 7.1.** Neutrino capture cross-sections for different isotopes from [86]. Note that  $(\sigma v)_\nu$  differ from those of [86] by two due to neutrino spin averaging, as pointed out in [227]. One can see that the parameter  $\delta$  defined by Eq. (7.10) varies only by a factor of two from the identity that signals that Eq. (7.9) gives a good approximation for the capture rates of the given isotopes.

We are interested in neutrino capture by possible candidates for solid-state based  $C\nu B$  detection experiments — <sup>171</sup>Tm and <sup>151</sup>Sm. For these isotopes, the parameterization (7.10) reads

$$\begin{aligned}
 (\sigma v)_{171\text{Tm}} &= 2.1 \cdot 10^{-46} \text{ cm}^2 \times \delta_{171\text{Tm}} \approx 0.054 (\sigma v)_{3\text{H}} \times \delta_{171\text{Tm}} \\
 (\sigma v)_{151\text{Sm}} &= 9.1 \cdot 10^{-48} \text{ cm}^2 \times \delta_{151\text{Sm}} \approx 0.0023 (\sigma v)_{3\text{H}} \times \delta_{151\text{Sm}}. \quad (7.11)
 \end{aligned}$$

However, unlike the isotopes listed in Table 7.1, the theoretical values of the  $\delta$  factors for <sup>171</sup>Tm and <sup>151</sup>Sm are not known. This is because both isotopes have a rather peculiar structure of the matrix element (7.5), as explained in the following paragraph.

For purely illustrative purposes we neglect the effect of the Coulomb attraction between the  $\beta$ -electron and the daughter nucleus, bearing in mind that in practice such an approximation may result in significant inaccuracy. We recall that the function  $J_{\text{nuclear}}^\mu(\mathbf{r})$  is mainly localized inside the nucleus  $r < R$ , and decays rapidly with increasing  $r$  for  $r > R$ . Here  $R = A^{1/3} \times 1.2 \times 10^{-13}$  cm is the radius of the nucleus. Since the typical lepton momentum is on the order  $1 \text{ MeV} \ll R^{-1}$ , one can expand the matrix elements and the sum  $\sum |\mathcal{M}_{\text{if}}|^2$  as a series in small parameters  $p_{e/\nu} R \ll 1^2$

<sup>2</sup>If Coulomb attraction is taken into account, the constants in this expansion get multiplied by correction factors  $F_i(p_e)$ , which do not depend on unknown nuclear physics and can be computed explicitly.

$$\sum |\mathcal{M}_{\text{if}}|^2 = c_0 + c_1 \cdot p_e R + c_2 \cdot p_\nu R + \dots \quad (7.12)$$

The constants  $c_i$  in this expression are in essence combinations of the spherical multipole moments of  $J_{\text{nuclear}}^\mu(\mathbf{r})$  containing structural information about the many-body wave functions of the parent and daughter nuclei. The simplifying approximation (7.7) amounts to keeping only the leading-order term  $c_0$  in the expansion (7.12), which in many cases is well justified. For some isotopes, however, electroweak selection rules demand that  $c_0 = 0$ . Indeed, if the mother and daughter isotopes have different spin and parity then at least one of the leptons is required to carry a non-vanishing orbital angular momentum. Since a lepton's wave function corresponding to the orbital angular momentum  $l$  has the asymptotic form  $(pr)^l$  at small  $r$ , the matrix element of such a transition, Eq. (7.5), will necessarily contain terms proportional to  $(p_e R)^l (p_\nu R)^{l'}$  with  $l + l' > 0$ . The worst case scenario, known as a *forbidden non-unique transition*, is when the selection rules admit for the presence of several commensurate leading-order terms on the right hand side of the asymptotic expansion Eq. (7.12). For such a transition one has to assume that the matrix element (7.12) contains several unknown constants  $c_i$  each multiplying its own unique function of energy. If that happens, the cancellation of the unknown constants, such as the one seen in Eq. (7.8), does not occur and the neutrino capture cross-section cannot be inferred from the isotope's life time. This is precisely what happens for  $^{171}\text{Tm}$  and  $^{151}\text{Sm}$ . We conclude, that for the isotopes of our interest,  $^{171}\text{Tm}$  and  $^{151}\text{Sm}$ , the values of the  $\delta$  factors, Eq. (7.11), are beyond the reach of pure theory, which naturally brings us to the next section.

### 7.3 Experimental determination of the neutrino capture rate from the end of the $\beta$ decay spectrum

We have established that for isotopes such as  $^{171}\text{Tm}$  and  $^{151}\text{Sm}$  the knowledge of the lifetime and the  $Q$ -value is insufficient in order to predict the neutrino capture cross-section. Here, we discuss how the required cross-section can be inferred directly from the experimentally measured  $\beta$ -spectrum. Our approach is based on two key observations. Firstly, both the emission and capture processes are governed by the same unknown structure function  $W_\beta(p_e, p_\nu)$ , albeit taken at different values of arguments. Specifically, a capture process corresponds to the limit  $p_\nu \rightarrow 0$  and  $p_e = \sqrt{(Q + m_e)^2 - m_e^2}$ , whilst in a

spontaneous  $\beta$ -decay process  $p_e = \sqrt{(Q + m_e - p_\nu)^2 - m_e^2}$ , where  $p_\nu$  can take any value between 0 and  $Q$ , resulting in a broad  $\beta$ -spectrum. Secondly, the function  $W_\beta(p_e, p_\nu)$  is an analytic function of both arguments near the endpoint  $p_\nu = 0$  of the  $\beta$ -spectrum [93]. We recall that in our discussion  $W_\beta(p_e, p_\nu)$  is the rate involving transitions with massless neutrino states (see discussion at the end of section 7.2).

Using the analyticity of  $W_\beta(p_e, p_\nu)$  and making use of equations (7.3) and (7.6) we write the following expansion<sup>3</sup> for the observable  $\beta$ -spectrum near the edge  $p_\nu = 0$

$$\frac{\pi^2}{p_\nu^2} \frac{d\Gamma_\beta}{dE_e} = (\sigma v)_\nu \times \left[ 1 + \alpha_1 p_\nu / Q + O(p_\nu^2 / Q^2) \right] \quad (7.13)$$

where  $\alpha_1$  is a constant. The characteristic energy scale where the linear approximation is applicable can be estimated from the microscopic theory of  $\beta$  decay [93]. For the purposes of the present work, we notice that the physics of  $\beta$  decay of heavy nuclei involves three important energy scales, that is  $Q$ ,  $m_e$ , and  $1/R_0$  where  $R_0$  is the radius of the nucleus. The smallest of the three defines the energy range where the expansion (7.13) works well. For  $^{171}\text{Tm}$  and  $^{151}\text{Sm}$  the smallest energy scale is  $Q$ .

Now we are in position to discuss the experimental procedure. We assume a finite energy resolution  $\Delta E$  of the experiment (say, 1 keV). We propose a way to deduce the neutrino capture rate of the  $^{171}\text{Tm}$  and  $^{151}\text{Sm}$  from the end of their experimentally measured  $\beta$  spectra:

1. Define some experimentally accessible energy resolution  $\Delta E \ll Q$  and measure the number of  $\beta$  decay events  $N$  in several energy bins<sup>4</sup>  $T_e \in [Q - (n+1)\Delta E, Q - n\Delta E]$  as a function of the electron energy residue  $\varepsilon_n = \Delta E(n + 1/2)$
2. We assume that all the decay events are detected. In this case, one can check whether the experimental points  $N(\varepsilon_n) \times (\varepsilon_n \text{ in keV})^{-2}$  fit the linear curve. If so, continue the obtained fit up till the value  $\varepsilon_n = 0$ .

<sup>3</sup>Such a linear behaviour can be seen in the spectra generated by the BetaShape software, which predicts  $(\sigma v)_\nu = 1.2 \cdot 10^{-46} \text{ cm}^2 (^{171}\text{Tm})$ ,  $4.8 \cdot 10^{-48} \text{ cm}^2 (^{151}\text{Sm})$  and  $\alpha_1 = 0.25 (^{171}\text{Tm})$ ,  $0.21 (^{151}\text{Sm})$ . For further discussion see Sec. 7.4 and our accompanying paper [93].

<sup>4</sup>We note that the spectrum itself behaves as  $d\Gamma/dE_e \sim p_\nu^2$  and, therefore, events within a single bin are not uniformly distributed. Most of the events occur near the left side of a bin, which may introduce an additional systematic uncertainty. A possible way to avoid this problem and is to measure the integral number of events  $N(p_\nu) = \int_{Q-p_\nu}^Q \frac{dN}{dT_e} dT_e$  and consider the function  $N(p_\nu) \cdot p_\nu^{-3}$ . This can be also fitted by a linear function and therefore used to extract  $(\sigma v)_\nu$ . In addition, this method allows to collect more statistics compared to the one with bins for sufficiently large  $p_\nu$ .

3. Assuming that the time of the measurement is  $T_m \ll \tau$  and there are  $N_{\text{at}}$  decaying atoms, the neutrino capture rate can be estimated as

$$(\sigma v)_\nu = \frac{7.0 \cdot 10^{-37} \text{ cm}^2}{(T_m \text{ in hours})(\Delta E \text{ in keV})} \times \frac{1}{N_{\text{at}}} \left( \frac{N(\varepsilon_n)}{(\varepsilon_n \text{ in keV})^2} \right) \Big|_{\varepsilon_n=0} \quad (7.14)$$

A remark should be made concerning the generality of (7.14). Until now we neglected possible contributions to the electron spectrum due to  $\beta$ -decay into excited states of daughter nuclear or/and electronic shell of the atom. Let us comment on these contributions:

1. Excited nuclear states have typical energies  $E_{\text{ex}} \sim 10 \text{ keV}$ , for instance, 66.7 keV for  $^{171}\text{Yb}$  [235] (daughter isotope for  $^{171}\text{Tm}$ ) and 21.5 keV of  $^{151}\text{Eu}$  [236] (daughter isotope of  $^{151}\text{Sm}$ ). They do not contribute to the spectrum near the endpoint for  $T_e > Q - E_{\text{ex}}$ . Therefore, they are not relevant for the energy resolution of order 1 keV.
2. Atomic excitations are of order 1 eV. If the energy resolution is much above this scale, Eq. (7.14) overestimates the value of cross-section. For  $Z \sim 60$ , the probability to excite the electronic configuration is expected to be less than 30% [237], which translates into the same possible error in the value of the cross-section.

The corrections discussed above may only introduce a difference by a prefactor of order one are therefore beyond our considerations.

## 7.4 Conclusion and discussion

The most promising route towards the relic neutrino detection is currently through the use of solid state based detectors where the  $\beta$  emitters are adsorbed on a substrate. Such a design has the potential to achieve sufficient density of emitters in a controllable way (such that electron scattering remains suppressed), and hence get a sufficient number of capture events. However, any  $\beta$  decay experiment that uses bound emitters (either in molecular form or adsorbed on a substrate) suffers from an irreducible intrinsic energy uncertainty due to the emitter's zero-point motion. It was shown in [91] that such an uncertainty is proportional to the dimensionless parameter  $\gamma = \sqrt{Q^2 m_e / m_{\text{nucl}}^3}$ ,  $Q$  being the energy released in the  $\beta$  decay,  $m_e, m_{\text{nucl}}$  - masses of the electron and nucleus respectively. It was also shown that this parameter is too large for

$^3\text{H}$ , therefore Tritium-based detectors are unable to achieve the required energy resolution. Instead, the most promising candidates are  $^{171}\text{Tm}$  and  $^{151}\text{Sm}$  as they have the intrinsic energy uncertainty that is an order of magnitude lower than that of  $^3\text{H}$ .

However, contrary to the case of  $^3\text{H}$  for which the neutrino cross section is known [86, 87], theoretical calculation of  $(\sigma v)_\nu$  for  $^{171}\text{Tm}$  and  $^{151}\text{Sm}$  poses a challenge. The quantum numbers (spin and parity) of the parent and daughter nuclei for these isotopes differ, hence the leptons are required to have a non-zero total orbital momentum. The latter can be composed in a non-unique way, which results in several different unknown nuclear constants entering the matrix element (7.5) that do not factor out.

We propose a way to estimate the relic neutrino capture cross section. Our proposal relies on the experimental measurement of the spectrum of  $\beta$ -decay near the endpoint. We show, that the extraction of the relic neutrino cross section can be achieved using the experimental data (via Eq. (7.14)) even if the energy resolution  $\Delta E$  of the experiment that is much larger than neutrino mass  $\Delta E \gg m_\nu$ .

Finally, to get a rough idea of the feasibility of the relic neutrino capture experiment based on  $^{171}\text{Tm}$  ( $Q = 96.5 \text{ keV}$ ,  $\tau = 2.77 \text{ years}$ ) or  $^{151}\text{Sm}$  ( $Q = 76.6 \text{ keV}$ ,  $\tau = 130 \text{ years}$ ), we estimate the corresponding cross sections using the  $\beta$ -decay spectra computed in BetaShape [238, 239]. For  $^{171}\text{Tm}$  and  $^{151}\text{Sm}$ , this code uses the so-called  $\xi$ -approximation, whose validity has to be established on the case to case basis.

BetaShape predicts the following neutrino capture rates  $\Gamma_\nu = \eta_\nu(\sigma v)_\nu$  per single atom:

$$\frac{\Gamma_{\text{capture}}}{\text{y}^{-1}} = \frac{\eta_\nu}{\langle \eta_\nu \rangle} \begin{cases} 12.7 (6.4) \times 10^{-27} & ^{171}\text{Tm} \\ 5.1 (2.5) \times 10^{-28}, & ^{151}\text{Sm} \end{cases} \quad (7.15)$$

for Majorana (Dirac) neutrino, where  $\eta_\nu$  is the local cosmic number density of one neutrino species which could be significantly larger than the average over the universe  $\langle \eta_\nu \rangle \sim 56 \text{ cm}^{-3}$  due to gravitational clustering. The corresponding cross-sections are in agreement with the crude estimate ( $\delta \approx 0.5$ ).

Since the emitters in the solid-state based experiments are attached to the substrate atom by atom, the single event exposure based on the estimate (7.4) corresponds to  $2 \cdot 10^{27} \text{ atoms} \cdot \text{year}$  of  $^{151}\text{Sm}$  or  $10^{26} \text{ atoms} \cdot \text{year}$  of  $^{171}\text{Tm}$ . For comparison, the same number of events can be achieved with  $2 \cdot 10^{24} \text{ atoms} \cdot \text{year}$  of  $^3\text{H}$ . According to this, using  $^{171}\text{Tm}$  as  $\beta$  emitter in a full size  $C\nu\text{B}$  experiment is promising since it can provide with *both* sufficient

event rate *and* energy resolution for the relic neutrino detection.

We emphasize that the results based on BetaShape might be inaccurate and the measurement is still needed to confirm them. We discuss the approximation used in BetaShape in the follow-up paper [93], together with independent theoretical bounds on  $(\sigma v)_\nu$ .



# Chapter 8

## Screening effects in the graphene-based relic neutrino detection experiment

### 8.1 Introduction.

The detection of the Cosmic Neutrino Background ( $C\nu B$ ) is a long standing highly important scientific goal [95, 209, 240]. Analogous to the CMB, it carries a photographic image of the early Universe, albeit from a much older epoch of neutrino decoupling. Indirect evidence for the existence of the relic neutrinos was found in the observed  $C\nu B$  [82], however, due to the extreme weakness of the interactions between neutrinos and other forms of matter, direct detection of the  $C\nu B$  remains a major experimental challenge.

Today it is widely accepted that the most practicable route to the direct detection of the  $C\nu B$  lies through the measurement of the fine structure of the  $\beta$ -spectrum of a radioactive element [84–87, 95]. The main challenges are: the weakness of the signal which can be only compensated by the large amounts of the radioactive atoms (at least 100 g in order to achieve one event per year in the case of atomic Tritium) and the need in the extraordinary high energy resolution (50 meV or better) of the experiment.

So far, the only the only known way to overcome these roadblocks is a solid state architecture where the  $\beta$ -emitters are adsorbed on a substrate [96]. Such a design can increase the event count by orders of magnitude while preserving the necessary degree of control over the emitted electrons.

State-of-the-art PTOLEMY experiment [96] that exploits Tritium adsorbed

on the graphene motivated deeper theoretical studies of the physics of the  $\beta$ -decay in the vicinity of the solid state substrate [91, 241, 242]. It was revealed, that deposition of  $\beta$ -emitters on a solid-state substrate produces a new intrinsic fundamental limitation on the experimental resolution originating in the zero-point motion of the emitter's centre of mass [91]. This limitation strongly depends on the properties of the  $\beta$ -emitter such as its mass and energy released in  $\beta$  decay. While for Tritium it yields the uncertainty in the spectrum that is of the order  $\Delta E \sim 0.5$  eV, heavier emitters such as  $^{171}\text{Tm}$  and  $^{151}\text{Sm}$  reduce it by an order of magnitude [91, 242].

Zero point motion is not the only effect that leads to the intrinsic energy uncertainty [92, 241]. Solid state substrate hosts a whole zoo of elementary excitations which will affect the intrinsic uncertainty of the detector through a range of mechanisms. Each of those has to be studied one by one in order to find the ways to mitigate it.

This paper offers a second step into the physics of the  $\beta$ -decay of the emitter bounded to a solid state substrate. After the first and most simple mechanism of the emitter zero point motion was understood and the ways to mitigate it were found [91, 242], we proceed to, subjectively, second most simple and important effect - electromagnetic interaction of the  $\beta$ -decaying system and substrate. Specifically, we consider two kinds of processes: screening of the Helium ion by the charges in graphene and promotion of the graphene electrons from the valence to conduction band by the electric field of the emitted  $\beta$ -electron.

For simplicity, we assume that the decaying atom is Tritium, although the calculation can be straightforwardly generalized to the arbitrary atom.

## 8.2 Defining the problem

Consider mono-atomic Tritium deposited on graphene sheets arranged into a parallel stack where a clever magneto-electric design is used to extract and measure the energy of the electrons created in the two  $\beta$ -decay channels.



As a result of these processes, a Helium ion is formed and a  $\beta$ -electron is emitted. Both the ion and the emitted electron interact electromagnetically with each other and with the surroundings, namely graphene substrate. While the former is also present in the vacuum and its effect is accounted for in what

we call the “bare”  $\beta$ -decay spectrum [230], the effect of the latter two on the bare spectrum has to be evaluated. Let us try to do it treating each of them independently:

1. *Electromagnetic interaction of the Helium ion with the substrate.* Conversion of the tritium atom into Helium ion acts as a sudden creation of the charged impurity that brings the electrons in graphene out of equilibrium. The corresponding rearrangement of the charges  $Q(\vec{r}, t)$  (see Fig. 8.1) leads to a higher charge concentration near the impurity that would effectively screen it. This reduces the interaction strength between the emitted  $\beta$ -electron and Helium ion thus changing the  $\beta$ -spectrum.
2. *Electromagnetic interaction of the emitted  $\beta$ -electron with the substrate.* Before reaching the detector, emitted  $\beta$ -electron can scatter on the electrons in graphene promoting them from the valence to conduction band. Each of such processes is accompanied by the energy loss of the emitted electron equivalent to  $\Delta E = v_F(|p| + |p'|)$ , where  $\vec{p}, \vec{p}'$  are respectively the initial and final momenta of the electron in graphene thus also changing the  $\beta$ -spectrum.

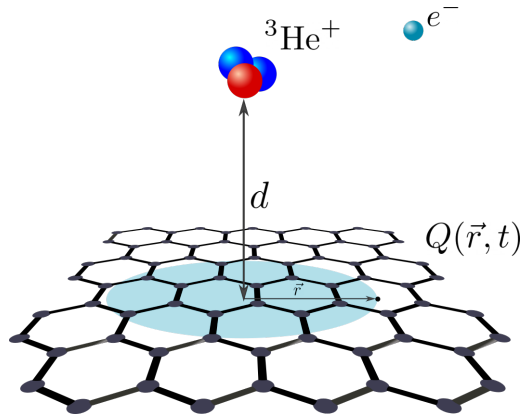


**Figure 8.1.** Schematic picture of screening mechanism in the graphene after the  $\beta$  decay of the Tritium bounded at the distance  $d$  from the substrate. As a result, a Helium ion is formed that leads to the rearrangement of the charges  $Q(\vec{r}, t)$  in the graphene. These charges screen the potential of the ion therefore performing work on the emitted  $\beta$ -electron.

Both of the processes described above have stochastic character (screened charge  $Q(\vec{r}, t)$  can have quantum fluctuations while the scattering of the elec-

tron on graphene is intrinsically probabilistic) which means that the change in the energy of the emitted  $\beta$ -electron is described by some distribution function  $\mathcal{F}(\cdot)$  and the initial  $\beta$ -spectrum  $\mathcal{G}(\cdot)$  changes to

$$\tilde{\mathcal{G}}(E_e) = \int d\varepsilon \mathcal{F}(\varepsilon) \mathcal{G}(E_e + \varepsilon) \quad (8.2)$$

if one is to account for the corresponding interaction process.

For simplicity, we discuss both the screening and electron scattering processes independent from all the other effects such as zero point motion, etc. [91] and independent from each other. So,  $\mathcal{G}(\cdot)$  is taken to be the one for the electron emitted by a free Tritium atom at rest.

### 8.3 Charge screening effects

Let us start from studying the effect of the screening of the Helium potential by electrons in graphene. In this case, the distribution function  $\mathcal{F}(\cdot)$  in Eq. (8.2) corresponds to the distribution of the work performed by the induced charge  $Q(\vec{r}, t)$  on the  $\beta$ -electron.

In this work, however, we are only going to calculate the average work  $\langle W(E_e) \rangle$  that is a purely classical contribution leaving out the calculation of the quantum fluctuations for the future studies. Large values of the average work ( $\langle W(E_e) \rangle \gtrsim m_\nu$ ) is going to be a signal that quantum mechanical fluctuations should be also taken into account. We also neglect the back-reaction of the induced charge on the ion assuming that it is fixed.

First, we make a dimensional estimate of the classical screening effect. The only dimension-full parameters relevant to this problem are:

1. Distance from the graphene substrate to the atom  $d \approx 3 \text{ \AA}$
2. Fermi velocity in graphene  $v_F \approx 10 \text{ \AA fs}^{-1}$ .

According to it, the typical time scale  $\tau_{\text{relax}}$  at which the electrons in graphene would screen the Helium ion can be estimated as

$$\tau_{\text{relax}} = \frac{d}{v_F} \approx 0.3 \times 10^{-15} \text{ s}. \quad (8.3)$$

During the relaxation time  $\tau_{\text{relax}}$ , the electron will fly away on the distance  $\lambda = v_\beta \tau_{\text{relax}}$ , where  $v_\beta$  is the typical velocity of the  $\beta$ -electron. For region of our interest that is the end of the  $\beta$  spectrum it that can be estimated as

$$\frac{v_\beta}{c} = \sqrt{\frac{2Q}{m_e c^2} \left( 1 + \underbrace{\frac{U}{Q}}_{\approx 0.001} \right)} \approx \frac{v_\infty}{c} \approx 0.27, \quad (8.4)$$

where  $Q = 18.6 \text{ keV}$  is the energy released in the  $\beta$ -decay and  $U$  is a Coulomb potential from the Helium ion that electron feels right after the decay.

This means that at the moment when the Helium ion is fully screened by the charges in the graphene,  $\beta$ -electron will fly away on

$$\lambda = v_\beta \tau_{\text{relax}} \approx 243 \text{ \AA}. \quad (8.5)$$

The difference in  $\beta$ -electron energy compared to unscreened case  $\Delta E_e$  is

$$\Delta E_e = k \frac{Z e^2}{\lambda} \approx 59 \text{ meV} \quad (8.6)$$

We see that already the classical effect of the charge screening in graphene leads to a significant shift in the  $\beta$ -electron energy  $\Delta E_e \gtrsim m_\nu$  that is comparable to the size of the energy gap that we want to measure.

The full quantum-mechanical calculation for the case of the perpendicular emission was also done using the linear response theory (see Appendix ??). The average work performed by the induced charge on the  $\beta$ -electron emitted with the velocity  $v_e$  is

$$\langle W(v_e) \rangle = \frac{\overbrace{\pi \alpha^2}^{\approx 0.5 \text{ eV}}}{16 E_F d^2} \tilde{W} \left( \frac{v_F}{v_e} \right), \quad (8.7)$$

where  $\tilde{W} \left( \frac{v_F}{v_e} \right)$  is defined by Eq. (8.21) and shown on (see Fig. 8.2).

For the  $\beta$ -electron at the edge of the spectrum ( $E_e = Q$ ), Eq. (8.7) yields  $\langle W(E_e = Q) \rangle \approx 75 \text{ meV}$ . This result is in a very good agreement (same order of magnitude) with the one that we have obtained with the simple estimate (8.6). We also see that the parameter that defines the relaxation time is indeed Fermi velocity in graphene  $v_F$ . The energy dependence of the work has the form of zeroth order Bessel function of the first kind  $\langle W(E_e) \rangle \sim J_0 \left( \sqrt{E_F/E_e} x \right)$  (see Fig. 8.2).

We emphasise, however, that despite the fact that the uncertainty in the energy of the  $\beta$ -electron at the edge of the spectrum is rather big as compared

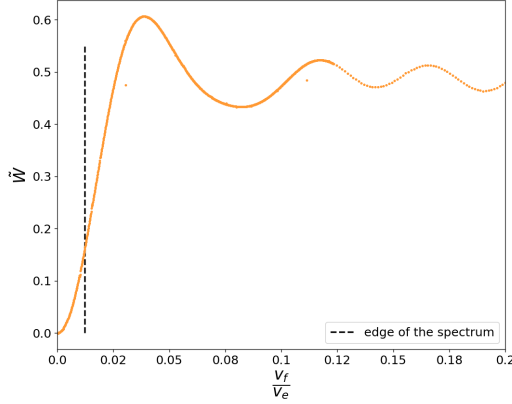


**Figure 8.2.** Average work (Eq. (8.21)) performed by the induced charges in graphene on the emitted  $\beta$ -electron depending on the ratio of the Fermi velocity in graphene  $v_F \approx 0.3 \times 10^{-15} \text{ s}$  to the velocity of the  $\beta$ -electron  $v_e$ .

to the required energy precision,  $\Delta E_e \approx 75 \text{ meV} \gtrsim m_\nu$ , it is not the right quantity that determines the final energy precision of the experiment. Instead, one should look at the functional dependence of the  $\langle W(E_e) \rangle$ , namely at the derivative like  $d\langle W(E_e) \rangle/dE_e$  since it determines the *relative* shift of the points of the spectrum. For example, if  $d\langle W(E_e) \rangle/dE_e \equiv 0$ , the whole spectrum will just shift and the energy gap between the bulk  $\beta$ -decay spectrum and neutrino capture part will remain unchanged.

$$|dW(E_e)| = \frac{\gamma}{2E_e} \frac{dW(\gamma)}{d\gamma} dE_e, \quad (8.8)$$

where we denoted  $\gamma = \sqrt{E_F/E_e}$ . For the edge of the spectrum,

$$|dW(E_e)|/dE_e|_{E_e=Q} \sim 10^{-5}.$$

This means that all the energies simply get “shifted” by the same amount and the gap in the spectrum does not disappear.

To conclude the analysis above, the classical screening effects in the graphene substrate appear to only lead to the total nearly constant energy shift of the end of the spectrum. This shift should be back-engineered and does not lead to any limitations on the energy resolution of the experiment.

Nevertheless, since the classical (mean) part of the work distributing appeared to be rather big, one needs to also study quantum charge fluctuations

$\sigma(W) = \langle \hat{W}^2 \rangle - W^2$ . As opposed to the classical effect, these lead to the irreducible changes in the spectrum. We leave the latter for future studies.

## 8.4 Electron-hole pair creation

The other electromagnetic effect that we consider in this work is the scattering process where the electron in graphene is promoted from the valence to the conduction band with possible momentum transfer  $\vec{p} \rightarrow \vec{p}'$ . As a result,  $\beta$  electron changes its momentum as well  $\vec{p}_\beta \rightarrow \vec{p}'_\beta$ .

Let us first estimate the average number such processes  $N_{\text{sc}}$  that will happen until the  $\beta$ -electron will leave the system. Using the Fermi Golden Rule (for the full calculation see Appendix ??), we obtain

$$N_{\text{sc}} = \frac{m_e}{v_\perp} \left( \frac{\kappa e^2}{2\pi} \right)^2 \int d^2q d^2p \frac{1 - \cos(\varphi(\vec{p}) - \varphi(\vec{q} + \vec{p}))}{p_\beta^\perp ((p_\beta^\perp - p_\beta'^\perp)^2 + q^2)^2} \quad (8.9)$$

where  $p_\beta^\perp = \sqrt{m_e v_F (|\vec{p}| + |\vec{q} + \vec{p}|) - (\vec{q} - \vec{p}_\beta^\parallel)^2 + p_\beta^2}$ .

For the  $\beta$ -decay of Tritium, the typical velocity of the emitted electron is  $v = 0.3c$ . We use system of units, where  $c = 1$ ,  $m_e = 1$  (and so  $\kappa e^2 = 14.4 \text{ eV \AA} = 7.5 \cdot 10^{-3}$  and  $v_F = 10 \text{ \AA fs}^{-1} = 3.3 \cdot 10^{-3}$ ). We see that  $v_e \gg v_F$ , so let us for simplicity re-scale everything introducing  $\vec{u} = \vec{q}/v_e$ ,  $\vec{w} = \vec{p}/v_e$  and write down an approximate simplified expression

$$N_{\text{sc}}^{3\text{H}}(\theta) = \frac{1.6 \times 10^{-5}}{\cos^2 \theta} \times I(\theta) \\ I(\theta) = \int d^2u d^2w \frac{1 - \cos(\varphi(\vec{w}) - \varphi(\vec{u} + \vec{w}))}{((\cos \theta - \delta(\theta, \vec{u}, \vec{w}))^2 + u^2)^2}, \quad (8.10)$$

where  $\theta$  is the emission angle with respect to the perpendicular to the graphene and  $\delta(\vec{u}, \vec{w}) = \sqrt{0.01(|\vec{w}| + |\vec{u} + \vec{w}|) - (\vec{u} - \sin \theta \vec{e}_\beta^\parallel)^2 + 1}$  ( $\vec{e}_\beta^\parallel$  is a projection of the initial  $\beta$ -electron velocity vector on the graphene plane).

It can be seen that the integral in Eq. (8.10) has both UV and IR divergences. However, one can introduce two natural cut-offs:

- IR cutoff that is defined by the system size ( $0.4 \cdot 10^{-12}$  for the system-size of 1 m).
- UV cutoff that is defined by the graphene lattice spacing ( $1/a = 1/(2.46 \text{ \AA}) = 1.5 \cdot 10^{-3}$ ).

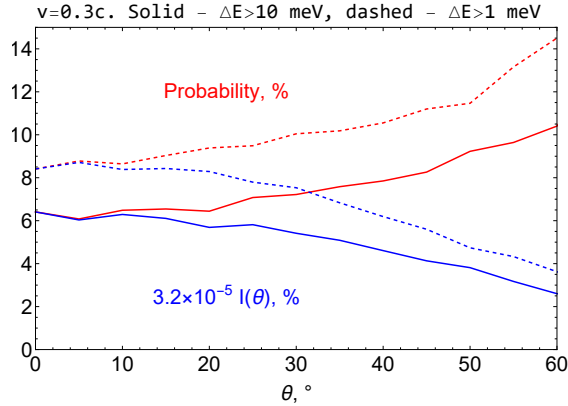


**Figure 8.3.** Red line: probability that the emitted electron will create a particle-hole excitation in graphene before it leaves the detector as a function of the emission angle  $\theta$ . The velocity of the emitted electron is  $0.3c$ . Blue line: value of the integral 8.10 for the same parameters. The solid and dashed lines correspond to different infra-red cut-offs that are defined by the size of the detector.

## 8.5 Conclusions

Solid state materials host a whole zoo of elementary excitations which will affect the intrinsic uncertainty of the detector through a range of mechanisms. For example, the sudden emission of an electron from a beta-decayer leaves behind a positively charged centre which attracts the electric current carriers in of the substrate. This effect results in what is known as the X-ray edge anomaly - a gamma-shaped broadening of the emission peak [92]. Other effects include the creation of vibrational excitations of the lattice, distortion of the spectrum due to the interaction of the beta-electron with its image charge, creation of shock wave emission due to the motion of the emitted electron at grazing angles at speeds exceeding the Fermi velocity, emission of plasmons and surface polaritons. The investigation of all these mechanisms and finding ways of mitigation requires a close collaboration between high-level experts in both theoretical and experimental solid state physics and may lead to further modifications of the experimental architecture.

## 8.6 Appendix: Average work performed by the electrons in graphene on the emitted $\beta$ -electron

Define  $Q(r, t)$  to be the total charge that has flown into the circle of radius  $r$  during the time  $t$  (See Fig. 8.1). For simplicity, we restrict ourselves to the case when the electron is emitted perpendicular to the substrate. Due to the rotational symmetry, it only depends on the absolute value of the distance  $r$ . Then, the total electrostatic potential at the point  $\vec{r}$  (see Fig. 8.1) is

$$\varphi_{\text{tot}}(r, t) = \varphi_{\text{bare}}(r) + k \frac{Q(r, t)}{r}, \quad (8.11)$$

where  $\varphi_{\text{bare}}(r) = -ke/\sqrt{r^2 + d^2}$  is the electrostatic potential of the bare Helium ion at the corresponding point. Performing the Fourier transformation gives:

$$\varphi_{\text{tot}}(q, \omega) = \varphi_{\text{bare}}(q) + 2\pi k \int_0^\infty dr J_0(qr) Q(r, \omega), \quad (8.12)$$

where  $J_n(x)$  is  $n^{\text{th}}$  Bessel function of the first kind.

The total electrostatic potential (8.12) can be also deduced from the response function of the graphene on charge impurity, so-called *polarization operator*  $\Pi(\omega, q)$  or, alternatively, its dielectric permittivity  $\varepsilon(\omega, q)$  [128]:

$$\varphi_{\text{tot}}(\omega, q) = \frac{1}{\varphi_{\text{bare}}^{-1}(q) - \Pi(\omega, q)} = \frac{\varphi_{\text{bare}}(q)}{\varepsilon(\omega, q)}. \quad (8.13)$$

The form of the polarization operator (or dielectric permittivity) depends on the type of the relaxation we are considering. We consider intrinsic (undoped) graphene where two valleys are independent, so no intra-valley scattering. In this case, the random phase approximation approach gives the following results for the polarization operator and dielectric permittivity [243]:

$$\Pi(q, t) = \frac{q^2}{8} J_0(v_F q t) \quad (8.14)$$

$$\varepsilon(q, t) = \left( \delta(t) + \frac{\alpha\pi}{4} q e^{-qd} J_0(v_F q t) \right), \quad (8.15)$$

where  $v_F$  is the Fermi velocity in graphene and  $\alpha = ke^2$ .

By requiring Eqns. (8.12),(8.13) be self-consistent, we can calculate the induced charge  $Q(r, t)$ :

$$\frac{\varphi_{\text{bare}}(q)}{2\pi k} \left( \frac{1}{\varepsilon(\omega, q)} - 1 \right) = \int_0^\infty dr J_0(qr) Q(r, \omega) \quad (8.16)$$

Using the orthogonality identity for Bessel functions  $\int_0^\infty x J_0(ux) J_0(vx) dx = \frac{1}{u} \delta(v - u)$  and the fact that  $\varphi_{\text{bare}}(q) = -e^{-qd} \times 2\pi k e/q$ , we find:

$$Q(r, \omega) = e \int_0^\infty r e^{-qd} J_0(qr) \left( 1 - \frac{1}{\varepsilon(\omega, q)} \right) dq. \quad (8.17)$$

The induced charge (8.17) creates repulsive Coulomb force  $F_{\text{ind}}$  acting on the  $\beta$ -electron that is flying away from the surface. Let us restrict ourselves to the case where the electron is flying away perpendicular from the surface. We believe that the result will be the same up to a pre-factor of order one for any emission angle due to the nature of the process. In this simplified case, due to the rotational symmetry, the force is perpendicular to the substrate and has the following magnitude:

$$F_{\text{ind}}(h) = ke(h + d) \int \frac{\partial_r Q(r, t) dr}{(r^2 + (h + d)^2)^{3/2}}, \quad (8.18)$$

where  $h = v_e t$  is the distance from the electron to the Helium ion. The corresponding work performed by the induced charge (8.17) on the  $\beta$ -electron is:

$$\langle W(E_e) \rangle = \int_0^\infty dh F_{\text{ind}}(h), \quad (8.19)$$

where we have neglected the deceleration of the electron. This is justified for the electrons near the edge of the spectrum <sup>1</sup>. Plugging in all the expressions, we obtain the final result

---

<sup>1</sup>The initial velocity  $v_0$  of the emitted electron is related to its velocity on infinity  $v_\infty$  as follows:

$$v_\infty = v_0 \sqrt{1 - \frac{2ke^2}{m_e d} \frac{1}{v_0^2}} = v_0 \sqrt{1 - \underbrace{\frac{0.18 \times 10^{-4} c^2}{v_0^2}}_\delta} \quad (8.20)$$

Since  $v_0 \approx 0.3c, \delta \ll 1$ , so  $v_\infty \approx v_0$ .

$$\begin{aligned}
 \langle W(v_e) \rangle &= \frac{\overbrace{\pi\alpha^2}^{\approx 0.5 \text{ eV}}}{16E_F d^2} \tilde{W}\left(\frac{v_F}{v_e}\right) \\
 \tilde{W}\left(\frac{v_F}{v_e}\right) &= \int_0^\infty y \left(1 - (1 + 2y)e^{-2y}\right) J_0\left(\frac{v_F}{v_e}y\right) dy \int_0^\infty \frac{(J_0(x) - xJ_1(x))}{(x^2 + y^2)^{3/2}} dx
 \end{aligned} \tag{8.21}$$

## 8.7 Appendix: Cross section of the process of the electron-hole creation in graphene

We denote  $d\omega_{i \rightarrow f}$  - the probability per unit time of the following event:  $\beta$ -electron with the momentum  $\vec{p}_\beta$  scatters with the electron in graphene that is in the valence band having momentum  $\vec{p}$ . After the scattering,  $\beta$ -electron changes its momentum to  $\vec{p}'_\beta$  and the electron in graphene is promoted to the conduction band with momentum  $\vec{p}'$ . According to the Fermi Golden Rule, it is equal to

$$\begin{aligned}
 d\omega_{i \rightarrow f}(\vec{p}_\beta, \vec{p}; \vec{p}'_\beta, \vec{p}') &= 4\pi \left| \int d^2\vec{\rho} d^2\vec{\rho}' dz' \langle \psi_f(\vec{p}'_\beta, \vec{p}') | \hat{W}(\vec{\rho}, \vec{\rho}', z') | \psi_i(\vec{p}_\beta, \vec{p}) \rangle \right|^2 \times \\
 &\times \delta\left(\frac{p'^2_\beta - p^2_\beta}{2m_e} - v_F(|p| + |p'|)\right) \frac{VS^2 d^3\vec{p}'_\beta d^2\vec{p} d^2\vec{p}'}{(2\pi)^7},
 \end{aligned} \tag{8.22}$$

where the additional factor 2 is accounted for that comes from the summation over the valleys in graphene. We assume that the initial  $\beta$ -electron has fixed chirality therefore it does not contribute to the sum. Writing down the interaction potential explicitly

$$\hat{W}(\vec{\rho}, \vec{\rho}', z') = \kappa e^2 \frac{\hat{\phi}^\dagger(\vec{\rho}', z') \hat{\phi}(\vec{\rho}, z') \hat{\psi}^\dagger(\vec{\rho}) \hat{\psi}(\vec{\rho})}{\sqrt{z'^2 + (\vec{\rho} - \vec{\rho}')^2}}, \tag{8.23}$$

where Fourier decomposition for field operators of the  $\beta$ -electron ( $\hat{\phi}$ ) and electron in graphene ( $\hat{\psi}$ ) are <sup>2</sup>

$$\hat{\phi}(\vec{\rho}, z) = \sum_s \int_{-\infty}^{\infty} \frac{d^3 \vec{k}}{(2\pi)^3} \frac{1}{\sqrt{2V E_{\vec{k}}}} e^{i(\vec{k}_{\parallel} \vec{\rho} + k_{\perp} z)} \left( \hat{c}_{\vec{k}}^s \tilde{u}^s(\vec{k}) + \hat{d}_{-\vec{k}}^s \tilde{v}^s(-\vec{k}) \right) \quad (8.24)$$

$$\hat{\psi}(\vec{\rho}) = \sum_{\alpha} \int_{-\infty}^{\infty} \frac{d^2 \vec{p}}{(2\pi)^2} \frac{1}{\sqrt{2S}} e^{i\vec{p}\vec{\rho}} \left( \hat{a}_{\vec{p}}^{\alpha} u^{\alpha}(\vec{p}) + \hat{b}_{-\vec{p}}^{\alpha} v^{\alpha}(-\vec{p}) \right). \quad (8.25)$$

The initial and final states are

$$|\psi_i\rangle = c_{p_{\beta}}^{\dagger} |FS\rangle, \quad |\psi_f\rangle = c_{p'_{\beta}}^{\dagger} a_{p'}^{\dagger} b_{-p} |FS\rangle. \quad (8.26)$$

Plugging everything in and treating  $\beta$ -electrons in the non-relativistic limit we arrive at

$$\begin{aligned} d\tilde{\omega}_{i \rightarrow f}(\vec{p}_{\beta}, \vec{p}; \vec{p}'_{\beta}, \vec{p}') &= \frac{\pi}{4V} (\kappa e^2)^2 \times \\ &\times \left| \int d^2 \vec{\rho} d^2 \vec{\rho}' dz' \frac{e^{i(\vec{p}_{\beta}^{\parallel} - \vec{p}'_{\beta}^{\parallel}) \vec{\rho}' + i(p_{\beta}^{\perp} - p'_{\beta}^{\perp}) z'}}{\sqrt{E_{\vec{p}_{\beta}} E_{\vec{p}'_{\beta}}} \sqrt{z'^2 + (\vec{\rho} - \vec{\rho}')^2}} e^{i(\vec{p} - \vec{p}') \vec{\rho}} \tilde{u}^{\dagger}(\vec{p}'_{\beta}) \tilde{u}(\vec{p}_{\beta}) u^{\dagger}(\vec{p}') v(-\vec{p})} \right|^2 \times \\ &\times \delta \left( \frac{p_{\beta}^{\prime 2} - p_{\beta}^2}{2m_e} - v_F (|\vec{p}| + |\vec{p}'|) \right) \frac{d^3 p'_{\beta} d^2 p' d^2 p}{(2\pi)^7}. \end{aligned} \quad (8.27)$$

The integral can be evaluated to be

$$\begin{aligned} d\tilde{\omega}_{i \rightarrow f}(\vec{p}_{\beta}, \vec{p}; \vec{p}'_{\beta}, \vec{p}') &= \frac{4\pi^3 S}{V} (\kappa e^2)^2 \frac{|\tilde{u}^{\dagger}(\vec{p}'_{\beta}) \tilde{u}(\vec{p}_{\beta}) u^{\dagger}(\vec{p}'_{\beta}^{\parallel} + \vec{p} - \vec{p}'_{\beta}^{\parallel}) v(-\vec{p})|^2}{((p_{\beta}^{\perp} - p'_{\beta}^{\perp})^2 + (p_{\beta}^{\parallel} - p'_{\beta}^{\parallel})^2)^2 E'_{\beta} E_{\beta}} \times \\ &\times \delta \left( \frac{p_{\beta}^{\prime 2} - p_{\beta}^2}{2m_e} - v_F (|\vec{p}| + |\vec{p}'_{\beta}^{\parallel}| + \vec{p} - \vec{p}'_{\beta}^{\parallel}) \right) \frac{d^3 p'_{\beta} d^2 p}{(2\pi)^5}. \end{aligned} \quad (8.28)$$

The spinors of the  $\beta$ -electron are

$$\tilde{u}(\vec{p}_{\beta}) = \sqrt{2E_{\vec{p}_{\beta}}} \vec{\chi}, \quad \text{where } \vec{\chi}_+ = (0, 0, 1, 0), \vec{\chi}_- = (1, 0, 0, 0), \quad (8.29)$$

---

<sup>2</sup>We note that we distinguish electrons in graphene and  $\beta$ -electron. Namely, no exchange can occur.

where  $\bar{\chi}$  denotes chirality. The spinors of the electron in graphene are

$$u^\alpha(p) = \frac{1}{\sqrt{2}} \begin{pmatrix} 1 \\ \alpha e^{i\varphi(p)} \end{pmatrix}, \quad v^\alpha(-p') = \frac{1}{\sqrt{2}} \begin{pmatrix} 1 \\ -\alpha e^{i\varphi(p')} \end{pmatrix} \quad (8.30)$$

with  $\varphi(p) = \arctan(p_y/p_x)$ . So, we arrive at

$$\begin{aligned} d\tilde{\omega}_{i \rightarrow f}(\vec{p}_\beta, \vec{p}; \vec{p}'_\beta, \vec{p}') &= \frac{(2\pi)^3 S}{V} (\kappa e^2)^2 \frac{1 - \cos(\varphi(\vec{p}) - \varphi(\vec{p}'_\beta + \vec{p} - \vec{p}'_\beta))}{((p_\beta^\perp - p'^\perp_\beta)^2 + (p_\beta^\parallel - p'^\parallel_\beta)^2)^2} \times \\ &\times \delta\left(\frac{p_\beta'^2 - p_\beta^2}{2m_e} - v_F(|p| + |p'_\beta + \vec{p} - p'_\beta|)\right) \frac{d^3 p'_\beta d^2 p}{(2\pi)^5}. \end{aligned} \quad (8.31)$$

where  $\varphi(\vec{k})$  denotes the angle in the polar coordinate system of the vector  $\vec{k}$ . The total probability per unit time of the transition into any final state can be obtained by integrating over all final states

$$\frac{dP}{dt} = \frac{(2\pi)^2 S m_e}{V} (\kappa e^2)^2 \int \frac{d^2 q d^2 p}{(2\pi)^4} \frac{1 - \cos(\varphi(\vec{p}) - \varphi(\vec{q} + \vec{p}))}{p_\beta'^\perp ((p_\beta^\perp - p_\beta'^\perp)^2 + q^2)^2}, \quad (8.32)$$

where  $\vec{q} = \vec{p}'_\beta - \vec{p}'_\beta$  and  $p_\beta'^\perp(\vec{q}, \vec{p}) = \sqrt{m_e v_F(|\vec{p}| + |\vec{q} + \vec{p}|) - (\vec{q} - \vec{p}'_\beta)^\perp^2 + p_\beta^2}$  due to energy conservation. In other words, the inverse time of a single interaction  $\tau$  is

$$\frac{1}{\tau} = \frac{(2\pi)^2 S m_e}{V} (\kappa e^2)^2 \int \frac{d^2 q d^2 p}{(2\pi)^4} \frac{1 - \cos(\varphi(\vec{p}) - \varphi(\vec{q} + \vec{p}))}{p_\beta'^\perp ((p_\beta^\perp - p_\beta'^\perp)^2 + q^2)^2}. \quad (8.33)$$

If the typical time that electron spends in the setup is  $t_{\text{measure}} = L/v_\perp = V/(Sv_\perp)$ , where  $v_\perp$  is the perpendicular component of the electron velocity then during this time electron will experience  $N_{\text{sc}} = t_{\text{measure}}/\tau$  number of events

$$N_{\text{sc}} = \frac{m_e}{v_\perp} \left(\frac{\kappa e^2}{2\pi}\right)^2 \int d^2 q d^2 p \frac{1 - \cos(\varphi(\vec{p}) - \varphi(\vec{q} + \vec{p}))}{p_\beta'^\perp ((p_\beta^\perp - p_\beta'^\perp)^2 + q^2)^2} \quad (8.34)$$

where  $p_\beta'^\perp(\vec{q}, \vec{p}) = \sqrt{m_e v_F(|\vec{p}| + |\vec{q} + \vec{p}|) - (\vec{q} - \vec{p}'_\beta)^\perp^2 + p_\beta^2}$ .



# Bibliography

- [1] R. Mann. *An introduction to particle physics and the standard model*. (Taylor & Francis, 2010).
- [2] L. Landau. *On the theory of the fermi liquid*. Sov. Phys. JETP **8**, 70 (1959).
- [3] P. W. Anderson. *More is different: broken symmetry and the nature of the hierarchical structure of science*. Science **177**, 393–396 (1972).
- [4] E. Majorana. *Teoria simmetrica dell’elettrone e del positrone*. Il Nuovo Cimento (1924-1942) **14**, 171–184 (1937).
- [5] K. Grotz and H. Klapdor. *The weak interaction in nuclear. Particle and Astrophysics’* (Adam Hilger: Bristol, Philadelphia) (1990).
- [6] J. Vergados, H. Ejiri, and F. Šimkovic. *Theory of neutrinoless double-beta decay*. Reports on Progress in Physics **75**, 106301 (2012).
- [7] W. Rodejohann. *Neutrino-less double beta decay and particle physics*. International Journal of Modern Physics E **20**, 1833–1930 (2011).
- [8] P. Agrawal, Z. Chacko, C. Kilic, and R. K. Mishra. *A classification of dark matter candidates with primarily spin-dependent interactions with matter*. arXiv:1003.1912 (2010).
- [9] Y. F. Perez-Gonzalez. *Massive neutrinos: phenomenological and cosmological consequences*. arXiv:1712.06675 (2017).
- [10] S. Matsumoto, S. Mukhopadhyay, and Y.-L. S. Tsai. *Effective theory of wimp dark matter supplemented by simplified models: singlet-like majorana fermion case*. Physical Review D **94**, 065034 (2016).
- [11] K. Moffat. *Some theory and phenomenology of neutrino masses and the baryon asymmetry*. PhD thesis (Durham University, 2019).
- [12] S. Biondini. *Effective field theories for heavy majorana neutrinos in a thermal bath*. (Springer, 2017).

- 
- [13] J. Penedo, S. Petcov, and T. T. Yanagida. *Low-scale seesaw and the  $cp$  violation in neutrino oscillations*. Nuclear Physics B **929**, 377–396 (2018).
- [14] C. W. J. Beenakker. *Search for non-abelian majorana braiding statistics in superconductors*. SciPost Physics Lecture Notes, 015 (2020).
- [15] G. Volovik. *Fermion zero modes on vortices in chiral superconductors*. Journal of Experimental and Theoretical Physics Letters **70**, 609–614 (1999).
- [16] L. Fu and C. L. Kane. *Superconducting proximity effect and majorana fermions at the surface of a topological insulator*. Phys. Rev. Lett. **100**, 096407 (2008).
- [17] A. Y. Kitaev. *Unpaired majorana fermions in quantum wires*. Physics-uspekhi **44**, 131 (2001).
- [18] D. A. Ivanov. *Non-abelian statistics of half-quantum vortices in  $p$ -wave superconductors*. Physical Review Letters **86**, 268 (2001).
- [19] J. Alicea. *Majorana fermions in a tunable semiconductor device*. Physical Review B **81**, 125318 (2010).
- [20] J. Alicea, Y. Oreg, G. Refael, F. Von Oppen, and M. Fisher. *Non-abelian statistics and topological quantum information processing in 1d wire networks*. Nature Physics **7**, 412–417 (2011).
- [21] S. Das Sarma, M. Freedman, and C. Nayak. *Majorana zero modes and topological quantum computation*. npj Quantum Information **1**, 1–13 (2015).
- [22] A. Chew, A. Essin, and J. Alicea. *Approximating the sachdev-ye-kitaev model with majorana wires*. Physical Review B **96**, 121119 (2017).
- [23] D. I. Pikulin and M. Franz. *Black hole on a chip: proposal for a physical realization of the sachdev-ye-kitaev model in a solid-state system*. Phys. Rev. X **7**, 031006 (2017).
- [24] S.-S. Lee. *Recent developments in non-fermi liquid theory*. arXiv:1703.08172 (2017).
- [25] A. Kitaev. *A simple model of quantum holography*. (KITP Program: Entanglement in Strongly-Correlated Quantum Matter, 2015).
- [26] S. Sachdev and J. Ye. *Gapless spin-fluid ground state in a random quantum heisenberg magnet*. Physical Review Letters **70**, 3339 (1993).

- [27] A. A. Patel and S. Sachdev. *Theory of a planckian metal*. Physical Review Letters **123**, 066601 (2019).
- [28] J. Maldacena, S. H. Shenker, and D. Stanford. *A bound on chaos*. Journal of High Energy Physics **2016**, 1–17 (2016).
- [29] S. A. Hartnoll, A. Lucas, and S. Sachdev. *Holographic quantum matter*. arXiv:1612.07324 (2016).
- [30] J. Polchinski and V. Rosenhaus. *The spectrum in the sachdev-ye-kitaev model*. Journal of High Energy Physics **2016**, 1–25 (2016).
- [31] J. Maldacena and D. Stanford. *Remarks on the sachdev-ye-kitaev model*. Physical Review D **94**, 106002 (2016).
- [32] M. E. Peskin. *An introduction to quantum field theory*. (CRC press, 2018).
- [33] O. Klein. *Quantentheorie und fünfdimensionale relativitätstheorie*. Zeitschrift für Physik **37**, 895–906 (1926).
- [34] P. A. M. Dirac. *The quantum theory of the electron*. Proceedings of the Royal Society of London. Series A, Containing Papers of a Mathematical and Physical Character **117**, 610–624 (1928).
- [35] A. K. Geim. *Graphene: status and prospects*. Science **324**, 1530–1534 (2009).
- [36] B. Yan and C. Felser. *Topological materials: weyl semimetals*. arXiv:1611.04182 (2016).
- [37] E. Lifshitz and L. Pitaevskii. *Statistical physics, part 2*. Course of Theoretical Physics, Vol. 9 **369** (1989).
- [38] J. Bardeen, L. N. Cooper, and J. R. Schrieffer. *Theory of superconductivity*. Physical Review **108**, 1175 (1957).
- [39] C. Caroli, P. De Gennes, and J. Matricon. *Bound fermion states on a vortex line in a type ii superconductor*. Physics Letters **9**, 307–309 (1964).
- [40] M. J. Klein. *On a degeneracy theorem of kramers*. American Journal of Physics **20**, 65–71 (1952).
- [41] S. Das Sarma, C. Nayak, and S. Tewari. *Proposal to stabilize and detect half-quantum vortices in strontium ruthenate thin films: non-abelian braiding statistics of vortices in a  $p_x + i p_y$  superconductor*. Physical Review B **73**, 220502 (2006).

- [42] M. Wimmer, A. Akhmerov, M. Medvedyeva, J. Tworzydło, and C. W. J. Beenakker. *Majorana bound states without vortices in topological superconductors with electrostatic defects*. Physical Review Letters **105**, 046803 (2010).
- [43] A. C. Potter and P. A. Lee. *Multichannel generalization of kitaev's majorana end states and a practical route to realize them in thin films*. Physical Review Letters **105**, 227003 (2010).
- [44] J. D. Sau, R. M. Lutchyn, S. Tewari, and S. Das Sarma. *Generic new platform for topological quantum computation using semiconductor heterostructures*. Physical Review Letters **104**, 040502 (2010).
- [45] M. Sato, Y. Takahashi, and S. Fujimoto. *Non-abelian topological order in s-wave superfluids of ultracold fermionic atoms*. Physical Review Letters **103**, 020401 (2009).
- [46] C. W. J. Beenakker. *Random-matrix theory of quantum transport*. Reviews of Modern Physics **69**, 731 (1997).
- [47] T. Guhr, A. Müller-Groeling, and H. A. Weidenmüller. *Random-matrix theories in quantum physics: common concepts*. Physics Reports **299**, 189–425 (1998).
- [48] A. Altland and M. R. Zirnbauer. *Nonstandard symmetry classes in mesoscopic normal-superconducting hybrid structures*. Physical Review B **55**, 1142 (1997).
- [49] C. W. J. Beenakker. *Random-matrix theory of majorana fermions and topological superconductors*. Reviews of Modern Physics **87**, 1037 (2015).
- [50] M. Bocquet, D. Serban, and M. Zirnbauer. *Disordered 2d quasiparticles in class d: dirac fermions with random mass, and dirty superconductors*. Nuclear Physics B **578**, 628–680 (2000).
- [51] M. L. Mehta. *Random matrices*. (Elsevier, 2004).
- [52] A. Y. Kitaev. *Fault-tolerant quantum computation by anyons*. Annals of Physics **303**, 2–30 (2003).
- [53] C. Nayak, S. H. Simon, A. Stern, M. Freedman, and S. Das Sarma. *Non-abelian anyons and topological quantum computation*. Reviews of Modern Physics **80**, 1083 (2008).

- [54] P. O. Boykin, T. Mor, M. Pulver, V. Roychowdhury, and F. Vatan, *On universal and fault-tolerant quantum computing: a novel basis and a new constructive proof of universality for shor's basis*, in 40th annual symposium on foundations of computer science (cat. no. 99cb37039) (IEEE, 1999), pp. 486–494.
- [55] M. A. Nielsen and I. Chuang, *Quantum computation and quantum information*, 2002.
- [56] P. Bonderson, M. Freedman, and C. Nayak. *Measurement-only topological quantum computation*. Physical Review Letters **101**, 010501 (2008).
- [57] B. Van Heck, A. Akhmerov, F. Hassler, M. Burrello, and C. W. J. Beenakker. *Coulomb-assisted braiding of majorana fermions in a josephson junction array*. New Journal of Physics **14**, 035019 (2012).
- [58] S. Vijay and L. Fu. *Teleportation-based quantum information processing with majorana zero modes*. Physical Review B **94**, 235446 (2016).
- [59] T. Karzig, C. Knapp, R. M. Lutchyn, P. Bonderson, M. B. Hastings, C. Nayak, J. Alicea, K. Flensberg, S. Plugge, Y. Oreg, et al. *Scalable designs for quasiparticle-poisoning-protected topological quantum computation with majorana zero modes*. Physical Review B **95**, 235305 (2017).
- [60] D. Aasen, M. Hell, R. V. Mishmash, A. Higginbotham, J. Danon, M. Leijnse, T. S. Jespersen, J. A. Folk, C. M. Marcus, K. Flensberg, et al. *Milestones toward majorana-based quantum computing*. Physical Review X **6**, 031016 (2016).
- [61] A. Blais, M. Boissonneault, J. Majer, J. Chow, J. Gambetta, J. Koch, B. Johnson, J. Schreier, L. Frunzio, D. Schuster, A. Houck, A. Wallraff, M. Devoret, G. S.M., and R. Schoelkopf. *Quantum information processing and quantum optics with superconducting circuits*. Phys. Rev. Lett **95** (2005).
- [62] D. Pekker, C.-Y. Hou, V. E. Manucharyan, and E. Demler. *Proposal for coherent coupling of majorana zero modes and superconducting qubits using the  $4\pi$  josephson effect*. Physical Review Letters **111**, 107007 (2013).
- [63] V. E. Manucharyan, J. Koch, L. I. Glazman, and M. H. Devoret. *Fluxonium: single cooper-pair circuit free of charge offsets*. Science **326**, 113–116 (2009).

- [64] A. Romito, J. Alicea, G. Refael, and F. Von Oppen. *Manipulating majorana fermions using supercurrents*. Physical Review B **85**, 020502 (2012).
- [65] S. Plugge, A. Rasmussen, R. Egger, and K. Flensberg. *Majorana box qubits*. New Journal of Physics **19**, 012001 (2017).
- [66] T. Hyart, B. Van Heck, I. Fulga, M. Burrello, A. Akhmerov, and C. W. J. Beenakker. *Flux-controlled quantum computation with majorana fermions*. Physical Review B **88**, 035121 (2013).
- [67] A. Larkin and Y. N. Ovchinnikov. *Quasiclassical method in the theory of superconductivity*. Sov Phys JETP **28**, 1200–1205 (1969).
- [68] R. A. Davison, W. Fu, A. Georges, Y. Gu, K. Jensen, and S. Sachdev. *Thermoelectric transport in disordered metals without quasiparticles: the sachdev-ye-kitaev models and holography*. Physical Review B **95**, 155131 (2017).
- [69] X.-Y. Song, C.-M. Jian, and L. Balents. *Strongly correlated metal built from sachdev-ye-kitaev models*. Physical Review Letters **119**, 216601 (2017).
- [70] H. Takagi, B. Batlogg, H. Kao, J. Kwo, R. J. Cava, J. Krajewski, and W. Peck Jr. *Systematic evolution of temperature-dependent resistivity in  $La_{2-x}Sr_xCuO_4$* . Physical Review Letters **69**, 2975 (1992).
- [71] L. Taillefer. *Scattering and pairing in cuprate superconductors*. Annu. Rev. Condens. Matter Phys. **1**, 51–70 (2010).
- [72] J. Bruin, H. Sakai, R. Perry, and A. Mackenzie. *Similarity of scattering rates in metals showing  $t$ -linear resistivity*. Science **339**, 804–807 (2013).
- [73] A. Legros, S. Benhabib, W. Tabis, F. Laliberté, M. Dion, M. Lizaire, B. Vignolle, D. Vignolles, H. Raffy, Z. Li, et al. *Universal  $t$ -linear resistivity and planckian dissipation in overdoped cuprates*. Nature Physics **15**, 142–147 (2019).
- [74] Y. Nakajima, T. Metz, C. Eckberg, K. Kirshenbaum, A. Hughes, R. Wang, L. Wang, S. R. Saha, I.-L. Liu, N. P. Butch, et al. *Quantum-critical scale invariance in a transition metal alloy*. Communications Physics **3**, 1–8 (2020).
- [75] Y. Cao, D. Chowdhury, D. Rodan-Legrain, O. Rubies-Bigorda, K. Watanabe, T. Taniguchi, T. Senthil, and P. Jarillo-Herrero. *Strange metal in magic-angle graphene with near planckian dissipation*. Physical Review Letters **124**, 076801 (2020).

- [76] A. Kamenev, *Course 3 many-body theory of non-equilibrium systems*, in *Nanophysics: coherence and transport*, Vol. 81, edited by H. Bouchiat, Y. Gefen, S. Guéron, G. Montambaux, and J. Dalibard, Les Houches (Elsevier, 2005), pp. 177–246.
- [77] A. Chen, R. Ilan, F. De Juan, D. Pikulin, and M. Franz. *Quantum holography in a graphene flake with an irregular boundary*. *Physical Review Letters* **121**, 036403 (2018).
- [78] I. Danshita, M. Hanada, and M. Tezuka. *Creating and probing the sachdev-ye-kitaev model with ultracold gases: towards experimental studies of quantum gravity*. *Progress of Theoretical and Experimental Physics* **2017** (2017).
- [79] M. Franz and M. Rozali. *Mimicking black hole event horizons in atomic and solid-state systems*. *Nature Reviews Materials* **3**, 491–501 (2018).
- [80] A. V. Lunkin, K. S. Tikhonov, and M. V. Feigel'man. *Sachdev-ye-kitaev model with quadratic perturbations: the route to a non-fermi liquid*. *Phys. Rev. Lett.* **121**, 236601 (2018).
- [81] D. S. Gorbunov and V. A. Rubakov. *Introduction to the theory of the early universe: cosmological perturbations and inflationary theory*. (World Scientific, 2011).
- [82] B. Follin, L. Knox, M. Millea, and Z. Pan. *First Detection of the Acoustic Oscillation Phase Shift Expected from the Cosmic Neutrino Background*. *Phys. Rev. Lett.* **115**, 091301 (2015) [arXiv:1503.07863 \[astro-ph.CO\]](#).
- [83] S. Weinberg. *Universal Neutrino Degeneracy*. *Phys. Rev.* **128**, 1457–1473 (1962).
- [84] C. Weinheimer and K. Zuber. *Neutrino masses*. *Annalen Phys.* **525**, 565–575 (2013) [arXiv:1307.3518 \[hep-ex\]](#).
- [85] M. Betti et al. *Neutrino physics with the PTOLEMY project: active neutrino properties and the light sterile case*. [arXiv:1902.05508](#) (2019).
- [86] A. G. Cocco, G. Mangano, and M. Messina. *Probing low energy neutrino backgrounds with neutrino capture on beta decaying nuclei*. *Journal of Cosmology and Astroparticle Physics* **2007**, 015 (2007).
- [87] A. Faessler, R. Hodak, S. Kovalenko, and F. Simkovic. *Beta Decaying Nuclei as a Probe of Cosmic Neutrino Background*. [arXiv:1102.1799](#) (2011).

- [88] X. Qian and P. Vogel. *Neutrino mass hierarchy*. Progress in Particle and Nuclear Physics **83**, 1–30 (2015).
- [89] C. Akers, N. Engelhardt, and D. Harlow. *Simple holographic models of black hole evaporation*. JHEP **08**, 032 (2020).
- [90] KATRIN. *Katrin design report 2004*. Wissenschaftliche Berichte FZKA **7090** (2005).
- [91] Y. Cheipesh, V. Cheianov, and A. Boyarsky. *Navigating the pitfalls of relic neutrino detection*. Physical Review D **104**, 116004 (2021).
- [92] Z. Tan. *Effects of x ray edge in the ptolemy project*. (Master Thesis, 2021).
- [93] O. Mikulenko, Y. Cheipesh, V. Cheianov, and A. Boyarsky. *Can we use heavy nuclei to detect relic neutrinos?*, arXiv:2111.09292 (2021).
- [94] M. S. Athar, S. W. Barwick, T. Brunner, J. Cao, M. Danilov, K. Inoue, T. Kajita, M. Kowalski, M. Lindner, K. R. Long, et al. *Status and perspectives of neutrino physics*. Progress in Particle and Nuclear Physics, 103947 (2022).
- [95] S. Weinberg. *Universal neutrino degeneracy*. Physical Review **128**, 1457 (1962).
- [96] E. Baracchini, M. Betti, M. Biasotti, A. Bosca, F. Calle, J. Carabe-Lopez, G. Cavoto, C. Chang, A. Cocco, A. Colijn, et al. *Ptolemy: a proposal for thermal relic detection of massive neutrinos and directional detection of mev dark matter*. arXiv:1808.01892 (2018).
- [97] A. V. Balatsky, I. Vekhter, and J.-X. Zhu. *Impurity-induced states in conventional and unconventional superconductors*. Reviews of Modern Physics **78**, 373 (2006).
- [98] A. Sakurai. *Comments on superconductors with magnetic impurities*. Progress of Theoretical Physics **44**, 1472–1476 (1970).
- [99] D. J. Clarke, J. D. Sau, and S. Das Sarma. *Probability and braiding statistics in majorana nanowires*. Physical Review B **95**, 155451 (2017).
- [100] J. Perk and H. Capel. *Time-dependent  $xx$ -correlation functions in the one-dimensional  $xy$ -model*. Physica A: Statistical Mechanics and its Applications **89**, 265–303 (1977).
- [101] J. Perk, H. Capel, G. Quispel, and F. Nijhoff. *Finite-temperature correlations for the ising chain in a transverse field*. Physica A: Statistical Mechanics and its Applications **123**, 1–49 (1984).

- [102] S. Bravyi. *Lagrangian representation for fermionic linear optics*. arXiv: 0404180 (2004).
- [103] B. Bauer, T. Karzig, R. Mishmash, A. Antipov, and J. Alicea. *Dynamics of majorana-based qubits operated with an array of tunable gates*. SciPost Physics **5**, 004 (2018).
- [104] I. Klich. *A note on the full counting statistics of paired fermions*. Journal of Statistical Mechanics: Theory and Experiment **2014**, P11006 (2014).
- [105] J. C. Budich and E. Ardonne. *Equivalent topological invariants for one-dimensional majorana wires in symmetry class d*. Physical Review B **88**, 075419 (2013).
- [106] P. De Gennes. *Superconductivity of metals and alloys wa benjamin*. Inc., New York (1966).
- [107] J. Rubow and U. Wolff. *A factorization algorithm to compute pfaffians*. Computer Physics Communications **182**, 2530–2532 (2011).
- [108] M. Wimmer. *Algorithm 923: efficient numerical computation of the pfaffian for dense and banded skew-symmetric matrices*. ACM Transactions on Mathematical Software (TOMS) **38**, 1–17 (2012).
- [109] C. W. J. Beenakker, A. Grabsch, and Y. Herasymenko. *Electrical detection of the majorana fusion rule for chiral edge vortices in a topological superconductor*. SciPost Physics **6**, 022 (2019).
- [110] J. Dahlhaus, B. Béri, and C. W. J. Beenakker. *Random-matrix theory of thermal conduction in superconducting quantum dots*. Physical Review B **82**, 014536 (2010).
- [111] F. J. Dyson. *The threefold way. algebraic structure of symmetry groups and ensembles in quantum mechanics*. Journal of Mathematical Physics **3**, 1199–1215 (1962).
- [112] D. Ivanov. *The supersymmetric technique for random-matrix ensembles with zero eigenvalues*. Journal of Mathematical Physics **43**, 126–153 (2002).
- [113] D. I. Pikulin, J. Dahlhaus, M. Wimmer, H. Schomerus, and C. W. J. Beenakker. *A zero-voltage conductance peak from weak antilocalization in a majorana nanowire*. New Journal of Physics **14**, 125011 (2012).

- [114] C. Barbosa, T Guhr, and H. Harney. *Impact of isospin breaking on the distribution of transition probabilities*. Physical Review E **62**, 1936 (2000).
- [115] B. Dietz, T. Guhr, H. Harney, and A. Richter. *Strength distributions and symmetry breaking in coupled microwave billiards*. Physical Review Letters **96**, 254101 (2006).
- [116] V. L. Girko. *Theory of random determinants*. Vol. 45 (Springer Science & Business Media, 2012).
- [117] P. J. Forrester and E. Nordenstam. *The anti-symmetric gue minor process*. arXiv:0804.3293 (2008).
- [118] A. Edelman and M. La Croix. *The singular values of the gue (less is more)*. Random Matrices: Theory and Applications **4**, 1550021 (2015).
- [119] P. J. Forrester. *Log-gases and random matrices (lms-34)*. (Princeton University Press, 2010).
- [120] E. C. Rowell and Z. Wang. *Degeneracy and non-abelian statistics*. Physical Review A **93**, 030102 (2016).
- [121] N. Read and D. Green. *Paired states of fermions in two dimensions with breaking of parity and time-reversal symmetries and the fractional quantum hall effect*. Physical Review B **61**, 10267 (2000).
- [122] A. Grabsch, Y. Cheipesh, and C. W. J. Beenakker. *Pfaffian formula for fermion parity fluctuations in a superconductor and application to majorana fusion detection*. Annalen der Physik **531**, 1900129 (2019).
- [123] Y. Makhlin, G. Schön, and A. Shnirman. *Quantum-state engineering with josephson-junction devices*. Reviews of Modern Physics **73**, 357 (2001).
- [124] R. Zitko. *Sneg-mathematica package for symbolic calculations with second-quantization-operator expressions*. arXiv:1105.4697 (2011).
- [125] D. Litinski and F. Von Oppen. *Braiding by majorana tracking and long-range cnot gates with color codes*. Physical Review B **96**, 205413 (2017).
- [126] D. Razmadze. *Charge sensing of epi-al inas nanowire devices: towards majorana fusion rule experiment*. (Niels Bohr Institute, Copenhagen University, 2017).

- [127] S. Albrecht, E. Hansen, A. P. Higginbotham, F. Kuemmeth, T. Jespersen, J. Nygård, P. Krogstrup, J. Danon, K. Flensberg, and C. Marcus. *Transport signatures of quasiparticle poisoning in a majorana island*. Physical Review Letters **118**, 137701 (2017).
- [128] A. Altland and B. D. Simons. *Condensed matter field theory*. (Cambridge university press, 2010).
- [129] T. Senthil. *Critical fermi surfaces and non-fermi liquid metals*. Physical Review B **78**, 035103 (2008).
- [130] B. Keimer, S. A. Kivelson, M. R. Norman, S. Uchida, and J. Zaanen. *From quantum matter to high-temperature superconductivity in copper oxides*. Nature **518**, 179–186 (2015).
- [131] C. Varma, P. B. Littlewood, S. Schmitt-Rink, E. Abrahams, and A. Ruckenstein. *Phenomenology of the normal state of cu-o high-temperature superconductors*. Physical Review Letters **63**, 1996 (1989).
- [132] S. Sachdev. *Quantum phase transitions*. (Cambridge university press, 2011).
- [133] J. Zaanen. *Why the temperature is high*. Nature **430**, 512–513 (2004).
- [134] S. H. Shenker and D. Stanford. *Stringy effects in scrambling*. Journal of High Energy Physics **2015**, 1–34 (2015).
- [135] D. A. Roberts and B. Swingle. *Lieb-robinson bound and the butterfly effect in quantum field theories*. Physical Review Letters **117**, 091602 (2016).
- [136] A. Kitaev, *Kitp program: entanglement in strongly-correlated quantum matter*, 2015.
- [137] S. Sachdev. *Bekenstein-hawking entropy and strange metals*. Physical Review X **5**, 041025 (2015).
- [138] K. Bulycheva. *A note on the syk model with complex fermions*. Journal of High Energy Physics **2017**, 1–29 (2017).
- [139] A. A. Patel, M. J. Lawler, and E.-A. Kim. *Coherent superconductivity with a large gap ratio from incoherent metals*. Physical Review Letters **121**, 187001 (2018).
- [140] I. Esterlis and J. Schmalian. *Cooper pairing of incoherent electrons: an electron-phonon version of the sachdev-ye-kitaev model*. Physical Review B **100**, 115132 (2019).

- [141] Y. Wang. *Solvable strong-coupling quantum-dot model with a non-fermi-liquid pairing transition*. Physical Review Letters **124**, 017002 (2020).
- [142] D. Chowdhury and E. Berg. *Intrinsic superconducting instabilities of a solvable model for an incoherent metal*. Physical Review Research **2**, 013301 (2020).
- [143] L. Kouwenhoven and C. Marcus. *Quantum dots*. Physics World **11**, 35 (1998).
- [144] M. Maple, W. Fertig, A. Mota, L. DeLong, D. Wohlleben, and R. Fitzgerald. *The re-entrant superconducting-normal phase boundary of the kondo system (La, Ce)Al<sub>2</sub>*. Solid State Communications **11**, 829–834 (1972).
- [145] Y. B. Simons, O. Entin-Wohlman, Y. Oreg, and Y. Imry. *Phase diagram of reentrant and magnetic-field-induced superconducting states with kondo impurities in bulk and proximity-coupled compounds*. Physical Review B **86**, 064509 (2012).
- [146] E. Müller-Hartmann and J. Zittartz. *Kondo effect in superconductors*. Physical Review Letters **26**, 428 (1971).
- [147] G. Riblet and K. Winzer. *Vanishing of superconductivity below a second transition temperature in (La<sub>1-x</sub>Ce<sub>x</sub>)Al<sub>2</sub> alloys due to the kondo effect*. Solid State Communications **9**, 1663–1665 (1971).
- [148] E. Müller-Hartmann, B. Schuh, and J. Zittartz. *Pair-breaking in kondo superconductors*. Solid State Communications **19**, 439–442 (1976).
- [149] J. Melsen, P. Brouwer, K. Frahm, and C. W. J. Beenakker. *Superconductor-proximity effect in chaotic and integrable billiards*. Physica Scripta **1997**, 223 (1997).
- [150] H. Schomerus and C. W. J. Beenakker. *Excitation spectrum of andreev billiards with a mixed phase space*. Physical Review Letters **82**, 2951 (1999).
- [151] A. Lodder and Y. V. Nazarov. *Density of states and the energy gap in andreev billiards*. Physical Review B **58**, 5783 (1998).
- [152] I. Adagideli and C. W. J. Beenakker. *Ehrenfest-time-dependent excitation gap in a chaotic andreev billiard*. Physical Review Letters **89**, 237002 (2002).

- [153] M. Vavilov and A. Larkin. *Quantum disorder and quantum chaos in andreev billiards*. Physical Review B **67**, 115335 (2003).
- [154] R. Richardson. *A restricted class of exact eigenstates of the pairing-force hamiltonian*. (1963).
- [155] J. von Delft, A. D. Zaikin, D. S. Golubev, and W. Tichy. *Parity-affected superconductivity in ultrasmall metallic grains*. Physical Review Letters **77**, 3189 (1996).
- [156] K. Matveev and A. Larkin. *Parity effect in ground state energies of ultrasmall superconducting grains*. Physical Review Letters **78**, 3749 (1997).
- [157] S. Banerjee and E. Altman. *Solvable model for a dynamical quantum phase transition from fast to slow scrambling*. Physical Review B **95**, 134302 (2017).
- [158] X. Chen, R. Fan, Y. Chen, H. Zhai, and P. Zhang. *Competition between chaotic and nonchaotic phases in a quadratically coupled sachdev-ye-kitaev model*. Physical Review Letters **119**, 207603 (2017).
- [159] S.-K. Jian and H. Yao. *Solvable sachdev-ye-kitaev models in higher dimensions: from diffusion to many-body localization*. Physical Review Letters **119**, 206602 (2017).
- [160] L. Gor’Kov. *On the energy spectrum of superconductors*. Sov. Phys. JETP **7**, 158 (1958).
- [161] Y. Malitsky. *Golden ratio algorithms for variational inequalities*. Mathematical Programming **184**, 383–410 (2020).
- [162] A. Karch, K. Limtragool, and P. W. Phillips. *Unparticles and anomalous dimensions in the cuprates*. Journal of High Energy Physics **2016**, 1–18 (2016).
- [163] C. W. J. Beenakker, *Andreev billiards*, in *Quantum dots: a doorway to nanoscale physics* (Springer, 2005), pp. 131–174.
- [164] J. Couch, S. Eccles, P. Nguyen, B. Swingle, and S. Xu. *Speed of quantum information spreading in chaotic systems*. Physical Review B **102**, 045114 (2020).
- [165] S. Grozdanov, K. Schalm, and V. Scopelliti. *Black hole scrambling from hydrodynamics*. Physical Review Letters **120**, 231601 (2018).
- [166] S. Grozdanov, K. Schalm, and V. Scopelliti. *Kinetic theory for classical and quantum many-body chaos*. Physical Review E **99**, 012206 (2019).

- [167] M. Abramowitz and I. A. Stegun. *Handbook of mathematical functions with formulas, graphs, and mathematical tables*. Vol. 55 (US Government printing office, 1964).
- [168] Y.-M. Wu, A. Abanov, Y. Wang, and A. V. Chubukov. *Special role of the first matsubara frequency for superconductivity near a quantum critical point: nonlinear gap equation below  $t_c$  and spectral properties in real frequencies*. *Physical Review B* **99**, 144512 (2019).
- [169] A. Romero-Bermúdez, K. Schalm, and V. Scopelliti. *Regularization dependence of the otoc. which lyapunov spectrum is the physical one?*, *Journal of High Energy Physics* **2019**, 1–32 (2019).
- [170] A. Almheiri, A. Milekhin, and B. Swingle. *Universal constraints on energy flow and syk thermalization*. arXiv:1912.04912.
- [171] P. Zhang. *Evaporation dynamics of the sachdev-ye-kitaev model*. *Phys. Rev. B* **100**, 245104 (2019).
- [172] S. W. Hawking. *Black hole explosions?*, *Nature* **248**, 30–31 (1974).
- [173] S. W. Hawking. *Breakdown of predictability in gravitational collapse*. *Phys. Rev. D* **14**, 2460–2473 (1976).
- [174] D. N. Page. *Information in black hole radiation*. *Phys. Rev. Lett.* **71**, 3743–3746 (1993).
- [175] A. Almheiri, N. Engelhardt, D. Marolf, and H. Maxfield. *The entropy of bulk quantum fields and the entanglement wedge of an evaporating black hole*. *J. High Energy Phys.* **2019**, 63 (2019).
- [176] A. Almheiri, R. Mahajan, and J. Maldacena. *Islands outside the horizon*. arXiv:1910.11077.
- [177] I. Danshita, M. Hanada, and M. Tezuka. *Creating and probing the Sachdev-Ye-Kitaev model with ultracold gases: Towards experimental studies of quantum gravity*. *PTEP* **2017**, 083I01 (2017).
- [178] C. Wei and T. A. Sedrakyan. *Optical lattice platform for the sachdev-ye-kitaev model*. *Phys. Rev. A* **103**, 013323 (2021).
- [179] L. García-Álvarez, I. L. Egusquiza, L. Lamata, A. del Campo, J. Sonner, and E. Solano. *Digital quantum simulation of minimal AdS/CFT*. *Phys. Rev. Lett.* **119**, 040501 (2017).
- [180] Z. Luo, Y.-Z. You, J. Li, C.-M. Jian, D. Lu, C. Xu, B. Zeng, and R. Laflamme. *Quantum simulation of the non-fermi-liquid state of sachdev-ye-kitaev model*. *npj Quantum Information* **5**, 53 (2019).

- [181] R. Babbush, D. W. Berry, and H. Neven. *Quantum simulation of the sachdev-ye-kitaev model by asymmetric qubitization*. *Phys. Rev. A* **99**, 040301(R) (2019).
- [182] Y. Gu, A. Kitaev, S. Sachdev, and G. Tarnopolsky. *Notes on the complex Sachdev-Ye-Kitaev model*. *J. High Energy Phys.* **2020**, 157 (2020).
- [183] N. V. Gnezdilov, J. A. Hutasoit, and C. W. J. Beenakker. *Low-high voltage duality in tunneling spectroscopy of the sachdev-ye-kitaev model*. *Phys. Rev. B* **98**, 081413(R) (2018).
- [184] O. Can, E. M. Nica, and M. Franz. *Charge transport in graphene-based mesoscopic realizations of sachdev-ye-kitaev models*. *Phys. Rev. B* **99**, 045419 (2019).
- [185] A. Altland, D. Bagrets, and A. Kamenev. *Sachdev-ye-kitaev non-fermi-liquid correlations in nanoscopic quantum transport*. *Phys. Rev. Lett.* **123**, 226801 (2019).
- [186] A. Kruchkov, A. A. Patel, P. Kim, and S. Sachdev. *Thermoelectric power of sachdev-ye-kitaev islands: probing bekenstein-hawking entropy in quantum matter experiments*. *Phys. Rev. B* **101**, 205148 (2020).
- [187] A. I. Pavlov and M. N. Kiselev. *Quantum thermal transport in the charged sachdev-ye-kitaev model: thermoelectric coulomb blockade*. *Phys. Rev. B* **103**, L201107 (2021).
- [188] D. V. Khveshchenko. *One SYK single electron transistor*. *Lithuanian Journal of Physics* **60**, 3 (2020).
- [189] D. V. Khveshchenko. *Connecting the SYK dots*. *Condensed Matter* **5**, 37 (2020).
- [190] A. Eberlein, V. Kasper, S. Sachdev, and J. Steinberg. *Quantum quench of the sachdev-ye-kitaev model*. *Phys. Rev. B* **96**, 205123 (2017).
- [191] R. Bhattacharya, D. P. Jatkar, and N. Sorokhaibam. *Quantum quenches and thermalization in SYK models*. *J. High Energy Phys.* **2019**, 66 (2019).
- [192] C. Kuhlenskamp and M. Knap. *Periodically driven sachdev-ye-kitaev models*. *Phys. Rev. Lett.* **124**, 106401 (2020).
- [193] A. Halder, P. Halder, S. Bera, I. Mandal, and S. Banerjee. *Quench, thermalization, and residual entropy across a non-fermi liquid to fermi liquid transition*. *Phys. Rev. Research* **2**, 013307 (2020).

- [194] X.-Y. Song, C.-M. Jian, and L. Balents. *Strongly correlated metal built from sachdev-ye-kitaev models*. *Phys. Rev. Lett.* **119**, 216601 (2017).
- [195] Y. Malitsky. *Golden ratio algorithms for variational inequalities*. *Mathematical Programming* **184**, 383–410 (2020).
- [196] Y. Cheipesh, A. I. Pavlov, V. Scopelliti, J. Tworzydło, and N. V. Gnezdilov. *Reentrant superconductivity in a quantum dot coupled to a sachdev-ye-kitaev metal*. *Phys. Rev. B* **100**, 220506(R) (2019).
- [197] O. Parcollet, A. Georges, G. Kotliar, and A. Sengupta. *Overscreened multichannel  $SU(N)$  kondo model: large- $N$  solution and conformal field theory*. *Phys. Rev. B* **58**, 3794–3813 (1998).
- [198] O. Can and M. Franz. *Solvable model for quantum criticality between the sachdev-ye-kitaev liquid and a disordered fermi liquid*. *Phys. Rev. B* **100**, 045124 (2019).
- [199] D. Chowdhury, Y. Werman, E. Berg, and T. Senthil. *Translationally invariant non-fermi-liquid metals with critical fermi surfaces: solvable models*. *Phys. Rev. X* **8**, 031024 (2018).
- [200] M. Tikhanovskaya, H. Guo, S. Sachdev, and G. Tarnopolsky. *Excitation spectra of quantum matter without quasiparticles. i. sachdev-ye-kitaev models*. *Phys. Rev. B* **103**, 075141 (2021).
- [201] L. S. Levitov and G. B. Lesovik. *Charge distribution in quantum shot noise*. *JETP Lett.* **58**, 230 (1993).
- [202] L. S. Levitov, H. Lee, and G. B. Lesovik. *Electron counting statistics and coherent states of electric current*. *Journal of Mathematical Physics* **37**, 4845–4866 (1996).
- [203] C. Varma, Z. Nussinov, and W. van Saarloos. *Singular or non-fermi liquids*. *Physics Reports* **361**, 267–417 (2002).
- [204] B. Follin, L. Knox, M. Millea, and Z. Pan. *First detection of the acoustic oscillation phase shift expected from the cosmic neutrino background*. *Physical Review Letters* **115**, 091301 (2015).
- [205] A. Faessler, R. Hodák, S. Kovalenko, and F. Šimkovic, *Can one measure the cosmic neutrino background?*, in *Quarks, nuclei and stars: memorial volume dedicated to gerald e. brown* (World Scientific, 2017), pp. 81–91.
- [206] A. G. Cocco, G. Mangano, and M. Messina. *Low energy antineutrino detection using neutrino capture on electron capture decaying nuclei*. *Physical Review D* **79**, 053009 (2009).

- [207] J. Wolf and KATRIN. *The katrin neutrino mass experiment*. Nuclear Instruments and Methods in Physics Research Section A: Accelerators, Spectrometers, Detectors and Associated Equipment **623**, 442–444 (2010).
- [208] L. Bodine, D. Parno, and R. Robertson. *Assessment of molecular effects on neutrino mass measurements from tritium  $\beta$  decay*. Physical Review C **91**, 035505 (2015).
- [209] S Betts, W. Blanchard, R. Carnevale, C Chang, C Chen, S Chidzik, L Ciebiera, P Cloessner, A Cocco, A Cohen, et al. *Development of a relic neutrino detection experiment at ptolemy: princeton tritium observatory for light, early-universe, massive-neutrino yield*. arXiv:1307.4738 (2013).
- [210] M. Messina. *The ptolemy project: from an idea to a real experiment for detecting cosmological relic neutrinos*. Frascati Phys. Ser. (2018).
- [211] A. G. Cocco. *Ptolemy - towards cosmological relic neutrino detection*. PoS (2017) **10.22323/1.283.0092**.
- [212] Y.-F. Li. *Detection prospects of the cosmic neutrino background*. International Journal of Modern Physics A **30**, 1530031 (2015).
- [213] A. J. Long, C. Lunardini, and E. Sabancilar. *Detecting non-relativistic cosmic neutrinos by capture on tritium: phenomenology and physics potential*. Journal of Cosmology and Astroparticle Physics **2014**, 038 (2014).
- [214] S. Mertens, T. Lasserre, S. Groh, G. Drexlin, F. Glueck, A. Huber, A. Poon, M. Steidl, N. Steinbrink, and C. Weinheimer. *Sensitivity of next-generation tritium beta-decay experiments for kev-scale sterile neutrinos*. Journal of Cosmology and Astroparticle Physics **2015**, 020 (2015).
- [215] S. S. Masood, S. Nasri, J. Schechter, M. A. Tórtola, J. W. Valle, and C. Weinheimer. *Exact relativistic  $\beta$  decay endpoint spectrum*. Physical Review C **76**, 045501 (2007).
- [216] M. Moaied, J. Moreno, M. Caturla, F. Ynduráin, and J. Palacios. *A theoretical study of the dynamics of atomic h on graphene bilayers*. arXiv:1405.3165 (2014).
- [217] D. Henwood and J. D. Carey. *Ab initio investigation of molecular hydrogen physisorption on graphene and carbon nanotubes*. Physical Review B **75**, 245413 (2007).

- [218] H. González-Herrero, E. Cortés-del Río, P. Mallet, J. Veuillen, J. Palacios, J. Gómez-Rodríguez, I. Brihuega, and F. Ynduráin. *Hydrogen physisorption channel on graphene: a highway for atomic h diffusion*. 2D Materials **6**, 021004 (2019).
- [219] V. Ivanovskaya, A. Zobelli, D. Teillet-Billy, N. Rougeau, V. Sidis, and P. Briddon. *Hydrogen adsorption on graphene: a first principles study*. The European Physical Journal B **76**, 481–486 (2010).
- [220] D. Boukhvalov. *Modeling of hydrogen and hydroxyl group migration on graphene*. Physical Chemistry Chemical Physics **12**, 15367–15371 (2010).
- [221] A. Faessler, R. Hodak, S. Kovalenko, and F. Simkovic. *Search for the cosmic neutrino background and katrin*. arXiv:1304.5632 (2013).
- [222] J. A. Formaggio, A. L. C. de Gouvêa, and R. H. Robertson. *Direct measurements of neutrino mass*. Physics Reports **914**, 1–54 (2021).
- [223] J. Wolf. *The KATRIN Neutrino Mass Experiment*. arXiv:0810.3281 (2010).
- [224] R. Lazauskas, P. Vogel, and C. Volpe. *Charged current cross section for massive cosmological neutrinos impinging on radioactive nuclei*. J. Phys. G **35**, 025001 (2008) arXiv:0710.5312 [astro-ph].
- [225] M. Blennow. *Prospects for cosmic neutrino detection in tritium experiments in the case of hierarchical neutrino masses*. Phys. Rev. D **77**, 113014 (2008) arXiv:0803.3762 [astro-ph].
- [226] Y. F. Li, Z.-z. Xing, and S. Luo. *Direct Detection of the Cosmic Neutrino Background Including Light Sterile Neutrinos*. Phys. Lett. B **692**, 261–267 (2010) arXiv:1007.0914 [astro-ph.CO].
- [227] A. J. Long, C. Lunardini, and E. Sabancilar. *Detecting non-relativistic cosmic neutrinos by capture on tritium: phenomenology and physics potential*. JCAP **08**, 038 (2014) arXiv:1405.7654 [hep-ph].
- [228] A. Loureiro, A. Cuceu, F. B. Abdalla, B. Moraes, L. Whiteway, M. McLeod, S. T. Balan, O. Lahav, A. Benoit-Lévy, M. Manera, et al. *Upper bound of neutrino masses from combined cosmological observations and particle physics experiments*. Physical Review Letters **123**, 081301 (2019).
- [229] K. Siegbahn. *Beta-and gamma-ray spectroscopy*. Indian Journal of Physics **30**, 47–49 (1955).

- [230] E. Konopinski. *The theory of beta radio activity*. (Oxford, Clarendon P., 1966).
- [231] H. Schopper. *Weak interactions and nuclear beta decay*. (Amsterdam, North-Holland Pub. Co., 1966).
- [232] M. Gell-Mann and M. Levy. *The axial vector current in beta decay*. *Nuovo Cim.* **16**, 705 (1960).
- [233] P. A. Zyla et al. *Review of Particle Physics*. *PTEP* **2020**, 083C01 (2020).
- [234] W. Bühring. *Beta decay theory using exact electron radial wave functions*. *Nuclear Physics* **40**, 472–488 (1963).
- [235] C. M. Baglin and E. A. McCutchan. *Nuclear Data Sheets for A=171*. *Nucl. Data Sheets* **151**, 334–718 (2018).
- [236] B. Singh. *Nuclear Data Sheets for A = 151*. *Nucl. Data Sheets* **110**, 1–264 (2009).
- [237] T. A. Carlson, C. W. Nestor, T. C. Tucker, and F. B. Malik. *Calculation of Electron Shake-Off for Elements from Z=2 to 92 with the Use of Self-Consistent-Field Wave Functions*. *Phys. Rev.* **169**, 27–36 (1968).
- [238] X. Mougeot. *Reliability of usual assumptions in the calculation of  $\beta$  and  $\nu$  spectra*. *Phys. Rev. C* **91**, [Erratum: *Phys.Rev.C* 92, 059902 (2015)], 055504 (2015).
- [239] X. Mougeot, M.-M. Bé, and C. Bisch. *Calculation of beta spectral shapes*. *Radioprotection* **49**, 269–273 (2014).
- [240] S. Ando and K. Sato. *Relic neutrino background from cosmological supernovae*. *New Journal of Physics* **6**, 170 (2004).
- [241] S. Nussinov and Z. Nussinov. *Quantum induced broadening—a challenge for cosmic neutrino background discovery*. arXiv:2108.03695 (2021).
- [242] O. Mikulenko, Y. Cheipesh, V. Cheianov, and A. Boyarsky. *Can we use heavy nuclei to detect relic neutrinos?*, (2021) arXiv:2111.09292 [hep-ph].
- [243] E. Hwang and S. Das Sarma. *Dielectric function, screening, and plasmons in two-dimensional graphene*. *Physical Review B* **75**, 205418 (2007).



# Summary

Majorana fermions have never been observed as fundamental particles. However, they appear in various system as low energy excitations - quasiparticles. Moreover, ordinary Standard Model neutrinos as well as a dark matter particle may appear to be Majorana fermion. This thesis studies different aspects and properties of the Majorana fermions in free and interacting systems.

Lowest energy excitations in topological superconductor have Majorana nature (called Majorana zero modes or MZMs). These modes are not fermions in a normal sense, but when the two of them are coupled such that their wavefunctions overlap (fused) - they form a fermion. Such MZMs are spatially separated, pinned to have exactly zero energy, are free of decoherence and have a non-abelian anyonic statistics under the exchange. One can see signatures of MZMs and their anyonic statistic through fusion. If one prepares four MZMs (denoted  $\gamma_i$ ) in the state where  $\gamma_1, \gamma_2$  and  $\gamma_3, \gamma_4$  form states with definite fermion parity, the outcome for the parity of the state formed from  $\gamma_2, \gamma_3$  will be non-deterministic, namely  $\langle i\gamma_2\gamma_3 \rangle = 0$ . This happens for an ideal system where the MZMs are well separated from the continuum. However, as was shown in chapter 2, in a real system with some degree of disorder this is no longer a distinctive feature of non-abelian MZMs. The underlying reason for this is an unfortunate coincidence that the systems that host topologically protected MZMs are also prone to accumulate other parasitic states near zero energy that can mimic the true MZMs in the observables.

Nevertheless, as is shown in chapter 3, one can overcome this obstacle by looking at the dynamical signatures of the ground-state degeneracy. In particular, one needs to compare the time-dependent evolution in the parameter space of coupling constants via two alternative pathways. The topological ground-state degeneracy of Majorana zero-modes causes a breakdown of adiabaticity that can be measured as a pathway-dependent fermion parity. The correlation between two pathways for the accidental degeneracies of the Andreev levels is distinct from what would follow from the Majorana fusion rule.

An opposite case of strongly interacting Majorana fermions becomes very interesting if the number of fermions  $N$  is big, interactions are all-to-all and randomly distributed. Such a model is called Sachdev-Ye-Kitaev model (SYK) and it comprises several peculiar properties: it possesses an exact solution at strong coupling lacking quasiparticles, it has an emergent conformal symmetry in the infrared and it saturates the upper bound on quantum chaos. In this thesis we study how these properties manifest themselves in observables. In particular, in chapter 4 we find that if one couples the SYK system to a superconductor, upon increasing the coupling strength up to the critical value, the pairing gap  $\Delta$  behaves as  $\eta\hbar/t_P$  at low temperatures, where  $\eta \sim 1$ . The lower critical temperature emerges with a further increase of the coupling strength so that the finite  $\Delta$  domain is settled between the two critical temperatures. This does not happen if one, instead, couples the superconductor to disordered but non-interacting fermions. In that case, upon increasing the coupling the superconductivity just dies out.

In chapter 5 we studied SYK system at initial temperature  $T$  coupled by a quench to a large fermionic reservoir kept at zero temperature. In such a system, a tunneling current appears and the dynamics of the discharging process of the SYK quantum dot reveals a distinctive characteristic of the non-Fermi liquid state. In particular, the current's half-life scales linearly in  $T$  at low temperatures, while for the Fermi liquid it scales as  $T^2$ .

The last part of this thesis which is chapters 6,7 and 8 is devoted to an experiment that aims at the detection of relic neutrinos. We show that in case of solid state base experimental architecture, namely when the  $\beta$ -decayers are attached to some kind of substrate (which is the only viable possibility so far) there is a fundamental intrinsic limitation on its energy resolution. It comes from a simple Heisenberg's uncertainty principle: when we restrict the  $\beta$ -emitter to a finite volume in space, it acquires uncertainty in its momentum which smears the spectrum. We also show that the only way to mitigate this effect is to use a heavier  $\beta$ -emitter, more detailed study shows that the only viable candidate is  $^{171}\text{Tm}$ . However, this does not solve all the problems since solid state materials host a whole zoo of elementary excitations that affect the intrinsic uncertainty of the detector through a range of mechanisms. The investigation of all these mechanisms and finding ways of mitigation requires close collaboration between high-level experts in both theoretical and experimental solid state physics and may lead to further modifications of the experimental architecture.

# Samenvatting

Majorana-fermionen zijn nooit waargenomen als fundamentele deeltjes. Ze verschijnen echter in verschillende systemen als excitaties met lage energie - quasideeltjes. Bovendien kunnen gewone neutrino's uit het Standaardmodel en een deeltje van donkere materie lijken op Majorana-fermionen. Dit proefschrift bestudeert verschillende aspecten en eigenschappen van de Majorana-fermionen in vrije en wisselwerkende systemen. De laagste energie-excitaties in topologische supergeleiders hebben Majorana-aard (de zogenaamde Majorana-zero-modes of MZM's). Deze toestanden zijn geen fermionen in de normale zin, maar wanneer de twee zodanig worden gekoppeld dat hun golf functies elkaar overlappen (fusion), vormen ze een fermion. Dergelijke MZM's zijn ruimtelijk gescheiden, hebben precies nul excitatie-energie, zijn vrij van decoherentie en hebben een niet-abelse anyonische statistiek onder de uitwisseling. Men kan tekenen van MZM's en hun anyonische statistiek zien door middel van fusie. Als men vier MZM's (aangeduid met  $\gamma_i$ ) voorbereidt in de toestand waarin  $\gamma_1, \gamma_2, \gamma_3, \gamma_4$  een toestand vormen met een bepaalde fermionpariteit, dan zal de uitkomst voor de pariteit van de toestand gevormd uit  $\gamma_2, \gamma_3$  niet-deterministisch zijn, namelijk  $\langle i\gamma_2\gamma_3 \rangle = 0$ . Dit gebeurt voor een ideaal systeem waarbij de MZM's goed gescheiden zijn van het continuüm. Zoals echter in hoofdstuk 2 wordt aangetoond, is dit in een echt systeem met enige mate van wanorde niet langer een onderscheidend kenmerk van niet-abelse MZM's. De onderliggende reden hiervoor is dat de systemen die topologisch beschermde MZM's hosten ook vatbaar zijn voor andere parasitaire toestanden in de buurt van nul-energie die de echte MZM's in de waarneembare objecten kunnen nabootsen. Desalniettemin, zoals wordt aangetoond in hoofdstuk 3, kan men dit obstakel overwinnen door te kijken naar de dynamische kenmerken van de ontarding van de grondtoestand. In het bijzonder moet men de tijdsafhankelijke evolutie in de parameterruimte van koppelingsconstanten vergelijken via twee alternatieve routes. De topologische ontarding van de grondtoestand van Majorana-zero-modes veroorzaakt een afbraak van adiabaticiteit die kan

worden gemeten als een padafhankelijke fermionpariteit. De correlatie tussen twee paden voor de toevallige ontaarding van de Andreev-niveaus is verschillend van wat zou volgen uit de Majorana-fusieregel. Een systeem van sterk wisselwerkende Majorana-fermionen wordt erg interessant als het aantal fermionen  $N$  groot is, interacties allen-op-allen zijn en willekeurig worden verdeeld. Zo'n model wordt het Sachdev-Ye-Kitaev-model (SYK) genoemd en bevat verschillende speciale eigenschappen: het heeft een exacte oplossing bij sterke koppeling zonder quasideeltjes, het heeft een conforme symmetrie in het infrarood en het is quantum-chaotisch. In dit proefschrift bestuderen we hoe deze eigenschappen zich manifesteren in waarneembare objecten. In het bijzonder vinden we in hoofdstuk 4 hoe de paar gap  $\Delta$  zich gedraagt als men het SYK-systeem koppelt aan een supergeleider. Een lagere kritische temperatuur ontstaat met een verdere toename van de koppelingssterkte. Dit gebeurt niet als men in plaats daarvan de supergeleider koppelt aan ongeordende maar niet-wisselwerkende fermionen. In dat geval valt bij het vergroten van de koppeling de supergeleiding gewoon weg. In hoofdstuk 5 hebben we het SYK-systeem bestudeerd als het gekoppeld is aan een groot fermionische reservoir dat op temperatuur nul wordt gehouden. In een dergelijk systeem verschijnt een tunnelstroom en de dynamiek van het ontladproces van het SYK-systeem (een quantum dot) onthult een onderscheidend kenmerk van de niet-Fermi toestand. In het bijzonder schaalde de halfwaardetijd van de stroom lineair met de temperatuur bij lage temperaturen, terwijl deze voor de Fermivloeistof kwadratisch schaalde. Het laatste deel van dit proefschrift, de hoofdstukken 6, 7 en 8, is gewijd aan een experiment dat zich richt op de detectie van neutrino's. We laten zien dat er een fundamentele intrinsieke beperking is op de energieresolutie van een gangbaar experiment. Het komt voort uit het onzekerheidsprincipe van Heisenberg: wanneer we de  $\beta$ -straal-emitter beperken tot een eindig volume in de ruimte, verwerft het een onzekerheid in zijn impuls die het spectrum uitsmeert. We laten ook zien dat de enige manier om dit effect te verminderen is om een zwaardere  $\beta$ -emitter te gebruiken. Meer gedetailleerd onderzoek toont aan dat de enige levensvatbare kandidaat  $^{171}\text{Tm}$  is. Dit lost echter niet alle problemen op, aangezien vastestofmaterialen een hele reeks elementaire excitaties herbergen die de intrinsieke onzekerheid van de detector beïnvloeden via een reeks mechanismen. Het onderzoek van al deze mechanismen vereist nauwe samenwerking tussen experts in zowel theoretische als experimentele vastestoffysica en kan leiden tot verdere aanpassingen van de experimentele apparatuur.

# Curriculum Vitæ

I was born on the 30th of September 1994 in Uzhgorod, Ukraine. When I was four, my family moved to Kyiv where I attended the primary and middle school in Lyceum 157. For the high school I went to Kyiv Natural Science Lyceum 145. During the last two years there I participated in various Ukrainian competitions in physics and math.

In 2012 I entered the Faculty of Physics of the Taras Shevchenko National University of Kyiv and in 2014 I was assigned to the Department of Quantum Field Theory. There, I completed my bachelor degree in 2016 under the supervision of Viktor Reshetnyak. After one year on the master program at the same university, I moved to Göttingen where I completed my master degree in physics (2017-2018) in the University of Göttingen under the supervision of Stefan Kehrein. During my master degree, I was a teaching assistant for the Introduction to Solid State Physics course at the same university.

In October 2017 I started my Ph.D. studies in The Netherlands, as a part of a joint project with Carlo Beenakker (Leiden University) and Anton Akhmerov (Delft University of Technology). I investigated how Andreev bound states can mimic topologically protected Majorana zero modes in various observables. Second direction of my research was the study of the signatures of the non-Fermi liquid phase of the SYK model. The third direction of my research was studying the role of the many-body phenomena in the experimental setup for the relic neutrino detection.

During my Ph.D. studies, I presented my research in The Netherlands, Germany, Italy and France. I was a teaching assistant for the Theory of Condensed Matter course and for the Advanced Theory Track program for bachelor students. I have also actively participated in scientific outreach by being a co-organizer and lecturer of the popular science courses for high-school pupils from Ukraine “Scientific revolutions of the beginning of XXth century”, co-organizer and mentor of the KAU BITP winter school "Frontiers in the condensed matter physics".



# List of Publications

- [1] V. Ohanesjan, Y. Cheipesh, N. V. Gnezdilov, A. I. Pavlov, K. Schalm *Energy dynamics, information and heat flow in quenched cooling and the crossover from quantum to classical thermodynamics*. [preprint arXiv:2204.12411](#), (2022).
- [2] PTOLEMY collaboration *Heisenberg's uncertainty principle in the PTOLEMY project: a theory update*. [preprint arXiv:2203.11228](#), (2022).
- [3] N. V. Gnezdilov, A. I. Pavlov, V. Ohanesjan, Y. Cheipesh, K. Schalm *Ultrafast dynamics of cold Fermi gas after a local quench* . [preprint arXiv:2108.12031](#), (2022).
- [4] Y. Cheipesh, V. Cheianov, A. Boyarsky *Navigating the pitfalls of relic neutrino detection*. [Physical Review D \*\*104\*\*, 11 \(2021\)](#) [Chapter 6].
- [5] O. Mikulenko, Y. Cheipesh, V. Cheianov, A. Boyarsky *Can we use heavy nuclei to detect relic neutrinos?* [preprint arXiv:2111.09292](#), (2021) [Chapter 7].
- [6] Y. Cheipesh, A. I. Pavlov, V. Ohanesjan, K. Schalm, N. V. Gnezdilov *Quantum tunneling dynamics in a complex-valued Sachdev-Ye-Kitaev model quenched-coupled to a cool bath*. [Physical Review B \*\*104\*\*, 11 \(2021\)](#) [Chapter 5].
- [7] D. O. Oriekhov, Y. Cheipesh, C. W. J. Beenakker *Voltage staircase in a current-biased quantum-dot Josephson junction*. [Physical Review B \*\*103\*\*, 9 \(2021\)](#).
- [8] Y. Cheipesh, L. Cevolani, S. Kehrein *Entanglement correction due to local interactions in many-body systems*. [preprint arXiv:2007.15908](#), (2020).

- [9] A. Grabsch, Y. Cheipesh, C. W. J. Beenakker *Dynamical Signatures of Ground-State Degeneracy to Discriminate against Andreev Levels in a Majorana Fusion Experiment*. [Advanced Quantum Technologies](#) **3**, 1 (2020) [Chapter 3].
- [10] Y. Cheipesh, A. I. Pavlov, V. Scopelliti, J. Tworzydło and N. V. Gnezdilov, *Reentrant superconductivity in a quantum dot coupled to a Sachdev-Ye-Kitaev metal*. [Physical Review B](#) **100**, 22 (2019) [Chapter 4].
- [11] A. Grabsch, Y. Cheipesh, C. W. J. Beenakker, *Pfaffian formula for fermion parity fluctuations in a superconductor and application to Majorana fusion detection*. [Annalen der Physik](#) **531**, 10 (2019) [Chapter 2].
- [12] Y. Cheipesh, L. Cevolani, S. Kehrein, *Exact description of the boundary theory of the Kitaev Toric Code with open boundary conditions*. [Physical Review B](#) **99**, 2 (2019)
- [13] Y. Hsiao, Ch. Su, Z. Yang, Y. Cheypesh, Jh. Yang, V. Reshetnyak, K. Chen, W. Lee, *Electrically active nanoantenna array enabled by varying the molecular orientation of an interfaced liquid crystal*. [RSC advances](#) **6**, 87 (2016)

# Stellingen

behorende bij het proefschrift

*Anyonic, cosmic, and chaotic: three faces of Majorana fermions*

1. A vanishing fermion parity in a superconductor fusion experiment can not become a distinctive signature of an isolated Majorana zero-mode. [chapter 2].
2. The absence of quasiparticles in SYK model manifests itself in a linear in temperature dependence of the tunneling current between it and the fermion bath. [chapter 5].
3. Many-body effects in the nano-device present in the experimental setup for the relic neutrino detection impose fundamental intrinsic limitation on its energy resolution. [chapter 6].
4. The detection of relic neutrinos in the  $\beta$ -decay spectrum of  ${}^3\text{H}$  is fundamentally impossible. The only viable isotope for neutrino detection is  ${}^{171}\text{Tm}$ . [chapter 7].
5. Any gauge-invariant lattice theory of Dirac fermions which preserves chiral symmetry must have a vanishing topological index.
6. Entanglement entropy is not a good measure of the complexity of the fermionic system.
7. There is a  $k$ -body basis independent measure of fermionic complexity  $C(k)$  that is zero for a product state, exponentially decreasing for a Fermi liquid state and  $\delta(k - k^*)$  with  $k^* \propto$  volume of the system for a chaotic state.
8. If one couples two fermionic systems, their internal energies will grow at timescales of the Fermi time  $\tau_F \sim 1/\varepsilon_F$  independently of their initial temperatures.

Yevheniia Cheipesh

27 november 2022